Delft University of Technology

Solidification modelling in metallic melt-pools
with application to welding and additive manufacturing

Liang, X.

Important note
To cite this publication, please use the final published version (if applicable).
Please check the document version above.

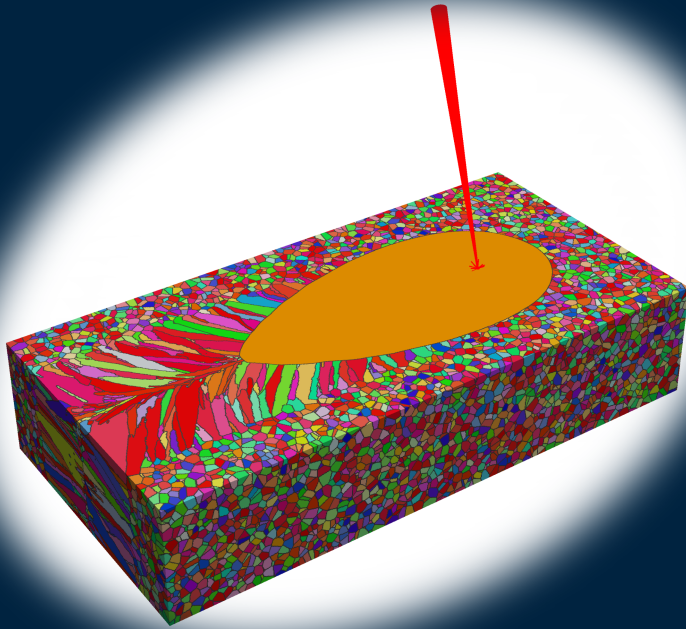# Solidification modelling in metallic melt-pools

with application to welding and additive manufacturing

Xiaohui Liang

SOLIDIFICATION MODELLING IN METALLIC MELT-POOLS

WITH APPLICATION TO WELDING AND ADDITIVE MANUFACTURING

Solidification modelling in metallic melt-pools

with application to welding and additive manufacturing

Dissertation

for the purpose of obtaining the degree of doctor
at Delft University of Technology,
by the authority of the Rector Magnificus Prof. dr. ir. T.H.J.J. van der Hagen,
chair of the Board for Doctorates,
to be defended publicly on
Tuesday 4 June 2024 at 12:30 o'clock

by

Xiaohui LIANG

Master of Science in Metallurgical Engineering,
RWTH Aachen University, Germany,
born in Henan, China.

This dissertation has been approved by the promotors.

Composition of the doctoral committee:

Rector Magnificus,	chairperson
Prof. dr. I.M. Richardson,	Delft University of Technology, promotor
Dr. ir. M.J.M. Hermans,	Delft University of Technology, promotor
Dr. ir. C. Bos,	Delft University of Technology, copromotor

Independent members:	
Prof. dr. ir. J.M.C. Mol,	Delft University of Technology
Prof. dr. S. Kenjeres,	Delft University of Technology
Prof. dr. D. Eskin,	Brunel University, England
Prof. dr. ir. L.A.I. Kestens,	Ghent University, Belgium
Dr. ir. S.E. Offerman,	Delft University of Technology, reserve member

An electronic version of this dissertation is available at http://repository.tudelft.nl/.

CONTENTS

SUMMARY

Advanced high strength steels (AHSS) have been widely employed in the automotive industry to meet the requirements of improving crash performance while reducing vehicle weight. The excellent performance of AHSS in strength and ductility comes from a dedicated design of alloy composition and microstructure. However, the addition of some alloying elements may lead to poor weldability. Solidification cracking tends to occur in AHSS containing detrimental elements such as phosphorous or sulfur under unfavorable welding conditions.

Solidification cracking is a complex problem associated with multiple physical phenomena at different length scales. During welding, with a localized heat input, the material is heated to melt, forming a weld pool. Upon cooling, a mushy zone consisting of solid grains and liquid channels forms behind the weld pool. As temperature drops, solid grains in the mushy zone grow, which tends to close liquid channels in the mushy zone. However, during solidification, detrimental elements segregate in the liquid, inhibiting the closure of the liquid channel. Meanwhile, due to solidification shrinkage and thermal contraction, the liquid channels experience a tensile load, which tends to open the liquid channel. If there is insufficient liquid feeding, solidification cracking occurs. Solidification cracking can be avoided by controlling parameters including alloy composition, microstructure and processing conditions like power, welding velocity, laser beam shapes, etc.

Due to the complexity, an accurate prediction of solidification cracking under various welding conditions is challenging. A full-field simulation of a welded component which incorporates all the physical phenomena and is capable of handling various welding conditions is not realistic with current computational power. To achieve an accurate prediction of solidification cracking, approximations and simplifications must be made while major physical mechanisms are still properly captured. Moreover, existing modelling techniques should be improved or adapted to fulfill the requirements of welding simulations.

This research starts from explicitly modelling segregation and solidification during welding. In the literature, cellular automata (CA) models and phase field (PF) models have been widely used to simulate segregation and solidified microstructure. The CA method is more computationally efficient compared to the PF method and thus is mainly adopted in the current research. A cellular automata solidification model is developed, where the growth velocity is determined based on kinetic undercooling at the interface. The state-of-the-art model incorporates a decentered growth algorithm to suppress grid anisotropy and a generalized height function method to calculate curvature accurately. To remove the dependency on the mesh size, a new diffusion term is proposed to handle the diffusion between the interface cells and liquid cells. Moreover, a solute redistribution method has been applied for each interface cell to resolve the mass balance error introduced by the virtual liquid cell assumption. The developed CA model is validated by simulating single-dendritic solidification in an Al-3Cu (wt.%) alloy. The simulated tip velocities agree with the prediction of the Kurz-Giovanola-Trivedi (KGT) model. With improvements in the

aspects of mesh-size independency and mass balance, the developed CA model is suitable for solidification simulation with a high undercooling, as is common in welding. It also provides an easier way to achieve multi-component solidification simulation compared to conventional CA solidification models, which need to solve a system of mass balance equations in interface cells. Despite the improvements made, due to the poor discretization of the solid-liquid interface, the CA method is less accurate compared to the phase field method. Up to now, no CA models can reproduce the dendrite tip velocity predicted by a Green function method in single-dendritic solidification simulations.

For better accuracy, the research was extended with a focus on PF modelling of segregation in the liquid channels in the mushy zone during welding. Following the frozen temperature gradient approximation, the complex thermal conditions during welding are approximated with a directional solidification condition defined by a constant temperature gradient and pulling velocity, which is the moving velocity of the liquidus isotherm. Under directional solidification conditions, columnar dendrite grains form and liquid channels exist in between neighboring grains, where solutes accumulate. The liquid channel structure and segregation is simulated with the PF model, while the solidification cracking susceptibility (SCS) is then quantified by calculating the pressure drop from the dendrite tip to the coalescence point of the liquid channels with an analytical model, the Rappaz-Drezet-Gremaud (RDG) model. A larger pressure drop represents a larger SCS. With the modelling setup, the influence of the temperature gradient and the pulling velocity on SCS have been investigated. Increasing the pulling velocity or decreasing the temperature gradient increases the pressure drop from the dendrite tip to the coalescence point, leading to an increase in SCS. Decreasing the primary dendrite arm spacing (PDAS) decreases the permeability of the liquid channel and the liquid channel length at the same time, resulting in a decrease in the pressure drop and SCS when the PDAS is small. Consideration of the PDAS dependency on the temperature gradient and the pulling velocity influences the value of the pressure drop but does not change the tendency of the SCS. The findings indicate that solidification cracking can be avoided by either decreasing the pulling velocity or increasing the temperature gradient or refining the grain size, as supported by experimental results. However, due to the high computational cost, the size of the simulation domain is limited. Moreover, the influence of process parameters on SCS cannot be considered directly due to the lack of macroscopic modelling.

To include the influence of process parameters, macroscopic thermal-mechanical modelling and microstructure modelling of the whole weld pool are necessary. The former is relatively easy to achieve, while the latter is, nevertheless, not achievable with the aforementioned CA model or PF model, as both models require a fine mesh size to simulate the liquid channel structure and segregation within the liquid channels. Simulating the solidification microstructure for the whole weld pool or the whole mushy zone requires a huge amount of computational resources. As an alternative to the numerical solution, the segregation in the liquid channel can be calculated analytically with the Scheil-Gulliver calculation, while the remaining question is how to achieve the microstructure simulation of the whole weld pool.

Therefore, the research addressed microstructure modelling of the whole weld pool. To this purpose, a special kind of CA model is adopted, which calculates the growth velocity as a function of local undercooling based on analytical models (LGK model or KGT model). In

this case, there is no need to solve the concentration profiles numerically, which permits a coarse mesh size and thus a reduction in the requirement of computational resources. These kind of CA models are called CAFE models, as such CA models are always coupled with a thermal finite element (FE) model. In this research, a CAFE model which is two orders of magnitude faster than conventional CAFE models has been developed. The acceleration comes from three different sources. Firstly, by adopting an exact temporal integration and a multi-layer capture algorithm, a large time step can be employed without compromising the simulation results. Secondly, the parallelism of the simulation codes is achieved in a shared-memory environment, enabling a more efficient load balance. Thirdly, a subdomain activation and deactivation method is employed to reduce the computation tasks. The proposed model is validated by simulating the grain morphology and texture of additively manufactured samples. A good agreement is achieved between the simulations and the experiments.

By coupling the CAFE model with a thermo-mechanical FE model and a granular model to calculate liquid pressure, a multi-physics multi-scale modelling framework is developed to predict solidification cracking. The thermo-mechanical FE model calculates the profiles of temperature and strain rate for the welded component during welding; the CAFE model simulates the solidification microstructure in the whole weld pool; and the granular model calculates the pressure drop in the liquid channel network determined based on the simulated microstructure and the Scheil-Gulliver calculations. The developed modelling framework is then validated by simulating welding experiments of a TRIP steel. With a constant ratio between the power and the welding velocity, increasing the welding velocity increases the maximum pressure drop in the mushy zone, indicating an increase in SCS. Grain refinement or decreasing the freezing temperature by changing the alloy composition leads to a decrease in the maximum pressure drop in the mushy zone, representing a decrease in SCS. The predictions from the modelling framework are supported by experimental findings in the literature.

In conclusions, the research starts from microstructure modelling of segregation and liquid channel structure with both the CA method and the PF method and finalizes with a multi-physics multi-scale modelling framework of solidification cracking. In this approach, several approximations and simplifications have been made to reach the final modelling framework for solidification cracking. The developed multi-scale multi-physics modelling framework incorporates major physical mechanisms at different length scales and paves a way to understand and predict solidification cracking under various welding conditions. It provides a theoretical basis to eliminate solidification cracking by tuning parameters including alloy composition, microstructure and processing parameters like power, welding velocity and laser beam shapes, etc. Moreover, with the acceleration in microstructure simulation, the developed CAFE model contributes to the development of a digital twin of additive manufacturing.

SAMENVATTING

Geavanceerde hogesterktestaalsoorten (AHSS) worden op grote schaal gebruikt in de auto-industrie om te voldoen aan de eisen van het verbeteren van de crashprestaties en tegelijkertijd het verminderen van het voertuiggewicht. De uitstekende prestaties van AHSS op het gebied van sterkte en ductiliteit zijn te danken aan een speciaal ontwerp van de legeringssamenstelling en microstructuur. de toevoeging van sommige legeringselementen kan leiden tot een slechte lasbaarheid. Stollingsscheuren hebben de neiging op te treden in AHSS die schadelijke elementen zoals fosfor of zwavel bevatten onder ongunstige lasomstandigheden.

Stollingsscheuren zijn een complex probleem dat verband houdt met meerdere fysische verschijnselen op verschillende lengteschalen. Tijdens het lassen wordt het materiaal, met een plaatselijke warmte-inbreng, verwarmd om te smelten, waardoor een smeltbad ontstaat. Bij afkoeling ontstaat een papperige zone bestaande uit vaste korrels en vloeistofkanalen vormt zich achter het smeltbad. Naarmate de temperatuur daalt, groeien vaste korrels in de papperige zone, waardoor de vloeistofkanalen in de papperige zone worden gesloten. Tijdens het stollen scheiden schadelijke elementen zich echter af in de vloeistof, waardoor de sluiting van het vloeistofkanaal wordt belemmerd. als gevolg van stollingskrimp en thermische samentrekking ondergaan de vloeistofkanalen een trekbelasting, waardoor het vloeistofkanaal de neiging heeft te openen. Als er onvoldoende vloeistoftoevoer is, treden stollingsscheuren op. Stollingsscheuren kunnen worden vermeden door parameters te controleren, waaronder de samenstelling van de legering, de microstructuur en de verwerking omstandigheden zoals vermogen, lassnelheid, laserstraalvormen, enz.

Vanwege de complexiteit is een nauwkeurige voorspelling van stollingsscheuren onder verschillende lasomstandigheden een uitdaging. Een full-field simulatie van een gelast onderdeel dat alle fysieke verschijnselen omvat en in staat is verschillende lasomstandigheden aan te kunnen, is met de huidige rekenkracht niet realistisch. Om een nauwkeurige voorspelling van stollingsscheuren te bereiken, moeten benaderingen en vereenvoudigingen worden gemaakt terwijl de belangrijkste fysieke mechanismen in kaart worden gebracht. Bovendien moeten bestaande modelleringstechnieken worden verbeterd of aangepast om aan de eisen van lassimulaties te voldoen.

Dit onderzoek vertrekt van het expliciet modelleren van segregatie en stolling tijdens het lassen. In de literatuur worden cellulaire automaten (CA)-modellen en faseveld-modellen (PF) op grote schaal gebruikt om segregatie en gestolde microstructuur te simuleren. De CA-methode is computationeel efficiënter vergeleken met de PF-methode en wordt daarom toegepast in het huidige onderzoek. Er is een stollingsmodel voor cellulaire automaten ontwikkeld, waarbij de groeisnelheid wordt bepaald op basis van kinetische onderkoeling op het grensvlak. Het state-of-the-art model omvat een gedecentreerd groeialgoritme om roostervorming te onderdrukken. anisotropie en een gegeneraliseerde hoogtefunctiemethode om de kromming nauwkeurig te berekenen. Om de afhankelijkheid van de maaswijdte weg te nemen, wordt een nieuwe diffusieterm voorgesteld om de diffusie tussen

de grensvlakcellen en vloeibare cellen te behandelen. Bovendien is voor elke cel een her-verdelingsmethode voor opgeloste stoffen toegepast. interfacecel om de massabalansfout op te lossen die wordt geïntroduceerd door de aanname van virtuele vloeibare cellen. Het ontwikkelde CA-model is gevalideerd door het simuleren van single-dendritische stolling in een Al-3Cu (wt.%) legering. De gesimuleerde tipsnelheden komen overeen met de voor-spelling van het Kurz-Giovanola-Trivedi (KGT)-model. Met verbeteringen in de aspecten van maaswijdte-onafhankelijkheid en massabalans is het ontwikkelde CA-model geschikt voor stollingssimulatie met een hoge onderkoeling, zoals gebruikelijk is bij lassen. Het biedt ook een eenvoudiger manier om multi-component stollingssimulatie te bereiken in vergelijking met conventionele CA-stollingsmodellen, die een systeem van massabalansver-gelijkingen in grensvlakcellen moeten oplossen. Ondanks de aangebrachte verbeteringen is de CA-methode, als gevolg van de slechte discretisatie van het vast-vloeistofgrensvlak, minder nauwkeurig vergeleken met de faseveldmethode. Tot nu toe kunnen geen enkele CA-modellen de dendriettipsnelheid reproduceren die wordt voorspeld door een Green-functiemethode in single-dendritische stollingssimulaties.

Voor een betere nauwkeurigheid werd het onderzoek uitgebreid met een focus op PF-modellering van de segregatie in de vloeistofkanalen in de papperige zone tijdens het lassen. Na de bevroren temperatuurgradiëntbenadering worden de complexe thermische omstandigheden tijdens het lassen benaderd met een directionele stollingsconditie gedefi-nieerd door een constante temperatuurgradiënt en treksnelheid, wat de bewegingssnelheid is van de liquidus-isotherm. Onder directionele stollingsomstandigheden vormen zich kolomvormige dendrietkorrels en bestaan er vloeistofkanalen tussen aangrenzende korrels, waar opgeloste stoffen zich ophopen. De vloeistofkanaalstructuur en segregatie wordt gesi-muleerd met de PF model, terwijl de gevoeligheid voor stollingsscheuren (SCS) vervolgens wordt gekwantificeerd door de drukval van de dendrietpunt naar het escentiesteenpunt van de vloeistofkanalen te berekenen met een analytisch model, het Rappaz-Drezet-Gremaud (RDG)-model. druppel vertegenwoordigt een grotere SCS. Met de modelleringsopstelling is de invloed van de temperatuurgradiënt en de treksnelheid op SCS onderzocht. Het verhogen van de treksnelheid of het verkleinen van de temperatuurgradiënt verhoogt de drukval van de dendriettip naar het coalescentiepunt, wat leidt tot Het verkleinen van de primaire dendrietarmafstand (PDAS) vermindert tegelijkertijd de permeabiliteit van het vloeistofkanaal en de lengte van het vloeistofkanaal, wat resulteert in een afname van de drukval en SCS wanneer de PDAS klein is. de PDAS-afhankelijkheid van de tempera-tuurgradiënt en de treksnelheid beïnvloedt de waarde van de drukval, maar verandert de neiging van de SCS niet. De bevindingen geven aan dat stollingsscheuren kunnen worden vermeden door de treksnelheid te verlagen of de temperatuurgradiënt te vergroten of door te verfijnen de korrelgrootte, zoals ondersteund door experimentele resultaten. Vanwege de hoge rekenkosten is de omvang van het simulatiedomein echter beperkt. Bovendien kan de invloed van procesparameters op SCS niet direct in aanmerking worden genomen vanwege het gebrek aan macroscopische modellering.

Om de invloed van procesparameters mee te nemen zijn macroscopische thermisch-mechanische modellering en microstructuurmodellering van het gehele smeltbad nood-zakelijk. Het eerste is relatief eenvoudig te realiseren, terwijl het laatste met het eerder genoemde CA-model of PF-model niettemin niet haalbaar is. aangezien beide modellen een fijne maaswijdte vereisen om de vloeistofkanaalstructuur en de segregatie binnen de

vloeistofkanalen te simuleren. Het simuleren van de stollingsmicrostructuur voor het hele smeltbad of de hele papperige zone vereist een enorme hoeveelheid computerhulpbronnen. Als alternatief voor de numerieke oplossing kan de segregatie in het vloeistofkanaal analytisch worden berekend met de Scheil-Gulliver-berekening, terwijl de resterende vraag is hoe de microstructuursimulatie van het hele smeltbad kan worden bereikt.

Daarom heeft het onderzoek zich gericht op het modelleren van de microstructuur van het hele smeltbad, waarvoor een speciaal soort CA-model wordt gebruikt, dat de groeisnelheid berekent als functie van lokale onderkoeling op basis van analytische modellen (LGK-model of KGT-model). In dit geval is het niet nodig om de concentratieprofielen numeriek op te lossen, wat een grove maaswijdte mogelijk maakt en dus de behoefte aan computerhulpbronnen vermindert. Dit soort CA-modellen worden CAFE-modellen genoemd, omdat dergelijke CA-modellen altijd gekoppeld zijn aan een thermisch eindige elementenmodel (FE). In dit onderzoek is een CAFE-model ontwikkeld dat twee ordes van grootte sneller is dan conventionele CAFE-modellen. De versnelling komt uit drie verschillende bronnen. Ten eerste door een exacte temporele integratie en een multi- Layer Capture-algoritme kan een grote tijdstap worden gebruikt zonder de simulatieresultaten in gevaar te brengen. Ten tweede wordt de parallelliteit van de simulatiecodes bereikt in een omgeving met gedeeld geheugen, waardoor een efficiëntere belastingsverdeling mogelijk is. Ten derde wordt er een subdomeinactiverings- en deactiveringsmethode gebruikt. gebruikt om de rekentaken te verminderen. Het voorgestelde model wordt gevalideerd door de korrelmorfologie en textuur van additief vervaardigde monsters te simuleren. Er wordt een goede overeenkomst bereikt tussen de simulaties en de experimenten.

Door het CAFE-model te koppelen aan een thermomechanisch FE-model en een granulair model om de vloeistofdruk te berekenen, wordt een multifysisch modelleringsraamwerk op meerdere schaal ontwikkeld om stollingsscheuren te voorspellen. Het thermomechanische FE-model berekent de profielen van temperatuur en rek snelheid voor het gelaste onderdeel tijdens het lassen, het CAFE-model simuleert de stollingsmicrostructuur in het gehele smeltbad en het granulaire model berekent de drukval in het vloeistofkanaalnetwerk, bepaald op basis van de gesimuleerde microstructuur en de Scheil-Gulliver-berekeningen. Het raamwerk wordt vervolgens gevalideerd door lasexperimenten met TRIP-staal te simuleren. Bij een constante verhouding tussen het vermogen en de lassnelheid verhoogt het verhogen van de lassnelheid de maximale drukval in de papperige zone, wat wijst op een toename van de SCS. De vriestemperatuur door het veranderen van de legeringssamenstelling leidt tot een afname van de maximale drukval in de papperige zone, wat een afname van de SCS betekent. De voorspellingen uit het modelleringsraamwerk worden ondersteund door experimentele bevindingen in de literatuur.

Concluderend: het onderzoek vertrekt van microstructuurmodellering van segregatie en vloeistofkanaalstructuur met zowel de CA-methode als de PF-methode en eindigt met een multifysisch multi-schaal modelleringsraamwerk van stollingsscheuren. gemaakt om het uiteindelijke modelleringsraamwerk voor stollingsscheuren te bereiken. Het ontwikkelde multi-schaal multi-fysische modelleringsraamwerk omvat belangrijke fysieke mechanismen op verschillende lengteschalen en maakt een manier vrij om stollingsscheuren onder verschillende lasomstandigheden te begrijpen en te voorspellen. Het biedt een theoretische basis voor elimineer stollingsscheuren door parameters af te stemmen, waaronder legeringssamenstelling, microstructuur en verwerkingsparameters zoals vermogen,

lassnelheid en laserstraalvormen, enz. Bovendien draagt het ontwikkelde CAFE-model, met de versnelling in microstructuursimulatie, bij aan de ontwikkeling van een digitale tweeling van additieve productie.

1

1

INTRODUCTION

1

1.1 Introduction

In the past decades, the increased importance of safety and vehicle emission has led to the need for higher-strength steels to improve the crash performance of automotive structures while allowing for a reduction in thickness and weight [1]. Meanwhile, formability is required to satisfy the manufacturing requirements and design flexibility [1]. This has led to the development of advanced high strength steels, such as DP (dual-phase) steel and TRIP (Transformation-induced-plasticity) steels, which possess higher strain hardening rates and formability compared to conventional high strength steels. The excellent performance of AHSS in mechanical properties and formability is achieved by engineering the microstructure through alloying and thermo-mechanical treatments. However, the high alloying contents in AHSS may result in a poor weldability. For example, solidification cracking tends to occur in laser welded TRIP steel components under unfavorable welding conditions [2]. Despite this, development of new steel grades is dedicated to increasing strength and ductility, while weldability tests can only be done in the later stage of steel development, when larger quantities of a trial steel are available.

Recently, the concept of digital twins has pave the way to next-generation industry [3, 4]. In the steel industry, a digital twin can be developed with through-process-modelling of the steel production route. With quick predictions of the microstructure and the mechanical properties of the material, through-process-modelling enables a better control of the quality of the steel products and provides a more efficient and less expensive way to design new steel grades compared to the traditional iterative trial-and-error approach. In this case, by integrating weldability prediction into the through-process-modelling framework, weldability can be considered in the early stage of new steel development.

The major weldability problem with AHSS is solidification cracking, which is studied in this research. Solidification cracking is a complex problem associated with multiple physical phenomena at different length scales. During welding, with a localized heat input, the material is heated to melt, forming a weld pool. Upon cooling, a mushy zone consisting of solid grains and liquid channels forms behind the weld pool. As temperature drops, solid grains in the mushy zone grow, which tends to close liquid channels in the mushy zone. However, during solidification, detrimental elements segregate in the liquid, inhibiting the closure of the liquid channel. Meanwhile, due to solidification shrinkage and thermal contraction, the liquid channels experienced a tensile loading, which tends to open the liquid channel. If there is insufficient liquid feeding, solidification cracking occurs. Solidification cracking can be avoided by controlling parameters including alloy composition, microstructure and processing condition like power, welding velocity and laser beam shapes, etc.

1.2 Aim of the study

The aim of this study is to develop a modelling approach to predict solidification cracking under various welding conditions, which can be integrated into the through-process-modelling framework. Inherent to this goal are several challenges:

- challenges with multiple physics. Firstly, solidification cracking occurs in the mushy zone during welding. Determination of the mushy zone requires thermal modelling. Secondly, the liquid channels in the mushy zone experience tensile loading due

1

to solidification shrinkage, thermal contraction and mechanical constraints, which should be considered with mechanical modelling. Thirdly, the liquid channels close and detrimental elements may accumulate in the liquid as temperature drops, which requires metallurgical modelling. Fourthly, the liquid feeding in the liquid channel should be modelled with fluid dynamics. Each physical mechanism can be modelled either with an analytical model or with a numerical model. Analytical models are more computationally efficient compared to numerical models, while numerical models are more flexible and can handle different boundary conditions. This research addresses how to appropriately choose the modelling method for each physical phenomenon and how to couple the different physical models.

- challenges with length scales. Thermal modelling and mechanical modelling are performed at the scale of the welded component (cm or mm), while metallurgical modelling and liquid feeding modelling are performed at the scale of the liquid channels (μm). In this case, macroscopic models usually include the whole welded component [5], while microscopic models only include a small volume of the weld pool or mushy zone [6, 7] due to the high computational cost. However, microscopic simulations of a small volume are not representative, as the solidification conditions change site by site in the mushy zone. This research examines how to improve the microscopic models to achieve microscopic simulation of the whole mushy zone with an acceptable computational cost and how to couple the models at different length scales.

In summary, a full-field model for solidification cracking which captures all the physical mechanisms at different length scales, which is capable to handle various welding conditions, is not realistic with the available computational power. To achieve an accurate prediction of solidification cracking under various welding conditions, it is necessary to make simplifications and approximations while capturing the major physical mechanisms. This research explores the possibility of developing such a modelling framework for solidification cracking.

1.3 Outline of the thesis

In Chapter 2, the basic knowledge for solidification and solidification cracking is introduced. Firstly, solidification theories including the thermodynamics and the kinetics are described; subsequently, solidification models including analytical models and numerical models like cellular automata models and phase field models are introduced. Then, the experimental and simulation works of solidification cracking are reviewed.

In Chapter 3, a cellular automata (CA) model is presented, which calculates the segregation and microstructure in the mushy zone numerically. The CA model based on kinetic undercooling is improved in the aspects of mesh-size dependency and mass balance.

In Chapter 4, a phase field (PF) model is employed to study the influence of pulling velocity and temperature gradient on solidification cracking susceptibility (SCS). The Rappaz-Drezet-Gremaud (RDG) model is employed to quantify SCS under different solidification conditions. Decreasing pulling velocity or increasing temperature gradient or refining the grain size decreases SCS, which agrees with the experimental results.

1

In Chapter 5, a cellular automata finite element (CAFE) model is developed for the purpose of simulating microstructure in the whole weld pool. Compared to traditional CAFE models, the newly developed CAFE model is accelerated in terms of computational speed by two orders of magnitude by increasing the time step without compromising the simulation accuracy and by implementing shared-memory parallelism and a subdomain activation-and-deactivation method. The developed CAFE model is validated with additive manufacturing experiments.

In Chapter 6, a multi-physics multi-scale modelling framework is developed to predict solidification under various welding conditions. The framework includes a thermal-mechanical FE model to simulate temperature and strain rate profiles, a CAFE model for microstructure simulation and a granular model for pressure drop calculation. The SCS prediction from the modelling framework matches the experimental observations.

In Chapter 7, the models developed in this research are reviewed in terms of their scientific contributions and limitations. Additionally, potential directions for further work are outlined.

References

[1] TB Hilditch, Timothy De Souza, and PD Hodgson. Properties and automotive applications of advanced high-strength steels (ahss). In *Welding and joining of advanced high strength steels (AHSS)*, pages 9–28. Elsevier, 2015.

[2] Gautam Agarwal, A Kumar, IM Richardson, and MJM Hermans. Evaluation of solidification cracking susceptibility during laser welding in advanced high strength automotive steels. *Materials & Design*, 183:108104, 2019.

[3] Qinglin Qi and Fei Tao. Digital twin and big data towards smart manufacturing and industry 4.0: 360 degree comparison. *Ieee Access*, 6:3585–3593, 2018.

[4] Fei Tao, He Zhang, Ang Liu, and Andrew YC Nee. Digital twin in industry: State-of-the-art. *IEEE Transactions on industrial informatics*, 15(4):2405–2415, 2018.

[5] He Gao, Gautam Agarwal, Muru Amirthalingam, MJM Hermans, and IM Richardson. Investigation on hot cracking during laser welding by means of experimental and numerical methods. *Welding in the World*, 62:71–78, 2018.

[6] Lei Wang, Nan Wang, and Nikolas Provatas. Liquid channel segregation and morphology and their relation with hot cracking susceptibility during columnar growth in binary alloys. *Acta Materialia*, 126:302–312, 2017.

[7] Shaoning Geng, Ping Jiang, Xinyu Shao, Gaoyang Mi, Han Wu, Yuewei Ai, Chunming Wang, Chu Han, Rong Chen, Wei Liu, et al. Effects of back-diffusion on solidification cracking susceptibility of al-mg alloys during welding: A phase-field study. *Acta Materialia*, 160:85–96, 2018.

2

BACKGROUND

In this chapter, basic knowledge and existing works related to solidification and solidification cracking are introduced. The thermodynamics for solidification, which determines whether solidification occurs and the equilibrium concentrations of the solid and the liquid, is described in Section 2.1. Two kinds of thermodynamic conditions including equilibrium and quasi-equilibrium are described here. The solidification kinetics and analytical models for problems like solidification under a constant undercooling, directional solidification, columnar to equiaxed transition and segregation, are discussed in Section 2.2. Numerical solidification models including cellular automata models and phase field models, which simulate the microstructure explicitly, are described in Section 2.3. Solidification cracking in the perspective of experiments and modelling is discussed in Section 2.4.

Solidification cracking occurs when the liquid channels in the mushy zone cannot close due to element segregation within the liquid and the existence of a tensile load introduced by solidification shrinkage and thermal contraction. Solidification plays an important role in solidification cracking, as it governs the liquid channel structure and the element segregation in the liquid. In this chapter, the knowledge of solidification thermodynamics and kinetics are described. In addition, some analytical solidification models and numerical solidification models including cellular automata (CA) models and phase field (PF) models are introduced. Furthermore, existing works of solidification cracking are reviewed in the perspective of experiments and modelling.

2.1 Solidification thermodynamics

2.1.1 The molar Gibbs energy

Phase transformation tends to occur in a direction that lowers the total energy of a system. The CALPHAD (CALculation of PHAse Diagrams) method [1, 2] has proved to be a powerful tool to calculate phase stability, equilibrium thermodynamic properties and driving forces for phase transformation.

In a multi-component system, the molar Gibbs energy G_m^α of a substitutional regular-solution phase α is written as [2]

$$G_m^\alpha = \sum_i {}^{ref}G_i^\alpha x_i^\alpha + RT \sum_i x_i^\alpha \ln\left(x_i^\alpha\right) + {}^E G_m^\alpha + {}^{phy}G_m^\alpha, \tag{2.1}$$

where x_i^α is the mole fraction of element i in phase α, ${}^{ref}G_i^\alpha$ the Gibbs energy of component i relative to the same standard state in phase α, R the gas constant, ${}^E G_m^\alpha$ the excess Gibbs energy and ${}^{phy}G_m^\alpha$ the Gibbs energy contribution due to physical phenomena like ferromagnetism. The excess Gibbs energy depends on the phase composition and the temperature T and is modelled with [2]

$$^E G_m^\alpha = \sum_i \sum_{j>i} x_i^\alpha x_j^\alpha \left(L_{ij}^\alpha + \sum_k x_k^\alpha \left(L_{ijk}^\alpha + \cdots \right) \right), \tag{2.2}$$

where L_{ij}^α describes the compositional dependence and is usually given by a Redlich-Kister polynomial [3]

$$L_{ij}^\alpha = \sum_{v=0} (x_i^\alpha - x_j^\alpha)^v \cdot {}^v L_{ij}^\alpha, \tag{2.3}$$

where ${}^v L_{ij}^\alpha$ may depend on T.

2.1.2 The chemical potential

In a single-phase multi-component system, which contains N^α mole atoms, the total Gibbs energy G^α is written as,

$$G^\alpha = N^\alpha G_m^\alpha \tag{2.4}$$

The total number of moles N^α can be written as

$$N^\alpha = \sum_i n_i^\alpha \tag{2.5}$$

where n_i^α is the number of moles of element i in phase α. The derivative of G^α with respect to n_i^α, in the condition of constant temperature T, pressure P and $n_{j \neq i}^\alpha$, is called the chemical potential μ_i^α and is given by [4]

$$
\mu_i^\alpha = \left(\frac{\partial G^\alpha}{\partial n_i^\alpha} \right)_{T,P,n_{j\neq i}^\alpha} = \left(\frac{\partial \left(N^\alpha G_m^\alpha \right)}{\partial n_i^\alpha} \right)_{T,P,n_{j\neq i}^\alpha} = G_m^\alpha + N^\alpha \left(\frac{\partial G_m^\alpha}{\partial n_i} \right)_{T,P,n_{j\neq i}^\alpha},
$$

$$
= G_m^\alpha + N^\alpha \sum_j \frac{\partial G_m^\alpha}{\partial x_j^\alpha} \frac{\partial x_j^\alpha}{\partial n_i^\alpha}
$$

(2.6)

with

$$
x_j^\alpha = \frac{n_j^\alpha}{N^\alpha} = \frac{n_j^\alpha}{\sum_k n_k^\alpha},
$$

(2.7)

and the derivative of x_j^α with respect to n_i^α given by

$$
\frac{\partial x_j^\alpha}{\partial n_i^\alpha} = \begin{cases} \left(N^\alpha - n_j^\alpha \right) / (N^\alpha)^2, & \text{for } i = j \\ -n_j^\alpha / (N^\alpha)^2, & \text{for } i \neq j \end{cases}.
$$

(2.8)

Thus, the chemical potential is written as [4]

$$
\mu_i^\alpha = G_m^\alpha + \left(1 - x_i^\alpha \right) \frac{\partial G_m^\alpha}{\partial x_i^\alpha} - \sum_{j \neq i} x_j^\alpha \frac{\partial G_m^\alpha}{\partial x_j^\alpha}
$$

$$
= G_m^\alpha + \frac{\partial G_m^\alpha}{\partial x_i^\alpha} - \sum_j x_j^\alpha \frac{\partial G_m^\alpha}{\partial x_j^\alpha}
$$

(2.9)

With Equation (2.9), it is easy to get

$$
G_m^\alpha = \sum_i x_i^\alpha \mu_i^\alpha.
$$

(2.10)

2.1.3 Equilibrium and phase diagram

In a multi-phase multi-component system, the total Gibbs energy G is

$$
G = \sum_\alpha \phi_\alpha G_m^\alpha,
$$

(2.11)

where ϕ_α is the fraction of phase α. With a mass balance, we have

$$
x_i = \sum_\alpha \phi_\alpha x_i^\alpha,
$$

(2.12)

where x_i is the mole fraction of element i in the system.

An equilibrium condition is obtained by minimizing G under the constraints of Equation (2.12). The corresponding Lagrange function L to minimize is thus [5]

$$
L = G + \sum_i \mu_i (x_i - \sum_\alpha \phi_\alpha x_i^\alpha) = \sum_\alpha \phi_\alpha G_m^\alpha + \sum_i \mu_i (x_i - \sum_\alpha \phi_\alpha x_i^\alpha),
$$

(2.13)

where μ_i is the Lagrange multiplier. At equilibrium, all partial derivates of L should be zero and in particular that with respect to the phase fractions [5]:

$$\frac{\partial L}{\partial \phi_\alpha} = G_m^\alpha - \sum_i \mu_i x_i^\alpha = 0. \tag{2.14}$$

Comparing Equation (2.10) with Equation (2.14), it is clear that the Lagrange multiplier μ_i is the chemical potential of element i. Thus, for an equilibrium condition, we have

$$\mu_i = \mu_i^\alpha = \mu_i^\beta = \cdots. \tag{2.15}$$
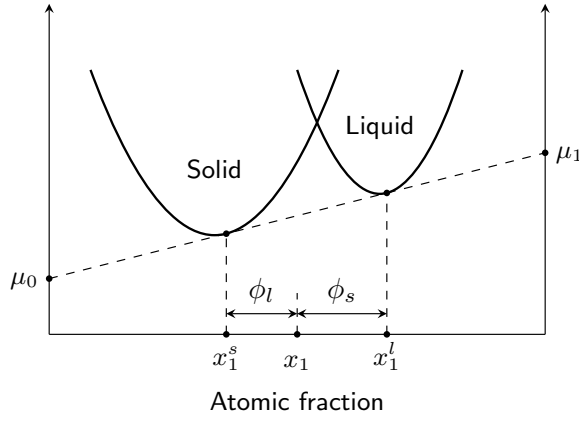
Figure 2.1: A schematic illustration of an equilibrium condition between the solid phase and the liquid phase in a binary system. The chemical potentials of the solvent element and the solute element are μ_0 and μ_1, respectively.

Normally, in equilibrium calculations, the system concentration x_i and the temperature T are fixed, while the phase fractions and the concentrations within each phase are unknown variables to solve. A detailed algorithm for equilibrium calculation can be found in the work of Sundman et al. [6]. Packages like Thermal-Calc and OpenCALPHAD are available for such calculations based on the CALPHAD databases. Performing the equilibrium calculations at different temperatures T with different system compositions x_i and plotting the equilibrium phases under different conditions gives a phase diagram.

For solidification, phase transformation occurs from liquid l to solid s. In a diffusion-controlled solidification simulation, equilibrium is assumed at the interface. With

$$\mu_i^s = \mu_i^l, \tag{2.16}$$

the corresponding driving force ΔG_m^{ls} is then

$$\Delta G_m^{ls} = \sum_i x_i^s \left(\mu_i^l - \mu_i^s \right) = 0. \tag{2.17}$$

2.1.4 Quasi-equilibrium

In the interface region of phase field simulations, the phase fractions, the overall composition and the temperature are fixed, which, in most cases, does not match equilibrium condition. Instead, quasi-equilibrium [7] is considered in the interface region. With $\sum_{i=0} x_i^\alpha = 1$ and Equation (2.10), the molar Gibbs energy of phase α can be written as [8]

$$G_m^\alpha = \sum_{i=0} x_i^\alpha \mu_i^\alpha = \mu_0^\alpha + \sum_{i=1} x_i^\alpha \left(\mu_i^\alpha - \mu_0^\alpha \right), \tag{2.18}$$

where μ_0^α is the chemical potential of the solvent element in phase α. Here, diffusion potential of solute element i in phase α is defined as the derivative of G_m^α with respect to x_i^α in the condition of fixed $x_i^\alpha + x_0^\alpha$

$$\tilde{\mu}_i^\alpha = \left(\frac{\partial G_m^\alpha}{\partial x_i^\alpha} \right)_{x_i^\alpha + x_0^\alpha} = \mu_i^\alpha - \mu_0^\alpha, \tag{2.19}$$

where x_0^α is the mole fraction of the solvent element in phase α. The total Gibbs energy of the system G is then

$$G = \sum_\alpha \phi_\alpha G_m^\alpha = \sum_\alpha \phi_\alpha \left(\mu_0^\alpha + \sum_{i=1} x_i^\alpha \tilde{\mu}_i^\alpha \right) \tag{2.20}$$

In quasi-equilibrium, it is assumed that the mass transport between the different phases, which co-exist in an infinitesimal interfacial region, is fast enough to change the phase concentrations x_i^α in a short time so that the phase fractions ϕ_α and the mixture concentration x_i can be considered as constant. Mathematically speaking, this requires minimization of the Gibbs energy with respect to the phase concentrations c_i^α while the phase fractions ϕ_α, the mixture concentration c_i and the temperature T are fixed [8]. With a mass balance, we have

$$x_i = \sum_\alpha \phi_\alpha x_i^\alpha. \tag{2.21}$$

The corresponding Lagrange function to optimize is

$$\begin{aligned} L &= G + \sum_{i=1} \tilde{\mu}_i \left(x_i - \sum_\alpha \phi_\alpha x_i^\alpha \right) \\ &= \sum_\alpha \phi_\alpha \left(\mu_0^\alpha + \sum_{i=1} x_i^\alpha \tilde{\mu}_i^\alpha \right) + \sum_{i=1} \tilde{\mu}_i \left(x_i - \sum_\alpha \phi_\alpha x_i^\alpha \right), \end{aligned} \tag{2.22}$$

where $\tilde{\mu}_i$ is the Lagrange multiplier. Note L is equal to G in the mass balance constraint Equation (2.21). Taking the derivative of L with x_i^α, we have

$$\frac{\partial L}{\partial x_i^\alpha} = \phi_\alpha \tilde{\mu}_i^\alpha - \phi_\alpha \tilde{\mu}_i = 0. \tag{2.23}$$

In this case, the minimum Gibbs energy is obtained when the diffusion potential in each phase is equal to the Lagrange multiplier $\tilde{\mu}_i$ [8],

$$\tilde{\mu}_i = \tilde{\mu}_i^\alpha = \tilde{\mu}_i^\beta = \cdots. \tag{2.24}$$

For a solidification simulation, the chemical driving force ΔG_m^{ls} is given by

$$\Delta G_m^{ls} = \frac{\mathrm{d}G}{\mathrm{d}\phi_l} - \frac{\mathrm{d}G}{\mathrm{d}\phi_s} = \frac{\partial L}{\partial \phi_l} - \frac{\partial L}{\partial \phi_s} = \mu_0^l - \mu_0^s, \tag{2.25}$$

where partial derivatives of L are employed since the phase fractions ϕ_α and the phase concentrations x_i^α are dependent on G but independent of L. With Equation (2.24), the driving force can also be written as

$$\Delta G_m^{ls} = \mu_i^l - \mu_i^s. \tag{2.26}$$
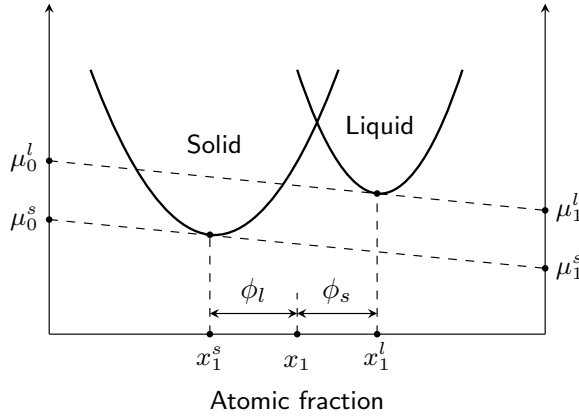
Figure 2.2: A schematic illustration of a quasi-equilibrium condition between the solid phase and the liquid phase in a binary system. The chemical potentials of the element i in the solid and the liquid are μ_i^s and μ_i^l, respectively. The solvent element is indexed with 0, while the solute element is indexed with 1.

For interface-controlled solidification, the velocity of the interface movement v is related to the driving force ΔG_m^{ls} by [9]

$$v = v_0 \left[1 - \exp\left(-\frac{\Delta G_m^{ls}}{RT} \right) \right] \tag{2.27}$$

where R is the gas constant, T the temperature and v_0 a constant which is of the order of the velocity of sound for pure metals. In the case of $v \ll v_0$, the relationship between v and ΔG_m^{ls} can be simplified to [9]

$$v = M_k \Delta G_m^{ls}, \tag{2.28}$$

where M_k is the kinetic mobility of the interface. In the condition of an infinite mobility $M_k = \infty$, the driving force ΔG_m^{ls} is close to 0. Thus, quasi-equilibrium approaches the equilibrium condition in the limit of $M_k = \infty$.

2.1.5 Undercooling
In solidification simulations, the phase concentrations at the solid-liquid interface are normally determined by equilibrium or quasi-equilibrium. Upon continuous cooling, the

equilibrium concentrations vary with decreasing temperature. For simplicity, the change in the equilibrium concentrations can be approximated by linear approximations of the liquidus line and the solidus line. The linear approximations are developed by extrapolating from a reference point, as shown in Figure 2.3. At the reference point for the extrapolation, the temperature is termed T_0 and the concentrations in the liquid and the solid are $c_i^{l,eq0}$ and $c_i^{s,eq0}$, respectively. The derivative $\partial T_l / \partial c_i^{l,eq}$ of the liquidus temperature T_l with respective to the liquid concentration $c_i^{l,eq}$ of element i, in other words, liquidus slope, is m_i^l, while the solidus slope is termed m_i^s. The ratio between m_i^l and m_i^s is called partitioning coefficient k_i,

$$k_i = m_i^l / m_i^s. \tag{2.29}$$

In special cases, if the equilibrium concentrations $c_i^{l,eq0}$ and $c_i^{s,eq0}$ at the reference point satisfy

$$k_i = \frac{c_i^{s,eq0}}{c_i^{l,eq0}}, \tag{2.30}$$

then we have

$$k_i = \frac{c_i^{s,eq}}{c_i^{l,eq}}. \tag{2.31}$$
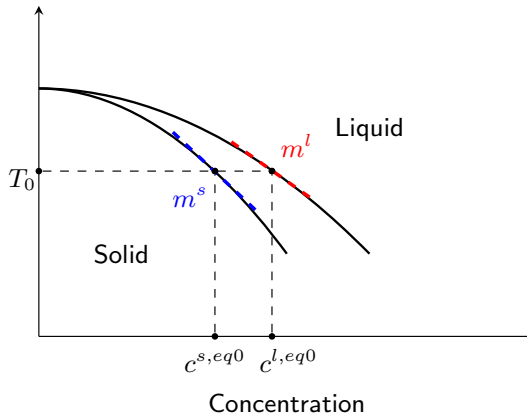
Figure 2.3: A schematic illustration of a linearized phase diagram approximation.

For a given solidification temperature T, the undercooling ΔT can be defined as

$$\Delta T = T_0 - T. \tag{2.32}$$

The undercooling can be decomposed into three parts: the constitutional undercooling ΔT_c, the curvature undercooling ΔT_r and the kinetic undercooling ΔT_k [10],

$$\Delta T = \Delta T_c + \Delta T_r + \Delta T_k. \tag{2.33}$$

The constitutional undercooling ΔT_c is attributed to the compositional dependence of the liquidus temperature and is related to the equilibrium concentrations with

$$\Delta T_c = \sum_i (c_i^{l,eq} - c_i^{l,eq0}) m_i^l, \tag{2.34}$$

and

$$\Delta T_c = \sum_i (c_i^{s,eq} - c_i^{s,eq0}) m_i^s. \tag{2.35}$$

The curvature undercooling ΔT_r is the contribution from the curvature, which increases the Gibbs energy and is given by [10]

$$\Delta T_r = \Gamma \kappa, \tag{2.36}$$

where κ is the curvature and Γ the Gibbs-Thomson coefficient, which is given by

$$\Gamma = \frac{\gamma V_m}{\Delta S_m^{ls}} \tag{2.37}$$

where γ is the interfacial energy, V_m the molar volume and ΔS_m^{ls} the molar entropy change of solidification. The kinetic undercooling ΔT_k is a non-equilibrium effect introduced by rapid solidification and is related to the driving force ΔG_m^{ls} in quasi-equilibrium by

$$\Delta G_m^{ls} = \Delta T_k \Delta S_m^{ls}. \tag{2.38}$$

Substituting Equation (2.38) into Equation (2.28), the kinetic undercooling ΔT_k is then

$$\Delta T_k = \frac{v}{M_k \Delta S_m^{ls}} = \frac{v}{M_T}, \tag{2.39}$$

where $M_k \Delta S_m^{ls}$ is defined as the interface mobility M_T with respect to undercooling.

2.2 Solidification kinetics

With equilibrium calculations, the equilibrium concentrations in the solid and the liquid can be determined, which defines the boundary conditions at the solid-liquid interface. Assuming the solute diffusion in the solid and the liquid is infinitely fast, the concentration profiles within the liquid and solid are always homogeneous and equal to the equilibrium concentrations. However, this assumption is not valid in the real world; the diffusivities of solutes in the liquid and the solid are usually finite, leading to inhomogeneous concentration profiles in the solid and the liquid. In case of a low cooling rate, the solidification process is diffusion-controlled due to the finite diffusivity.

2.2.1 Solidification at a constant undercooling

In mathematics, solidification can be described as a free boundary problem, which needs to solve partial differential equations for both an unknown function and an unknown domain. The unknown boundary is called a free boundary. In a diffusion-controlled solidification simulation, the partial differential equations to be solved are [11]

$$\frac{\partial c_i^l}{\partial t} = \nabla \left(D_i^l \nabla c_i^l \right) \quad \text{in } \Omega^l, \tag{2.40}$$

and

$$\frac{\partial c_i^s}{\partial t} = \nabla \left(D_i^s \nabla c_i^s \right) \quad \text{in } \Omega^s, \tag{2.41}$$

where c_i^l and c_i^s are the concentrations of the element i in the liquid and the solid, D_i^l and D_i^s are the diffusion coefficients of the element i in the liquid and the solid, respectively. Ω^l and Ω^s represent the liquid and the solid region, respectively. At the solid-liquid interface Γ^{ls} between Ω^l and Ω^s, the concentrations in the solid $c_i^{s,*}$ and the liquid $c_i^{l,*}$ are defined by the equilibrium condition,

$$c_i^{s,*} = c_i^{s,eq} \tag{2.42}$$

and

$$c_i^{l,*} = c_i^{l,eq}. \tag{2.43}$$

The movement of the solid-liquid interface is described by [11]

$$v(c_i^{l,*} - c_i^{s,*}) = -D_i^l \partial_n c_i^l + D_i^s \partial_n c_i^s \quad \text{on } \Gamma^{ls}, \tag{2.44}$$

where v is the interface velocity, $\partial_n c_i^l$ and $\partial_n c_i^s$ the derivative of liquid concentration and the solid concentration in the direction of the interface normal direction, respectively. Note solidification under a constant undercooling is also known as a two-phase Stefan problem, as the concentration values at the solid-liquid interface are constant in the steady state.

Needle-like stationary solutions were obtained by Ivantsov [12], which describe a parabolic interface growing into an infinite supercooled melt. The Ivantsov solution is

$$\Omega = I_v(P) = \begin{cases} \sqrt{\pi P} \exp(P) \text{erfc} \left(\sqrt{P} \right), & \text{2D} \\ P \exp(P) E_1(P), & \text{3D} \end{cases}. \tag{2.45}$$

where $I_v(P)$ is the Ivantsov function, P the Peclet number and $E_1(P)$ the exponential integral function. Ω is the supersaturation given by

$$\Omega = \frac{c_i^{l,*} - c_i^0}{c_i^{l,*} - c_i^{s,*}} \tag{2.46}$$

where c_i^0 is the nominal concentration. The Peclet number P is given by

$$P = \frac{vr}{2D_i^l} \tag{2.47}$$

where r is the tip radius.

In the LGK (Lipton-Glicksman-Kurz) model [13], the Ivantsov solution is coupled with a stability criterion given by

$$r = \sqrt{\frac{\Gamma}{\sigma^* \left(\sum_i m_i G_i^c - G \right)}}, \tag{2.48}$$

where G_i^c is the concentration gradient in the liquid at the interface, G the temperature gradient, σ^* a stability constant which is of the order of $1/4\pi^2$. With Equation (2.46) and

assuming the diffusion in the solid is negligible ($D_i^s \ll D_i^l$), the concentration gradient G_i^c at the interface is given by

$$G_i^c = \frac{v}{D_i^l}\left(c_i^{l,*} - c_i^{s,*}\right).$$ (2.49)

In the LGK model, by selecting the reference point with $k_i = c_i^{s,eq}/c_i^{l,eq}$, the interface concentration in the liquid $c_i^{l,*}$ is given by

$$c_i^{l,eq} = c_i^{l,*} = \frac{c_i^0}{1 - (1 - k_i)I_v(P)}.$$ (2.50)

Substituting Equation (2.50) into Equation (2.33) and assuming an infinite interface mobility M_T gives

$$\Delta T = \sum_i m_i \left(c_i^{l,eq0} - \frac{c_i^0}{1 - (1 - k_i)I_v(P)}\right) + \Gamma\kappa.$$ (2.51)

Neglecting the temperature gradient G, the growth velocity v can be obtained by solving Equations (2.48), (2.49) and (2.51) under different undercooling ΔT, as shown in Figure 2.4. The resultant relation between v and ΔT can be fitted with a polynomial, which is widely employed in cellular automata solidification simulations [14–16].
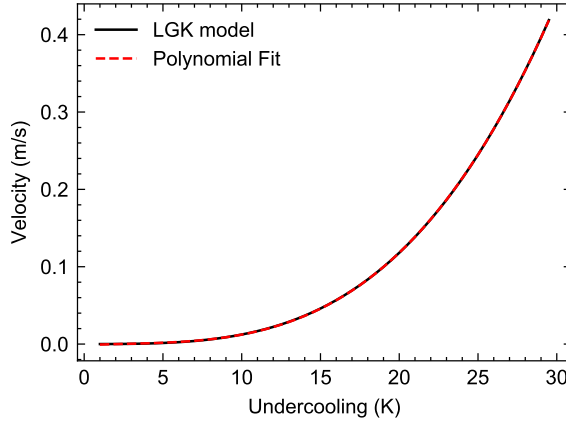
Figure 2.4: The relationship between growth velocity v and the undercooling ΔT and the corresponding fitted curve.

For directional solidification, the KGT (Kurz-Giovanola-Trivedi) model [17] considers a marginal stability condition,

$$r = \sqrt{\frac{\Gamma}{\sigma^*\left(\sum_i m_i G_i^c \xi_c - G\right)}}.$$ (2.52)

At high Peclet number ($P > \pi^2/\sqrt{k}$), ξ_c is given by [17]

$$\xi_c = \frac{\pi^2}{k_i P^2}.$$ (2.53)

2.2.2 Directional solidification

The directional solidification condition is characterized by a temperature gradient G and a cooling rate $\dot{T}$. The velocity at which the liquidus isotherm moves is called the pulling velocity v_T and is given by

$$v_T = \frac{\dot{T}}{G}. \tag{2.54}$$

In directional solidification, solidification occurs in the direction of the temperature gradient. Depending on the value of the temperature gradient G and the gradient of the liquidus temperature G^{T_l}, the growth mode can be planar, cellular or dendritic [10]. The growth mode is planar in the condition of $G > G^{T_l}$ and is cellular or dendritic in the condition of $G < G^{T_l}$. With Equation (2.49), the slope G^{T_l} of the liquidus line at the interface is

$$G^{T_l} = \sum_i m_i G_i^c = \sum_i \frac{m_i v \left(c^{l,*} - c^{s,*} \right)}{D_i^l}. \tag{2.55}$$

As show in Figure 2.5 (a), the growth mode is planar if the pulling velocity v_T and the gradient G^{T_l} of the liquidus temperature are very small. With increasing pulling velocity v_T, the gradient G^{T_l} of the liquidus temperature increases and the growth mode changes from planar (Figure 2.5 (a)) to cellular (Figure 2.5 (b) and (c)). As the pulling velocity is further increased, the growth mode changes into dendritic.
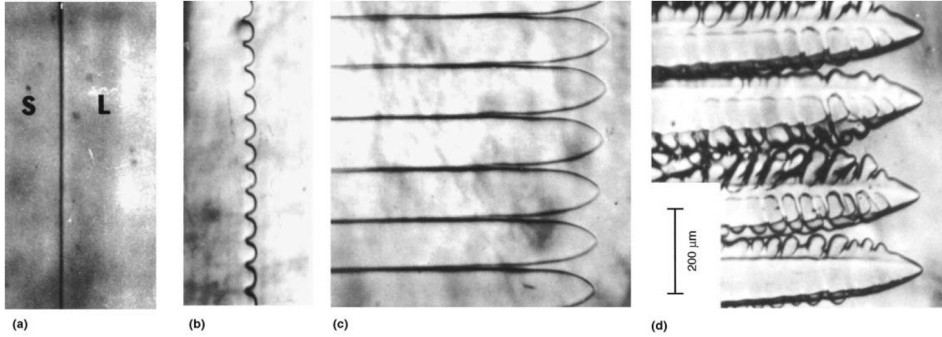
Figure 2.5: The evolution of the solid/liquid interface as a function of growth velocity (V) in a transparent organic system (pivalic acid, 0.076% ethanol) directionally solidified under a thermal gradient of 2.98 K/mm. Planar interface, $v_T = 0.2\,\mu\text{m/s}$ (a). Cellular interface, $v_T = 1.0\,\mu\text{m/s}$ (b). Cellular interface, $v_T = 3.0\,\mu\text{m/s}$ (c). Dendritic interface, $v_T = 7.0\,\mu\text{m/s}$ (d). [10]

For columnar or dendritic solidification, multiple dendrites form and grow in the direction of the temperature gradient. In the steady state, the growth velocity v_{tip} at the dendrite tip is equal to the pulling velocity v_T. The average spacing between neighboring dendrites is called the primary dendrite arm spacing (PDAS) λ, which can be calculated analytically based on the temperature gradient G and the pulling velocity v_T [18, 19],

$$\lambda = A v_T^{-0.25} G^{-0.5}, \tag{2.56}$$

where A is a pre-factor. In the model of Kurz and Fisher [18], A is given by

$$A = 4.3 \left(1 - \Omega \right)^{0.5} \left(\Gamma \Delta T_0 D^l k \right)^{0.25}. \tag{2.57}$$

For welding and additive manufacturing, the solidification condition is complex as the the temperature gradient and the cooling rate are site dependent. For simplicity, the frozen temperature approximation is usually employed [20, 21], which is to approximate the real solidification condition by a directional solidification condition.

2.2.3 Columnar to equiaxed transition

In directional solidification, if a sufficient amount of equiaxed grains from in front of the dendrite tip, the microstructure may change from columnar to equiaxed, which is known as the columnar-to-equiaxed transition. The columnar-to-equiaxed transition can be observed in welding or additive manufacturing.

Hunt [22] developed an analytical model to predict the columnar-to-equiaxed transition. In his model, the nucleation rate I per unit volume is given in the form of

$$I = (N_0 - N) I_0 \exp\left(-\frac{\Delta G_c}{kT}\right) \tag{2.58}$$

where N_0 is the total number of heterogeneous substrate particles originally available per unit volume, N is the number that have nucleated, I_0 a constant, ΔG_c the Gibbs energy change associated with the critical nucleus and k the Boltzmann constant. Assuming the growth velocity v is related to the undercooling ΔT by

$$v = \frac{A}{c_0}(\Delta T)^2, \tag{2.59}$$

the radius r of the equiaxed grains formed in front of the dendrite tip is given by

$$r = \int_{\Delta T_n}^{\Delta T_t} \frac{A(\Delta T)^2}{c_0 v_T G} d(\Delta T) = \frac{A(\Delta T_t)^3 - (\Delta T_n)^3}{3c_0 v_T G}. \tag{2.60}$$

Considering the impingement effect, the volume fraction of the equiaxed grains ϕ is equal to

$$\phi = 1 - \exp\left(-\frac{4\pi r^3 N_0}{3}\right). \tag{2.61}$$

In Hunt's model, the fully equiaxed microstructure is defined as $\phi > 0.49$, corresponding to

$$G < 0.617 N_0^{1/3} \left[1 - \left(\frac{\Delta T_n}{\Delta T_{tip}}\right)^3\right] \Delta T_{tip}, \tag{2.62}$$

while the fully columnar microstructure is defined as $\phi < 0.0066$, corresponding to

$$G > 0.617 (100 N_0)^{1/3} \left[1 - \left(\frac{\Delta T_n}{\Delta T_{tip}}\right)^3\right] \Delta T_{tip}. \tag{2.63}$$

Note that the velocity calculation Equation (2.59) is an empirical expression and is less accurate than that from the LGK model, which may have higher-order terms. Later, following Hunt's approach, Gäumann et al. recalculated the columnar-to-equiaxed transition considering nonequilibrium effects and found that the columnar-to-equiaxed transition occurs at lower solidification velocities compared to Hunt's model. The results are more meaningful for solidification conditions with a high solidification velocity, where nonequilibrium effects are not negligible.

2.2.4 Segregation models

With infinite diffusivities in both the liquid and the solid, the concentrations in the liquid and solid match the equilibrium concentrations from the phase diagram. In a binary system, the solid fraction f_s and the liquid fraction can be determined with a lever rule,

$$f_s = \frac{c^{l,eq} - c^0}{c^{l,eq} - c^{s,eq}}, \tag{2.64}$$

$$f_l = \frac{c^0 - c^{s,eq}}{c^{l,eq} - c^{s,eq}}, \tag{2.65}$$

However, due to the finite diffusivities, the equilibrium concentrations are only valid at the interface. In this case, the evolution of the solid fraction does not match the lever rule.

The Scheil-Gulliver model [23] describes the solute redistribution during solidification. In a binary system, it is assumed that

- No diffusion occurs in the solid ($D^s = 0$);

- The diffusion in the liquid is infinitely fast ($D^l = \infty$ and $c^{l,*} = c^l$);

- Equilibrium exists at the solid-liquid interface ($c^{l,*} = c^{l,eq}$ and $c^{s,*} = c^{s,eq}$).

For a small increase in the solid fraction df_s, the amount of solutes partitioned at the interface is $(c^{l,eq} - c^{s,eq})df_s$, which leads to an increase in the liquid concentration,

$$(c^{l,eq} - c^{s,eq})df_s = (1 - f_s)dc^l. \tag{2.66}$$

With a linearized phase diagram ($c^{l,eq} = kc^{s,eq}$) and $c^{l,*} = c^{l,eq} = c^l$, we have

$$c^l(1-k)df_s = (1 - f_s)dc^l. \tag{2.67}$$

After integration, we have

$$c^l = c^0(1 - f_s)^{k-1}. \tag{2.68}$$

The solid fraction f_s is given by

$$f_s = 1 - \left[\frac{c^{l,eq0} + (T - T_0)/m}{c^0}\right]^{1-k}. \tag{2.69}$$

In the Scheil-Gulliver model, back diffusion which can reduce segregation in the liquid and promote solidification is not considered. To include this effect, Brody and Flemings [24] proposed a model to describe the evolution of micro-segregation and solid fraction. Then, Clyne and Kurz [25] introduced an intermediate parameter to make the segregation model compatible with the lever rule and the Scheil-Gulliver model under different diffusion conditions. The solid fraction f_s is given by

$$f_s = \frac{1}{1 - 2\alpha'k}\left[1 - \left(\frac{T_m - T}{T_m - T_l}\right)^{\frac{1-2\alpha'k}{k-1}}\right] \tag{2.70}$$

with

$$\alpha' = \alpha \left[1 - \exp\left(-\frac{1}{\alpha} \right) \right] - \frac{1}{2} \exp\left(-\frac{1}{2\alpha} \right) \tag{2.71}$$

and

$$\alpha = \frac{4 D^s t_f}{\lambda^2}, \tag{2.72}$$

where α is a parameter related to the solidification condition, T_m the melting temperature of pure substance, T_l the liquidus temperature, t_f the solidification time and λ the dendrite arm spacing. α' is an intermediate parameter to make sure that Equation (2.70) matches the Scheil-Gulliver model when $\alpha \to 0$ and the lever rule when $\alpha \to \infty$.

2.3 Numerical models for solidification

Nowadays, with ever increasing available computational power, explicit simulations of microstructure have become feasible. In explicit models, grains or phases are considered as fields and the evolution of those fields can be solved numerically. Depending on the treatment of the interfaces, existing numerical models can be divided into two types: sharp-interface models and models with a finite interface width. In this section, a type of sharp-interface model (cellular automata model) and a type of model with a finite interface width (phase field model) are described.

2.3.1 Cellular automata model

For a solidification problem, a field variable φ can be defined, which is 0 for liquid and 1 for solid. In a sharp interface model, a sharp transition from 0 to 1 occurs at the interface. A typical φ profile is given in Figure 2.6. In a cellular automata (CA) model, the simulation domain is discretized into cells [26], which are line segments in 1D, typically squares in 2D and cubes in 3D. To track the solid-liquid interface, the solid fraction f_s is defined for each cell. In a solidification problem, depending on the location of the cells, they are divided into three types:

- solid cells ($f_s = 1.0$): the cells behind the solid-liquid interfaces are solid cells;

- liquid cells ($f_s = 0.0$): the cells in front of the solid-liquid interface are liquid cells;

- interface cells ($0.0 < f_s < 1.0$): the cells where the solid-liquid interface exists.

Despite the employment of the solid fraction, CA models are still considered as sharp-interface models, as long as a sharp interface between the solid and the liquid parts is assumed inside each interface cell.

Solidification is then simulated based on transition rules [27].

- a liquid cell transforms into an interface cell when it is captured by a neighboring interface cell;

- growth in an interface cell is performed by updating its solid fraction f_s;

- an interface cell transforms into a solid cell if it does not have a liquid neighbor or its solid fraction f_s is equal to 1.0.
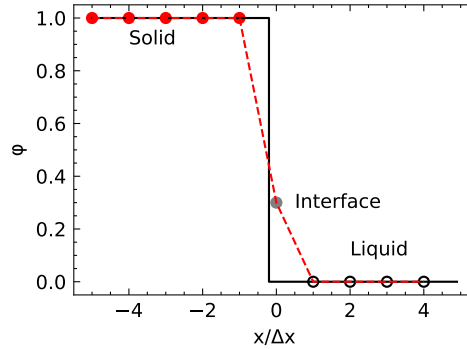
Figure 2.6: A schematic illustration of the profile of the phase status φ and the solid fraction f_s in a 1D cellular automata (CA) simulation. The circles represents cell centers. The solid fraction of the interface cell corresponds to the fraction of the solid within the considered cell.

In summary, the cell status is changed based on the information from its neighborhood. In 2D and 3D simulations, two kinds of neighborhood are widely employed: the von Neumann neighborhood and the Moore neighborhood. The former consists of 4 or 6 nearest cells in 2D or 3D cases, while the latter includes 8 or 26 cells, as shown in Figure 2.7 for the 2D case. With transition rules in the CA models, the calculation is limited in the interface cells and their neighbors, which is computationally efficient compared with algorithms which need to loop over all the cells. However, the quantitativeness of CA models is limited by issues like grid anisotropy. For solidification simulation of a single dendrite, when the von Neumann neighborhood is employed, the dendrite arms propagate in the vertical and the horizontal directions of the grid; when the Moore neighborhood is employed, the dendrite arms propagate in the diagonal directions of the grid.

Figure 2.7: Illustration of the von Neumann neighborhood and the Moore neighborhood in the 2D case.

To improve the quantitativeness of the CA model, different growth algorithms have

been developed for liquid cell capture and solid fraction update in CA models. Gandin and Rappaz [28] proposed a decentered growth algorithm to capture liquid cells. In the decentered growth algorithm, each interface cell is assigned with a growth envelope (growth octahedron in 3D) with its diagonals parallel with the crystallographic preferential growth directions. When a liquid cell is captured and transforms into a new interface cell, a new growth envelope is formed in the newly captured cell inheriting the orientation of the original growth envelope. The center of the new growth envelop is not in the center of the newly captured cell, which is why this algorithm is called decentered growth algorithm. The decentered growth algorithm has a good performance in suppressing grid anisotropy in solidification simulations of crystals with a cubic symmetry; therefore, it has been employed for solidification simulations in many works [29–31]. Beltran and Stefanescu [32] developed a virtual front tracking method to simulate dendrite formation quantitatively. In their model, the first and the secondary dendrite arms form in the direction of the preferential growth directions instead of the grid directions, indicating a reduction in grid anisotropy. However, the dendrite morphology with different rotation angles still differs, which means grid anisotropy is still not negligible. Wei et al. [33] proposed a limited neighbor solid fraction (LNSF) method to suppress the grid anisotropy in 3D solidification simulations. A liquid cell is captured when it has a solid neighbor and the average solid fraction in its neighborhood is larger than a critical value. The simulated grain morphology structure qualitatively matched the favorable growth directions defined by the crystal anisotropy. However, the grain morphology simulated with an isotropic interfacial energy differed a lot from the theoretical spherical shape, due to the grid anisotropy. Marek [34] proposed a growth anisotropy reduction with diffusion method (GARED). The GARED introduces a growth rate reduction factor to scale the actual growth rate and reduce the grid anisotropy. The simulated grain morphology under an isotropic interfacial energy agreed well with the theoretical spherical shape. However, the growth rate reduction factor was calculated with a diffusion-like scheme, leading to a large increase in the computational cost. Arote et al. [35] developed a limited circular neighborhood (LCN) method, which is actually a modified LNSF method. In the LCN method, a circular neighborhood, which is larger than traditional Moore neighborhood, is employed. Depending on the distance to the considered cell, the neighboring cells can be unconditionally captured or conditionally captured. The LCN method provides a better simulation accuracy compared to the LNSF method and requires a shorter computation time compared to the GARED method. However, due to the consideration of a circular neighborhood, the computational cost of the LNSF method is larger than the decentered growth algorithm. In case of solidification simulations of crystals with a cubic symmetry, the decentered growth algorithm is still the best method, considering the balance between the simulation accuracy and the computational cost.

In general, the methods for solid fraction update in the literature can be divided into three types: a flux balance (FB) method [26, 29, 30, 32, 35–37], a cellwise mass balance (CMB) method [38–42] and a kinetic method [43–46]. In the FB method, the growth velocity v is calculate with a mass balance which is expressed in the form of fluxes. In Nastac's model [26], the velocity components v_x and v_y at an interface cell are calculated with

$$v_x \left(c^{l,*} - c^{s,*} \right) = -D^l \frac{\partial c^l}{\partial x} + D^s \frac{\partial c^s}{\partial x}, \tag{2.73}$$

2

and

$$v_x \left(c^{l,*} - c^{s,*} \right) = -D^l \frac{\partial c^l}{\partial y} + D^l \frac{\partial c^s}{\partial y}. \tag{2.74}$$

Then, the solid fraction change Δf_s in a time step Δt is given by

$$\Delta f_s = \frac{v_e \Delta t}{L_{\max}}, \tag{2.75}$$

where v_e is the effective growth velocity and $L_{\max}$ the maximum growth length within an interface cell. In the considered interface cell, considering two planar interfaces moving in the direction of x and y, the effective growth velocity can be calculated by [26]

$$v_e = v_x + v_y - v_x v_y. \tag{2.76}$$

Beltran and Stefanescu [32] calculated the effective growth velocity in the direction of the interface normal $\vec{n}$

$$v_e = v_x n_x + v_y n_y, \tag{2.77}$$

where n_x and n_y are the components of the interface normal unit vector $\vec{n}$. The v_e calculation method by Beltran and Stefanescu is widely employed [29, 30, 36, 37]. $L_{\max}$ is usually calculated based on the cell size Δx. In Nastac's work, the cell size Δx is employed as $L_{\max}$,

$$L_{\max} = \Delta x. \tag{2.78}$$

In the work of Beltran and Stefanescu [32], $L_{\max}$ is calculated based on the angle φ between the interface normal $\vec{n}$ and the x axis

$$L_{\max} = \frac{\Delta x}{\max\left(|\sin \varphi|, |\cos \varphi|\right)}. \tag{2.79}$$

In the model of Tan et al. [47], $L_{\max}$ is calculated by

$$L_{\max} = \Delta x \left(|\sin \varphi| + |\cos \varphi|\right), \tag{2.80}$$

which is more accurate compared to Equations (2.78) and (2.79), as it is the moving distance required for an interface to sweep over a square cell.

In the CMB method, the change in the solid fraction Δf_s is calculated with a cellwise mass balance [38],

$$\Delta f_s = \frac{c^{l,*} - c^l}{c^{l,*} - c^{s,*}}, \tag{2.81}$$

where c^l is the concentration of the considered interface cell. With an increase in solid fraction Δf_s, solute is partitioned into the liquid within the considered interface cell, compensating the solute diffusing out of the interface cell; thus, the liquid concentration is kept at $c^{l,*}$. The CMB method has been employed for solidification under melt convection [39], 3D solidification simulation [40], eutectic solidification [41] and solidification in a multi-component system. However, the CMB method does not ensure a strict mass balance. Following the CMB approach, Krane et al. [42] proposed an equation to calculate solid fraction change in a finite volume scheme,

$$\Delta f_s = \frac{\Delta c^l + (1 - f_s)(c^{l,*} - c^l)}{c^{l,*} - c^{s,*}}, \tag{2.82}$$

where Δc^l is the concentration change due to diffusion. With the equation from Krane et al., a strict mass balance can be ensured. However, problems may be encountered when solving Equation (2.82) for a multi-component system.

In the FB and the CMB methods, the solid fraction change Δf_s and the interface concentrations are determined by solving Equation (2.75) or Equation (2.81) with equilibrium conditions,

$$\begin{aligned}\Delta T &= \Delta T_c + \Delta T_r + \Delta T_k \\ &= m(c^{l,eq0} - c^l) + \Gamma\kappa + \Delta T_k\end{aligned} \tag{2.83}$$

In most cases, the kinetic undercooling ΔT_k is not considered. In the kinetic method, the solid fraction change Δf_s is calculated based on the kinetic undercooling ΔT_k [43–46],

$$\Delta f_s = \frac{v\Delta t}{L_{\max}} = \frac{M_T \Delta T_k \Delta t}{L_{\max}}. \tag{2.84}$$

The kinetic undercooling ΔT_k is determined based on the liquid concentration c^l and the curvature κ at the considered interface cell,

$$\Delta T_k = \Delta T - \sum_i m_i(c^{l,eq0} - c^l) - \Gamma\kappa. \tag{2.85}$$

As the kinetic method does not solve the mass balance at the interface, the mass balance is achieved with a self-controlled mechanism. If the solid fraction change Δf_s in one step is larger than required, it leads to a smaller or a negative kinetic undercooling ΔT_k in the next step and thus a smaller or zero Δf_s, compensating for the overgrowth in the previous step. Conversely, if the solid fraction change Δf_s in one step is smaller than required, a larger kinetic undercooling and a larger Δf_s are expected in the next step. In this case, the kinetic method is more favorable for multi-component solidification problems compared to the FB and CMB methods. However, CA simulations with the kinetic method are dependent on mesh size. This problem will be solved in Chapter 3.

In the CA solidification simulation, the dendrite morphology is controlled with curvature, which is calculated based on the solid fraction field. Various methods have been proposed to achieve an accurate curvature calculation. Nastac [26] employed a cell counting method for curvature calculation in a 2D simulation, in which the curvature κ is given by

$$\kappa = \frac{1}{\Delta x}\left(1 - 2\frac{f_s + \sum_{nb} f_s^{nb}}{N^{nb} + 1}\right), \tag{2.86}$$

where f_s is the solid fraction of the considered interface cell, $\sum_{nb} f_s^{nb}$ the sum of solid fraction in the Moore neighborhood and N^{nb} the number of cells in the Moore neighborhood. Following this approach, Yu et al. [48] proposed the following equation for curvature calculation in a 3D simulation,

$$\kappa = \frac{4.3899}{\Delta x}\frac{51 - \sum_{nb} f_s}{81}, \tag{2.87}$$

where $\sum_{nb} f_s$ are the sum of solid fraction of cells whose distance from the considered interface cell are smaller than $\sqrt{6}\Delta x$. Apart from the cell counting method, the level set

method is also widely employed [32, 38] for curvature calculation in CA simulations,

$$\kappa = \frac{2\frac{\partial f_s}{\partial x}\frac{\partial f_s}{\partial y}\frac{\partial^2 f_s}{\partial x \partial y} - \left(\frac{\partial f_s}{\partial x}\right)^2 \frac{\partial^2 f_s}{\partial^2 y} - \left(\frac{\partial f_s}{\partial y}\right)^2 \frac{\partial^2 f_s}{\partial^2 x}}{\left[\left(\frac{\partial f_s}{\partial x}\right)^2 + \left(\frac{\partial f_s}{\partial x}\right)^2\right]^{3/2}}. \tag{2.88}$$

Although the cell counting method and the level set method give a quick estimation of the curvature, the accuracy of the curvature calculation is not enough for a quantitative solidification simulation, as indicated in [49]. Compared to the cell counting method and the level set method, the height function method provides a better accuracy in curvature calculation [49, 50]. In the 2D height function method, the sum of solid fraction in each column of the constructed stencil is considered as height function values, which are used to calculate the first h' and the second h'' derivatives of the height function. The curvature κ is then given by

$$\kappa = \frac{h''}{(1+h'^2)^{3/2}}. \tag{2.89}$$

The accuracy of the 2D height function method is limited when the interface normal direction is close to the diagonal directions of the square grid. To overcome this limitation, Popinet [51] proposed a generalized height function and combined it with a parabola fitting method to accurately calculate curvature under different conditions. Popinet's method is employed in the CA solidification model described in Chapter 3.

In the CA solidification models, the concentration profiles in the liquid and the solid are obtained by solving the governing equation numerically. In early CA solidification models, a one-domain method is employed [38], which removes the discontinuity in the concentration profile at the interface by dividing the solid concentration with the partitioning coefficient. This approach requires a fixed partitioning coefficient [52] and does not work for a multi-component system. In later works [48, 50, 53], the concentration profiles are obtained by solving the diffusion in the liquid and the solid separately with

$$\frac{\partial c^l}{\partial t} = D^l \nabla^2 c^l + (c^{l,*} - c^{s,*})\frac{\partial f_s}{\partial t}, \tag{2.90}$$

and

$$\frac{\partial c^s}{\partial t} = D^s \nabla^2 c^s. \tag{2.91}$$

2.3.2 CAFE MODEL

The CA model described in the previous section requires numerically solved concentration profiles, which is computationally expensive. When the segregation profiles are not required, the solidification morphology can be simulated based on the results from analytical models. With analytical models like the LGK model, the growth velocity v can be obtained as a function of the local undercooling ΔT. As this kind of CA model is usually coupled with a finite element (FE) model, which provides the temperature profiles for CA simulations, this kind of CA model is called a CAFE model.

Similar to the typical CA model, the simulation domain in the CAFE model is discretized into cells [26], which are squares in 2D and cubes in 3D. The cells are divided into three types: solid, liquid and interface. The transition rules in the CAFE model are defined as:

- a liquid cell transforms into a new interface cell if it is captured by a neighboring interface cell;

- growth within an interface cell is tracked by increasing its growth length l;

- an interface cell transforms into a solid cell if it has no liquid neighbor.

To suppress the grid anisotropy, the decentered growth algorithm proposed by Gandin and Rappaz [28] is employed to capture liquid cells. Each interface cell has a growth envelope (2D) or growth octahedron (3D). The half diagonal of the growth envelope is called the growth length l, which is updated in each time increment with

$$\Delta l = v \Delta t. \tag{2.92}$$

The growth velocity v is calculated as a function of the undercooling ΔT based on analytical models like the LGK model.

The CAFE model has been widely employed to simulate grain morphology and texture evolution during welding [14, 54] and additive manufacturing [55–57]. Pineau et al. [58] employed a CAFE model to simulate the grain structure of directionally solidified silicon. The twin relationship observed in the experiments was successfully reproduced in the CAFE simulations. Rolchigo [59, 60] employed a CAFE model to study the influence of alloying elements, quantities and nucleation parameters on the columnar-to-equiaxed-transition behaviors. Based on CAFE simulations, Shi et al. [16] increased the fraction of equiaxed grains in the solidified microstructure by tweaking the laser beam shaping strategy. Teferra [61] optimized a CAFE model for texture prediction of multi-layer additive manufacturing processes and the simulated Goss texture agreed well with the experimental results. In Chapter 5, a CAFE model is further examined in the perspective of computational speed.

2.3.3 Phase field model

Different from sharp interface models, phase field models have a solid-liquid interface with a finite width. With a finite interface width, as shown in Figure 2.8, the solid-liquid interface is discretized with more cells, which enables a better description of the interface normal direction and the curvature (implicitly included in the governing equations of phase field). Moreover, quantitative phase field models with a thin-interface limit and an anti-trapping flux [62] ensure a correct partitioning behavior over the finite interface region. As a result, phase field models are more accurate compared to cellular automata models.

Development of phase field models

The 2D model developed by Kobayashi [63] was the first large-scale phase field model to simulate dendritic crystal growth, which resemble the experimental observations. In his model, the Stefan problem of solidification of pure substances is solved with a diffuse interface scheme. Later, the WBM (Wheeler-Boettinger-McFadden) model [64] was derived in a thermodynamically consistent way and was employed to simulate dendrite formation in ideal binary alloys by solving the governing equations for the phase field variable and the concentrations. Early phase field models including the WBM model are only quantitative in the so-called sharp-interface limit. In this limit, the driving force over the interface region can be considered as constant, which requires very small interface width and cell size. To
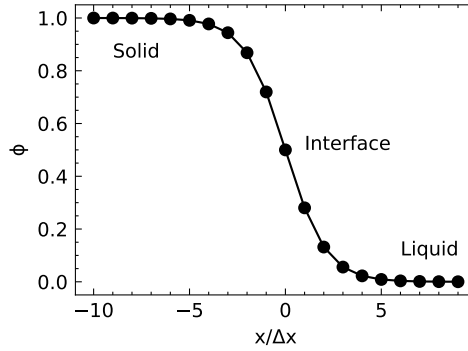
Figure 2.8: A schematic illustration of phase field variable ϕ in the interface region of a 1D simulation. The circles represent cell centers.

overcome this limitation, Karma [62] introduced a thin-interface limit which assumes that the interface width is small compared to the mesoscale of the diffusion field, but remains finite. In the asymptotic analysis performed by Karma [62], correct interface movement was ensured by considering the variation of the driving force in the finite interface region [62]. In the thin-interface limit, quantitative phase field simulations can be achieved with a larger interface width and diffusion-controlled solidification simulations are possible with an infinite kinetic mobility. Following the thin-interface limit, the KKS (Kim-Kim-Suzuki) model [11] was developed for solidification of binary alloys, which solved the phase field equation and the diffusion equation at the same time. However, due to the finite interface width, solutes could be artificially trapped in the interface region in phase field simulations for solidification of alloys. To solve this problem, Karma [65, 66] introduced an anti-trapping flux into the diffusion equation assuming the diffusion in the solid is negligible. Kim [67] extended the anti-trapping flux into a multi-component system and eliminated the chemical potential jump in the interface region. Ohno and Matsuura [68] derived the anti-trapping flux considering the diffusion in the solid in a binary system [68] and in a multi-component system [69].

Initially, phase field models were limited to two-phase and binary systems. Tiaden et al. [70] developed a multi-phase phase field model for peritectic solidification simulations in a binary system. Eiken et al. [7] further extended the multi-phase phase field model into a multi-component system. Quasi-equilibrium was proposed to define the condition in the interface region [7], which is achieved when the diffusion potential of the solute element in each phase is equal. Following the model of Eiken et al., Galenko et al. [71] developed a phase field model considering solute trapping and nonequilibrium effects during rapid solidification.

Governing equations

Define a phase field variable ϕ, which is 0 in the liquid and 1 in the solid. In the solid-liquid interface region, ϕ changes from 0 to 1 smoothly. The free energy functional F of a

representative volume is given by [7, 11, 62]

$$F = \int_V f(\phi, \nabla\phi, c, T) \, \mathrm{d}V. \tag{2.93}$$

The free energy density f is written as the sum of the interface energy density f^{intf} and the chemical free energy density $f^{\mathrm{chem}}(\phi, c, T)$ [7],

$$f(\phi, \nabla\phi, c, T) = f^{\mathrm{intf}}(\phi, \nabla\phi) + f^{\mathrm{chem}}(\phi, c, T), \tag{2.94}$$

The interface energy density f^{intf} is given by [72]

$$f^{\mathrm{intf}} = \frac{\sigma}{W} \left(\frac{W^2}{2} (\nabla\phi)^2 + g(\phi) \right) \tag{2.95}$$

where W is the interface width and $g(\phi)$ the potential function. The chemical free energy density $f^{\mathrm{chem}}(\phi, c, T)$ is given by [72]

$$f^{\mathrm{chem}}(\phi, c, T) = \frac{a_1}{V_m} \left[h(\phi) G_m^s + (1 - h(\phi)) G_m^l \right] \tag{2.96}$$

where V_m is the molar volume, a_1 a numerical constant, $h(\phi)$ the interpolation function, G_m^s and G_m^l the molar Gibbs energy of the solid and the liquid, respectively. To minimize the system energy, the evolution of ϕ is governed by [62]

$$\tau_0 \frac{\partial \phi}{\partial t} = -\frac{\delta F}{\delta \phi} \tag{2.97}$$

where $\frac{\delta F}{\delta \phi}$ is the functional derivative of F with respect to ϕ and is given by

$$\begin{aligned} \frac{\delta F}{\delta \phi} &= \frac{\partial f}{\partial \phi} - \nabla \frac{\partial f}{\partial \nabla \phi} \\ &= \frac{\sigma}{W} \left(-W^2 \nabla^2 \phi + g_\phi \right) - a_1 h_\phi \Delta G_v^{ls} \end{aligned} \tag{2.98}$$

where ΔG_v^{ls} is the driving force for solidification per unit volume, g_ϕ and h_ϕ the derivatives of $g(\phi)$ and $h(\phi)$ with respect to ϕ, respectively. The driving force per unit volume for solidification ΔG_v^{ls} can be determined with a quasi-equilibrium condition [7]. The governing equation is then [72]

$$\tau \frac{\partial \phi}{\partial t} = W^2 \nabla^2 \phi - g_\phi + \frac{a_1 W}{\sigma} h_\phi \Delta G_v^{ls}, \tag{2.99}$$

where τ is the kinetic parameter.

In theory, the potential function $g(\phi)$ and the interpolation function $h(\phi)$ can be arbitrarily chosen in the limit of a finite interface width. Two different potentials are widely employed: the double well potential and the double obstacle potential. In the case of the double well potential [72, 73], the potential function $g(\phi)$ and the interpolation function $h(\phi)$ are given by

$$g(\phi) = \phi^2 (1 - \phi)^2 \tag{2.100}$$

and

$$h(\phi) = \phi^3(10 - 15\phi + 6\phi^2). \tag{2.101}$$

Their derivatives are

$$g_\phi = 2\phi(1-\phi)(1-2\phi) \tag{2.102}$$

and

$$h_\phi = 30\phi^2(1-\phi)^2. \tag{2.103}$$

In the case of the double obstacle potential [62, 72], the potential function $g(\phi)$ is

$$g(\phi) = \frac{1}{2}|\phi(1-\phi)|. \tag{2.104}$$

The derivatives of the potential function $g(\phi)$ and the interpolation function $h(\phi)$ are given by

$$g_\phi = \frac{1}{2} - \phi \quad \text{for } 0 \le \phi \le 1 \tag{2.105}$$

and

$$h_\phi = \sqrt{\phi(1-\phi)}. \tag{2.106}$$

Note that both the double well potential and the double obstacle potential can be employed for quantitative phase field simulations [72]. There is no preference in terms of the simulation accuracy.

In the thin-interface limit, for diffusion-controlled solidification simulations with an infinite kinetic mobility, the kinetic parameter τ is given by [62]

$$\tau = \frac{a_1 a_2 W^3 \Delta S m_l \left(c^l - c^s\right)}{\sigma D^l}, \tag{2.107}$$

where a_2 is a numerical constant, ΔS the entropy change during solidification, m_l the liquidus slope and D^l the diffusion coefficient in the liquid. In the case of the double well potential, the numerical constants are $a_1 = \sqrt{2}/6$ and $a_2 = 2.35$, while the numerical constants are $a_1 = 1$ and $a_2 = 0.36$ in the case of the double obstacle potential.

The concentration within the simulation domain is defined as c. The governing equation for diffusion is given by [72]

$$\frac{\partial c}{\partial t} = \nabla \cdot \left(D^l(1-\phi)\nabla c^l + D^s \phi \nabla c^s + \frac{W}{\sqrt{2}}(c^l - c^s)\frac{\nabla \phi}{|\nabla \phi|}\frac{\partial \phi}{\partial t} \right) \tag{2.108}$$

where c^l is the liquid concentration, c^s the solid concentration and D^s the diffusion coefficients in the solid, respectively. The liquid concentration c^l and the solid concentration c^s are determined by the quasi-equilibrium condition based on c and ϕ. The term $\frac{W}{\sqrt{2}}(c^l - c^s)\frac{\nabla \phi}{|\nabla \phi|}\frac{\partial \phi}{\partial t}$ is the anti-trapping flux, which is introduced by Karma [65] to compensate for asymmetrical fluxes in the interface region if the diffusivity within the two phases differs significantly.

The sharp-interface limit

In the case of 1D steady state, a travelling wave solution can be obtained with velocity v,

$$v = M_k \Delta G_v^{ls}. \tag{2.109}$$

The travelling wave solution for the double well potential is [72, 73]

$$\phi(x,t) = \frac{1}{2} \left(1 - \tanh\left(\frac{1}{\sqrt{2}W}(x - vt) \right) \right), \tag{2.110}$$

while the travelling wave solution for the double obstacle potential is [72, 73]

$$\phi(x,t) = \frac{1}{2} \left(1 - \sin\left(\frac{1}{W}(x - vt) \right) \right). \tag{2.111}$$

In the case of the double obstacle condition, we have

$$\frac{\partial \phi}{\partial x} = -\frac{1}{2W} \cos\left(\frac{1}{W}(x - vt) \right) = -\frac{1}{W} \sqrt{\phi(1 - \phi)} \tag{2.112}$$

and

$$\frac{\partial^2 \phi}{\partial x^2} = \frac{1}{2W^2} \sin\left(\frac{1}{W}(x - vt) \right) = \frac{1}{W^2} \left(\frac{1}{2} - \phi \right). \tag{2.113}$$

In the case of the double obstacle potential, expanding the Laplacian $\nabla^2 \phi$ of a spherically symmetric problem in the radius coordinate ρ gives [73]

$$\begin{aligned} \nabla^2 \phi &= \frac{\partial^2 \phi}{\partial \rho^2} + \frac{1}{\rho} \frac{\partial \phi}{\partial \rho} \\ &= \frac{1}{W^2} \left(\frac{1}{2} - \phi \right) - \frac{1}{\rho W} \sqrt{\phi(1 - \phi)} + O\left(\frac{1}{\rho^2} \right) \end{aligned} \tag{2.114}$$

Substitute Equation (2.114) into Equation (2.99) gives

$$\begin{aligned} \tau \frac{\partial \phi}{\partial t} &= W^2 \nabla^2 \phi - \left(\frac{1}{2} - \phi \right) + \frac{W}{\sigma} \sqrt{\phi(1 - \phi)} \Delta G_v^{ls} \\ &\approx \frac{W}{\sigma} \sqrt{\phi(1 - \phi)} \left(-\frac{\sigma}{\rho} + \Delta G_v^{ls} \right) \end{aligned} \tag{2.115}$$

Substituting Equations (2.112) and (2.115) into Equation (2.109) and with $\kappa = 1/\rho$, the interface velocity v can be written as

$$v = \frac{\partial \phi / \partial t}{\partial \phi / \partial x} = \frac{W^2}{\tau \sigma} \left(-\sigma \kappa + \Delta G_v^{ls} \right), \tag{2.116}$$

which is in fact the Gibbs-Thomson equation. Note Equation (2.116) is only valid in the condition that the simulation is independent of the interface width. In the case of a finite interface width and if the phase field equation is coupled with the diffusion equation, the driving force ΔG_v^{ls} is not constant in the interface region, leading to spurious effects [73]. To remove the spurious effects, the interface width must be very small so that the driving force in the interface region can be considered as constant, which is known as the sharp-interface limit.

The thin-interface limit

With a finite interface width, the driving force in the interface region is not constant if there is a significant concentration gradient on the scale of the interface width W used in the numerical simulations [73]. In steady-state motion of a planar solidification interface (1D), assuming the diffusion in the solid is negligible ($D^s \approx 0$), Equation (2.108) can be written as [73]

$$-v\frac{\mathrm{d}c}{\mathrm{d}x} = \frac{\partial c}{\partial t} = \frac{\mathrm{d}}{\mathrm{d}x}\left(D^l(1-\phi)\frac{\mathrm{d}c^l}{\mathrm{d}x} + \frac{W}{\sqrt{2}}(c^l-c^s)v\frac{\mathrm{d}\phi}{\mathrm{d}x}\right). \tag{2.117}$$

Integration over the interface region yields [73]

$$v(c^s|_{\phi\approx1} - c^l|_{\phi\approx0}) = D^l(1-\phi)\frac{\mathrm{d}c^l}{\mathrm{d}x} + \frac{W}{\sqrt{2}}(c^l-c^s)v\frac{\mathrm{d}\phi}{\mathrm{d}x}. \tag{2.118}$$

In the steady state, according to Kim [67] the liquid concentration gradient $\mathrm{d}c^l/\mathrm{d}x$ is

$$\frac{\mathrm{d}c^l}{\mathrm{d}x} = v(1-\phi)(D^l)^{-1}(c^s|_{\phi\approx1} - c^l|_{\phi\approx0}). \tag{2.119}$$

In the steady state, we have

$$v\frac{\mathrm{d}\phi}{\mathrm{d}x} = M_p\Delta G_{\mathrm{v}}^{ls}\frac{\mathrm{d}\phi}{\mathrm{d}x}. \tag{2.120}$$

In the interface region, v is constant while the phase field mobility M_p and the local driving force G_{v}^{ls} vary. Integration over the whole system yields

$$\begin{aligned}
v\int_{-\infty}^{\infty}\frac{\mathrm{d}\phi}{\mathrm{d}x}\mathrm{d}x &= M_p\int_{-\infty}^{\infty}\Delta G_{\mathrm{v}}^{ls}\frac{\mathrm{d}\phi}{\mathrm{d}x}\mathrm{d}x \\
&= M_p\left[\Delta G_{\mathrm{v}}^{ls}|_{\phi\approx0} - \int_{-\infty}^{\infty}\phi\frac{\mathrm{d}\Delta G_{\mathrm{v}}^{ls}}{\mathrm{d}x}\mathrm{d}x\right].
\end{aligned} \tag{2.121}$$

With Equation (2.119), we have

$$\frac{\mathrm{d}\Delta G_{\mathrm{v}}^{ls}}{\mathrm{d}x} = \Delta Sm^l\frac{\mathrm{d}c^l}{\mathrm{d}x} = \Delta Sm^l v(1-\phi)(D^l)^{-1}(c^s|_{\phi\approx1} - c^l|_{\phi\approx0}), \tag{2.122}$$

$$v = M_p\left\{\Delta G_{\mathrm{v}}^{ls}|_{\phi\approx0} - v\frac{\pi W}{8}\Delta Sm^l(D^l)^{-1}(c^s|_{\phi\approx1} - c^l|_{\phi\approx0})\right\}. \tag{2.123}$$

The velocity v is thus written as

$$\begin{aligned}
v &= \frac{M_p\Delta G_{\mathrm{v}}^{ls}|_{\phi\approx0}}{1 - M_p\frac{\pi W}{8}\Delta Sm^l(D^l)^{-1}(c^s|_{\phi\approx1} - c^l|_{\phi\approx0})} \\
&= M_k\Delta G_{\mathrm{v}}^{ls}|_{\phi\approx0},
\end{aligned} \tag{2.124}$$

with

$$M_k = \frac{M_p}{1 - M_p\frac{\pi W}{8}\Delta Sm^l(D^l)^{-1}(c^s|_{\phi\approx1} - c^l|_{\phi\approx0})}. \tag{2.125}$$

For a diffusion-controlled solidification simulation, the kinetic mobility M_k is infinite. The phase field mobility M_p is then

$$M_p = \frac{8D^l}{\pi W \Delta S m^l (c^s - c^l)}. \tag{2.126}$$

From Equation (2.116), it is clear that

$$M_p = \frac{W^2}{\tau \sigma}. \tag{2.127}$$

Then, the kinetic parameter τ is given by

$$\tau = \frac{\pi W^3 \Delta S m^l (c^s - c^l)}{8 \sigma D^l}. \tag{2.128}$$

Note the solvability condition is not considered here, which is why the constant ($\pi/8 = 0.3927$) in Equation (2.128) is different from the constant $a_1 a_2 = 0.36$ given in Equation (2.107). A detailed analysis considering the solvability condition can be found in [72]. Moreover, a detailed asymptotic analysis for the thin-interface limit is described in [62].

2.4 SOLIDIFICATION CRACKING

Solidification cracking, also known as hot tearing in casting [74, 75], is a type of solidification defect which forms in the mushy zone of welded [76, 77] or additively manufactured [78–80] components. In the mushy zone, liquid channels exist at a relatively low temperature due to solute segregation, which may experience a tensile loading due to thermal contraction and solidification shrinkage. Cracks form if there is not sufficient liquid feeding. Solidification cracking is a complex phenomenon which is associated with thermal, metallurgical and mechanical phenomena [81]. In general, whether solidification cracks form depends on the alloy composition and the process parameters like power, welding velocity and the mechanical fixing constraints. The alloy composition and the process parameters determine local conditions in the mushy zone like the temperature range of the mushy zone, temperature gradient, cooling rate, stress, strain, strain rate, grain morphology and fluid flow in the liquid channels.

2.4.1 EXPERIMENTAL WORKS

Numerous experimental studies have been performed to understand the mechanisms of solidification cracking. The influence of the alloy composition on solidification cracking susceptibility (SCS) was extensively studied. Suyitno et al. [82] investigated the effects of the copper contents and the casting speed on the solidification cracking susceptibility of Al-Cu alloys. A "lambda" (Λ) shape was reported for the compositional dependence of SCS and the composition range associated with the maximum SCS was between 0.5 and 1.5 wt.% Cu [82, 83], as shown in Figure 2.9. Similarly, the "lambda" (Λ) shape was also reported in many other alloys [84, 85], as shown in Figure 2.10. Li et al. [86] indicated that increasing the solute content extends the temperature range of the mushy zone and increases the amount of contraction and SCS, while further alloying beyond the solid solution limit generates more eutectics, leading to a decrease in SCS.
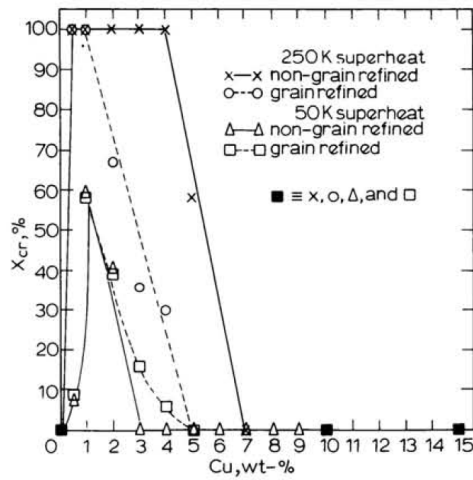
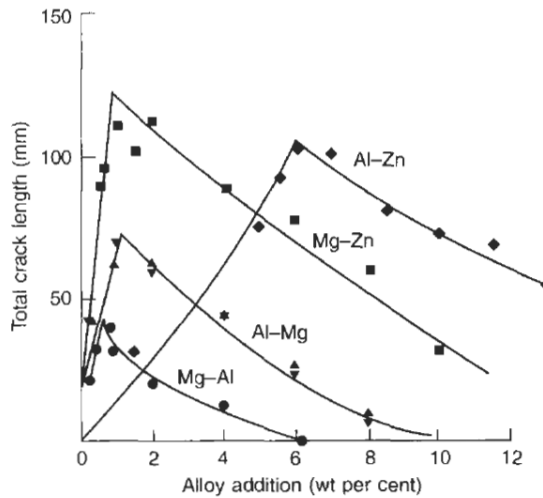Figure 2.9: Solidification cracking susceptibility (X_{cr}) of Al-Cu alloy [83].

Figure 2.10: Solidification cracking susceptibility of various alloys [85].

The influence of process parameters like power and velocity on SCS have been investigated by many researchers. Slyvinsky et al. [87] reported that increasing the welding velocity v_s with a constant power Q leads to a decrease in SCS for a nickel-base alloy. The decrease in SCS with increasing welding velocity while keeping the power constant was confirmed by Goodwin [88] and Agarwal et al. [89]. This was explained by the smaller thermal strain generated during welding at a faster welding velocity v_s [89]. Differently, when the welding velocity v_s is increased with a constant Q/v_s ratio, an increase in SCS was reported by Ohshita et al. [90], Shibahara et al. [91], Suyitno et al. [82], Cicală et al. [92] and Goodwin [88]. Nevertheless, it was also found [93] that increasing the welding velocity promotes the transition from a columnar to an equiaxed structure in the weld pool and thus inhibits solidification cracking in aluminum alloy 6082, as shown in Figure 2.11. Hyer et al. [78] found that with increasing scanning velocity, SCS first increased and then decreased during laser powder bed fusion, as shown in Figure 2.12; the peak value of SCS was observed at around 2.0 m/s.
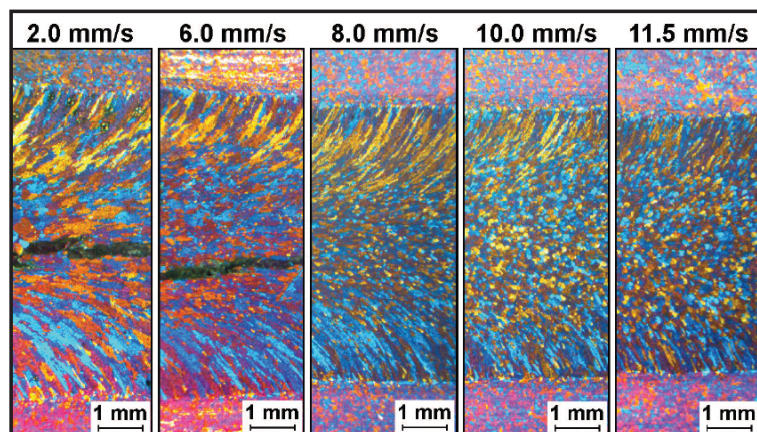

Figure 2.11: Microstructure in the melt pool under different welding velocities. Gas-tungsten-arc bead-on-plate welds (no grain refiner addition), Alloy 6082, plate thickness 3 mm. [93].

Coniglio and Cross reviewed the effects of the welding velocity on solidification cracking behavior [81, 94]. It was indicated [81, 94] that increasing welding velocity decreases the centerline temperature gradient, leading to an increase in the mushy zone length and thus an increase in SCS. Conversely, increasing welding velocity shifts the compressional region to the mushy zone, reduces the time exposed to strain and refines the grains, which hinders the formation of solidification cracks. The combined effects determine the influence of the welding velocity on SCS.

Grain refinement has been an effective approach to reduce SCS. In a refined microstructure, the tensile loading exerted on each liquid channel is smaller, leading to a decrease in SCS. Warrington and McCartney [95] found that grain refinement by adding grain refiners reduced SCS in AA7010 and AA7050. Easton et al. [96] indicated that grain refinement delayed the onset of load development in the mushy zone and reduce the severity of hot tearing in AA6061. Martin et al. [97] added hydrogen-stabilized zirconium particles to
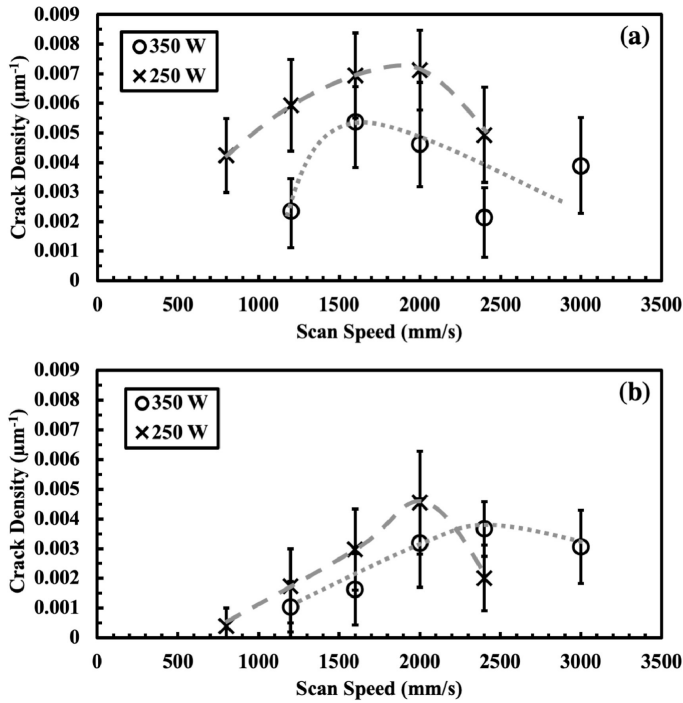
Figure 2.12: SCS as a function of laser power and scan speed for Al-Si alloys with 1.0 wt.% Si (a) and 2.0 wt.% Si (b) [78].
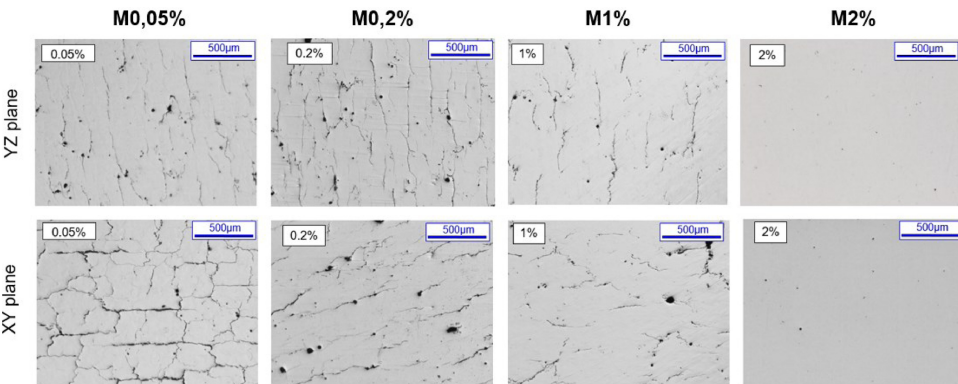

Figure 2.13: The density of solidification cracks reduces with increasing addition of the grain refiner (M) [80].

AA7075 and AA6061 to refine the AM microstructure and thus avoid the occurrence of solidification cracks. Opprecht et al. [80] added Yttrium Stabilized Zirconia into 6061 alloy powder during additive manufacturing to achieve grain refinement and eliminated solidification cracks successfully, as shown in Figure 2.13.

2.4.2 Modelling works

Compared to experimental studies, modelling works provide a way to unravel the mechanisms of solidification cracking with theoretical basis and to predict SCS. In this section, existing models including stress-based criteria, strain-based criteria, Kou's model, the RDG model and a 3D granular model are described.

Stress-based criteria

Novikov [98] and Dickhaus [99] reported a stress-based solidification cracking criterion, in which the critical stress to pull apart two parallel plates separated by a thin liquid film is given by

$$\sigma_{fr} = \frac{2\gamma}{b} \tag{2.129}$$

where γ is the surface tension and b the film thickness. This model neglects the liquid viscosity and the wetting angle [100]. To overcome this limitation, Dickhaus [99] introduced viscosity; the resultant separation force of the parallel plates of radius R separated by a liquid film is given by

$$F_z = \frac{3\pi\eta R^4}{8t} \left(\frac{1}{b_1^1} - \frac{1}{b_1^2} \right), \tag{2.130}$$

where F_z is the force required to increase the film thickness from b_1 to b_2, η the viscosity, R the radius of the plate and t the time required to increase the film thickness from b_1 to b_2. Following Equation (2.129), Lahaie and Bouchard [101] calculated the fracture stress as a function of solid fraction f_s, strain ε and microstructure parameter m,

$$\sigma_{fr} = \frac{4\eta}{3b} \left(1 + \frac{(f_s)^m}{1 - (f_s)^m} \varepsilon \right)^{-1}. \tag{2.131}$$

The microstructure parameter m is $1/3$ for equiaxed and $1/2$ for columnar structures. According to the model of Lahaie and Bouchard [101], the fracture stress increased with decreased grain size, which agreed with the low SCS for fine-grained structures. However, the negligible effects of the grain size on fracture strain is questionable [100]. Besides, this model did not consider the liquid feeding, which is an important parameter for solidification cracking.

Williams and Singer [102] modified the Griffith cracking criteria in fracture mechanics for solidification cracking prediction. The fracture stress σ_{fr} is given by

$$\sigma_{fr} = \sqrt{\frac{8G_s\gamma}{\pi(1-\upsilon)AV_l^{1/2}}}, \tag{2.132}$$

where A is a constant dependent on the grain size and the dihedral angle, G_s the shear modulus, γ the effective fracture surface energy, V_l the volume of the liquid and υ the

Poisson's ratio. This model gives an accurate prediction of the critical fracture stress at various Sn concentrations in Al-Sn alloys. However, it predicts an increase in SCS with decreasing grain size, which contradicts the experimental observations [100].

STRAIN-BASED CRITERIA

Novikov [98] proposed a hot shortness criterion. A characteristic called "reserve of plasticity in the solidification range" p_r is employed to evaluate SCS, which is the difference between the average failure strain ε_p and the average shrinkage strain ε_{sh} in the brittle temperature range ΔT_{br},

$$p_r = \frac{\int \varepsilon_p - \int \varepsilon_{sh}}{\Delta T_{br}}. \tag{2.133}$$

Magnin et al. [103] used a similar model to predict solidification cracking of an Al-4.5% Cu alloy. It was assumed that cracking occurs when the maximum principle plastic strain exceeds the experimentally determined fracture strain in the solidification range. They found that with increasing casting speeds, the cracking susceptibility increases, which matches industrial experiences. Following Equation (2.133), Prokhorov [104] defined the reserve of technological strength in the semi-solid state $\Delta \varepsilon_{res}$ in the form

$$\Delta \varepsilon_{\text{res}} = D_{\min} - \left(\Delta \varepsilon_{\text{free}} + \Delta \varepsilon_{\text{app}} \right), \tag{2.134}$$

where $\varepsilon_{\text{free}}$ is the free thermal contraction strain, ε_{app} the actual strain in the solidifying body and $D_{\min}$ the minimum point of the ductility curve, as shown in Figure 2.14. After reformulation, the cracking condition is given by a strain-rate based criterion

$$\dot{\varepsilon}_{\text{res}} = \dot{\varepsilon}_{\min} - \dot{\varepsilon}_{\text{free}} - \dot{\varepsilon}_{\text{app}} \leq 0, \tag{2.135}$$

$$\dot{\varepsilon}_{\min} - \dot{\varepsilon}_{\text{free}} \leq \dot{\varepsilon}_{\text{app}}. \tag{2.136}$$

Compared to Novikov's criterion, Prokhorov employed strain rate and the lowest point in the ductility curve for SCS evaluation while Novikov employed strain and the whole ductility curve for calculation. Moreover, Prokhorov considered the contribution of the body constraints on strain, while Novikov did not.

KOU'S MODEL

Kou [105] proposed a model for solidification cracking in the liquid channel between columnar grains. It considers separation of the grains due to tensile loading, growth of the grains and the liquid feeding in the liquid channel. The cracking condition is given as

$$\left[\underbrace{\frac{d\varepsilon}{dt}}_{\text{separation}} > \underbrace{(1-\beta)\frac{d\sqrt{f_s}}{dt}}_{\text{solidification}} + \underbrace{\frac{d}{dz}\left[\left(1 - \sqrt{1-\beta}\sqrt{f_s}\right) v_z \right]}_{\text{liquid feeding}} \right]_{\sqrt{f_s} \to 1}, \tag{2.137}$$
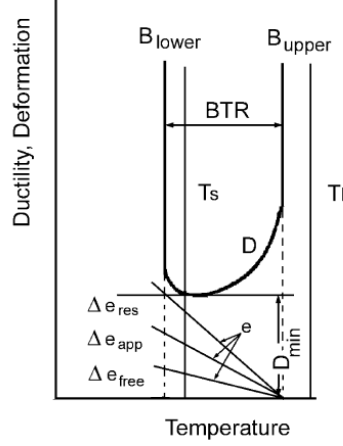
Figure 2.14: Ductility of semi-solid alloys and strain caused by solidification shrinkage and configuration of the semisolid body [104].

where β is the shrinkage factor during solidification, $\frac{d\varepsilon}{dt}$ the local strain rate and v_z the liquid feeding velocity. After dividing by the cooling rate dT/dt, Equation (2.137) becomes

$$
\left[\underbrace{\frac{d\varepsilon}{dT}}_{\text{separation}} > \underbrace{(1-\beta)\frac{d\sqrt{f_s}}{dT}}_{\text{solidification}} + \underbrace{\frac{1}{dT/dt}\frac{d}{dz}\left[\left(1-\sqrt{1-\beta}\sqrt{f_s}\right)v_z\right]}_{\text{liquid feeding}} \right]_{\sqrt{f_s}\to 1} . \qquad (2.138)
$$

Based on Equation (2.138), the derivative $dT/d\sqrt{f_s}\,|_{\sqrt{f_s}\to 1}$ of temperature with respect to $\sqrt{f_s}$ near $\sqrt{f_s} = 1$ is proposed as a hot cracking susceptibility (SCS) index.

Kou's SCS index is then employed to evaluate SCS of Al-Cu alloys based on Scheil-Gulliver calculations. It successfully predicts the "lambda" (Λ) shape in the compositional dependence of SCS with the maximum SCS at round 1.0 wt.% Cu [106], as shown in Figure 2.15, which agrees with the experiments of Pumphrey [107]. Kou's SCS index also successfully predicted the compositional dependence curves of SCS in Al-Mg alloys, Al-Zn alloys and Al-Sn alloys [106]. Geng et al. [108] studied the influence of back-diffusion on SCS of Al-Mg alloys during welding. Kou's SCS index was employed to evaluate SCS based on the segregation curves obtained from phase field simulations of directional solidification. The results explained the low SCS in Al-4.0 wt.% alloy despite its wide freezing temperature range. Han et al. [109] studied the grain coalescence behavior and its influence on SCS with a multi-phase phase field model and Kou's SCS index. It was found that grain boundary energy suppressed grain coalescence and increased SCS.

RDG model

Rappaz et al. [74] derived an equation to calculate the pressure drop in the liquid channel from the dendrite tip to the coalescence point. In this two-phase model, the mushy zone is
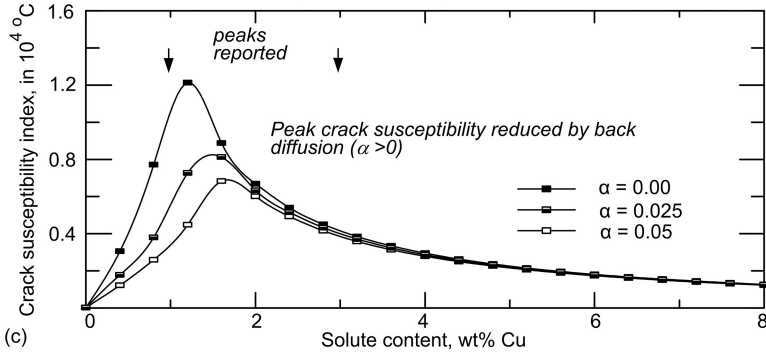
Figure 2.15: Crack susceptibility curves of Al-Cu alloys based on Kou's SCS index. α represents the intensity of back diffusion. [106].

treated as a whole, as shown in Figure 2.16. The mass balance is written as [74]

$$\nabla \cdot \langle \rho v \rangle - v_T \frac{\partial \langle v \rangle}{\partial x} = 0, \tag{2.139}$$

where the notation $\langle \cdot \rangle$ is used to indicate values locally averaged over the liquid and the solid phases and v_T the pulling velocity. The average mass flow $\langle \rho v \rangle$ and the average velocity $\langle v \rangle$ are given by

$$\langle \rho v \rangle = \rho_s f_s v_s + \rho_l f_l v_l \tag{2.140}$$

and

$$\langle v \rangle = f_s v_s + f_l v_l \tag{2.141}$$

where ρ_l and ρ_s are the densities of the liquid and the solid, f_l and f_s the fraction of the liquid and the solid, v_l and v_s the velocity of the liquid and the solid. Considering the liquid flows in the x direction and the solid deforms in the y direction, the mass balance equation can be written as [74]

$$\frac{\partial \rho_l f_l v_{l,x}}{\partial x} + \frac{\partial \rho_s f_s v_{s,y}}{\partial y} - v_T \left[\frac{\mathrm{d}\rho_s f_s}{\mathrm{d}x} + \frac{\mathrm{d}\rho_l f_l}{\mathrm{d}x} \right] = 0. \tag{2.142}$$

With $\beta = \rho_s/\rho_l - 1$ and $\dot{\varepsilon}_p = \partial v_{s,y}/\partial y$, the mass balance takes the form [74]

$$\frac{\mathrm{d} f_l v_{l,x}}{\mathrm{d}x} + (1+\beta) f_s \dot{\varepsilon}_p - v_T \beta \frac{\mathrm{d} f_s}{\mathrm{d}x} = 0. \tag{2.143}$$

Integrating the above equation over x and considering the boundary condition ($v_{l,x} = 0$ and $f_s = 1$ at $x = 0$) gives the liquid velocity as a function of x [74]

$$f_l v_{l,x} = -(1+\beta) \int f_s \dot{\varepsilon}_p \mathrm{d}x - v_T \beta f_l. \tag{2.144}$$

The liquid velocity can be related to the pressure gradient $\frac{\mathrm{d}p}{\mathrm{d}x}$ in the liquid with the Darcy equation [74]

$$f_l v_{l,x} = -\frac{K}{\eta} \frac{\mathrm{d}p}{\mathrm{d}x}, \tag{2.145}$$
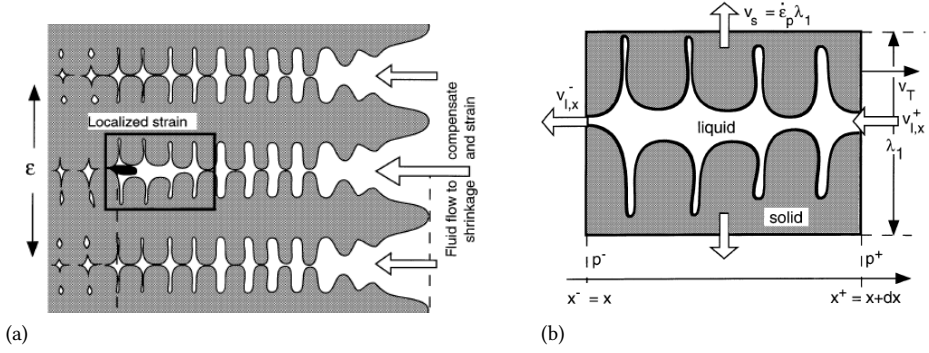
Figure 2.16: A schematic illustration of the solidification cracking condition in the RDG model (a); a representative volume element is enlarged in (b).

where η is the liquid viscosity and K the permeability of the mushy zone, which is given by the Carman-Kozeny approximation

$$K = \frac{\lambda_2^2}{180}\frac{(1-f_s)^3}{f_s^2},$$ (2.146)

where λ_2 is the secondary dendrite arm spacing. After integration, the pressure drop from the dendrite tip to the coalescence point is given by

$$\Delta p_{\max} = \Delta p_m + \Delta p_{sh}$$ (2.147)

where Δp_m and Δp_{sh} are the mechanical contribution and the shrinkage contribution to pressure drop, which are given by

$$\Delta p_m = \frac{180}{\lambda_2^2}\frac{(1+\beta)\eta}{G}\int_{T_s}^{T_l}\frac{E(T)f_s^2}{(1-f_s)^3}dT,$$ (2.148)

$$\Delta p_{sh} = \frac{180}{\lambda_2^2}\frac{v_T\beta\eta}{G}\int_{T_s}^{T_l}\frac{f_s^2}{(1-f_s)^3}dT,$$ (2.149)

where G is the temperature gradient. $E(T)$ is an integral given by

$$E(T) = \frac{1}{G}\int_{T_s}^{T_l}f_s\dot{\varepsilon}_p dT.$$ (2.150)

Under a condition of $\dot{T} = -1\,\text{K/s}$ and $\dot{\varepsilon}_p = 10^{-4}\,\text{s}^{-1}$, the RDG model predicts the maximum SCS of the Al-Cu alloy at around 1.4 wt.% Cu, as shown in Figure 2.17, which agrees with the experimental results. Yang et al. [110] performed phase field simulations and employed the RDG model to study the influence of attractive, neural and repulsive grain boundaries on SCS. The Λ-shape variation of SCS as a function of solute concentration was reproduced, as shown in Figure 2.18. It was found that the Λ curve peak shifts to higher SCS and lower concentrations as grain boundary energy increases [110]. By comparing with the theoretical fracture stress, it was shown that the RDG model is able to predict the solidification cracking accurately.
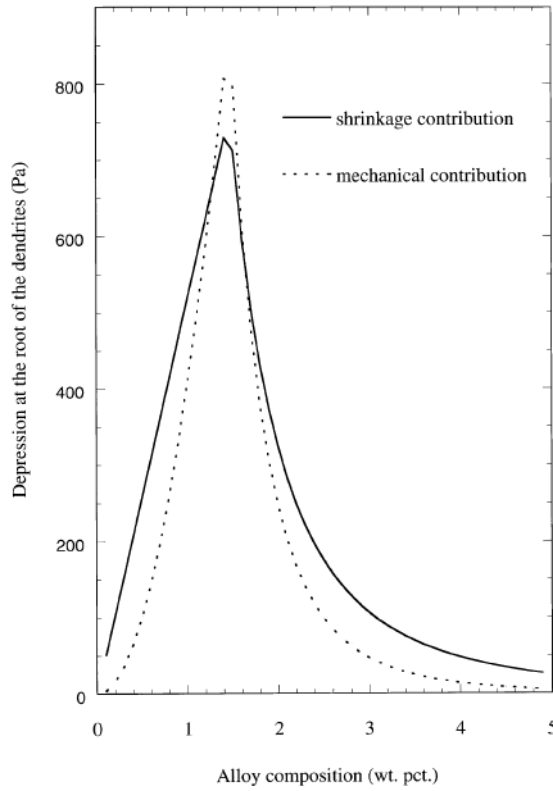
Figure 2.17: The relation between SCS and solute concentration for Al-Cu alloys predicted by the RDG model [74].
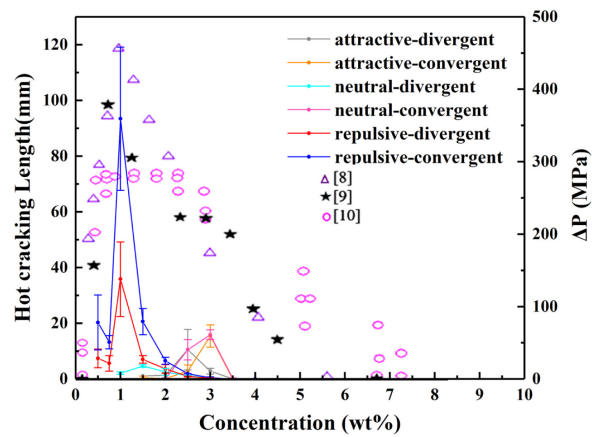

Figure 2.18: The relation between SCS and solute concentration for Al-Cu alloys predicted by the RDG under different grain boundaries [110].

3D granular model

Sistaninia et al. [111] proposed a 3D granular model which calculated the 3D intergranular pressure in the mushy zone during casting. It was assumed that the fluid flow in the liquid channels can be approximated with the Poiseuille flow between two parallel plates, which is given by

$$\vec{v}_l = \frac{1}{2\mu_v} \nabla p \left(z^2 - h^2 \right),$$ (2.151)

where the liquid channel width is $2h$, μ_v the liquid viscosity, p the liquid pressure and z the axis which is perpendicular to the liquid channel.

Consider mass balance in a representative volume V_l of the liquid channel. The mass balance is given by [111]

$$\int_{V_l} \nabla \cdot \vec{v}_l = \int_{S_{sl}} \vec{v_{sl}} \cdot \vec{n} dS + \int_{S_l} \vec{v}_l \cdot \vec{n} dS,$$ (2.152)

where S_{sl} is the solid-liquid interface, S_l the liquid interface of the considered volume, $\vec{v_{sl}}$ the separation velocity at the solid-liquid interface and $\vec{n}$ the interface normal unit vector. Assuming incompressible liquid gives [111]

$$\int_{V_l} \nabla \cdot \vec{v}_l = 0.$$ (2.153)

The first term on the right-hand side of Equation (2.152) is given by [111]

$$\int_{S_{sl}} \vec{v_{sl}} \cdot \vec{n} dS = S_{sl} v_{sl} = S_{sl} \left(2\beta v_{ln} + \Delta v_{sn} \right),$$ (2.154)

where β is the shrinkage factor, v_{ln} the solidification velocity, $2\beta v_{ln}$ the separation velocity due to solidification shrinkage and Δv_{sn} the separation velocity due to deformation in the solid. The second term on the right-hand side of Equation (2.152) is given by [111]

$$\int_{S_l} \vec{v}_l \cdot \vec{n} dS = \frac{1}{2\mu_v} \int_{S_l} \nabla p \cdot \vec{n} \left(z^2 - h^2 \right) dz dS$$
$$= -\frac{2h^3}{3\mu_v} \nabla^2 p S_{sl}$$ (2.155)

Thus, Equation (2.152) gives [111]

$$\frac{2h^3}{3\mu_v} \nabla^2 p = 2\beta v_{ln} + \Delta v_{sn}.$$ (2.156)

In the work of Sistaninia et al. [111], the microstructure in the mushy zone was generated artificially with a Voronoi tessellation. The grain boundary structure was employed as the liquid channel network, on which the intergranular liquid pressure is calculated by solving Equation (2.156) with a finite element method. This model was further coupled with a failure criterion [112], in which the critical stress p_l^c to overcome the capillary force at the liquid-atmosphere interface is given by

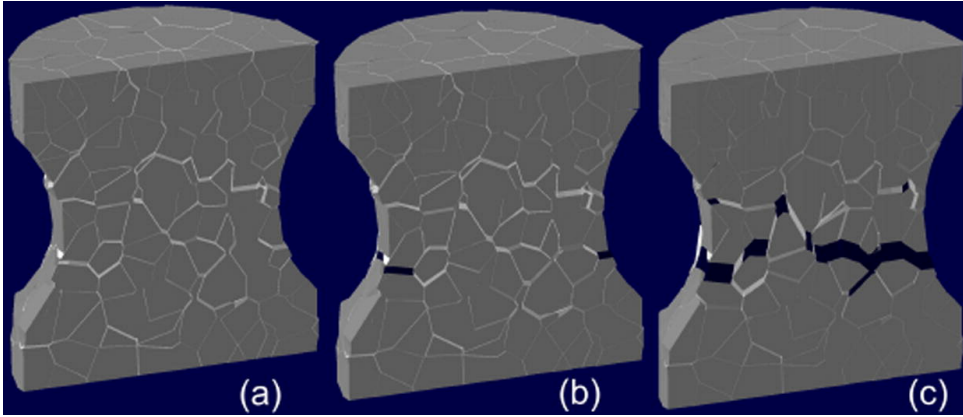$$p_l^c = p_a - \frac{\gamma \cos\theta}{h},$$ (2.157)

Figure 2.19: Evolution in the semi-solid microstructure under tensile loading as predicted by the 3D granular model at $t = 405$ s (a), $t = 729$ s (b) and $t = 1215$ s (c). The white areas outline the intergranular liquid, the dark areas the growing voids and the gray areas the solid phase. [112].
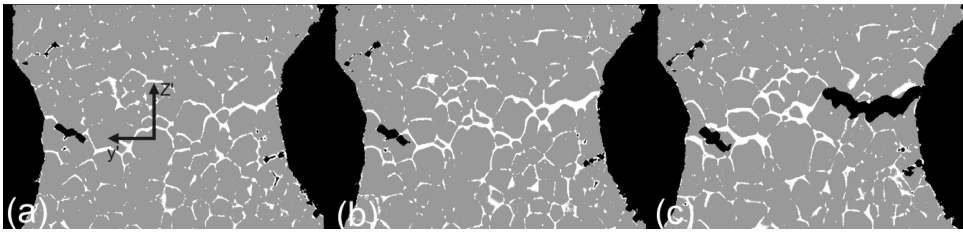

Figure 2.20: Evolution in the semi-solid microstructure under tensile loading as predicted by the 3D granular model as observed by X-ray tomography at $t = 486$ s (a), $t = 729$ s (b) and $t = 1215$ s (c). [112].

where p_a the atmospheric pressure, γ the surface tension at the liquid-atmosphere interface and θ the dihedral angle. In the work of Sistaninia et al. [112], the value of $\gamma \cos \theta$ was fixed to be $5 \, \text{J/m}^2$. The model was then validated with an in-situ semi-solid tensile test using X-ray microtomography and the results are given in Figures 2.19 and 2.20. The stress predicted by the granular model under tensile and shear deformations agreed well with the experimental results. Rajani et al. [113, 114] then employed the 3D granular model to predict the occurrence of solidification cracking during welding. Instead of the critical stress approach, Kou's cracking model was employed as the cracking criterion. In this case, the results from Rajani et al. are questionable. In the 3D granular model, Equation (2.156) implicitly assumes a mass balance, which contradicts Kou's cracking criterion that solidification cracking occurs when the mass balance is not satisfied.

2.5 SUMMARY AND CONCLUSIONS

In this chapter, solidification thermodynamics and kinetics have been described, which provides a basis for solidification modelling. Many decades ago, analytical models were employed to described solidification behavior like the parabolic growth under a constant

undercooling, columnar to equiaxed transition and segregation. Nowadays, thanks to the development of computational power, numerical simulations via the cellular automata method or the phase field method are possible, which predict the evolution of microstructure explicitly. Moreover, a solidification related problem, solidification cracking is introduced from the perspectives of experiments and modelling. It is found that existing models show a good performance in predicting the dependence on solidification cracking susceptibility (SCS). However, a comprehensive study of the influence of process parameters on SCS is not available and needs development.

References

[1] Larry Kaufman and Harold Bernstein. Computer calculation of phase diagrams. with special reference to refractory metals. 1970.

[2] Bo Sundman, Qing Chen, and Yong Du. A review of calphad modeling of ordered phases. *Journal of Phase Equilibria and Diffusion*, 39:678–693, 2018.

[3] Otto Redlich and AT Kister. Algebraic representation of thermodynamic properties and the classification of solutions. *Industrial & Engineering Chemistry*, 40(2):345–348, 1948.

[4] Mats Hillert. *Phase equilibria, phase diagrams and phase transformations: their thermodynamic basis*. Cambridge university press, 2007.

[5] Bo Sundman, Ursula R Kattner, Christophe Sigli, Matthias Stratmann, Romain Le Tellier, Mauro Palumbo, and Suzana G Fries. The opencalphad thermodynamic software interface. *Computational materials science*, 125:188–196, 2016.

[6] Bo Sundman, Xiao-Gang Lu, and Hiroshi Ohtani. The implementation of an algorithm to calculate thermodynamic equilibria for multi-component systems with non-ideal phases in a free software. *Computational Materials Science*, 101:127–137, 2015.

[7] Janin Eiken, Bernd Böttger, and Ingo Steinbach. Multiphase-field approach for multicomponent alloys with extrapolation scheme for numerical application. *Physical review E*, 73(6):066122, 2006.

[8] B Böttger, J Eiken, and M Apel. Multi-ternary extrapolation scheme for efficient coupling of thermodynamic data to a multi-phase-field model. *Computational Materials Science*, 108:283–292, 2015.

[9] R Trivedi and W Kurz. Dendritic growth. *International Materials Reviews*, 39(2):49–74, 1994.

[10] Doru M Stefanescu and Roxana Ruxanda. Fundamentals of solidification. 2004.

[11] Seong Gyoon Kim, Won Tae Kim, and Toshio Suzuki. Phase-field model for binary alloys. *Physical review e*, 60(6):7186, 1999.

[12] GP Ivantsov. The temperature field around a spherical, cylindrical, or pointed crystal growing in a cooling solution. In *Dokl. Akad. Nauk SSSR*, volume 58, pages 567–569, 1947.

[13] J Lipton, ME Glicksman, and W Kurz. Dendritic growth into undercooled alloy metals. *Materials Science and Engineering*, 65(1):57–63, 1984.

[14] Shijia Chen, Gildas Guillemot, and Charles-André Gandin. Three-dimensional cellular automaton-finite element modeling of solidification grain structures for arc-welding processes. *Acta materialia*, 115:448–467, 2016.

[15] Yanping Lian, Stephen Lin, Wentao Yan, Wing Kam Liu, and Gregory J Wagner. A parallelized three-dimensional cellular automaton model for grain growth during additive manufacturing. *Computational Mechanics*, 61:543–558, 2018.

[16] Rongpei Shi, Saad A Khairallah, Tien T Roehling, Tae Wook Heo, Joseph T McKeown, and Manyalibo J Matthews. Microstructural control in metal laser powder bed fusion additive manufacturing using laser beam shaping strategy. *Acta Materialia*, 184:284–305, 2020.

[17] W 1 Kurz, B Giovanola, and R Trivedi. Theory of microstructural development during rapid solidification. *Acta metallurgica*, 34(5):823–830, 1986.

[18] David Fisher and W Kurz. Fundamentals of solidification. *Fundamentals of Solidification*, pages 1–316, 1998.

[19] Rohit Trivedi. Interdendritic spacing: Part ii. a comparison of theory and experiment. *Metallurgical and Materials Transactions A*, 15:977–982, 1984.

[20] Fengyi Yu, Yanhong Wei, and Xiangbo Liu. The evolution of polycrystalline solidification in the entire weld: A phase-field investigation. *International Journal of Heat and Mass Transfer*, 142:118450, 2019.

[21] Xing Zhang, Bo Mao, Leslie Mushongera, Julia Kundin, and Yiliang Liao. Laser powder bed fusion of titanium aluminides: An investigation on site-specific microstructure evolution mechanism. *Materials & Design*, 201:109501, 2021.

[22] James D Hunt. Steady state columnar and equiaxed growth of dendrites and eutectic. *Materials science and engineering*, 65(1):75–83, 1984.

[23] Erich Scheil. Bemerkungen zur schichtkristallbildung. *International Journal of Materials Research*, 34(3):70–72, 1942.

[24] HD BRODY. Solute redistribution in dendritic solidification. *Trans. TMS-AIME*, 236:615–624, 1966.

[25] TW Clyne and W Kurz. Solute redistribution during solidification with rapid solid state diffusion. *Metallurgical Transactions A*, 12(6):965–971, 1981.

[26] L Nastac. Numerical modeling of solidification morphologies and segregation patterns in cast dendritic alloys. *Acta Materialia*, 47(17):4253–4262, 1999.

[27] Xiaohui Liang, Cornelis Bos, Marcel Hermans, and Ian Richardson. An improved cellular automata solidification model considering kinetic undercooling. *Metallurgical and Materials Transactions B*, 54(3):1088–1098, 2023.

2

[28] Ch-A Gandin and Michel Rappaz. A 3d cellular automaton algorithm for the prediction of dendritic grain growth. *Acta Materialia*, 45(5):2187–2195, 1997.

[29] Weiling Wang, Cheng Ji, Sen Luo, and Miaoyong Zhu. Modeling of dendritic evolution of continuously cast steel billet with cellular automaton. *Metallurgical and Materials Transactions B*, 49:200–212, 2018.

[30] Sen Luo and Miao Yong Zhu. A two-dimensional model for the quantitative simulation of the dendritic growth with cellular automaton method. *Computational materials science*, 71:10–18, 2013.

[31] Shunyu Liu, Kyung-min Hong, and Yung C Shin. A novel 3d cellular automata-phase field model for computationally efficient dendrite evolution during bulk solidification. *Computational Materials Science*, 192:110405, 2021.

[32] Lazaro Beltran-Sanchez and Doru M Stefanescu. A quantitative dendrite growth model and analysis of stability concepts. *Metallurgical and Materials Transactions A*, 35:2471–2485, 2004.

[33] Lei Wei, Xin Lin, Meng Wang, and Weidong Huang. Orientation selection of equiaxed dendritic growth by three-dimensional cellular automaton model. *Physica B: Condensed Matter*, 407(13):2471–2475, 2012.

[34] M Marek. Grid anisotropy reduction for simulation of growth processes with cellular automaton. *Physica D: Nonlinear Phenomena*, 253:73–84, 2013.

[35] Ashish Arote, Junji Shinjo, D Graham McCartney, and Roger C Reed. Grid anisotropy reduction method for cellular automata based solidification models. *Computational Materials Science*, 217:111880, 2023.

[36] Sebastian C Michelic, Jörg M Thuswaldner, and Christian Bernhard. Polydimensional modelling of dendritic growth and microsegregation in multicomponent alloys. *Acta materialia*, 58(7):2738–2751, 2010.

[37] Xianfei Zhang, Jiuzhou Zhao, Hongxiang Jiang, and Mingfang Zhu. A three-dimensional cellular automaton model for dendritic growth in multi-component alloys. *Acta Materialia*, 60(5):2249–2257, 2012.

[38] MF Zhu and DM Stefanescu. Virtual front tracking model for the quantitative modeling of dendritic growth in solidification of alloys. *Acta materialia*, 55(5):1741–1755, 2007.

[39] Dongke Sun, Mingfang Zhu, Shiyan Pan, and Dierk Raabe. Lattice boltzmann modeling of dendritic growth in a forced melt convection. *Acta Materialia*, 57(6):1755–1767, 2009.

[40] Shiyan Pan and Mingfang Zhu. A three-dimensional sharp interface model for the quantitative simulation of solutal dendritic growth. *Acta Materialia*, 58(1):340–352, 2010.

[41] Mingfang Zhu, Lei Zhang, Honglei Zhao, and Doru M Stefanescu. Modeling of microstructural evolution during divorced eutectic solidification of spheroidal graphite irons. *Acta Materialia*, 84:413–425, 2015.

[42] Matthew John M Krane, David R Johnson, and Srinivasan Raghavan. The development of a cellular automaton-finite volume model for dendritic growth. *Applied Mathematical Modelling*, 33(5):2234–2247, 2009.

[43] AA Burbelko, W Kapturkiewicz, D Gurgul, and P Strek. Modeling of the dendrite arms behavior during solidification. *Arch. Foundry Eng*, 9:13–16, 2009.

[44] M-F Zhu, W Cao, S-L Chen, C-P Hong, and YA Chang. Modeling of microstructure and microsegregation in solidification of multi-component alloys. *Journal of Phase Equilibria and Diffusion*, 28:130–138, 2007.

[45] Y Zhao, RS Qin, and DF Chen. A three-dimensional cellular automata model coupled with finite element method and thermodynamic database for alloy solidification. *Journal of crystal growth*, 377:72–77, 2013.

[46] Shaoning Geng, Ping Jiang, Yuewei Ai, Rong Chen, LongChao Cao, Chu Han, Wei Liu, and Yang Liu. Cellular automaton modeling for dendritic growth during laser beam welding solidification process. *Journal of Laser Applications*, 30(3), 2018.

[47] Wenda Tan, Neil S Bailey, and Yung C Shin. A novel integrated model combining cellular automata and phase field methods for microstructure evolution during solidification of multi-component and multi-phase alloys. *Computational Materials Science*, 50(9):2573–2585, 2011.

[48] Yefeng Yu, Yang Li, Feng Lin, and Wentao Yan. A multi-grid cellular automaton model for simulating dendrite growth and its application in additive manufacturing. *Additive Manufacturing*, 47:102284, 2021.

[49] Klemens Reuther and Markus Rettenmayr. A comparison of methods for the calculation of interface curvature in two-dimensional cellular automata solidification models. *Computational Materials Science*, 166:143–149, 2019.

[50] Lei Wei, Yongqing Cao, Xin Lin, Meng Wang, and Weidong Huang. Quantitative cellular automaton model and simulations of dendritic and anomalous eutectic growth. *Computational Materials Science*, 156:157–166, 2019.

[51] Stéphane Popinet. An accurate adaptive solver for surface-tension-driven interfacial flows. *Journal of Computational Physics*, 228(16):5838–5866, 2009.

[52] K Reuther and M Rettenmayr. Perspectives for cellular automata for the simulation of dendritic solidification–a review. *Computational materials science*, 95:213–220, 2014.

[53] Cheng Gu, Colin D Ridgeway, and Alan A Luo. Examination of dendritic growth during solidification of ternary alloys via a novel quantitative 3d cellular automaton model. *Metallurgical and Materials Transactions B*, 50:123–135, 2019.

[54] Tommy Carozzani, Ch-A Gandin, and Hugues Digonnet. Optimized parallel computing for cellular automaton–finite element modeling of solidification grain structures. *Modelling and Simulation in Materials Science and Engineering*, 22(1):015012, 2013.

[55] Xiaohui Ao, Huanxiong Xia, Jianhua Liu, and Qiyang He. Simulations of microstructure coupling with moving molten pool by selective laser melting using a cellular automaton. *Materials & Design*, 185:108230, 2020.

[56] Johannes A Koepf, Martin R Gotterbarm, Matthias Markl, and Carolin Körner. 3d multi-layer grain structure simulation of powder bed fusion additive manufacturing. *Acta Materialia*, 152:119–126, 2018.

[57] Yanping Lian, Zhengtao Gan, Cheng Yu, Dmitriy Kats, Wing Kam Liu, and Gregory J Wagner. A cellular automaton finite volume method for microstructure evolution during additive manufacturing. *Materials & Design*, 169:107672, 2019.

[58] Adrian Pineau, Gildas Guillemot, Guillaume Reinhart, Gabrielle Regula, Nathalie Mangelinck-Noël, and Ch-A Gandin. Three-dimensional cellular automaton modeling of silicon crystallization with grains in twin relationships. *Acta Materialia*, 191:230–244, 2020.

[59] MR Rolchigo and R LeSar. Application of alloy solidification theory to cellular automata modeling of near-rapid constrained solidification. *Computational Materials Science*, 163:148–161, 2019.

[60] Matthew Rolchigo, Alex Plotkowski, and James Belak. Sensitivity of cellular automata grain structure predictions for high solidification rates. *Computational Materials Science*, 196:110498, 2021.

[61] Kirubel Teferra and David J Rowenhorst. Optimizing the cellular automata finite element model for additive manufacturing to simulate large microstructures. *Acta materialia*, 213:116930, 2021.

[62] Alain Karma and Wouter-Jan Rappel. Quantitative phase-field modeling of dendritic growth in two and three dimensions. *Physical review E*, 57(4):4323, 1998.

[63] Ryo Kobayashi. Modeling and numerical simulations of dendritic crystal growth. *Physica D: Nonlinear Phenomena*, 63(3-4):410–423, 1993.

[64] Adam A Wheeler, William J Boettinger, and Geoffrey B McFadden. Phase-field model for isothermal phase transitions in binary alloys. *Physical Review A*, 45(10):7424, 1992.

[65] Alain Karma. Phase-field formulation for quantitative modeling of alloy solidification. *Physical review letters*, 87(11):115701, 2001.

[66] Blas Echebarria, Roger Folch, Alain Karma, and Mathis Plapp. Quantitative phase-field model of alloy solidification. *Physical review E*, 70(6):061604, 2004.

[67] Seong Gyoon Kim. A phase-field model with antitrapping current for multicomponent alloys with arbitrary thermodynamic properties. *Acta Materialia*, 55(13):4391–4399, 2007.

[68] Munekazu Ohno and Kiyotaka Matsuura. Quantitative phase-field modeling for dilute alloy solidification involving diffusion in the solid. *Physical Review E*, 79(3):031603, 2009.

[69] Munekazu Ohno. Quantitative phase-field modeling of nonisothermal solidification in dilute multicomponent alloys with arbitrary diffusivities. *Physical Review E*, 86(5):051603, 2012.

[70] Janin Tiaden, Britta Nestler, Hermann-Josef Diepers, and Ingo Steinbach. The multiphase-field model with an integrated concept for modelling solute diffusion. *Physica D: Nonlinear Phenomena*, 115(1-2):73–86, 1998.

[71] PK Galenko, EV Abramova, David Jou, DA Danilov, VG Lebedev, and DM Herlach. Solute trapping in rapid solidification of a binary dilute system: a phase-field study. *Physical Review E*, 84(4):041143, 2011.

[72] Julia Kundin and Ingo Steinbach. Comparative study of different anisotropy and potential formulations of phase-field models for dendritic solidification. *Computational Materials Science*, 170:109197, 2019.

[73] Ingo Steinbach. Phase-field models in materials science. *Modelling and simulation in materials science and engineering*, 17(7):073001, 2009.

[74] M Rappaz, J M Drezet, and Met Gremaud. A new hot-tearing criterion. *Metallurgical and materials transactions A*, 30:449–455, 1999.

[75] Mohammed M'hamdi, Asbjørn Mo, and Christophe L Martin. Two-phase modeling directed toward hot tearing formation in aluminum direct chill casting. *Metallurgical and materials transactions a*, 33:2081–2093, 2002.

[76] Gautam Agarwal, A Kumar, IM Richardson, and MJM Hermans. Evaluation of solidification cracking susceptibility during laser welding in advanced high strength automotive steels. *Materials & Design*, 183:108104, 2019.

[77] He Gao, Gautam Agarwal, Muru Amirthalingam, MJM Hermans, and IM Richardson. Investigation on hot cracking during laser welding by means of experimental and numerical methods. *Welding in the World*, 62:71–78, 2018.

[78] Holden Hyer, Le Zhou, Abhishek Mehta, Sharon Park, Thinh Huynh, Shutao Song, Yuanli Bai, Kyu Cho, Brandon McWilliams, and Yongho Sohn. Composition-dependent solidification cracking of aluminum-silicon alloys during laser powder bed fusion. *Acta Materialia*, 208:116698, 2021.

[79] Paraskevas Kontis, Edouard Chauvet, Zirong Peng, Junyang He, Alisson Kwiatkowski da Silva, Dierk Raabe, Catherine Tassin, Jean-Jacques Blandin, Stéphane Abed, Rémy Dendievel, et al. Atomic-scale grain boundary engineering to overcome hot-cracking in additively-manufactured superalloys. *Acta Materialia*, 177:209–221, 2019.

[80] Mathieu Opprecht, Jean-Paul Garandet, Guilhem Roux, Camille Flament, and Mathieu Soulier. A solution to the hot cracking problem for aluminium alloys manufactured by laser beam melting. *Acta Materialia*, 197:40–53, 2020.

[81] Nicolas Coniglio and CE Cross. Effect of weld travel speed on solidification cracking behavior. part 1: weld metal characteristics. *The International Journal of Advanced Manufacturing Technology*, 107:5011–5023, 2020.

[82] Suyitno, VI Savran, L Katgerman, and DG Eskin. Effects of alloy composition and casting speed on structure formation and hot tearing during direct-chill casting of al-cu alloys. *Metallurgical and Materials Transactions A*, 35:3551–3561, 2004.

[83] JA Spittle and AA Cushway. Influences of superheat and grain structure on hot-tearing susceptibilities of ai-cu alloy castings. *Metals Technology*, 10(1):6–13, 1983.

[84] TW Clyne and DAVIES GJ. A quantitative solidification cracking test for castings and an evaluation of cracking in aluminium-magnesium alloys. 1975.

[85] John Campbell. *Castings*. Elsevier, 2003.

[86] Yue Li, Hongxiang Li, Laurens Katgerman, Qiang Du, Jishan Zhang, and Linzhong Zhuang. Recent advances in hot tearing during casting of aluminium alloys. *Progress in Materials Science*, 117:100741, 2021.

[87] A Slyvinsky, H Herold, and M Streitenberger. Influence of welding speed on the hot cracking resistance of the nickel-base alloy nicr25fealy during tig-welding. *Hot Cracking Phenomena in Welds*, 1:42, 2005.

[88] GM Goodwin. The effects of heat input and weld process on hot cracking in stainless steel. *Weld J*, 67(4):88s–94s, 1988.

[89] Gautam Agarwal, He Gao, Murugaiyan Amirthalingam, and Marcel Hermans. Study of solidification cracking susceptibility during laser welding in an advanced high strength automotive steel. *Metals*, 8(9):673, 2018.

[90] S Ohshita, N Yurioka, N Mori, and T Kimura. Prevention of solidification cracking in very low carbon steel welds. *WELDING J.*, 62(5):129, 1983.

[91] Masakazu Shibahara, Hisashi Serizawa, and Hidekazu Murakawa. Finite element method for hot cracking using temperature dependent interface element (report ii): Mechanical study of houldcroft test (mechanics, strength & structure design). *Transactions of JWRI*, 29(1):59–64, 2000.

[92] E Cicală, G Duffet, H Andrzejewski, D Grevey, and S Ignat. Hot cracking in al–mg–si alloy laser welding–operating parameters and their effects. *Materials Science and Engineering: A*, 395(1-2):1–9, 2005.

[93] Philipp Schempp, CE Cross, Andreas Pittner, Gabriele Oder, R Saliwan Neumann, Heidemarie Rooch, Ilona Dörfel, Werner Österle, and Michael Rethmeier. Solidification of gta aluminum weld metal: Part 1—grain morphology dependent upon alloy composition and grain refiner content. *Weld. J*, 93(2):53s–59s, 2014.

[94] Nicolas Coniglio and CE Cross. Effect of weld travel speed on solidification cracking behavior. part 2: testing conditions and metrics. *The International Journal of Advanced Manufacturing Technology*, 107:5025–5038, 2020.

[95] D Warrington and DG McCartney. Hot-cracking in aluminium alloys 7050 and 7010—a comparative study. *Cast metals*, 3(4):202–208, 1990.

[96] M Easton, Hao Wang, J Grandfield, D St John, and Elizabeth Sweet. An analysis of the effect of grain refinement on the hot tearing of aluminium alloys. In *Materials forum*, volume 28, pages 224–229, 2004.

[97] John H Martin, Brennan D Yahata, Jacob M Hundley, Justin A Mayer, Tobias A Schaedler, and Tresa M Pollock. 3d printing of high-strength aluminium alloys. *Nature*, 549(7672):365–369, 2017.

[98] Ilya I Novikov. Hot shortness of non-ferrous metals and alloys, 1966.

[99] CH Dickhaus, L Ohm, and S Engler. Mechanical properties of solidifying shells of aluminum alloys. *Transactions-American Foundrymens Society*, pages 677–677, 1993.

[100] DG Eskin, L Katgerman, et al. Mechanical properties in the semi-solid state and hot tearing of aluminium alloys. *Progress in materials science*, 49(5):629–711, 2004.

[101] DJ Lahaie and M Bouchard. Physical modeling of the deformation mechanisms of semisolid bodies and a mechanical criterion for hot tearing. *Metallurgical and materials Transactions B*, 32:697–705, 2001.

[102] JA Williams and ARE Singer. Deformation, strength, and fracture above the solidus temperature. *J Inst Metals*, 96(1):5–12, 1968.

[103] B Magnin, L Maenner, Laurens Katgerman, and S Engler. Ductility and rheology of an al-4.5 cu alloy from room temperature to coherency temperature. In *Materials Science Forum*, volume 217, pages 1209–1214. Trans Tech Publ, 1996.

[104] NN Prokhorov. Refinement in the hot tearing of cast al-cu alloy. *Russian Castings Production*, 2:172–175, 1962.

[105] Sindo Kou. A criterion for cracking during solidification. *Acta Materialia*, 88:366–374, 2015.

[106] Jiangwei Liu and Sindo Kou. Crack susceptibility of binary aluminum alloys during solidification. *Acta Materialia*, 110:84–94, 2016.

[107] WI Pumphrey. Behaviour of crystal boundaries in aluminium and its alloys during melting. *Nature*, 163(4155):960–961, 1949.

[108] Shaoning Geng, Ping Jiang, Xinyu Shao, Gaoyang Mi, Han Wu, Yuewei Ai, Chunming Wang, Chu Han, Rong Chen, Wei Liu, et al. Effects of back-diffusion on solidification cracking susceptibility of al-mg alloys during welding: A phase-field study. *Acta Materialia*, 160:85–96, 2018.

2

[109] Chu Han, Ping Jiang, Shaoning Geng, Song Gao, Gaoyang Mi, and Chunming Wang. Multiphase-field simulation of grain coalescence behavior and its effects on solidification cracking susceptibility during welding of al-cu alloys. *Materials & Design*, 211:110146, 2021.

[110] Laishan Yang, Jing Yang, Fang Han, Zhihang Zhang, Qinghua Li, Zhibo Dong, Lei Wang, Nana Ofori-Opoku, and Nikolas Provatas. Hot cracking susceptibility prediction from quantitative multi-phase field simulations with grain boundary effects. *Acta Materialia*, 250:118821, 2023.

[111] M Sistaninia, AB Phillion, J-M Drezet, and M Rappaz. Three-dimensional granular model of semi-solid metallic alloys undergoing solidification: Fluid flow and localization of feeding. *Acta materialia*, 60(9):3902–3911, 2012.

[112] M Sistaninia, S Terzi, AB Phillion, J-M Drezet, and M Rappaz. 3-d granular modeling and in situ x-ray tomographic imaging: A comparative study of hot tearing formation and semi-solid deformation in al–cu alloys. *Acta materialia*, 61(10):3831–3841, 2013.

[113] HR Zareie Rajani and AB Phillion. 3-d multi-scale modeling of deformation within the weld mushy zone. *Materials & Design*, 94:536–545, 2016.

[114] HR Zareie Rajani and AB Phillion. 3d multi-scale multi-physics modelling of hot cracking in welding. *Materials & Design*, 144:45–54, 2018.

3

CELLULAR AUTOMATA MODELLING OF DENDRITE FORMATION DURING SOLIDIFICATION

Dendrites are common metallurgical features in a solidified microstructure. In this chapter, a cellular automata (CA) model for solidification simulation is described considering kinetic undercooling at the interface. The state-of-the-art model incorporates a decentered growth algorithm to suppress grid anisotropy and a generalized height function method to accurately calculate the curvature. To develop a CA model which is independent of the mesh size, a new diffusion term is proposed to handle the diffusion between the interface cells and liquid cells. The developed CA model is employed to simulate the single-dendritic solidification of an Al-3Cu (wt.%) alloy. The simulated tip velocities agree with the prediction of the Kurz-Giovanola-Trivedi (KGT) model. Further studies show that the developed CA model converges to an equilibrium model with increasing kinetic mobility values. Moreover, it is found that the virtual liquid cell assumption which is commonly used in existing CA models, may lead to a deviation in the mass balance. This mass balance error has been resolved by redistributing solutes to neighboring liquid cells in each time step. The developed CA model is optimally tailored to simulate solidification in processes with high undercooling like welding and additive manufacturing.

3.1 Introduction

Dendrite formation is commonly observed during solidification of welding or casting. Solidification simulation is important for a better understanding of dendrite formation and a better control of welding or casting processes, as it can provide in-situ information which is inaccessible through an experimental approach [2]. Various models including phase field [3–6], cellular automata (CA) [7–10] and level set [11–13] models have been employed for solidification simulations. Compared to other approaches, cellular automata models require only moderate computational resources and are widely used for solidification simulations.

Most CA models [14–16] assume local equilibrium at the interface and calculate the growth velocity with a diffusion-controlled method. Nastac [14] developed a time-dependent CA model where the interface velocity v is calculated with a flux balance at the interface

$$v = \frac{1}{c^{l,eq}(1-k)} \left(\nabla c^l - \nabla c^s \right) \cdot \vec{n},$$
(3.1)

where $c^{l,eq}$ is the equilibrium liquid concentration at the interface, k the partitioning coefficient, $\vec{n}$ the interface normal unit vector, c^l and c^s the liquid and solid concentration, respectively. This method is called a front velocity method by Reuther and Rettenmayr [2]. Following this approach, Beltran- Sanchez and Stefanescu [17, 18] proposed a virtual front tracking method to capture liquid cells within a CA simulation. The stable tip velocity obtained from their CA simulations agreed with prediction from the Lipton-Glicksman-Kurz model [19]. Later, Michelic et al. [20] extended the virtual front tracking model to simulate solidification in a multi-component system. Zhang et al. [21] employed a CALPHAD approach to calculate the equilibrium concentrations and the growth velocity in 3D solidification simulations of an Al-Cu-Mg melt.

Apart from the approach of Nastac [14], Zhu and Stefanescu [22] proposed a cellwise mass balance method to calculate the growth velocity in a CA model assuming local equilibrium condition. Assuming the liquid concentration of the interface cells is always equal to the equilibrium concentration, the solid fraction change Δf_s in a time increment is given by a lever rule [22]

$$\Delta f_s = \frac{c^{l,eq} - c^l}{c^{l,eq}(1-k)}.$$
(3.2)

This approach has been employed by Pan and Zhu [23] to simulate the solidification in a 3D case. Yin et al. [24] coupled a cellwise mass balance CA model with a lattice Boltzmann model to simulate solidification under a melt flow.

For the rapid solidification encountered in welding and additive manufacturing, consideration of non-equilibrium effects is necessary. According to the interface attachment kinetics, the interface velocity v is related to the kinetic undercooling ΔT_k by [25]

$$v = v_0 \left(1 - \exp \left(-\frac{\Delta S \Delta T_k}{RT} \right) \right),$$
(3.3)

where R is the gas constant, T the temperature, ΔS the entropy change and v_0 a constant which is of the order of the velocity of sound for pure metals. When $v \ll v_0$, this relationship can be simplified to

$$v = M_T \Delta T_k,$$
(3.4)

where M_T is the kinetic mobility with respect to the kinetic undercooling.

Several CA models [16, 26, 27] have been developed which consider non-equilibrium effects during solidification. Zhao et al. [28] developed a 3D CA model which calculated the growth velocity based on Equation (3.3) and simulated the solidification of a Fe-1.5C (wt.%) alloy in a 3D case. Burbelko et al. [26] calculated the growth velocity as a linear function of the kinetic undercooling and studied the formation of the primary austenite and globular eutectic grains during the solidification of a ductile iron in a thin wall casting process. Zhu et al. [16] developed a two-dimensional CA model to predict the microstructures and micro-segregation in a solidified ternary alloy and Geng et al. [27] used a non-equilibrium CA model to simulate the dendrite growth along the fusion boundary of a laser beam weld.

To improve the quantitative accuracy of CA models, a number of works have been published in different areas including curvature calculation [29, 30], grid anisotropy [31, 32], and mesh size dependency [17, 20, 22]. For a quantitative solidification simulation, curvature at the CA interface cells needs to be calculated accurately. In early CA models, a cell counting method [14, 31] or a level set method [17, 20, 22] was employed to calculate the curvature at the interface cells based on the solid fraction field. Previously, Reuther and Rettenmayr [29] compared the performance of the cell counting method, the level set method and a height function method in two benchmark problems and concluded that the height function method calculates curvature more accurately than the other two methods. Wei et al. [30] adopted a modified height function method to calculate curvature in a eutectic solidification simulation.

Grid anisotropy is commonly observed when a simple capture rule is used for dendrite growth [32]. Without any crystal anisotropy, dendrite arms tend to form in the grid directions when a von Neumann capture rule is employed, whereas dendrite arms tend to form in the diagonal directions of the grid when a Moore capture rule is employed. To suppress the grid anisotropy, different growth algorithms have been developed. Zhu and Stefanescu [22] employed a virtual front tracking method to capture liquid cells. The decentered growth algorithm proposed by Gandin and Rappaz [33] has been widely used to simulate formation of dendrites with different orientations in 2D [31, 34] and 3D [35] simulations. The decentered growth algorithm exhibited a good performance in suppressing the grid anisotropy.

A quantitative CA model should be independent of the mesh size. In most equilibrium CA models [17, 20, 22], convergence analyses have been performed. The growth velocity at the dendrite tip in single-dendritic solidification simulations converges to a stable value with decreasing mesh size. However, no convergence analysis has been found in any non-equilibrium CA model. In this case, existing non-equilibrium CA models must be regarded as qualitative.

Moreover, a quantitative CA model should be mass conserved. In most CA models [17, 20], diffusion within the liquid and solid regions are solved separately. To handle the discontinuity at the interface, interface cells are treated as virtual liquid cells. The virtual liquid assumption neglects the solid fraction of the interface cells and may lead to a mass balance deviation in CA models with a front velocity method, as mentioned by Michelic et al. [20]. Reuther and Rettenmayr [2] indicated that CA models based on a cellwise mass balance offer a better solute conservation compared to CA models with a front velocity method. To develop a quantitative CA model, further study on the influence of the virtual

liquid cell assumption is necessary.

In this chapter, a quantitative non-equilibrium CA model is described. A decentered growth algorithm [33] is employed to suppress the grid anisotropy and a generalized height function method [36] is adopted to accurately calculate the curvature. To make a CA model which is independent of the mesh size, a new diffusion term is proposed to handle the diffusion between interface cells and liquid cells. In addition, the influence of the virtual liquid cell assumption is studied within a multi-dendritic solidification simulation. A correction term is defined and applied to ensure a mass balance within the CA simulation.

3.2 CA Model setup

3.2.1 Basics

In the CA model, the domain to be studied is discretized into many square cells. Each cell has state variables including phase state (to which phase it belongs), grain index (to which grain it belongs), solid fraction f_s and concentration c. For a solidification problem, possible phase states and solid fraction are liquid ($f_s = 0$), interface ($0 < f_s < 1$) and solid ($f_s = 1$). The interface cells also have additional state variables including growth velocity v, growth length l and interface normal vector $\vec{n}$.

Solidification within the CA model is simulated by updating the solid fraction and the phase status of the cells near the solidification interface, which is performed based on following transition rules:

- a liquid cell transforms into an interface cell when it is captured by a growing interface cell with a decentered growth envelope capture algorithm;

- an interface cell transforms into a solid cell, when it has no liquid neighbor in its von Neumann neighborhood.

3.2.2 The decentered growth algorithm

The decentered growth algorithm developed by Gandin and Rappaz [33] is employed in the current model. The growth of each interface cell is described by a growth envelope, which is a quadrilateral in the 2D case. Each growth envelope is orientated with its half diagonals parallel with the <10> preferential growth directions of the solid grain. The length of the envelope half diagonal is defined as the growth length l, which records dendrite growth in the preferential growth direction. In each time increment, the growth length of each interface cell is updated according to

$$\Delta l = l^{t+\Delta t} - l^t = v\Delta t, \tag{3.5}$$

where v is the growth velocity in the interface cell, Δl the increase in the growth length and Δt the time increment.

The capture rule of the decentered growth algorithm is shown in Figure 3.1. If the center of a liquid cell falls in the growth envelope of an interface cell, then this liquid cell is captured and transforms into a new interface cell. Within the new interface cell, a new growth envelope is formed with one of its vertices overlapping with the nearest vertex of the parent growth envelope. The new growth envelope inherits the orientation of the parent growth envelope. Its initial growth length is defined as a ratio (α) of the growth
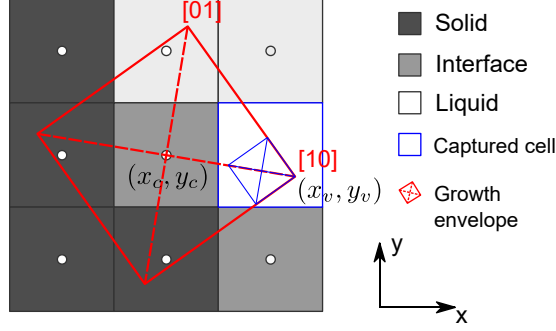
Figure 3.1: Illustration of the capturing rule in the decentered growth algorithm.

length of the parent growth envelope. Here, the coordinates of the center and the nearest vertex of the parent growth envelope are denoted with (x_c, y_c) and (x_v, y_v). The center of the new growth envelope is given by $((1-\alpha)x_c + \alpha x_v, (1-\alpha)y_c + \alpha y_v)$.

3.2.3 Calculation of the growth velocity

At the interface, thermodynamic equilibrium is given by [25]

$$\Delta T = T_0 - T = \Delta T_k + \Delta T_c + \Delta T_r, \tag{3.6}$$

where ΔT is the local undercooling, T_0 the liquidus temperature, ΔT_k the kinetic undercooling, ΔT_c the constitutional undercooling and ΔT_r the curvature undercooling. The kinetic undercooling ΔT_k [25], the constitutional undercooling ΔT_c [25] and the curvature undercooling ΔT_r [22] are given by

$$\Delta T_k = \frac{v}{M_T}, \tag{3.7}$$

$$\Delta T_c = -m(c^{l,*} - c^0), \tag{3.8}$$

$$\Delta T_r = \Gamma \kappa f(\phi, \theta), \tag{3.9}$$

where $c^{l,*}$ is the liquid concentration of the interface cell, m the slope of liquidus line in the linearized phase diagram, c^0 the nominal concentration, Γ the Gibbs-Thomson coefficient, κ the curvature and $f(\phi, \theta)$ the anisotropic function for the interfacial energy, which is given by [22]

$$f(\phi, \theta) = 1 - 15\varepsilon \cos(4(\phi - \theta)), \tag{3.10}$$

where ε is the anisotropy coefficient of the interfacial energy, θ the angle between the preferential growth direction and the x axis and ϕ the angle between the interface normal $\vec{n}$ and the x axis. The interface normal vector $\vec{n}$ is determined by [20]

$$\vec{n} = \frac{\nabla f_s}{|\nabla f_s|}. \tag{3.11}$$

The interface velocity v is then given by

$$v = M_T \left(T_0 - T + m(c^{l,*} - c^0) - \Gamma \kappa f(\phi, \theta) \right). \tag{3.12}$$

After reformulation, the interface velocity v may be written as

$$v = M_T m(c^{l,*} - c^{l,eq}), \tag{3.13}$$

with the equilibrium concentration $c^{l,eq}$ under a Gibbs-Thomson effect given by

$$c^{l,eq} = c^0 - \frac{T_0 - T - \Gamma \kappa f(\phi, \theta)}{m}. \tag{3.14}$$

In some cases, the interface concentration $c^{l,*}$ might be larger than the equilibrium concentration $c^{l,eq}$, which leads to a negative interface velocity for an alloy with $m < 0$. This is because the partitioned solutes in previous time steps do not have enough time to diffuse out of the interface cell. As a solidification problem is being simulated without considering remelting, the interface velocity is limited with

$$v = \max(v, 0). \tag{3.15}$$

After several time steps, the interface concentration drops to a value below the equilibrium concentration due to diffusion, which brings the interface velocity back to a positive value.

The solid fraction of each interface cell is updated in each time increment with [34]

$$\Delta f_s = \frac{v \Delta t}{\Delta x(|\cos \theta| + |\sin \theta|)}, \tag{3.16}$$

where Δt is the time increment.

The interface solid concentration $c^{s,*}$ is given by

$$c^{s,*} = k c^{l,*}. \tag{3.17}$$

The solid concentration c^s of each interface cell is calculated by averaging the interface solid concentration $c^{s,*}$ over different time increments [22]

$$c^s = \frac{\sum c_n^{s,*} \Delta f_s}{\sum \Delta f_s}, \tag{3.18}$$

where $c_n^{s,*}$ is the solid concentration at the interface in increment n.

3.2.4 Calculation of the curvature

In this work, the generalized height function method proposed by Popinet [36] is adopted to calculate the curvature of each interface cell.

Consider an interface cell with index (m, n), as shown in Figure 3.2. To calculate the curvature, an adaptive stencil consisting of three columns is constructed in the direction of the largest component of the interface normal $\vec{n}$. A column is called consistent if it has a base cell ($f_s = 1$) and a top cell ($f_s = 0$) and the solid fraction decreases monotonically from the base cell to the top cell. The indices of the base cell and the top cell within the column

are b and t, respectively. If all columns in this stencil are consistent, then the height of each column is calculated by summing up the solid fraction from the base cell to the top cell. If the largest component of the interface normal $\vec{n}$ is in the y direction, then the height of each column is written as [36]

$$h_i = b_i + \Delta x \sum_{j=b_i}^{j=t_i} f_s(i,j), \quad \text{for } i = m-1, m, m+1. \tag{3.19}$$

A height function $H(x)$ is defined between the heights of the three columns and their distances to the central column. Curvature is calculated based on the derivatives of the height function [36],

$$\kappa = -\frac{H_{xx}}{\left(1 + H_x^2\right)^{\frac{3}{2}}}, \tag{3.20}$$

where H_x and H_{xx} are the first and the second derivative of the height function, which are calculated with a central finite difference method.

If it is not possible to construct a consistent stencil, then curvature is determined by fitting the interface with a parabola [36]. First, the interface segments in the considered interface cell and neighboring interface cells are determined with a piecewise linear interface calculation [18]. Then, the barycenter of the interface segments in the considered interface cell and neighboring interface cells are fitted with a parabola in a rotated coordinate system which is defined with its y axis parallel with the interface normal $\vec{n}$ of the considered interface cell. The parabola function is [36]

$$y = a_0 + a_1 x + a_2 x^2, \tag{3.21}$$

where a_0, a_1 and a_2 are fitting parameters. Curvature at the considered interface cell is then given by [36]

$$\kappa = -\frac{2a_2}{\left(1 + a_1^2\right)^{\frac{3}{2}}}. \tag{3.22}$$

3.2.5 DIFFUSION AND PARTITIONING

In the current CA model, diffusion is solved for the solid and liquid regions separately. The governing equations for the diffusion between the liquid cells and the diffusion between the solid cells are given by

$$\frac{\partial c^l}{\partial t} = \nabla \cdot \left(D^l \nabla c^l\right), \tag{3.23}$$

$$\frac{\partial c^s}{\partial t} = \nabla \cdot (D^s \nabla c^s), \tag{3.24}$$

where D^l and D^s are the diffusion coefficients in the liquid and solid, respectively.

In traditional CA models [18, 20, 21], partitioning at the interface is considered by adding a source term on the right-hand side of Equation (3.23),

$$\frac{\partial c^l}{\partial t} = \nabla \cdot \left(D^l \nabla c^l\right) + \frac{\partial f_s}{\partial t}\left(c^{l,*} - c^{s,*}\right), \tag{3.25}$$
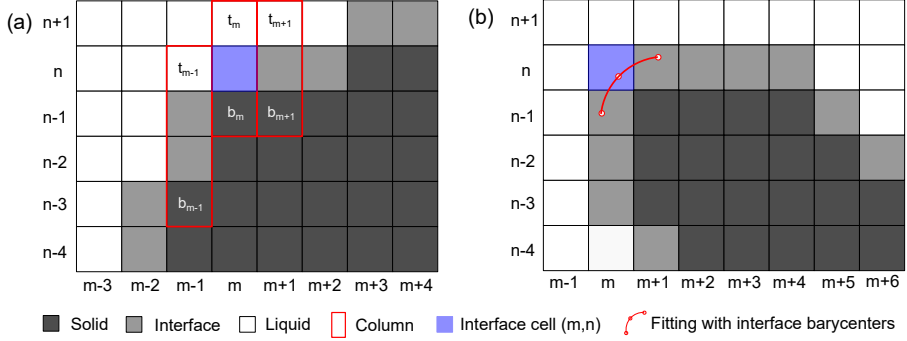
Figure 3.2: Illustration of the GHF curvature calculation method: when it is possible to establish an adaptive stencil with three consistent columns, generalized height function is employed for curvature calculation (a); when it is not possible to establish an adaptive stencil with three consistent columns in any principal direction, curvature is evaluated by fitting the barycenter of the interface segments (b).

where $c^{l,*}$ and $c^{s,*}$ are the interface concentration in the liquid and solid. However, as will be shown in Section 3.3.1, directly using Equation (3.25) in a non-equilibrium CA model leads to a large mesh size dependency. In order to avoid this, the diffusion between interface cells and the liquid cells is handled with a new equation,

$$\frac{\partial c^l}{\partial t} = \nabla \cdot \left(D^l \nabla c^l \cdot \vec{n} \right) + \frac{\partial f_s}{\partial t} \left(c^{l,*} - c^{s,*} \right). \tag{3.26}$$

With Equation (3.26), the sum of the projections of the diffusion fluxes out of the interface cells onto the interface normal direction are calculated.

Equation (3.25) or Equation (3.26) is solved with a finite difference method and a Euler forward discretization. Meanwhile, the virtual liquid cell assumption has been employed, in which the interface cells within the CA model are treated as virtual liquid cells [18, 20, 21]. The virtual liquid cell assumption avoids extremely large concentration changes when the liquid fraction of the interface cell is close to 0. However, it introduces a deviation into the mass balance. Although the mass balance deviation problem may be insignificant in a single time step, the error adds up over numerous time steps as reported by Michelic et al. [20].

Consider an interface cell in a CA simulation using a virtual liquid cell assumption. In a time increment, the concentration change of the interface cell is Δc, which is calculated as the product of time step Δt and the right-hand side of the diffusion equation (Equation (3.25) or Equation (3.26)). The value of Δc corresponds to the concentration change in a liquid cell. The solid fraction of the interface cell is neglected, although it has a value which is larger than or equal to 1. In this case, an error of $-f_s \Delta c$ is introduced in the mass balance. Note Δc is equal to the sum of the concentration change due to diffusion Δc^d and the concentration change due to solute partitioning Δc^p, calculated from the first and the second term on the right-hand side of the diffusion equation. In this case, Δc can either be positive or negative, depending on the relative values of Δc^d and Δc^p. If Δc is positive, then solutes are artificially lost and the average concentration of the system decreases. If Δc is negative,

then solutes are artificially added and the average concentration of the system increases. To redress the mass balance error, the concentration of the neighboring liquid cells is modified by $\frac{f_s \Delta c}{n_l}$, where n_l is the number of liquid cells in the Moore neighborhood of the considered interface cell. In this case, the artificially lost or added solutes are added or removed from neighboring liquid cells to keep a mass balance.

3.2.6 Time increment

In the CA model, the time increment is determined by

$$\Delta t = \min\left(0.2\frac{\Delta x}{v_{\max}},\ 0.2\frac{\Delta x^2}{D^l}\right), \tag{3.27}$$

where $v_{\max}$ is the maximum growth velocity within the simulation domain and Δx the mesh size.

3.2.7 Material parameters

The presented model can be applied for the solidification simulation of any binary and (with small modification) multi-component alloys. Here, the performance of the model is illustrated by simulation of solidification in a Al-3Cu (wt. %) alloy which has been well studied in the literature [18, 37]. The parameters of the Al-3Cu (wt.%) alloy are given in Table 4.1.

Table 3.1: Material properties of an Al-3Cu (wt.%) alloy [37].

Symbol	Description	Value	Unit
c^0	Nominal concentration	3.0	wt%
D^l	Liquid diffusion coefficient	3.0×10^{-9}	m^2/s
D^s	Solid diffusion coefficient	3.0×10^{-13}	m^2/s
k	Partitioning coefficient	0.17	1
m	Liquidus slope	-2.6	K/(wt%)
T_0	Liquidus temperature	650.6	°C
Γ	Gibbs-Thomson coefficient	2.4×10^{-7}	K/m
ε	Anisotropy coefficient	0.0267	1
M_T	Kinetic mobility (default)	1×10^{-3}	m$\cdot$s^{-1}K^{-1}

3.3 Results and discussion

3.3.1 Mesh convergence tests

To test the mesh size dependency of the developed CA model, single dendritic growth of the Al-3Cu (wt.%) alloy has been simulated with different mesh sizes under a constant undercooling of 3 K. Due to the discretization of the CA model, the velocity at the dendrite tip does not change monotonically. To smooth the tip velocity curve, the tip velocity is averaged between two tip cell advancements. The averaged tip velocity decreases with

increasing time and eventually converges to a stable value. The stable tip velocity is evaluated at time 0.3 s.

The mesh size convergence test has been performed for the CA model with Equation (3.25) (D1) and Equation (3.26) (D2). In the D1 simulation, the diffusion between interface cells and liquid cells is calculated by summing up the magnitudes of all the diffusion fluxes, whereas in the D2 simulation, the diffusion between interface cells and liquid cells is calculated by summing up the projections of the diffusion fluxes onto the interface normal $\vec{n}$ direction. The choice of diffusion equation has an influence on the mesh size convergence behavior. As shown in Figure 3.3, with decreasing mesh size, the stable tip velocity in the D1 simulations first increases and then decreases. In the D2 simulations, the stable tip velocity converges to a value around 150 μm/s, indicating that simulations without a mesh size effect can be performed if Equation (3.26) is applied.

The different mesh size convergence behaviors can be explained by considering the interface cell at a dendrite tip in an isothermal solidification simulation. Discretizing the diffusion equation gives

$$\Delta c^l = -\frac{J\Delta t}{\Delta x} + \Delta f_s(c^{l,*} - c^{s,*}), \tag{3.28}$$

where J is the effective diffusion flux out of the tip cell and is equal to $D^l \nabla c^l$ in a D1 simulation and $D^l \nabla c^l \cdot \vec{n}$ in a D2 simulation. Substituting Equation (3.16) into Equation (3.28) with $\theta = 0$ gives

$$\Delta c^l = -\frac{J\Delta t}{\Delta x} + \frac{v\Delta t}{\Delta x}(c^{l,*} - c^{s,*}). \tag{3.29}$$

In the steady state, the liquid concentration of the tip cell is constant $\Delta c^l = 0$, which indicates a balance between the solute addition due to partitioning and solute removal due to diffusion. This means that the dendrite growth is diffusion-limited in the steady state. From Equation (3.29), the growth velocity at the steady-state dendrite tip in a D1 simulation can be written as

$$v = \frac{D^l \nabla c^l}{c^{l,*} - c^{s,*}}, \tag{3.30}$$

while the growth velocity at a steady-state dendrite tip in a D2 simulation can be written as

$$v = \frac{D^l \nabla c^l \cdot \vec{n}}{c^{l,*} - c^{s,*}}. \tag{3.31}$$

Equation (3.31) is in the same form as the equation proposed by Nastac [14]. In the D1 simulations, the tip velocity v is proportional to the sum of the magnitude of all the diffusion fluxes out the interface cell, while in the D2 simulation, the tip velocity v is proportional to the diffusion flux in the interface normal direction $\vec{n}$. In this case, the tip velocity tends to be overestimated especially when the tip cell is surrounded by three liquid cells in its von Neumann neighborhood, as indicated by Reuther [2]. This explains why the stable tip velocities in the D1 simulations are larger than the stable tip velocities in Figure 3.3. As the mesh size is decreased, the dendrite tip is discretized with more cells. In this case, the overestimation of tip velocity in the D1 simulations becomes weaker. Thus, the stable tip velocity in the D1 simulations decreases with a decreasing mesh size.
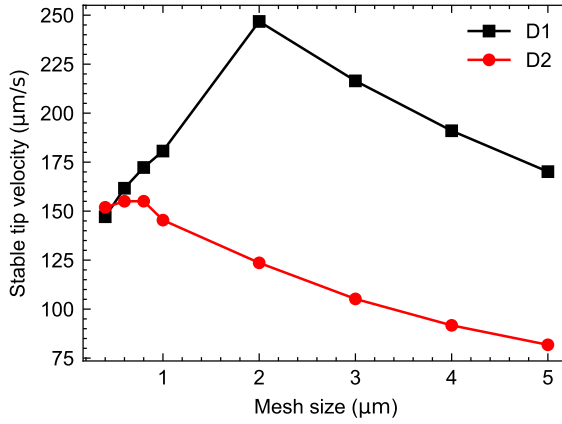
Figure 3.3: The stable tip velocity in the mesh convergence tests for the CA model using D1 and D2.

3.3.2 Influence of the kinetic mobility

In the current CA model, the growth velocity is calculated as a product of the kinetic mobility M_T and the kinetic undercooling ΔT_k. To test the influence of the kinetic mobility, single dendritic growth of the Al-3Cu (wt.%) alloy has been simulated with different mobility values under a constant undercooling of 3 K with a mesh size of 0.5 μm. The stable tip velocities are plotted in Figure 3.4. With increasing kinetic mobility, the stable tip velocity increases and tends to converge. As the kinetic mobility increases, the kinetic undercooling ΔT_k decreases and the simulation approaches a fully diffusion-controlled solidification simulation. Moreover, the Cu concentration $c^{l,*}$ at the dendrite tip approaches the equilibrium concentration $c^{l,eq}$ with increasing kinetic mobility, as shown in Figure 3.5. This is reasonable, as the non-equilibrium effect becomes less significant with increasing kinetic mobility M_T. When the kinetic mobility is infinite, local equilibrium is achieved at the interface.

Increasing the kinetic mobility makes the simulation more computationally expensive. A large kinetic mobility means that a small deviation of the interface concentration can lead to a large interface velocity. This results in a smaller time step, since the time step is limited by the maximum interface velocity in the system according to Equation (3.27). As the time step is decreased, the number of time steps to finish a simulation increases, which means the computational cost increases.

3.3.3 Comparison with the KGT model

The developed CA model is verified by comparing with the KGT model [19, 38], which gives an analytical solution for a dendrite growing into an infinite melt in the steady state. It is modified here to include the kinetic undercooling. At the interface, the total undercooling ΔT is given by [25]

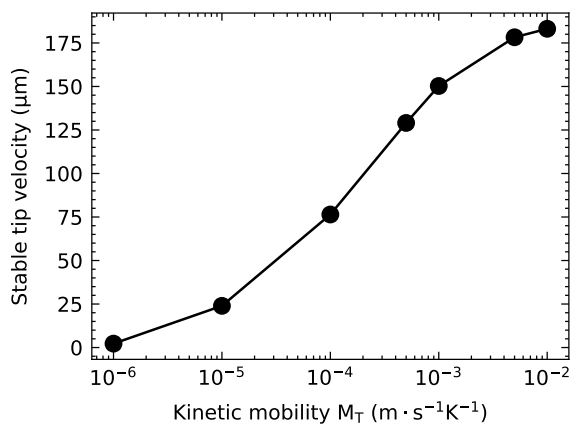$$\Delta T = \Delta T_k + \Delta T_c + \Delta T_r. \tag{3.32}$$

Figure 3.4: The stable tip velocity in the simulations with different kinetic mobility M_T values.
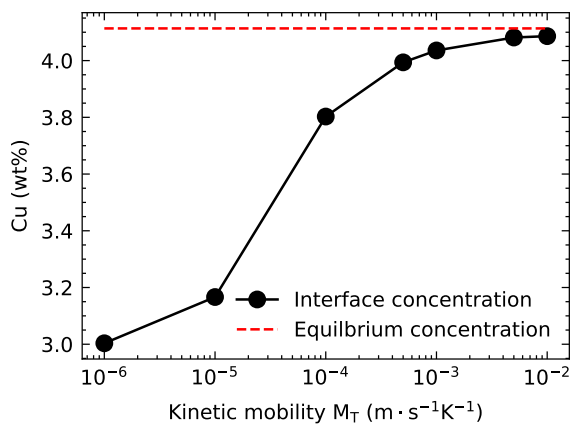

Figure 3.5: The Cu concentration at the dendrite tip in the simulations with different kinetic mobility M_T values.

The kinetic undercooling ΔT_k is given by [25]

$$\Delta T_k = \frac{v}{M_T}. \tag{3.33}$$

The constitutional undercooling is given by [38]

$$\Delta T_c = mc^0 \left(1 - \frac{1}{1-(1-k)I_v(P_e))} \right), \tag{3.34}$$

where $I_v(P_e)$ is the Ivantsov function and P_e the Peclet number given by [38]

$$P_e = \frac{rv}{2D}, \tag{3.35}$$

where r is the tip radius and v the tip velocity. The 2D Ivantsov function is given by [38]

$$I_v(P_e) = \sqrt{\Pi P_e} \exp(P_e) erfc(\sqrt{P_e}). \tag{3.36}$$

The curvature undercooling ΔT_r is given by [38]

$$\Delta T_r = \frac{\Gamma}{r}. \tag{3.37}$$

The tip radius is determined with a stability criterion [38]

$$-m\frac{vc^{l,*}(1-k)}{D^l} = \frac{1}{\sigma^*}\frac{\Gamma}{r^2}, \tag{3.38}$$

where $c^{l,*}$ the liquid concentration at the interface and σ^* the stability factor. The stability factor σ^* here is 0.10654 [39].

The stable tip velocities in the CA simulations with different undercoolings and different kinetic mobility M_T are compared with the predictions of the modified KGT model, as shown in Figure 3.6. As the kinetic mobility M_T increases, the stable tip velocities predicted by the CA model and KGT model under different undercooling conditions increases. When the undercooling is larger than 2 K, the stable tip velocities simulated by the CA model with different kinetic mobility M_T agree well with the KGT model. However, at the 2 K undercooling, the simulated tip velocities in the CA simulations with different kinetic mobility M_T are larger than the predictions of the modified KGT model. Besides, the stable tip velocity in the CA simulation with a 6 K undercooling and a 5×10^{-3} m·s^{-1}K^{-1} kinetic mobility is smaller than the prediction of the modified KGT model. The reason for the mismatch is that a constant stability factor σ^* is used in the KGT model. However, this factor varies with different nominal concentration c^0 and undercooling ΔT, as indicated by Ramirez and Beckermann [40].

3.3.4 Influence of the virtual liquid cell assumption
In the current CA model, interface cells are treated as virtual liquid cells to solve for diffusion between interface cells and liquid cells. As explained in Section 3.2.5, such an assumption neglects the solid amount of the interface cells and may lead to a deviation
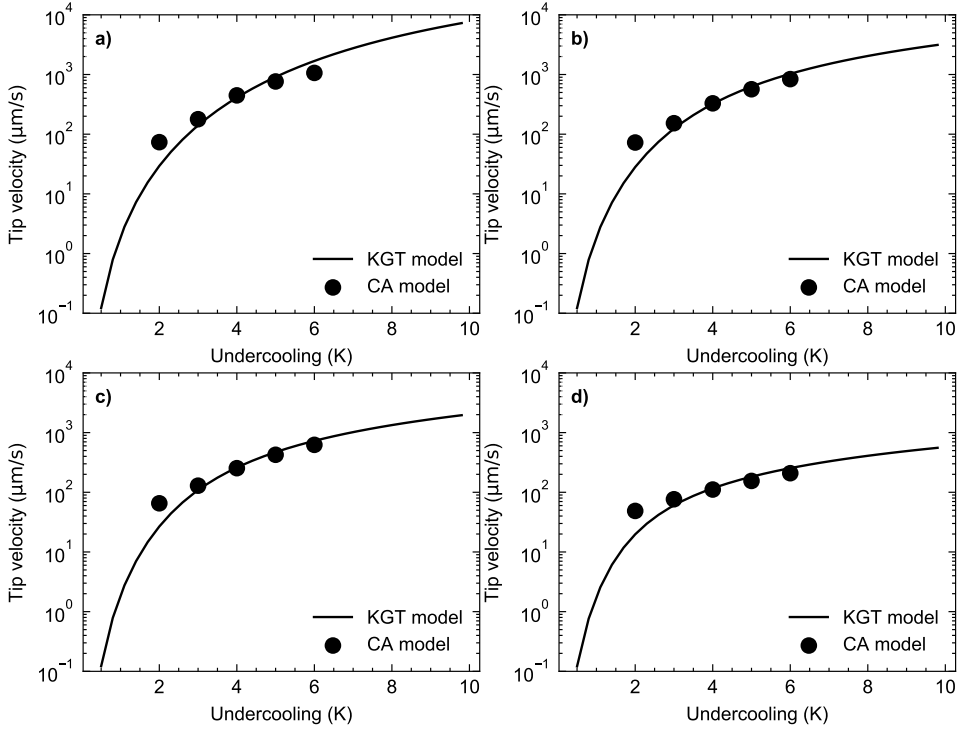
Figure 3.6: Comparison between the stable tip velocities predicted by the CA model and KGT model with different undercooling and different kinetic mobility M_T: $M_T = 5 \times 10^{-3}$ m·s^{-1}K^{-1} (a), $M_T = 1 \times 10^{-3}$ m·s^{-1}K^{-1} (b), $M_T = 5 \times 10^{-4}$ m·s^{-1}K^{-1} (c), $M_T = 1 \times 10^{-4}$ m·s^{-1}K^{-1} (d).

in the mass balance. To study the influence of the virtual liquid cell assumption on the mass balance, multi-dendritic solidification of the Al-3Cu (wt.%) alloy has been simulated with and without the mass balance correction. The simulation domain size is 300×300 μm^2 and the mesh size is 0.5 μm. A periodic boundary condition is employed for the simulation. The cooling rate is 50 K/s. The simulation finishes after 62000 steps and takes 13 minutes with 24 cores of Intel XEON E5-6248R at 3.0GHz. The concentration profiles at times 0.10 s, 0.15 s and 1.0 s in the simulations with and without the mass balance correction are given in Figure 3.7.
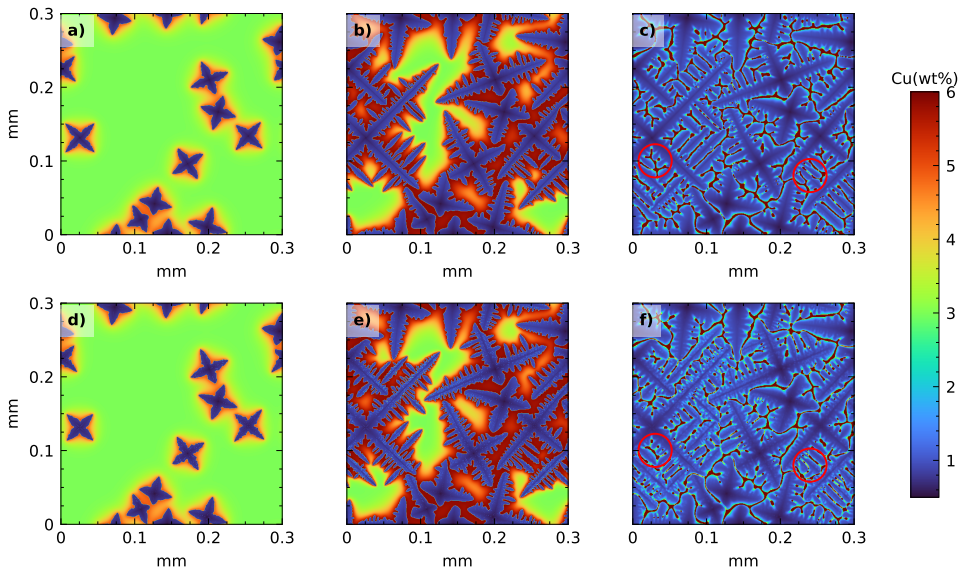

Figure 3.7: The concentration profiles at time 0.10 s (a, d), 0.15 s (b, e) and 1.0 s (c, f) in the multi-dendritic solidification simulations with (a-c) and without (d-f) the mass balance correction.

Initially, 12 nuclei with random orientations are placed randomly within the simulation domain. These nuclei grow and develop dendrite arms in their preferential growth directions, as shown in Figure 3.7(a, d). This shows that dendrites with different orientations can be well simulated with the decentered growth algorithm. As solidification proceeds, the growth of the primary arms is suppressed by nearby dendrites. Secondary dendrite arms form, as shown in Figure 3.7(b, e). Most liquid in the inter-dendritic regions is enriched to the equilibrium concentration. With further solidification, the dendrite arms coarsen and the liquid concentration increases with increasing undercooling, as shown in Figure 3.7(c, f). At this stage, the growth velocity and the kinetic undercooling in the interface cells are very small. In this case, the liquid concentration at the interface cells is close to the equilibrium liquid concentration and the solidification can be approximated by the Scheil-Gulliver solidification condition [41]. Comparing Figure 3.7 (a-c) with Figure 3.7 (d-f), the grain morphology difference between the simulations with and without the mass balance correction is insignificant. Red circles have been employed to highlight the small differences between Figure 3.7 (c) and Figure 3.7 (f). Compared to Figure 3.7 (c), the liquid

channels in Figure 3.7 (f) are smaller and more coalescence is observed, which indicates that the solid fraction in the simulation without the mass balance correction (Figure 3.7 (f)) is larger than the solid fraction in the simulation with the mass balance correction (Figure 3.7 (c)). In addition, the small difference between the two different simulations indicates that the mass balance correction has little influence on the growth kinetics.
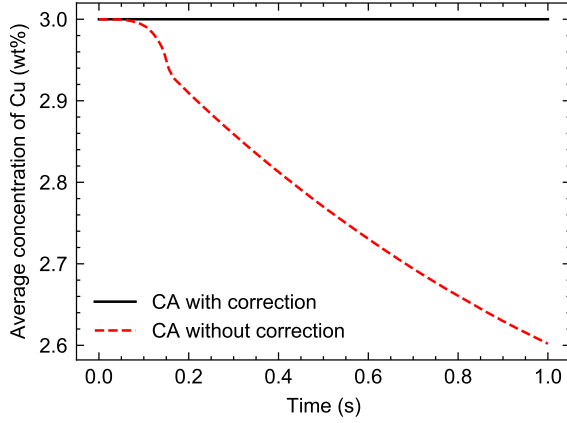

Figure 3.8: The evolution of the average concentration in the multi-dendritic solidification simulations with and without the mass balance correction.

Figure 3.8 shows the evolution of the average concentration in the simulations with and without the mass balance correction. The average concentration in the simulation with the mass balance correction remains constant, while the average concentration in the simulation without the mass balance correction decreases continuously, indicating that solutes are lost without the mass balance correction. In the multi-dendritic solidification simulation, the temperature drops continuously, which leads to an increase in the equilibrium liquid concentration. As shown in Section 3.3.2, the interface concentration is close to the equilibrium liquid concentration. Thus, the interface concentration tends to increase with decreasing temperature over numerous time steps. In this case, the sign of concentration change Δc of the interface cell is positive, which leads to a loss of the solutes. With the solutes artificially lost, the solid fraction in the simulation without the mass balance correction (Figure 3.7 (f)) is larger than the solid fraction in the simulation with the mass balance correction (Figure 3.7 (c)).

The results from the CA simulations are then compared with the Scheil-Gulliver model [41], which describes the solute redistribution during solidification of an alloy in a continuously cooling condition. It assumes the diffusion within the liquid is infinitely fast and the interface is always at a thermodynamic equilibrium. The liquid concentration c^l can be obtained as a function of the solid fraction of the system f_s [41]

$$c^l = c^0(1 - f_s)^{k-1}.$$
(3.39)

The relation between temperature T and the system solid fraction f_s is given by

$$T = T_0 + m\left(c^0(1 - f_s)^{k-1} - c^0\right).$$
(3.40)

Note that the Scheil-Gulliver model assumes a thermodynamic equilibrium at the interface, whereas the current CA model considers a non-equilibrium effect with the kinetic undercooling. Nevertheless, due to a relatively large kinetic coefficient (1×10^{-3} m·s^{-1}K^{-1}), the interface concentration is close to the equilibrium liquid concentration, as shown in Figure 3.5. Moreover, the solidification condition at the late stage can be approximated by the Scheil-Gulliver solidification condition due to the small growth velocity. In this case, the current CA model is comparable with the Scheil-Gulliver model.

The relationship between temperature T and the solid fraction f_s in the CA simulations with and without the mass balance correction are compared with the Scheil-Gulliver model in Figure 3.9. In the early stage of the solidification, the solid fraction predicted by the different CA simulations differs from the solid fraction predicted by the Scheil-Gulliver model. This is because the liquid diffusion coefficient in the CA simulation is finite, which leads to a hump in the concentration profile in front of the interface. At the interface, the Cu concentration is smaller than but close to the equilibrium concentration due to the non-equilibrium effect of the kinetic undercooling ΔT_k. In the liquid far from the interface, the Cu concentration is much smaller than the equilibrium concentration. In this case, the average Cu concentration in the liquid is smaller than the equilibrium concentration, which leads to a solid fraction smaller than the equilibrium solid fraction. As solidification proceeds, coarsening and coalescence of dendrites occurs. Liquid remains in the inter-dendritic region and the diffusion distance is much smaller, which decreases the required diffusion time. Moreover, the non-equilibrium effect introduced by the kinetic undercooling ΔT_k is negligible, as the interface velocity is very small in this stage. In this case, the diffusion condition can be approximated by the Scheil-Gulliver condition. The solid fraction in the CA simulation approaches the equilibrium solid fraction predicted by the Scheil-Gulliver model. At a temperature of 600 °C, the solid fraction in the CA simulation with the mass balance correction is close to the prediction of the Scheil-Gulliver model, while the solid fraction in the CA simulation without the mass balance correction is around 3 wt % larger. This agrees with the observations in Figure 3.7. The reason is that the solutes within the CA simulation without the mass balance correction are artificially lost, which leads to a larger equilibrium solid fraction. Moreover, the relationship between the average liquid concentration and the solid fraction f_s in the CA simulations and predicted by the Scheil-Gulliver model are given in Figure 3.10. For the same solid fraction, the liquid concentration in the CA simulation without the mass balance correction is smaller than the liquid concentration in the CA simulation with the mass balance correction and the Scheil-Gulliver calculation. This shows that solute segregation may be underestimated by the CA simulation without the mass balance correction.
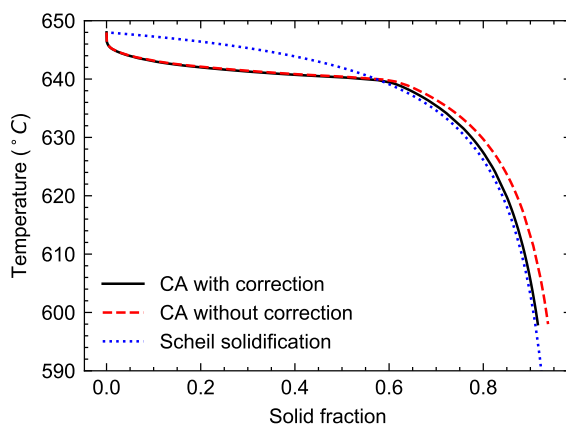
Figure 3.9: The relationship between temperature and the solid fraction in the multi-dendritic solidification simulations with and without the mass balance correction compared with the Scheil-Gulliver model.
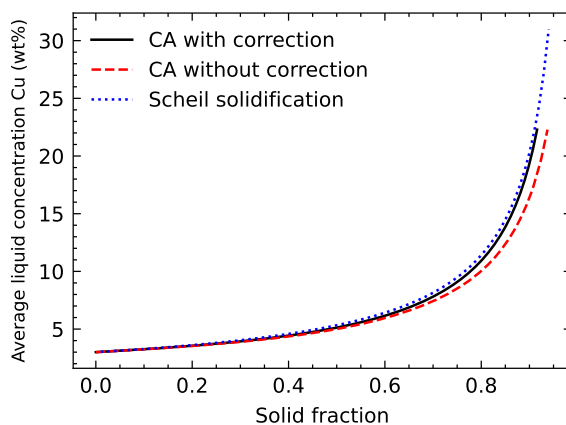

Figure 3.10: The relationship between the average liquid concentration and the solid fraction in the multi-dendritic solidification simulations with and without the mass balance correction compared with the Scheil-Gulliver model.

3.4 Conclusions

In this chapter, a non-equilibrium CA model has been described. The growth velocity is calculated as a linear function of the kinetic undercooling. To construct a CA model which is independent of the mesh size, a new diffusion term has been proposed to handle the diffusion between the interface cells and the liquid cells, in which the diffusion out of an interface cell is calculated by summing up the projections of diffusion fluxes onto the interface normal direction. With the new diffusion term, the stable tip velocity is proportional to the diffusion flux in the interface normal direction, which agrees with Nastac's equation for growth velocity calculation. Moreover, it minimizes the overestimation of tip velocity when the tip cell is surrounded by three liquid cells in its von Neumann neighborhood and improves the behavior in mesh size convergence tests.

The developed CA model has been employed to simulate single dendritic growth under different undercooling conditions. The simulated stable tip velocity agrees well with the prediction of a modified KGT model. With increasing kinetic mobility, the stable tip velocity tends to converge and the interface concentration at the dendrite tip approaches the equilibrium liquid concentration.

Moreover, the influence of the virtual liquid cell assumption has been studied in a multi-dendritic solidification simulation. In a continuously cooling solidification simulation, solutes are artificially lost due to the virtual interface cell assumption, which leads to a decrease in the average concentration. The mass balance error is removed by redistributing the lost solutes to neighboring liquid cells. With the mass balance correction, the average concentration remains constant throughout the simulation. Comparison with the prediction by the Scheil-Gulliver model shows a good agreement in the final stage of the solidification.

References

[1] Xiaohui Liang, Cornelis Bos, Marcel Hermans, and Ian Richardson. An improved cellular automata solidification model considering kinetic undercooling. *Metallurgical and Materials Transactions B*, 54(3):1088–1098, 2023.

[2] K Reuther and M Rettenmayr. Perspectives for cellular automata for the simulation of dendritic solidification–a review. *Computational materials science*, 95:213–220, 2014.

[3] Ryo Kobayashi. Modeling and numerical simulations of dendritic crystal growth. *Physica D: Nonlinear Phenomena*, 63(3-4):410–423, March 1993.

[4] Sebastian Gurevich, Alain Karma, Mathis Plapp, and Rohit Trivedi. Phase-field study of three-dimensional steady-state growth shapes in directional solidification. *Physical Review E*, 81(1):011603, January 2010.

[5] Jiangwei Liu, Henrique Pinho Duarte, and Sindo Kou. Evidence of back diffusion reducing cracking during solidification. *Acta Materialia*, 122:47–59, January 2017.

[6] Munekazu Ohno. Quantitative phase-field modeling of nonisothermal solidification in dilute multicomponent alloys with arbitrary diffusivities. *Physical Review E*, 86(5):051603, 2012.

[7] H Yin and SD Felicelli. Dendrite growth simulation during solidification in the lens process. *Acta Materialia*, 58(4):1455–1465, 2010.

[8] MR Rolchigo and R LeSar. Application of alloy solidification theory to cellular automata modeling of near-rapid constrained solidification. *Computational Materials Science*, 163:148–161, 2019.

[9] Xiaohui Ao, Huanxiong Xia, Jianhua Liu, and Qiyang He. Simulations of microstructure coupling with moving molten pool by selective laser melting using a cellular automaton. *Materials & Design*, 185:108230, 2020.

[10] Yi Zhang and Jing Zhang. Modeling of solidification microstructure evolution in laser powder bed fusion fabricated 316l stainless steel using combined computational fluid dynamics and cellular automata. *Additive Manufacturing*, 28:750–765, 2019.

[11] Frédéric Gibou, Ronald Fedkiw, Russel Caflisch, and Stanley Osher. A level set approach for the numerical simulation of dendritic growth. *Journal of Scientific Computing*, 19(1):183–199, 2003.

[12] Yung-Tae Kim, Nigel Goldenfeld, and Jonathan Dantzig. Computation of dendritic microstructures using a level set method. *Physical Review E*, 62(2):2471, 2000.

[13] Lijian Tan and Nicholas Zabaras. A level set simulation of dendritic solidification of multi-component alloys. *Journal of Computational Physics*, 221(1):9–40, 2007.

[14] L Nastac. Numerical modeling of solidification morphologies and segregation patterns in cast dendritic alloys. *Acta Materialia*, 47(17):4253–4262, 1999.

[15] W Wang, Peter D Lee, and M_ Mclean. A model of solidification microstructures in nickel-based superalloys: predicting primary dendrite spacing selection. *Acta materialia*, 51(10):2971–2987, 2003.

[16] M-F Zhu, W Cao, S-L Chen, C-P Hong, and YA Chang. Modeling of microstructure and microsegregation in solidification of multi-component alloys. *Journal of Phase Equilibria and Diffusion*, 28(1):130–138, 2007.

[17] Lazaro Beltran-Sanchez and Doru M Stefanescu. Growth of solutal dendrites: a cellular automaton model and its quantitative capabilities. *Metallurgical and Materials Transactions A*, 34(2):367–382, 2003.

[18] Lazaro Beltran-Sanchez and Doru M Stefanescu. A quantitative dendrite growth model and analysis of stability concepts. *Metallurgical and Materials Transactions A*, 35(8):2471–2485, 2004.

[19] J Lipton, ME Glicksman, and W Kurz. Dendritic growth into undercooled alloy metals. *Materials Science and Engineering*, 65(1):57–63, 1984.

[20] Sebastian C Michelic, Jörg M Thuswaldner, and Christian Bernhard. Polydimensional modelling of dendritic growth and microsegregation in multicomponent alloys. *Acta materialia*, 58(7):2738–2751, 2010.

[21] Xianfei Zhang, Jiuzhou Zhao, Hongxiang Jiang, and Mingfang Zhu. A three-dimensional cellular automaton model for dendritic growth in multi-component alloys. *Acta Materialia*, 60(5):2249–2257, 2012.

[22] MF Zhu and DM Stefanescu. Virtual front tracking model for the quantitative modeling of dendritic growth in solidification of alloys. *Acta materialia*, 55(5):1741–1755, 2007.

[23] Shiyan Pan and Mingfang Zhu. A three-dimensional sharp interface model for the quantitative simulation of solutal dendritic growth. *Acta Materialia*, 58(1):340–352, 2010.

[24] H. Yin, S. D. Felicelli, and L. Wang. Simulation of a dendritic microstructure with the lattice boltzmann and cellular automaton methods. *Acta Materialia*, 59(8):3124–3136, 2011.

[25] R Trivedi and W Kurz. Dendritic growth. *International Materials Reviews*, 39(2):49–74, 1994.

[26] AA Burbelko, D Gurgul, W Kapturkiewicz, J Początek, and M Wróbel. Cellular automaton modeling of ductile iron microstructure in the thin wall. *Archives of Foundry Engineering*, 11(1):13–18, 2011.

[27] Shaoning Geng, Ping Jiang, Yuewei Ai, Rong Chen, LongChao Cao, Chu Han, Wei Liu, and Yang Liu. Cellular automaton modeling for dendritic growth during laser beam welding solidification process. *Journal of Laser Applications*, 30(3):032406, 2018.

[28] Y Zhao, RS Qin, and DF Chen. A three-dimensional cellular automata model coupled with finite element method and thermodynamic database for alloy solidification. *Journal of crystal growth*, 377:72–77, 2013.

[29] Klemens Reuther and Markus Rettenmayr. A comparison of methods for the calculation of interface curvature in two-dimensional cellular automata solidification models. *Computational Materials Science*, 166:143–149, 2019.

[30] Lei Wei, Yongqing Cao, Xin Lin, Meng Wang, and Weidong Huang. Quantitative cellular automaton model and simulations of dendritic and anomalous eutectic growth. *Computational Materials Science*, 156:157–166, 2019.

[31] Sen Luo and Miao Yong Zhu. A two-dimensional model for the quantitative simulation of the dendritic growth with cellular automaton method. *Computational materials science*, 71:10–18, 2013.

[32] M Marek. Grid anisotropy reduction for simulation of growth processes with cellular automaton. *Physica D: Nonlinear Phenomena*, 253:73–84, 2013.

[33] Ch-A Gandin and Michel Rappaz. A 3d cellular automaton algorithm for the prediction of dendritic grain growth. *Acta Materialia*, 45(5):2187–2195, 1997.

3

[34] Wenda Tan, Neil S. Bailey, and Yung C. Shin. A novel integrated model combining Cellular Automata and Phase Field methods for microstructure evolution during solidification of multi-component and multi-phase alloys. *Computational Materials Science*, 50(9):2573–2585, July 2011.

[35] Shunyu Liu, Kyung-min Hong, and Yung C Shin. A novel 3d cellular automata-phase field model for computationally efficient dendrite evolution during bulk solidification. *Computational Materials Science*, 192:110405, 2021.

[36] Stéphane Popinet. An accurate adaptive solver for surface-tension-driven interfacial flows. *Journal of Computational Physics*, 228(16):5838–5866, 2009.

[37] Mohsen Asle Zaeem, Hebi Yin, and Sergio D Felicelli. Modeling dendritic solidification of al–3% cu using cellular automaton and phase-field methods. *Applied Mathematical Modelling*, 37(5):3495–3503, 2013.

[38] W 1 Kurz, B Giovanola, and R Trivedi. Theory of microstructural development during rapid solidification. *Acta metallurgica*, 34(5):823–830, 1986.

[39] Dongke Sun, Mingfang Zhu, Shiyan Pan, and Dierk Raabe. Lattice Boltzmann modeling of dendritic growth in a forced melt convection. *Acta Materialia*, 57(6):1755–1767, April 2009.

[40] J.C. Ramirez and C. Beckermann. Examination of binary alloy free dendritic growth theories with a phase-field model. *Acta Materialia*, 53(6):1721–1736, April 2005.

[41] Erich Scheil. Bemerkungen zur schichtkristallbildung. *International Journal of Materials Research*, 34(3):70–72, 1942.

4

SOLIDIFICATION CRACKING STUDY BY PHASE FIELD MODELLING OF DENDRITE FORMATION

In the previous chapter, the dendrite formation during solidification has been analyzed with a cellular automata model. During solidification, solutes accumulate in the liquid channels between the dendrites. Upon tensile loading due to thermal contraction and solidification shrinkage, cracking occurs if enough liquid feeding is not available to fill the voids; this is known as solidification cracking. In this chapter, the influence of the temperature gradient and the pulling velocity on solidification cracking susceptibility (SCS) during welding is addressed by simulating the liquid channel evolution with a quantitative phase field model. Increasing the pulling velocity or decreasing the temperature gradient increases the pressure drop from the dendrite tip to the coalescence point, leading to an increase in SCS. Decreasing the primary dendrite arm spacing (PDAS) decreases the permeability of the liquid channel and the liquid channel length at the same time, resulting in a decrease in the pressure drop and the SCS when the PDAS is small. Consideration of the PDAS dependency on the temperature gradient and the pulling velocity influences the value of the pressure drop but does not change the tendency of the SCS. The conclusions are also valid for alloys with strong back diffusion. As the temperature gradient and the pulling velocity within the melt pool are controlled by process parameters, the findings from this chapter provide a theoretical basis for optimization of process parameters to avoid solidification cracking.

4.1 Introduction

Solidification defects may form in the mushy zone of welded [2, 3] or additively manufactured [4–6] components. Solidification cracking is a complex phenomenon which is associated with thermal, metallurgical and mechanical factors [7]. In the mushy zone, liquid channels exist at a relatively low temperature due to solute segregation. When the liquid channel is exposed to a tensile strain due to thermal contraction or solidification contraction and sufficient liquid feeding is not available, cracks form.

Efforts have been made to avoid solidification cracking by controlling process parameters including power Q and welding scanning velocity v_s [7, 8]. It has been reported that increasing the scanning velocity v_s with a constant power Q leads to a decrease in SCS for a nickel-base alloy [9] and advanced high strength steels [10]. This was explained by the smaller thermal strain generated during welding at a faster scanning velocity v_s [10]. When the scanning velocity v_s is increased with a constant Q/v_s ratio, an increase in SCS was reported for an aluminum alloy [11] and a stainless steel [12]. However, it was also reported that increasing the scanning velocity promotes the transition from a columnar to an equiaxed structure in the weld pool and thus eliminates solidification cracking in aluminum alloy 6082 [13].

Several models have been proposed to explain the mechanisms behind solidification cracking. Kou [14, 15] proposed a model which includes solidification, strain rate and liquid feeding, where a crack forms when the separation strain rate is larger than the sum of the solidification rate and liquid feeding rate, as given by

$$\frac{d\varepsilon}{dT} > \sqrt{1-\beta}\frac{d\sqrt{f_s}}{dT} + \frac{1}{dT/dt}\frac{d}{dz}\left[\left(1-\sqrt{1-\beta}\sqrt{f_s}\right)v_z\right], \tag{4.1}$$

where ε is the strain, f_s the solid fraction, β the solidification shrinkage, dT/dt the cooling rate, v_z the liquid velocity and z the direction parallel to the liquid channel. The slope of temperature with respect to the square root of the solid fraction $dT/\sqrt{f_s}$ when f_s is close to 1.0 is defined as the SCS index, which is evaluated with the Scheil-Gulliver equation. A high SCS index represents a high SCS. Kou's SCS index successfully predicts the SCS peak in the Al-Cu alloys observed by Pumphrey et al. [16]. The Rappaz-Drezet-Gremaud (RDG) model [17] considers fluid flow and solid network deformation at the same time. A pressure drop is calculated considering the flow in the mushy zone. If the pressure drop is larger than a critical value, which is related to the critical strain rate, voids can form leading to the initiation of solidification cracks.

Phase field modelling is a powerful method to simulate the grain morphology and segregation formed during solidification and to evaluate SCS. Based on Kou's model, Wang et al. [18] performed phase field simulations to study the segregation and the morphology of liquid channels in directionally solidified Al-Cu alloys with different copper contents. In the Al-2Cu (wt.%) and Al-3Cu(wt.%) alloys, the liquid channel coalesces before the eutectic temperature, while the liquid channel in the Al-4Cu(wt.%) alloy transforms into an eutectic phase before coalescence. Geng et al. [19, 20] studied the influence of back diffusion on liquid channel morphology and SCS and found that the existence of Mg back diffusion promotes dendrite coalescence, thus decreasing the SCS of an Al-Mg alloy. Jiang et al. [21] found that a small primary dendrite arm spacing facilitates earlier coalescence of adjacent grains to resist cracking. Gong et al. [22] found that the influence of grain refinement and

grain morphology on micro-segregation during solidification is not significant. Chen et al. [23] calculated the pressure drop with a fluid dynamic model based on the microstructure obtained from a phase field model. It was found that the pressure drop near a dendrite tip increases as the misorientation angle between the columnar grains increases. Han et al. [24] employed a multi-phase phase field approach to simulate the coalescence behavior between columnar grains with different orientations. Attraction ($\sigma_{ss} < 2.0\sigma_{sl}$) or rejection ($\sigma_{ss} > 2.0\sigma_{sl}$) are found, where σ_{ss} and σ_{sl} are the interfacial energies for the solid-solid interface and solid-liquid interfaces, respectively. In the aforementioned micro-scale microstructure models, the frozen temperature gradient approximation [18, 20] is widely employed, in which the thermal condition during welding is approximated with a directional solidification condition. In a directional solidification condition, the thermal condition is controlled by the temperature gradient G and the pulling velocity V, which is the velocity at which the liquidus isotherm moves. Yang et al. [25] coupled a multi-order phase field model with the RDG model to study hot cracking susceptibility as a function of alloy composition under different grain boundary conditions. Accurate predictions of the liquid rupture states were obtained when the grain boundary effects were considered.

Despite so many experimental [26, 27] and modelling [14, 17, 28] studies on solidification cracking, a detailed study of the influence of the temperature gradient and the pulling velocity on SCS is not available. In welding experiments, the temperature gradient and the pulling velocity change at the same time when modifying any process parameter like the scanning velocity or the power. In this case, the influence of the temperature gradient and the pulling velocity on SCS cannot be studied univariately with welding experiments, which nevertheless is achievable with modelling. Moreover, the temperature gradient G and the pulling velocity V influence the PDAS, which also has an impact on SCS. Thus, when studying the influence of the temperature gradient and the pulling velocity on SCS, the dependency of the PDAS on G and V should be considered. In this case, large-scale simulations need to be done, which is time-consuming with phase field modelling.

In this chapter, the influence of the temperature gradient G and the pulling velocity V on micro-segregation and SCS is considered with a quantitative phase field model. An adaptive mesh refinement method is employed to reduce the computational cost, which enables large-scale simulations within a short time. First, directional solidification simulations are performed with different temperature gradients and pulling velocities to obtain steady-state PDAS. Then, univariate studies are performed to study the influence of the temperature gradient G and the pulling velocity V on micro-segregation within the liquid channel and SCS with and without considering the dependency of the PDAS on G and V. The studies are firstly performed in an alloy system with negligible solid diffusion, which means back diffusion is not considered. Secondly, the aforementioned univariate studies are repeated to study the influence of the temperature gradient G and the pulling velocity V on micro-segregation and SCS considering back diffusion with an artificially increased diffusion coefficient in the solid.

4.2 Model description

4.2.1 Equations of the phase field model

In a 2D phase field model, the governing equation for the phase field variable ϕ defined in the interval $[0, 1]$ is given by [29]

$$\tau a_s^2 \frac{\partial \phi}{\partial t} = W^2 \nabla \cdot \left[a_s^2 \nabla \phi \right] + W^2 \partial_x \left(|\nabla \phi|^2 a_s \frac{\partial a_s}{\partial (\partial_x \phi)} \right) + W^2 \partial_y \left(|\nabla \phi|^2 a_s \frac{\partial a_s}{\partial (\partial_y \phi)} \right)$$
$$- 2\phi(1-\phi)(1-2\phi) + \frac{30 a_1 W}{\sigma} \phi^2 (1-\phi)^2 \Delta G, \tag{4.2}$$

where τ is the kinetic parameter, W the interface width, a_1 a numerical constant, σ the interfacial energy, a_s the anisotropy function and ΔG the chemical driving force. To reduce the discretization error, a nonlinear preconditioning [29, 30] is employed,

$$\phi = \frac{1}{2} - \frac{1}{2} \tanh \left(\frac{\psi}{\sqrt{2}} \right). \tag{4.3}$$

The governing equation for the preconditioned phase field variable ψ is then given by [29]

$$\tau a_s^2 \frac{\partial \psi}{\partial t} = W^2 \nabla \cdot \left[a_s^2 \nabla \psi \right] + W^2 \partial_x \left(|\nabla \psi|^2 a_s \frac{\partial a_s}{\partial (\partial_x \psi)} \right) + W^2 \partial_y \left(|\nabla \psi|^2 a_s \frac{\partial a_s}{\partial (\partial_y \psi)} \right)$$
$$+ \sqrt{2} W (1 - 2\phi)(1 - a_s^2 |\nabla \psi|) - \frac{5 W^2}{\sigma} \phi(1-\phi)\Delta G. \tag{4.4}$$

The anisotropy function a_s is given by a fourfold anisotropic function [29]

$$a_s = (1 - 3\varepsilon_4) \left[1 + \frac{4\varepsilon_4}{1 - 3\varepsilon_4} \left(n_x^4 + n_y^4 \right) \right], \tag{4.5}$$

where ε_4 is the anisotropy strength, n_x and n_y are the components of the interface normal unit vector $\vec{n}$, which is determined with

$$\vec{n} = \frac{\nabla \psi}{|\nabla \psi|}. \tag{4.6}$$

In this chapter, the extrapolated phase diagram method proposed by Eiken et al. [31] is employed to calculate the chemical driving force and the solute redistribution. The concentration in the liquid c^l and solid c^s are given by

$$c^l = \frac{c - \phi(c^{s,*} - k c^{l,*})}{k\phi + 1 - \phi}, \tag{4.7}$$

and

$$c^s = \frac{c - \phi(c^{l,*} - c^{s,*}/k)}{\phi + (1 - \phi)/k}, \tag{4.8}$$

where $c^{l,*}$ and $c^{s,*}$ are the liquid and solid concentrations at the extrapolation point, and k the partitioning coefficient which is given by

$$k = \frac{m^l}{m^s},$$ (4.9)

where m^l and m^s are the slope of the liquidus and solidus lines. The chemical driving force ΔG is calculated by

$$\Delta G = \Delta S \left(\Delta T + m^l(c^l - c^{l,*}) \right),$$ (4.10)

where ΔS is the entropy change for solidification at the extrapolation point.

The kinetic parameter τ is given as [29, 32]

$$\tau = \frac{a_1 a_2 W^3 \Delta S m^l(c^l - c^s)}{\sigma D^l},$$ (4.11)

with $a_1 = \frac{\sqrt{2}}{6}$ and $a_2 = 2.35$ [33]. D^l is the diffusion coefficient in the liquid.

The diffusion equation with an anti-trapping flux to eliminate the chemical potential jump in the interface region is given by [34]

$$\frac{\partial c}{\partial t} = \nabla \cdot \left(D^l(1-\phi)\nabla c^l + D^s \phi \nabla c^s + \frac{W}{\sqrt{2}}(c^l - c^s)\frac{\nabla \psi}{|\nabla \psi|}\frac{\partial \phi}{\partial t} \right),$$ (4.12)

where c is the concentration, c^l the liquid concentration, c^s the solid concentration, and D^s the diffusion coefficients in the solid.

In directional solidification simulations to determine the PDAS, noise is introduced with the method described in the work of Warren and Boettinger [35]:

$$\theta = 16n_f\beta\phi^2(1-\phi)^2\left(-2\phi(1-\phi)(1-2\phi) + \frac{30a_1 W}{\sigma}\phi^2(1-\phi)^2\Delta G \right),$$ (4.13)

where n_f is the noise amplitude, β is a random number in the range [-1, 1].

4.2.2 Implementation of the phase field model

In the current work, the interface region is defined as the region where $\phi_{crit} < \phi < 1 - \phi_{crit}$. The preconditioned phase field variable ψ follows $-\psi_{crit} < \psi < \psi_{crit}$ in the interface region, where ψ_{crit} is calculated by

$$\psi_{crit} = \sqrt{2}W \tanh^{-1}(1 - 2\phi_{crit}).$$ (4.14)

Following the work of Gong et al. [36], a numerical cut-off has been used for the preconditioned variable ψ,

$$\psi = \begin{cases} -\psi_{crit}, & \text{if } \psi \leq -\psi_{crit}, \\ \sqrt{2}W \tanh^{-1}(1 - 2\phi), & \text{if } -\psi_{crit} < \psi < \psi_{crit}, \\ \psi_{crit}, & \text{if } \psi \geq \psi_{crit}. \end{cases}$$ (4.15)

Adaptive mesh refinement has been employed to reduce the computational cost. The simulation domain is first divided into coarse square cells with refinement level defined as

0. A cell at refinement level n can be further divided into 4 smaller cells at refinement level $n+1$ based on a quadtree structure. The difference in the refinement level of neighboring cells is limited to be 1 or 0. The maximum refinement level in our simulations is 5. Cells in the interface region ($\phi_{crit} < \phi < 1-\phi_{crit}$) are always refined to the maximum refinement level. In the bulk phase region, the criterion to update the grid is defined based on the magnitudes of the concentration gradients $|\nabla c|$. The criterion to determine whether to refine or coarsen a cell at refinement level n is given by

- Refinement : The considered cell at refinement is refined when $\Delta x_n |\nabla c| > \Delta c_{max}$,

- Coarsening : The cells which belong to the same parent cell are coarsened when each of them satisfy $\Delta x_n |\nabla c| < \Delta c_{min}$,

where Δx_n is the size of the cell at the refinement level n. Δc_{max} and Δc_{min} are the maximum and the minimum concentration changes within a cell.

Field data like phase field variables ϕ, ψ and concentration c are saved for the center of each cell. The governing equations Equation (4.4) and Equation (4.12) are solved with a finite difference method and a Euler forward discretization method. A moving frame method is employed in the current model to reduce the computational cost. The simulation domain is shifted by the size of the coarsest cell, Δx_0 for each moving frame operation.

In the current work, solidification simulations have been performed for an Al-4Cu (wt.%) alloy. The parameters of the Al-4Cu (wt.%) alloy [36–38] are given in Table 4.1.

Table 4.1: Thermodynamic parameters for the Al-4Cu (wt.%) alloy [36–38].

Symbol	Description	Value	Unit
$c^{l,*}$	Liquid concentration at the extrapolation point	4.0	wt%
$c^{s,*}$	Solid concentration at the extrapolation point	0.68	wt%
k	Partitioning coefficient	0.17	1
m^l	Liquidus slope	-2.6	K/(wt%)
σ	Interfacial energy	0.24	J/m^2
ΔS	Entropy change	1×10^6	J/(m^{3}K)
D^l	Liquid diffusion coefficient	3.0×10^{-9}	m^2/s
D^s	Solid diffusion coefficient	3.0×10^{-13}	m^2/s
ε_4	Anisotropy strength	0.05	1
ϕ_{crit}	Critical ϕ value for interface region	0.001	1

4.3 Results

4.3.1 Determination of PDAS for Al-4Cu (wt.%) alloy

Directional solidification simulations have been performed for the Al-4Cu (wt.%) alloy under different temperature gradients G (0.2 K/μm, 0.5 K/μm, 1.0 K/μm, 3.0 K/μm and 5.0 K/μm) and different pulling velocities V (50 mm/s, 40 mm/s, 30 mm/s, 20 mm/s and 10 mm/s). The temperature gradient is applied in the y direction. The simulation domain cools continuously with a constant cooling rate. Initially, 76 nuclei are randomly placed

at the bottom of the simulation domain, which ensures that the mean distance between the two neighboring nuclei is $20\Delta x_{min}$, where Δx_{min} is the minimum cell size in the current simulation. In the different simulations, the nuclei locations are the same. The nuclei then grow into columnar grains and growth competition occurs. After some time, a stable columnar microstructure is formed [38, 39]. A moving frame method is employed here to reduce the computational cost. The simulation time is determined such that the liquidus temperature line moves in the y direction for $100\,\mu m$, which ensures the formation of a stable columnar microstructure.
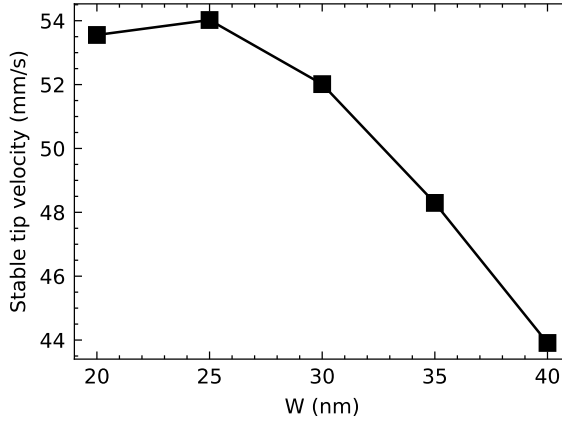
Figure 4.1: The stable tip velocity as a function of the interface width W in the convergence study.

Before the directional solidification simulation, a convergence study was performed to determine the optimal interface width W. Single dendritic solidification simulations were performed under a constant undercooling $\Delta T = 15\,K$ with different interface width W ($W = 1.5\Delta x_{min}$). The stable tip velocities in the different simulations are plotted as a function of the interface width W in Figure 4.1. The stable tip velocity tends to converge to around $53.5\,mm/s$, which is larger than the maximum pulling velocity $50\,mm/s$. Thus, the directional solidification simulations were performed with an interface width $W = 25\,nm$ and the minimum cell size $\Delta x = 16.67\,nm$.

The stable columnar microstructures under different temperature gradients G and pulling velocities V are given in Figure 4.2. The values of the PDAS are calculated by the domain size in the x direction divided by the number of solid columns in the simulation domain. The PDAS in the simulation with a temperature gradient $G = 0.2\,K/\mu m$ and a pulling velocity $V = 10\,mm/s$ is largest among the listed simulations. As the temperature gradient G increases and the pulling velocity V increases, the number of the columnar grains in the stable microstructure increases and the PDAS decreases. The columnar grains in the simulations with temperature gradients $G = 3.0\,K/\mu m$ and $G = 5.0\,K/\mu m$ grow in a cellular mode due to the large G/V ratio [40]. In the simulations with temperature gradients $G = 0.2\,K/\mu m$ and $G = 1.0\,K/\mu m$, as the pulling velocity V increases, the growth mode changes from cellular to cellular-dendritic due to the decreasing G/V ratio.

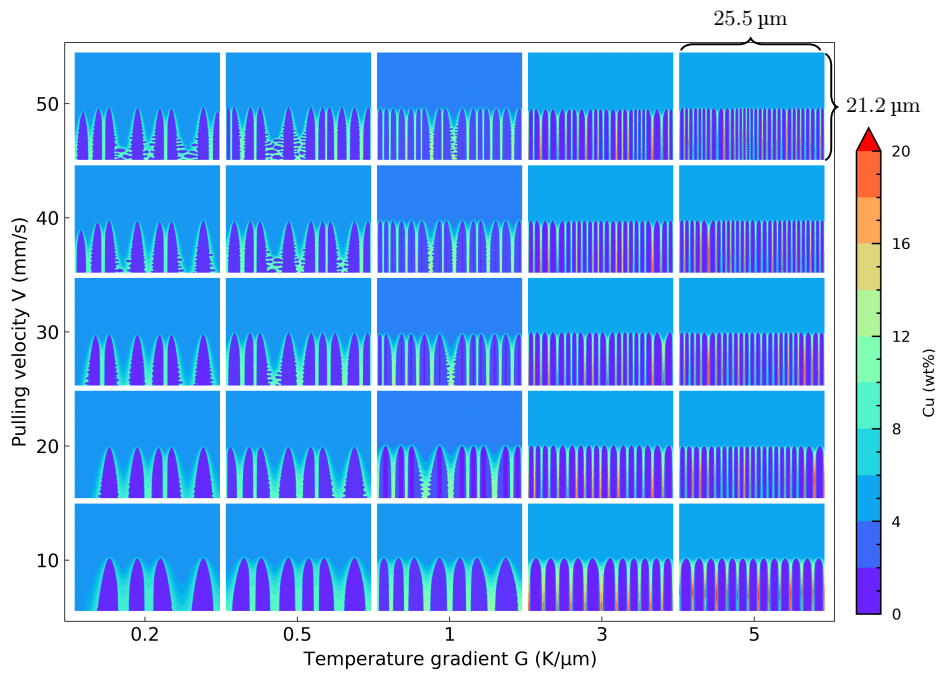According to the Kurz-Fisher model, the PDAS is proportional to $G^{-0.50}V^{-0.25}$. However,

Figure 4.2: Stable columnar microstructures during directional solidification with different temperature gradients G and pulling velocities V.

such a linear relationship between PDAS and $G^{-0.50}V^{-0.25}$ cannot be found with the PDAS values in our phase field results, as shown in Figure 4.3 (a). As found from experiments [41] and theory [42], the influence of the temperature gradient G on microstructure selection becomes weaker in rapid solidification, while the effect of the cooling rate $\dot{T}$ becomes more important. Kundin et al. [38] derived the dependency of PDAS on the temperature gradient G and the cooling rate $\dot{T}$ as $G^{0.09}\dot{T}^{-0.45}$ ($G^{-0.36}V^{-0.45}$) for an Fe-18.9Mn alloy. To calculate the dependency of PDAS (λ) on the temperature gradient G and the cooling rate $\dot{T}$, the PDAS values have been fitted by minimizing the mean square error

$$error = \frac{1}{n}\sum_{i}^{n}(\lambda_i - aG^bV^c)^2, \tag{4.16}$$

where a, b and c are fitting constants. It is found that PDAS (λ) is proportional to $G^{-0.40}\dot{V}^{-0.41}$ ($G^{0.01}\dot{T}^{-0.41}$), as shown in Figure 4.3 (b). The relation $\lambda \propto G^{0.01}\dot{T}^{-0.41}$ agrees well with the results ($\lambda \propto G^{0.09}\dot{T}^{-0.45}$) of Kundin et al. [38].
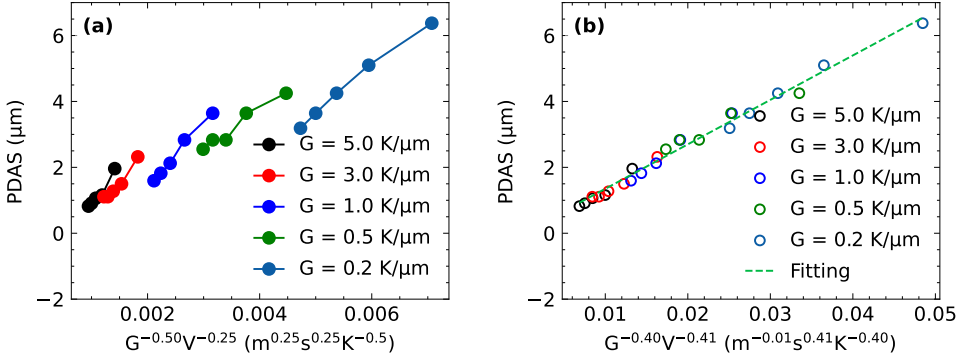

Figure 4.3: The relationship between the PDAS and $G^{-0.50}V^{-0.25}$ (a) and the fitted relationship between the PDAS and $G^{-0.50}V^{-0.25}$ (b) in different simulations.

4.3.2 Influence of the G, V and PDAS on SCS

Solidification cracking susceptibility is evaluated by simulating the evolution of the liquid channel between two columnar grains. To reduce the computational cost, only one liquid channel is simulated. Initially, a nucleus is placed in the bottom left corner, which then grows into a large columnar grain under the given temperature gradient G and cooling rate $\dot{T}$. With periodic boundary conditions on the left and the right boundaries, a liquid channel is formed in the center of the simulation domain. The width of the simulation domain is equal to the PDAS, while the height of the simulation domain is determined to capture the liquid channel evolution from the columnar tip to the closure of the liquid channel. In practice, a temperature difference of 160 K between the top and bottom boundaries is enough to determine a simulation domain which is sufficiently large.

Univariate studies are performed to check the influence of the pulling velocity V, the temperature gradient G and the PDAS on SCS (A1-A3). The settings of the univariate studies are given in Table 4.2. To simplify the problem, a constant PDAS value is employed

in the A1 and A2 studies, which is determined from the previous directional solidification simulation at $G = 1.0$ K/μm and $V = 30$ mm/s. In the A3 study, different PDAS values are tested to check the influence on SCS. The tested PDAS values in the A3 study correspond to the PDAS values in the directional solidification simulations at different pulling velocities (50 mm/s, 40 mm/s, 30 mm/s, 20 mm/s and 10 mm/s). Moreover, the A4 and A5 studies were performed to study the influence of the pulling velocity V and the temperature gradient G on SCS considering the dependency of the PDAS on the pulling velocity V and the temperature gradient G. The PDAS values in the A4 and A5 studies were determined in the previously described directional solidification simulations.

Table 4.2: Parameters in the A1-A5 studies with $D_s = 3 \times 10^{-13}$ m²/s.

Study	V (mm/s)	G (K/μm)	PDAS (μm)
A1	10, 20, 30, 40 and 50	1.0	2.13
A2	30	0.5, 1.0, 3.0 and 5.0	2.13
A3	30	1.0	1.59, 1.82, 2.13, 2.83, 3.64 and 4.00
A4	10, 20, 30, 40 and 50	1.0	Determined
A5	30	0.5, 1.0, 3.0 and 5.0	Determined

The SCS is evaluated with the pressure drop Δp from the dendrite tip to the coalescence point of the liquid channel, which is calculated by the RDG model [17],

$$\Delta p = \frac{180}{\lambda^2} \frac{(1+\beta)\mu_v}{G} \int_{T_S}^{T_L} \frac{E(T)f_s(T)^2}{(1-f_s(T))^3} dT + \frac{180}{\lambda^2} \frac{V\beta\mu_v}{G} \int_{T_S}^{T_L} \frac{f_s(T)^2}{(1-f_s(T))^2} dT \qquad (4.17)$$

with

$$E(T) = \frac{1}{G} \int f_s(T)\dot{\varepsilon}_p(T) dT, \qquad (4.18)$$

where μ_v is the viscosity, β the shrinkage factor, $\dot{\varepsilon}_p(T)$ is the strain rate and T_l and T_s the solidification start and end temperature, respectively. The first term and the second term on the right hand side represent the mechanical contribution due to strain rate and the shrinkage contribution due to solidification, respectively. A larger pressure drop represents a less favorable condition for liquid feeding and thus a larger SCS. For the pressure drop calculations, the employed parameter are $\mu_v = 1 \times 10^{-3}$ Pa·s, $\beta = 0.06$ and $\dot{\varepsilon}_p = 1 \times 10^{-4}$ s^{-1} [17]. T_l and T_s are determined as the temperature at the dendrite tip and the temperature at the coalescence point of the liquid channel. Note the integral divided by the temperature gradient G is in fact an integral over the distance from the coalescence point to the dendrite tip, which is the length of the liquid channel (LC length). Noise ($n_f = 0.1$) is considered to approach the coalescence of the liquid channel in the real world, which inevitably introduces randomness in the simulation results. In this case, each studied condition was simulated four times with different seeds for the generation of the random noise. The pressure drop and the LC length were then averaged for SCS evaluation. Error bars are determined with 99% confidence interval. However, in some cases, the error bars are too small to be seen. If the eutectic temperature (823 K) is reached before the liquid channel coalescence, then the eutectic point is determined as the coalescence point for the

calculation of the pressure drop and the LC length. The solid fraction f_s at temperature T is calculated by

$$f_s = \frac{\sum_i^n \phi \Delta x_i}{w},$$ (4.19)

where w is the domain width and ϕ and Δx_i the phase field value and cell size of the cells which intersects with the isothermal line at T.
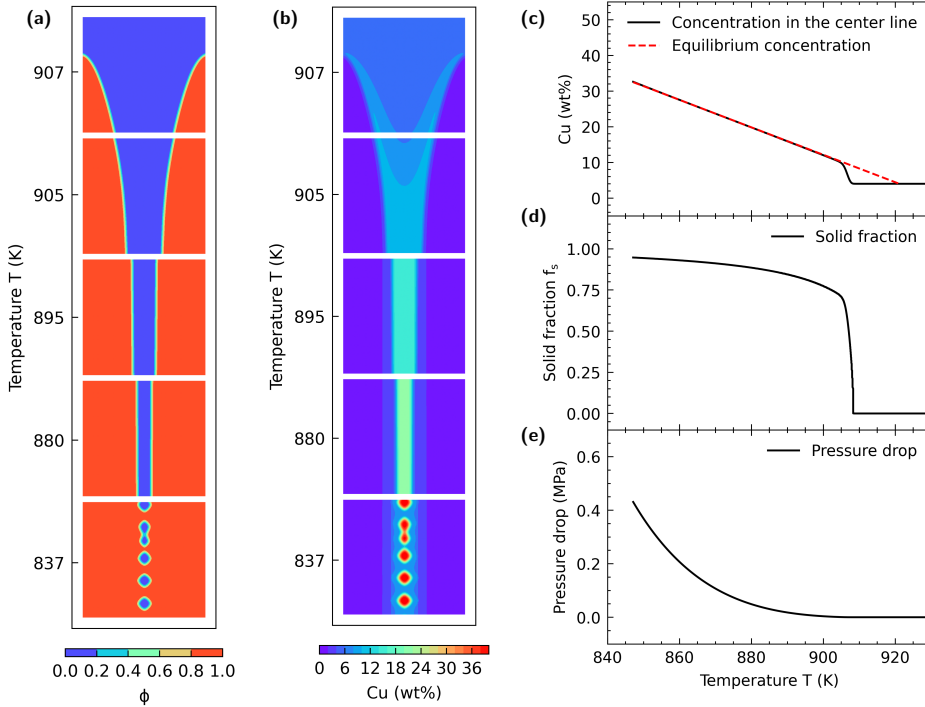

Figure 4.4: The final grain morphology (a) and the concentration profile (b) in the A1 simulation with $V = 30\,\text{mm/s}$. The concentration along the center line (c), the solid fraction (d) and the pressure drop in the liquid channel (e) are given as a function of temperature.

The final grain morphology and the concentration profile in the A1 simulation with $V = 30\,\text{mm/s}$ are given in Figure 4.4 (a) and (b), respectively. Due to the large ratio between the height and the width, the microstructure figures are truncated and the microstructure in the selected temperature ranges are shown. As periodic boundary conditions are employed for the left and the right boundaries, a liquid channel surrounded by a columnar grain is formed in the center of the simulation domain. As temperature drops in the y direction, the columnar grain widens in the horizontal direction, which closes the liquid channel. Solutes are rejected from the interface and a diffusion layer is formed due to the finite diffusivity in the liquid, as shown in Figure 4.4 (b). With decreasing liquid channel width, the diffusion layers of the opposite interfaces impinge and form a concentration valley in the center of the liquid channel. In this stage, the solid fraction is lower than the equilibrium solid

fraction and the average concentration in the liquid channel is below the equilibrium liquid concentration, as shown in Figure 4.4 (c); thus, it is called the non-equilibrium stage in the current work. In this stage, a steep increase is observed in the solid fraction with decreasing temperature, as shown in Figure 4.4 (d). As the temperature drops, the liquid channel becomes thinner, which promotes the homogenization of concentration within the liquid channel in the horizontal direction. Consequently, the depth of the concentration valley decreases with decreasing temperature. When the liquid channel is sufficiently thin, the concentration valley within the liquid channel is negligible and the concentration within the liquid channel can be considered homogeneous and is equal to the equilibrium liquid concentration, as shown in Figure 4.4 (c). The stage with a homogeneous concentration in the liquid channel is referred to as the equilibrium stage. In this stage, the solid fraction increases slowly with decreasing temperature, as shown in Figure 4.4 (d). The pressure drop along the liquid channel is given in Figure 4.4 (e). The maximum value of the pressure drop is employed for SCS evaluation. With decreasing temperature, the pressure drop curve becomes steeper, which indicates the choice of the coalescence point has a large influence on the maximum value of the pressure drop.

In the A1 simulations, different pulling velocities were employed. Consequently, the non-equilibrium stage starts and ends at different temperatures in the different A1 simulations, which means that the solid formed in the non-equilibrium stage in the different simulations has different concentrations. In the simulation with a larger pulling velocity V, the concentration of the solid formed in the non-equilibrium stage is larger and thus the solute enrichment in the liquid is less. The different solute partitioning in the non-equilibrium stage results in different $f_s \sim T$ curves and different coalescence points in the equilibrium stage, as shown in Figure 4.5 (a). The simulation with a larger pulling velocity and less solute enrichment solidifies faster in the equilibrium stage, resulting in an earlier liquid channel coalescence. In this case, the LC length decreases with increasing pulling velocity, leading to a potential decrease in the pressure drop. However, this effect is insignificant. With increasing pulling velocity, the shrinkage due to phase transition is faster (the second term in Equation (4.17)), resulting in an increase in the pressure drop. The shrinkage contribution dominates the pressure drop evolution and a significant increase is observed in the pressure drop with increasing pulling velocity, as shown in Figure 4.5 (b). With increasing pulling velocity, the SCS increases.

The influence of the temperature gradient G on SCS is studied in the A2 study without considering the dependency of the PDAS on G. As shown in Figure 4.5 (c), the non-equilibrium stage starts at the same temperature, as the pulling velocity is constant for the A2 simulations. However, the non-equilibrium stage ends at different temperatures in the different simulations. In the different A2 simulations, it takes similar time to enrich the liquid channel to the equilibrium liquid concentration, as the domain width is constant. Due to the different cooling rates, the corresponding temperature drops are different. Thus, the non-equilibrium stage ends at different temperatures. In the equilibrium stage, the $f_s \sim T$ curves for simulations with different temperature gradients G are close to each other and the liquid channel closes at similar temperature. In this case, the liquid channels exist in a similar temperature range, corresponding to different LC length. The simulation with a smaller temperature gradient has a larger LC length and thus a larger pressure drop, as shown in Figure 4.5 (d). With increasing temperature gradient, the SCS decreases.
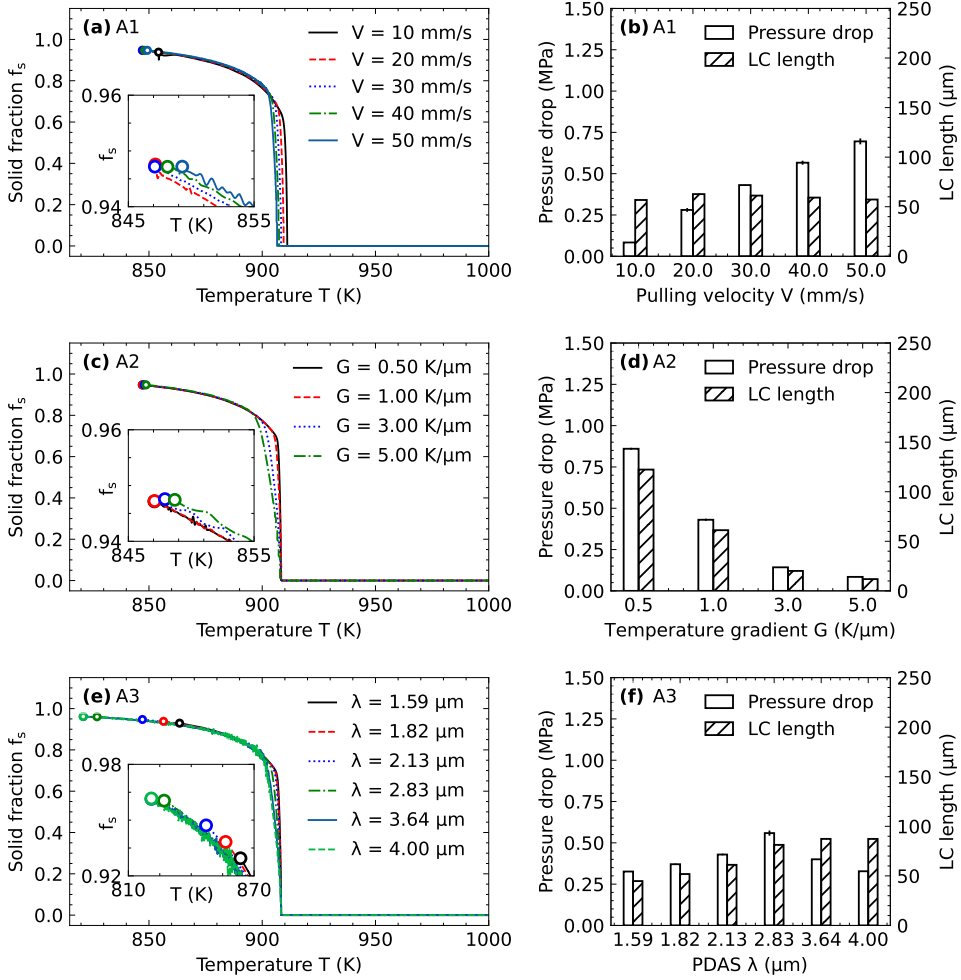
Figure 4.5: The relationship between the solid fraction f_s and the temperature T in the A1 (a), A2 (c) and A3 (e) simulations and the pressure drop and the LC length in the A1 (b), A2 (d) and A3 (f) simulations. The $f_s \sim T$ curves in the terminal solidification stage in the A1, A2 and A3 simulations are enlarged and embedded in (a), (c) and (e), respectively. The coalescence points are highlighted with unfilled circle.

The influence of the PDAS on SCS is studied in the A3 study. As shown in Figure 4.5 (e), the non-equilibrium stage starts at the same temperature but ends at different temperatures. This is because the width of the simulation domain is different, which means the time required for the diffusion layer to impinge and to obtain a homogeneous concentration profile in the liquid channel is different. In this case, the temperature at which the non-equilibrium stage ends is different. In a simulation with a larger PDAS, the non-equilibrium stage ends at a lower temperature. The different solidification behavior in the non-equilibrium stage does not have a significant influence on the $f_s \sim T$ curves in the equilibrium stage. The $f_s \sim T$ curves overlap with each other in the equilibrium stage. However, the liquid channels in the different A3 simulations close at different temperature. With a smaller PDAS, the critical liquid channel width for coalescence corresponds to a smaller solid fraction and thus coalescence occurs earlier. In this case, the LC length increases with increasing PDAS, leading to an increase in the pressure drop. Meanwhile, the PDAS also has an influence on the permeability of the liquid channel. With increasing PDAS, the permeability of the liquid channel increases, which tends to decrease the pressure drop. As a result of the combined effects of the LC length and the permeability, the SCS increases first and then decreases with increasing PDAS, as shown in Figure 4.5 (f).

In the A1-A3 studies, the dependency of the PDAS on the temperature gradient G and the pulling velocity V is neglected. To include this effect, A4 and A5 studies were performed to check the influence of the temperature gradient G and the pulling velocity V on SCS. The results from the A4 study are given in Figure 4.6 (a) and (b). With increasing pulling velocity, the PDAS decreases, which enhances the influence of the pulling velocity on the LC length. With increasing pulling velocity, the LC length decreases significantly, resulting in a potential decrease in the pressure drop. However, the shrinkage contribution due to solidification still dominates. As shown in Figure 4.6 (b), the pressure drop increases with increasing pulling velocity, representing an increase in SCS. Compared with the A1 study, consideration of the PDAS dependency on the pulling velocity V weakens the influence of the pulling velocity V on SCS.

In the A5 simulations, the temperature gradients and the PDAS are changed at the same time. In contrast to the A2 study, the non-equilibrium stage starts and ends at similar temperature in different A5 simulations, as shown in Figure 4.6 (c). In the A5 simulation with a larger temperature gradient, the PDAS is smaller and the time required to achieve a homogeneous concentration profile in the liquid channel is shorter. Meanwhile, a larger temperature gradient corresponds to a larger cooling rate. In this case, the influence of the temperature gradient on the required time and the cooling rate compensate each other, resulting in a similar temperature drop within the non-equilibrium stage. In the equilibrium stage, the simulation with a larger temperature gradient closes earlier due to the smaller PDAS. Thus, with increasing temperature gradient, the LC length decreases, leading to a decrease in the pressure drop and the SCS. Consideration of the PDAS dependency on the temperature gradient G strengthens the influence of the temperature gradient on the SCS.

4.3.3 Influence of G, V and PDAS on SCS with back diffusion

In previous section, the influence of G and V on SCS has been studied for the Al-4Cu (wt.%) alloy. The solid diffusion coefficient D_s is 3×10^{-13} m²/s, which essentially means the back diffusion is not considered. To study the influence of G and V on SCS for an alloy system
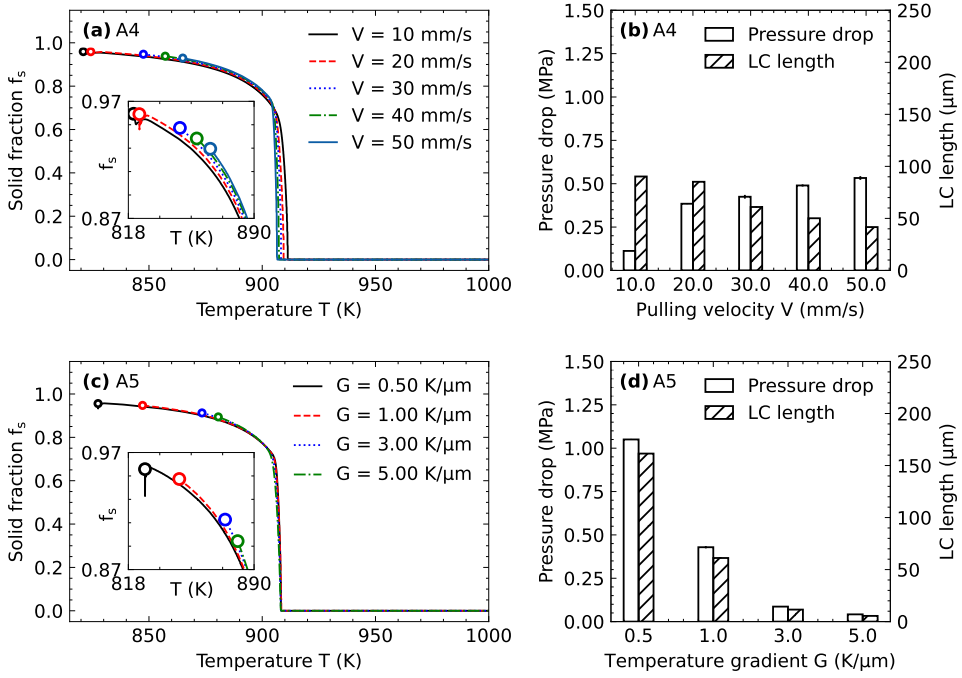
Figure 4.6: The relationship between the solid fraction f_s and the temperature T in the A4 (a) and A5 (c) simulations and the pressure drop and the LC length in the A4 (b) and A5 (d) simulations. The $f_s \sim T$ curves in the terminal solidification stage in the A4 and A5 simulations are enlarged and embedded in (a) and (c), respectively. The coalescence points are highlighted with unfilled circle.

with back diffusion, the solid diffusion coefficient D_s has been changed artificially from $3 \times 10^{-13}\,\mathrm{m^2/s}$ to $1 \times 10^{-9}\,\mathrm{m^2/s}$ and B1-B5 studies were then performed. The simulation conditions of B1-B5 studies are similar to the A1-A5 studies, as shown in Table 4.3. The PDAS values for the B3-B5 studies are redetermined with the directional solidification simulations with $D_s = 1 \times 10^{-9}\,\mathrm{m^2/s}$. After changing the solid diffusion coefficient, the PDAS changes slightly.

Table 4.3: Parameters in the B1-B5 studies with back diffusion ($D_s = 1 \times 10^{-9}\,\mathrm{m^2/s}$).

Study	V (mm/s)	G (K/µm)	PDAS (µm)
B1	10, 20, 30, 40 and 50	1.0	2.13
B2	30	0.5, 1.0, 3.0 and 5.0	2.13
B3	30	1.0	1.70, 1.96, 2.13, 2.83 and 3.64
B4	10, 20, 30, 40 and 50	1.0	Determined
B5	30	0.5, 1.0, 3.0 and 5.0	Determined

In the B1 simulations, different pulling velocities V were employed while keeping the PDAS and the temperature gradient G constant. As shown in Figure 4.7 (b), the pulling velocity has little influence on the LC length. In the B1 simulation with a larger pulling velocity, the required undercooling at the columnar tip is larger and thus the solidification starts at a lower temperature, as shown in Figure 4.7 (a). Meanwhile, a larger pulling velocity corresponds to a larger cooling rate and thus a shorter time for back diffusion. In this case, the liquid channel of the B1 simulation with a larger pulling velocity closes at a lower temperature. As a result of the combined effects, the LC length in the B1 simulations is similar. For the pressure drop calculation, similar to the A1 study, the shrinkage contribution dominates. Consequently, with increasing pulling velocity, the pressure drop and the SCS increase.

The influence of the temperature gradient G on SCS considering back diffusion is studied with the B2 simulations while keeping the PDAS constant. As the pulling velocity is constant, the solidification start temperatures of the different B2 simulations are similar, which is also similar to the A2 simulations. However, the coalescence temperature are different in the different B2 simulations. In the B2 simulations, a smaller temperature gradient corresponds to a longer time for back diffusion, which promotes solidification in the equilibrium stage. In this case, the B2 simulation with a smaller temperature gradient has a higher coalescence temperature, as shown in Figure 4.7 (c). With increasing temperature gradient, the liquid channel exists over a larger temperature range but for a shorter distance, as shown in Figure 4.7 (d). The decreased LC length leads to a smaller pressure drop and thus a smaller SCS.

The influence of the PDAS on SCS considering back diffusion is studies with B3 simulations. As shown in Figure 4.7 (e), the solidification start temperature in the simulations with different PDAS are similar, while the coalescence temperatures are different. The simulation with a smaller PDAS has a higher coalescence temperature. This is because the critical liquid channel width for coalescence corresponds to a smaller solid fraction in the simulation with a smaller PDAS. Thus, the coalescence in the simulation with a smaller PDAS occurs earlier. Moreover, the concentration gradient in the solid in the B3 simula-
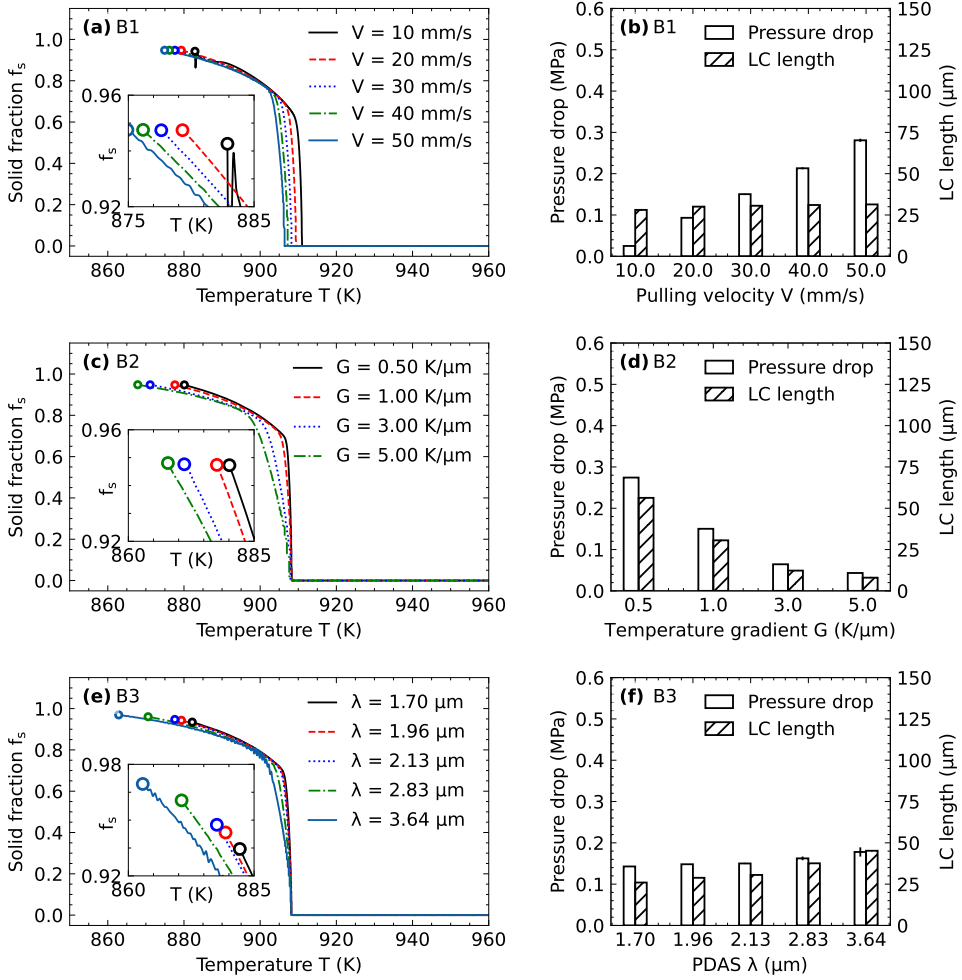
Figure 4.7: The relationship between the solid fraction f_s and the temperature T in the B1 (a), B2 (c) and B3 (e) simulations and the pressure drop and the LC length in the B1 (b), B2 (d) and B3 (f) simulations. The $f_s \sim T$ curves in the terminal solidification stage in the B1, B2 and B3 simulations are enlarged and embedded in (a), (c) and (e), respectively. The coalescence points are highlighted with unfilled circle.

tion with a smaller PDAS is larger, which promotes back diffusion and leads to an earlier coalescence. In this case, the LC length increases with increasing PDAS. For the tested PDAS values in the B3 simulations, the influence of the LC length on the pressure drop dominates, while the influence of the permeability on the pressure drop is not significant. With increasing PDAS, the pressure drop and the SCS increases.
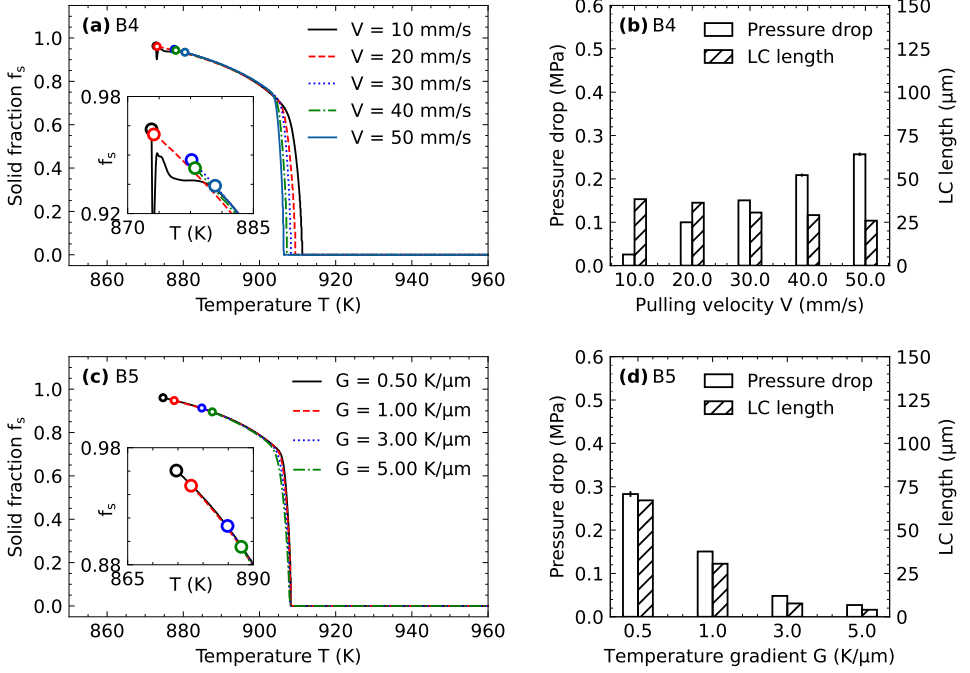

Figure 4.8: The relationship between the solid fraction f_s and the temperature T in the B4 (a) and B5 (c) simulations and the pressure drop and the LC length in the B4 (b) and B5 (d) simulations. The $f_s \sim T$ curves in the terminal solidification stage in the B4 and B5 simulations are enlarged and embedded in (a) and (c), respectively. The coalescence points are highlighted with unfilled circle.

In the B4 simulations, different pulling velocities V were employed, while the PDAS is determined with directional solidification considering back diffusion. Similar to B1 study, the solidification start temperature in the B4 study decreases with increasing pulling velocity. Nevertheless, the coalescence temperature increases with increasing pulling velocity. With increasing pulling velocity, the PDAS decreases, leading to an increase in the coalescence temperature. In this case, the LC length decreases with increasing pulling velocity, as shown in Figure 4.8 (b). Similar to the B1 and the A4 studies, the shrinkage contribution on the pressure drop dominates. With increasing pulling velocity, the pressure drop and the SCS increases. Consideration of the PDAS dependency on the pulling velocity weakens this effect.

The influence of the temperature gradient G on SCS considering back diffusion and the dependency of PDAS on G is studied with the B5 simulations. With increasing temperature gradient G, the PDAS and the LC length decreases. Similar to the B2 study, the decrease

in the LC length leads to a decrease in the pressure drop and thus a decrease in the SCS, as shown in Figure 4.8 (c) and (d). Compared with the B2 study, the consideration of the PDAS dependency on the temperature gradient enhances the influence of the temperature gradient on the pressure drop and the SCS.

4.4 Discussion

4.4.1 Comparison with Scheil-Gulliver calculations

Consider a liquid channel in an equilibrium stage. The liquid channel can be divided into multiple thin layers with their normal parallel to the liquid channel. In each layer, the liquid concentration profile is homogeneous due to the small channel width. The governing equation for the concentration c_i of the liquid channel layer i without back diffusion is

$$\frac{\partial c_i}{\partial t} = D^l \frac{\partial^2 c_i}{\partial y^2} + \frac{c^l - c^s}{1 - f_s} \frac{\partial f_s}{\partial t}, \tag{4.20}$$

where y is the axis along the liquid channel direction, and f_s the solid fraction, which is equal to the ratio between the liquid channel width and the PDAS. The liquid concentration c_i of layer i is equal to the equilibrium liquid concentration c_i^{eq}, which is given by

$$c_i = c_i^{eq} = c_0 + (T_i - T_0)/m, \tag{4.21}$$

where T_i is the temperature of the layer i. In this chapter, a linearized phase diagram is employed in the current simulation. As the temperature is linear in the y direction, the concentration profile is also linear in the y direction, which means $\frac{\partial^2 c_i}{\partial y^2} = 0$. It this case, Equation (4.20) can be written as

$$\frac{\partial c_i}{\partial t} = \frac{c^l - c^s}{1 - f_s} \frac{\partial f_s}{\partial t}, \tag{4.22}$$

$$dc_i = \frac{c^l - c^s}{1 - f_s} df_s, \tag{4.23}$$

which is actually the Scheil-Gulliver equation [43]. Segregation within the liquid channel follows this equation in the condition that the concentration profile within each liquid channel layer is homogeneous.

The Scheil-Gulliver equation can be employed to explain the solidification behaviors in the A1 study. Assuming the non-equilibrium stage starts and ends at the same temperature, the solid fraction and the liquid concentration at the end of the non-equilibrium stage can be determined with a lever rule, which gives different solute enrichment in the liquid. The solidification start temperature under different pulling velocities can be determined from the A1 study. Then, solidification in the equilibrium solidification stage is simulated by integrating Equation (4.23) from the end of the non-equilibrium stage to the coalescence point. Here, it is assumed that coalescence occurs when $f_s = 0.947$ based on the phase field simulations in A1 study. The calculated $f_s \sim T$ curves and the pressure drop under different pulling velocities are given in Figure 4.9 (a) and (b), respectively. With increasing pulling velocity, the non-equilibrium stage occurs at a lower temperature, resulting in less solute

enrichment in the liquid and thus earlier coalescence. In this case, with increasing pulling velocity, the LC length decreases, while the pressure drop increases due to the dominant effect of the shrinkage contribution, which agrees with the findings from the A1 study. The findings from the A2 study can also be reproduced in the same way. Nevertheless, the calculated pressure drop from the modified Scheil-Gulliver calculations is larger than that from the phase field simulations. The reason is that the Scheil-Gulliver equation tends to overestimate the segregation within the liquid channel in the equilibrium stage and the coalescence temperature in the modified Scheil-Gulliver calculations is lower than that in the phase field simulations.
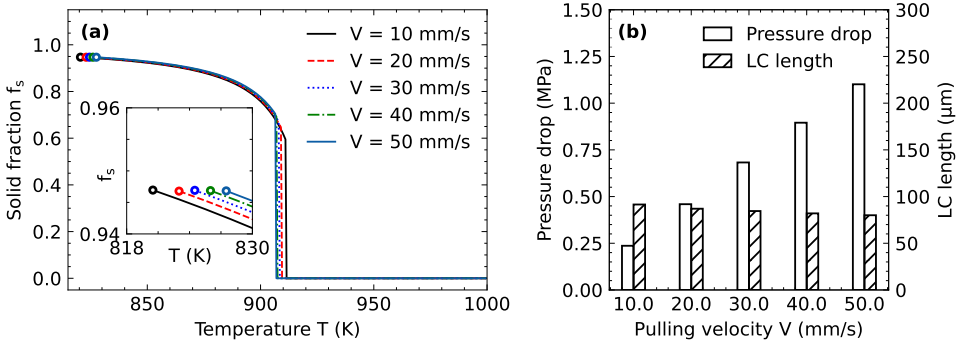
Figure 4.9: The relationship between the solid fraction f_s and the temperature (a) and the pressured drop (b) from the modified Scheil-Gulliver calculations under different pulling velocities. The non-equilibrium solidification stage is approximated with a lever rule, while the equilibrium solidification stage is governed by the Scheil-Gulliver equation (Equation (4.23)).

Following the Scheil-Gulliver equation, the derivative of the solid fraction with respect to the temperature is written as

$$\frac{\mathrm{d}f_s}{\mathrm{d}T} = \frac{1}{m}\frac{\mathrm{d}f_s}{\mathrm{d}c^l} = \frac{1-f_s}{m(c^l - c^s)}. \tag{4.24}$$

The derivative of the solid fraction with respect to the temperature $\mathrm{d}f_s/\mathrm{d}T$ in the A1 simulation with $V = 20.0\,\mathrm{mm/s}$ is calculated with a central difference method and compared with Scheil-Gulliver calculation (Equation (4.24)), as shown in Figure 4.10 (a). The absolute value of the $\mathrm{d}f_s/\mathrm{d}T$ calculated with a central difference method is larger than the Scheil-Gulliver calculation, especially at the temperature around 907 K, which corresponds to the non-equilibrium stage. As temperature drops, this difference becomes smaller but does exist. This means that the solidification in the equilibrium stage is faster than the Scheil-Gulliver calculation. The reason is that the assumption of a homogeneous concentration profile at the same temperature within the liquid channel is not completely valid.

The concentration within the liquid channel can be considered as the sum of the equilibrium liquid concentration $c^{l,eq}$ and the deviation from the equilibrium liquid concentration $c^l - c^{l,eq}$. The equilibrium liquid concentration $c^{l,eq}$ changes linearly in the direction of the liquid channel due to the constant temperature gradient, while the deviation part $c^l - c^{l,eq}$ varies due to the limited diffusivity in the liquid. The profiles of $c^l - c^{l,eq}$ in the direction
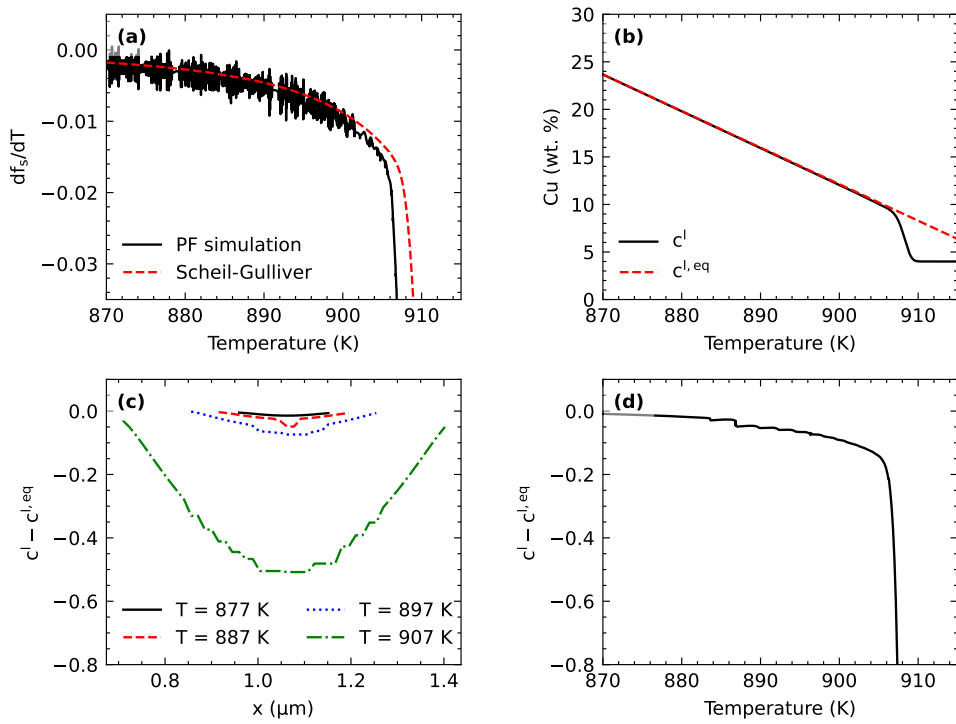
Figure 4.10: The derivative of the solid fraction with respect to the temperature $\mathrm{d}f_s / \mathrm{d}T$ calculated with a central difference and with the Scheil-Gulliver equation (a), the liquid concentration c^l in the center of the liquid channel (b), the concentration deviation $c^l - c^{l,eq}$ in the direction perpendicular to the liquid channel (c) and in the direction parallel to the liquid channel (d) in the A1 simulation with $V = 20.0\,\mathrm{mm/s}$.

perpendicular to the liquid channel at different temperatures in the A1 simulation with $V = 20.0$ mm/s are given in Figure 4.10 (c), while $c^l - c^{l,eq}$ in the center of the liquid channel in the direction parallel to the liquid channel is given in Figure 4.10 (d). As shown in Figure 4.10 (c), in the direction perpendicular to the liquid channel, at 907 K, the deviation $c^l - c^{l,eq}$ follows a valley shape as the diffusion layers from the opposite interfaces impinge in the center of the liquid channel. As the temperature drops, the width of the liquid channel decreases, which is more favorable to homogenize the concentration within the liquid channel. In this case, the concentration valley becomes more flat and the concentration in the center of the liquid channel becomes closer to the equilibrium liquid concentration, as shown in Figure 4.10 (d). Note the profile of the deviation value $c^l - c^{l,eq}$ in the direction parallel to the liquid channel is nonlinear. This means the diffusion term in Equation (4.20) is not equal to zero, which promotes solidification in the liquid channel. In this case, the solidification rate in the phase field simulation is faster than the Scheil-Gulliver calculation.

The deviation of the liquid concentration from the equilibrium liquid concentration in the liquid channel exists through a large temperature range. In this case, the term "equilibrium stage" can only be an approximation. In the case of the finite diffusivity in the liquid, a deviation always exists in the center of the liquid channel. With decreasing temperature, the deviation becomes smaller until the liquid channel closes or the machine accuracy is reached. In this case, an error exists when using the term "equilibrium stage" or the Scheil-Gulliver equation.

In summary, the influence of the pulling velocity and the temperature gradient can be qualitatively predicted with the Scheil-Gulliver calculation and the RDG model, while the phase field simulations provide more accurate predictions of the segregation and the pressure drop values. In addition, the phase field simulations are advantageous in simulating the coalescence behavior under different solidification conditions.

4.4.2 Correlation with the process parameters

In this chapter, the influence of the pulling velocity and the temperature gradient on SCS have been considered with a phase field method. However, the pulling velocity and the temperature gradient are only meaningful in the directional solidification case, which is basically at a micro-scale level.

In welding or additive manufacturing, the process is controlled with the power and the scanning velocity. A normal way to study the influence of scanning velocity on SCS is to change the scanning velocity while keeping the ratio between the power and the scanning velocity constant. As reported in the literature [11, 12], increasing scanning velocity tends to increase SCS. With increasing scanning velocity and a constant ratio between the power and the scanning velocity, the pulling velocity increases, while the temperature gradient in the tail of the melt pool decreases [7]. Based on results of the current work, increasing pulling velocity or decreasing the temperature gradient increases the pressure drop and SCS. In this case, the experiment results agrees with the findings in the current work.

Moreover, it has been reported that grain refinement in the melt pool decreases SCS [6]. Traditionally, it is explained that the grain refinement increases the number of liquid channels in the mushy zone, which partition the strain rate. In this case, the effective strain rate for each liquid channel is smaller, leading to a smaller SCS. The findings from this chapter show that with decreasing PDAS, the coalescence of the liquid channel occurs

earlier, while the permeability of the liquid channel is decreased. For small PDAS values, the influence of the earlier coalescence dominates, leading to a decrease in SCS with decreasing PDAS, which agrees with the effects of the grain refinement in the experiments.

In summary, the findings from the current work agree with welding experimental results. However, quantitative prediction of SCS under different process parameters is still a challenging task, since the current approach does not include all the possible parameters. First, the RDG model does not include the strain partitioning between the solid and the liquid. Upon tensile loading, the liquid tends to have a larger deformation rate than the solid, as the liquid is weaker than the solid [44]. Besides, the mechanical condition in the mushy zone is influenced by the process parameters. In some studies [7], increasing the scanning velocity changes the stress state in the mushy zone of the weld pool tail from tensile to compressional, thus hindering crack formation. Moreover, the fluid flow in the melt pool can have an influence on the PDAS [45] and the liquid feeding in the mush zone. However, as indicated in the A4 and A5 studies, the change in the PDAS may influence the pressure drop value but does not change the tendency of the SCS. Furthermore, the influence of the grain morphology on SCS is not considered. It is found [13] that the transition from directional microstructure to equiaxed microstructure suppresses cracking.

4.5 Conclusions

In this chapter, phase field simulations have been employed to study the influence of the temperature gradient and the pulling velocity on the primary dendrite arm spacing (PDAS), micro-segregation and solidification cracking susceptibility (SCS) in a directional solidification condition. The following conclusion can be drawn.

For the studied pulling velocity range, the PDAS (λ) is controlled by the cooling rate $\dot{T}$, while the dependency of the PDAS on the temperature gradient G is weak ($\lambda \propto G^{0.01}\dot{T}^{-0.41}$). Changing the solid diffusion coefficient has little influence on the relationship between PDAS and G and V.

For an alloy with negligible back diffusion, increasing the pulling velocity or decreasing the temperature gradient increases the pressure drop from the dendrite tip to the coalescence point, resulting in an increase in SCS. With decreasing PDAS, the permeability of the liquid channel decreases, which makes the liquid feeding more difficult and favors an increase in the pressure drop. Meanwhile, the liquid channel coalescence occurs earlier, leading to a smaller pressure drop. For the tested PDAS values, with decreasing PDAS, the pressure drop and the SCS first increases and then decreases. Moreover, considering the dependency of the PDAS on V weakens the influence of the pulling velocity V on SCS, while considering the dependency of the PDAS on G enlarges the influence of the temperature gradient G on SCS.

Consideration of back diffusion does not change the influence of the pulling velocity V and the temperature gradient G on SCS. For an alloy with strong back diffusion, increasing the pulling velocity V or decreasing the temperature gradient G increases the SCS. This effect remains when the dependency of the PDAS on G and V is considered.

In the solidification simulation for an alloy with negligible back diffusion, the evolution of the segregation and the solid fraction in the liquid channel can be approximated by the Scheil-Gulliver equation. The mismatch between the phase field simulation and the

Scheil-Gulliver calculation comes from the nonlinear part of the concentration profile in the center of the liquid channel due to the finite diffusivity in the liquid.

The temperature gradient G and the pulling velocity V changes at the same time when changing the process parameters like power and scanning velocity. Quantitative predictions of the SCS under different process parameters therefore remains challenging.

References

[1] Xiaohui Liang, Cornelis Bos, Marcel Hermans, and Ian Richardson. Influence of the temperature gradient and the pulling velocity on solidification cracking susceptibility during welding: A phase field study. *Materials & Design*, 235:112424, 2023.

[2] Gautam Agarwal, A Kumar, IM Richardson, and MJM Hermans. Evaluation of so-lidification cracking susceptibility during laser welding in advanced high strength automotive steels. *Materials & Design*, 183:108104, 2019.

[3] He Gao, Gautam Agarwal, Muru Amirthalingam, MJM Hermans, and IM Richardson. Investigation on hot cracking during laser welding by means of experimental and numerical methods. *Welding in the World*, 62:71–78, 2018.

[4] Holden Hyer, Le Zhou, Abhishek Mehta, Sharon Park, Thinh Huynh, Shutao Song, Yuanli Bai, Kyu Cho, Brandon McWilliams, and Yongho Sohn. Composition-dependent solidification cracking of aluminum-silicon alloys during laser powder bed fusion. *Acta Materialia*, 208:116698, 2021.

[5] Paraskevas Kontis, Edouard Chauvet, Zirong Peng, Junyang He, Alisson Kwiatkowski da Silva, Dierk Raabe, Catherine Tassin, Jean-Jacques Blandin, Stéphane Abed, Rémy Dendievel, et al. Atomic-scale grain boundary engineering to overcome hot-cracking in additively-manufactured superalloys. *Acta Materialia*, 177:209–221, 2019.

[6] Mathieu Opprecht, Jean-Paul Garandet, Guilhem Roux, Camille Flament, and Mathieu Soulier. A solution to the hot cracking problem for aluminium alloys manufactured by laser beam melting. *Acta Materialia*, 197:40–53, 2020.

[7] Nicolas Coniglio and CE Cross. Effect of weld travel speed on solidification cracking behavior. part 1: weld metal characteristics. *The International Journal of Advanced Manufacturing Technology*, 107:5011–5023, 2020.

[8] Nicolas Coniglio and CE Cross. Effect of weld travel speed on solidification cracking behavior. part 2: testing conditions and metrics. *The International Journal of Advanced Manufacturing Technology*, 107:5025–5038, 2020.

[9] A Slyvinsky, H Herold, and M Streitenberger. Influence of welding speed on the hot cracking resistance of the nickel-base alloy nicr25fealy during tig-welding. *Hot Cracking Phenomena in Welds*, 1:42, 2005.

[10] Gautam Agarwal, He Gao, Murugaiyan Amirthalingam, and Marcel Hermans. Study of solidification cracking susceptibility during laser welding in an advanced high strength automotive steel. *Metals*, 8(9):673, 2018.

[11] Aurélie Niel, Frédéric Deschaux-Beaume, Cyril Bordreuil, Gilles Fras, and J-M Drezet. Hot tearing test for tig welding of aluminum alloys: application of a stress parallel to the fusion line. *Hot cracking phenomena in welds III*, pages 43–58, 2011.

[12] GM Goodwin. The effects of heat input and weld process on hot cracking in stainless steel. *Weld J*, 67(4):88s–94s, 1988.

[13] Philipp Schempp, CE Cross, Andreas Pittner, Gabriele Oder, R Saliwan Neumann, Heidemarie Rooch, Ilona Dörfel, Werner Österle, and Michael Rethmeier. Solidification of gta aluminum weld metal: Part 1—grain morphology dependent upon alloy composition and grain refiner content. *Weld. J*, 93(2):53s–59s, 2014.

[14] Sindo Kou. A criterion for cracking during solidification. *Acta Materialia*, 88:366–374, 2015.

[15] Sindo Kou. Predicting susceptibility to solidification cracking and liquation cracking by calphad. *Metals*, 11(9):1442, 2021.

[16] WI Pumphrey and JV Lyons. Cracking during the casting and welding of the more common binary aluminium alloys. *Journal of the Institute of Metals*, 74(9):439, 1948.

[17] M Rappaz, J-M Drezet, and Met Gremaud. A new hot-tearing criterion. *Metallurgical and materials transactions A*, 30(2):449–455, 1999.

[18] Lei Wang, Nan Wang, and Nikolas Provatas. Liquid channel segregation and morphology and their relation with hot cracking susceptibility during columnar growth in binary alloys. *Acta Materialia*, 126:302–312, 2017.

[19] Shaoning Geng, Ping Jiang, Xinyu Shao, Gaoyang Mi, Han Wu, Yuewei Ai, Chunming Wang, Chu Han, Rong Chen, Wei Liu, et al. Effects of back-diffusion on solidification cracking susceptibility of al-mg alloys during welding: A phase-field study. *Acta Materialia*, 160:85–96, 2018.

[20] Shaoning Geng, Ping Jiang, Xinyu Shao, Gaoyang Mi, Han Wu, Yuewei Ai, Chunming Wang, Chu Han, Rong Chen, and Wei Liu. Comparison of solidification cracking susceptibility between al-mg and al-cu alloys during welding: A phase-field study. *Scripta Materialia*, 150:120–124, 2018.

[21] Ping Jiang, Shaoning Geng, Xinyu Shao, Gaoyang Mi, Chunming Wang, Han Wu, Chu Han, and Song Gao. Fine grains reduce cracking susceptibility during solidification: insights from phase-field simulations. *JOM*, 71:3223–3229, 2019.

[22] Tongzhao Gong, Yun Chen, Shanshan Li, Yanfei Cao, Dianzhong Li, Xing-Qiu Chen, Guillaume Reinhart, and Henri Nguyen-Thi. Revisiting dynamics and models of microsegregation during polycrystalline solidification of binary alloy. *Journal of Materials Science & Technology*, 74:155–167, 2021.

[23] Dongxu Chen, Junsheng Wang, and Chi Zhang. Coupling phase-field model and cfd for hot cracking predictions of al-li alloys. *Computational Materials Science*, 192:110361, 2021.

[24] Chu Han, Ping Jiang, Shaoning Geng, Song Gao, Gaoyang Mi, and Chunming Wang. Multiphase-field simulation of grain coalescence behavior and its effects on solidification cracking susceptibility during welding of al-cu alloys. *Materials & Design*, 211:110146, 2021.

[25] Laishan Yang, Jing Yang, Fang Han, Zhihang Zhang, Qinghua Li, Zhibo Dong, Lei Wang, Nana Ofori-Opoku, and Nikolas Provatas. Hot cracking susceptibility prediction from quantitative multi-phase field simulations with grain boundary effects. *Acta Materialia*, 250:118821, 2023.

[26] Zhongji Sun, Xipeng Tan, Chengcheng Wang, Marion Descoins, Dominique Mangelinck, Shu Beng Tor, Eric A Jägle, Stefan Zaefferer, and Dierk Raabe. Reducing hot tearing by grain boundary segregation engineering in additive manufacturing: example of an alxcocrfeni high-entropy alloy. *Acta Materialia*, 204:116505, 2021.

[27] Nadia Kouraytem, Po-Ju Chiang, Runbo Jiang, Christopher Kantzos, Joseph Pauza, Ross Cunningham, Ziheng Wu, Guannan Tang, Niranjan Parab, Cang Zhao, et al. Solidification crack propagation and morphology dependence on processing parameters in aa6061 from ultra-high-speed x-ray visualization. *Additive Manufacturing*, 42:101959, 2021.

[28] Chunzhi Xia and Sindo Kou. Calculating the susceptibility of carbon steels to solidification cracking during welding. *Metallurgical and Materials Transactions B*, 52:460–469, 2021.

[29] Julia Kundin and Ingo Steinbach. Comparative study of different anisotropy and potential formulations of phase-field models for dendritic solidification. *Computational Materials Science*, 170:109197, 2019.

[30] Karl Glasner. Nonlinear preconditioning for diffuse interfaces. *Journal of Computational Physics*, 174(2):695–711, 2001.

[31] J Eiken, B Böttger, and I Steinbach. Multiphase-field approach for multicomponent alloys with extrapolation scheme for numerical application. *Physical review E*, 73(6):066122, 2006.

[32] Ingo Steinbach. Phase-field models in materials science. *Modelling and simulation in materials science and engineering*, 17(7):073001, 2009.

[33] Alain Karma and Wouter-Jan Rappel. Quantitative phase-field modeling of dendritic growth in two and three dimensions. *Physical review E*, 57(4):4323, 1998.

[34] Seong Gyoon Kim. A phase-field model with antitrapping current for multicomponent alloys with arbitrary thermodynamic properties. *Acta Materialia*, 55(13):4391–4399, 2007.

[35] James A Warren and William J Boettinger. Prediction of dendritic growth and microsegregation patterns in a binary alloy using the phase-field method. *Acta Metallurgica et Materialia*, 43(2):689–703, 1995.

[36] Tong Zhao Gong, Yun Chen, Yan Fei Cao, Xiu Hong Kang, and Dian Zhong Li. Fast simulations of a large number of crystals growth in centimeter-scale during alloy solidification via nonlinearly preconditioned quantitative phase-field formula. *Computational Materials Science*, 147:338–352, 2018.

[37] Lazaro Beltran-Sanchez and Doru M Stefanescu. A quantitative dendrite growth model and analysis of stability concepts. *Metallurgical and Materials Transactions A*, 35:2471–2485, 2004.

[38] Julia Kundin, Ali Ramazani, Ulrich Prahl, and Christian Haase. Microstructure evolution of binary and multicomponent manganese steels during selective laser melting: phase-field modeling and experimental validation. *Metallurgical and Materials Transactions A*, 50(4):2022–2040, 2019.

[39] Zhijun Wang, Junjie Li, Jincheng Wang, and Yaohe Zhou. Phase field modeling the selection mechanism of primary dendritic spacing in directional solidification. *Acta Materialia*, 60(5):1957–1964, 2012.

[40] Doru M Stefanescu and Roxana Ruxanda. Fundamentals of solidification. *Materials Park, OH: ASM International, 2004.*, pages 71–92, 2004.

[41] GK Bouse and JR Mihalisin. Metallurgy of investment cast superalloy components. *Superalloys, supercomposites and superceramics*, pages 99–148, 1989.

[42] W Kurz and R Trivedi. Rapid solidification processing and microstructure formation. *Materials Science and Engineering: A*, 179:46–51, 1994.

[43] Erich Scheil. Bemerkungen zur schichtkristallbildung. *International Journal of Materials Research*, 34(3):70–72, 1942.

[44] HR Zareie Rajani and AB Phillion. 3-d multi-scale modeling of deformation within the weld mushy zone. *Materials & Design*, 94:536–545, 2016.

[45] Boyang Chen, Qingyu Zhang, Dongke Sun, and Zhijun Wang. Effects of shear flows on columnar dendritic microstructure during rapid solidification of in718 alloy: A cellular automaton-lattice boltzmann modeling study. *Journal of Crystal Growth*, 585:126583, 2022.

4

5

CELLULAR AUTOMATA SOLIDIFICATION MODELLING FOR ADDITIVE MANUFACTURING

In previous chapters, dendrite formation has been simulated with a cellular automata model and a phase field model, which calculate the solidification growth velocity based on numerically solved concentration profiles and thus are computationally expensive. In cases where concentration profiles are not required, analytical models (Lipton-Glicksman-Kurz or Kurz-Giovanola-Trivedi) can be employed to calculate growth velocity in cellular automata (CA) models, which accelerates the solidification simulation. These kinds of CA models are called CAFE models, as such CA models are always coupled with a finite element (FE) model, which calculates the temperature profiles. Here, a CAFE model which is around 280 times faster than traditional CAFE models, is proposed. By adopting an exact temporal integration and a multi-level capture algorithm, a large time step can be employed without impacting the simulation accuracy. The proposed model is validated with a 316L steel sample and three NiTi samples, produced by additive manufacturing. A good agreement is achieved between the simulations and the experiments. The findings reveal that during additive manufacturing, temperature gradients in neighboring laser passes select the preferential orientations, leading to different texture components. By manipulating melt pool geometry, customized crystallographic textures can be achieved in additively manufactured components. With a significant reduction in computational cost while maintaining accuracy, this approach marks a crucial step towards a practical implementation of a digital twin for additive manufacturing.

5.1 Introduction

For metallic materials, whether they are structural or functional, grain morphology and texture play vital roles in shaping properties. These microstructure features hold great significance as they allow for the customization and optimization of various material characteristics. By carefully manipulating the grain morphology and texture, scientists and engineers can effectively enhance properties such as strength [1], conductivity [2], magnetism [3], energy storage [4] and conversion [5], and super-elasticity [6], among other attractive properties.

Laser powder bed fusion (L-PBF) is often adopted for the additive manufacturing (AM) of metallic components [7], offering the opportunity to control microstructural features including grain morphologies and texture [8, 9]. Traditionally, building AM components with desirable microstructural features is achieved by trial-and-error, which is costly and time consuming [10]. Recently, digital twins of additive manufacturing (AM) have drawn particular attention [11–13], as they eliminate the need for numerous trial-and-error tests and thus shorten the path of AM product development. With advanced monitoring techniques [7, 14], thermal profiles can be monitored and controlled, which are essential for microstructure development. However, in-situ monitoring of microstructure is still not achievable; reliance must therefore be placed on model predictions . Cellular automata finite element (CAFE) models have been successfully used to predict microstructure evolution during casting [15, 16], welding [17] and additive manufacturing [18–22]. However, due to the high computational cost of three-dimensional simulations, integration of microstructure predictions into the digital twin framework is still challenging.

Efforts have been made to accelerate three-dimensional CAFE simulations. A common practice is to parallelize the calculation and distribute the computational loads to multiple processors. In most CAFE models [15, 17, 19, 22], the parallelism is achieved with distributed memory due to the high memory requirement. Each processor has its own private memory, which contains the data of a small part in the simulation domain. The private memory of each processor is not directly accessible to the other processors. Accessing data in the private memory of other processors is achieved by communication between different processors, which is time-consuming. Moreover, balancing the loads among all the processors is not a trivial task. Lian et al. [23] distribute the CAFE cells evenly over all the processors with a static decomposition method. However, in a CAFE simulation for additive manufacturing, most computation tasks occur near the melt pool. As the laser moves, the computationally intensive region moves. With a static decomposition method, the computational loads are not evenly distributed over the processors. In the model of Carozzani et al. [15], a coarse mesh is employed, where the elements are only activated and assigned to a processor when they are close to the melt pool. With this dynamic decomposition method, the computation loads are evenly distributed. Teferra and Rowenhorst [22] further optimized the CAFE model by first collecting the computational tasks from the whole simulation domain and then distributing the tasks evenly over all the processors. However, this method increases the time required for communication between the different processors. An AM simulation may take 2 to 3 days to finish [22]. Rolchigo [24] proposed a sparse temperature-time data format based on the final time when a cell solidifies and achieved an acceleration in the AM simulation by reducing the computation tasks. However, the sparse temperature-time data format leads to inaccurate calculations

in regions where the material solidifies and remelts several times. Despite so many improvements in accelerating CAFE simulations, a three-dimensional CAFE simulation still requires a long computation time [22] or a high computation power [24], which makes those models unsuitable for high-throughput numerical tests or as a building block in a digital twin framework for AM.

In this chapter, a computationally effective CAFE model is described, which reduces the computation time from days to minutes. The efficiency comes from two major optimizations. Firstly, the new CAFE model employs a time step which is around 20 times larger than that in traditional CAFE models. Traditional CAFE models employ a Euler forward method for temporal integration and require a small time step to minimize the truncation error and avoid a multi-capture problem, while the new CAFE model eliminates the temporal truncation error with an exact integration and solves the multi-capture problem with a multi-level capture algorithm, enabling the usage of a large time step. Secondly, after reducing the memory requirement through the optimization in memory usage and a subdomain activation and deactivation method on a regular coarse mesh, the new CAFE model is parallelized with shared memory, which achieves a balance between the computation loads of all the processors. The proposed CAFE model is verified in directional solidification simulations and shows an independency on the time step size. Subsequently, the new CAFE model is validated with a 316L AM case and three NiTi AM samples, manufactured under different conditions and having different textures. The new CAFE model produces fast and accurate predictions for the grain morphology and the texture of different AM samples. Furthermore, a discussion is provided on the mechanisms of texture formation and texture control during additive manufacturing.

5.2 METHODS

5.2.1 MODEL BASICS

In the current multi-grid CAFE model, the simulation domain is discretized into a number of rectangular cuboids, which are called subdomains. Each subdomain has a unique subdomain index and variables including the activation status (active or inactive), the phase status (solid, liquid or mushy) and the temperature at the cuboid vertices. Each subdomain is further discretized into cubic cells referenced with a local cell index. Each cell has variables including grain ID, phase status (solid, liquid and interface) and the temperature at the cell center at the start and the end of the CAFE time step. With the multi-grid setup, a CAFE cell can be uniquely identified with the combination of a subdomain index and a local cell index, which is called the cell ID in this work. Each interface cell also has additional variables related to growth. A subdomain is mushy if it includes at least one interface cell, while a solid or liquid subdomain contains only solid or liquid cells, respectively.

5.2.2 THE TEMPERATURE CALCULATION

To simulate solidification during additive manufacturing, temperature profiles are necessary inputs for the CAFE model, which can be obtained through various methods including computational fluid dynamics models, finite element models and analytical thermal models. Although analytical thermal models are less accurate due to the use of constant material properties and failure to explicitly incorporate convection and radiation, they have the

best computational efficiency and thus are employed in the current CAFE model.

In this work, the analytical model proposed by Schwalbach et al. [25] is employed to calculate the temperature profiles around the melt pool. In the model of Schwalbach et al., the moving heat source is approximated by a set of discrete heat sources, each of which lasts for a short time. The temperature T at a point with coordinates (x, y, z) at time t is given by [25]

$$T = T_0 + \sum_{i=1}^{n} \frac{\eta P \Delta t_T}{\pi^{1.5} \rho c_p \sqrt{2\lambda_{xi}\lambda_{yi}\lambda_{zi}}} \exp\left[-\frac{(x - x_i)^2}{2\lambda_{xi}} - \frac{(y - y_i)^2}{2\lambda_{yi}} - \frac{(z - z_i)^2}{2\lambda_{zi}} \right] \qquad (5.1)$$

with

$$\lambda_{qi} = \sigma_{qi}^2 + 2\alpha(t - \tau_i), \quad q = x, y, z, \qquad (5.2)$$

where T_0 is the ambient temperature, η the absorption efficiency, P the power, ρ the density, c_p the specific heat, α the thermal diffusivity and n the number of the considered discrete heat sources. σ_{xi}, σ_{yi} and σ_{zi} are the dimensions of the ith discrete heat source in the x, y and z directions, while x_i, y_i and z_i are the coordinates of the ith discrete heat source center. The ith heat source is activated at time τ_i and lasts for a short time period Δt_T, which is given by [25]

$$\Delta t_T = \frac{\sigma_x}{v_s}, \qquad (5.3)$$

where v_s is the scanning velocity of the laser beam. Only the discrete heat sources which satisfy $\tau_i > t - t_{cut}$ are considered in Equation (5.1), where t is the current time and t_{cut} the cutoff time given by [25]

$$t_{cut} = \frac{\eta P \Delta t_T}{2\sqrt{2}\pi^{1.5}\rho c_p \alpha}. \qquad (5.4)$$

In previous works [22, 25], the discrete heat sources are activated at fixed time points throughout the simulation. However, this may introduce fluctuations in the temperature profile, leading to solidification-remelting in the front of the melt pool. To remove this spurious effect and to keep a stable melt pool shape throughout the simulation, the activation time τ_i of the ith discrete heat source is determined based on current time t

$$\tau_i = t - i\Delta t_T. \qquad (5.5)$$

During additive manufacturing, the laser beam moves back and forth following the scanning pattern of the current layer. In the current CAFE model, a scan pattern is generated by calculating the heat source locations at different time points based on the hatching distance h_d and the scanning direction. At the boundary of the scan pattern, the discrete heat sources in one pass may influence the temperature profile in the next pass, leading to an enlarged melt pool. To remove this boundary effect and to simulate the texture evolution in the center of the additively manufactured component, a padding distance is applied at the beginning and the end of each pass. In additive manufacturing experiments, the scanning direction may rotate after finishing one layer, which is also considered in the current CAFE model.

5.2.3 The growth algorithm

Following the decentered growth algorithm proposed by Gandin and Rappaz [16], each interface cell is associated with a growth octahedron with its diagonals parallel with the preferential growth direction, namely the $\langle 100 \rangle$ crystallographic direction in a cubic crystal system. The half diagonal of the growth octahedron is called growth length l and is updated in each CAFE time step with

$$\Delta l = l_2 - l_1 = \int_{t_1}^{t_2} v_g(\Delta T) \mathrm{d}t, \tag{5.6}$$

where v_g is the growth velocity, l_1 and l_2 the growth length at the start and the end of the CAFE time step, t_1 and t_2 the time at the start and the end of the CAFE time step.

The growth velocity is determined with the KGT (Kurz-Giovanola-Trivedi) model [26], which describes directional growth at a high growth rate. In the current CA model, an approximated solution [22, 27, 28] of the KGT model is employed, which gives the growth velocity v_g as a function of undercooling $\Delta T = T_l - T$,

$$v_g(\Delta T) = a\Delta T^{2.5}, \tag{5.7}$$

with

$$a = \frac{D_l}{5.51\pi^2(-m_l(1-k)c_0)^{1.5}\Gamma}, \tag{5.8}$$

and

$$\Delta T = T_l - T, \tag{5.9}$$

where D_l is the diffusion coefficient in the liquid, m_l the slope of the liquidus line, k the partitioning coefficient, Γ the Gibbs Thomson coefficient, c_0 the nominal concentration, T_l the liquidus temperature and T the temperature of the considered interface cell.

In traditional CAFE models, the growth length change Δl in each time step is estimated with

$$\Delta l = v_g \Delta t, \tag{5.10}$$

where Δt is the time step. This may lead to a discretization error, especially in conditions with a high cooling rate. In the current CAFE model, the growth length is updated in each time step by calculating the integral in Equation (5.6) directly. Combining Equations 5.6, 5.7 and 5.12 gives

$$\Delta l = \int_{t_1}^{t_2} a[T_l - T(t)]^{2.5} \mathrm{d}t. \tag{5.11}$$

With a linear interpolation, the temperature $T(t)$ of the considered interface cell at time t can be written as

$$T(t) = T_1 + \frac{t - t_1}{t_2 - t_1}(T_2 - T_1), \tag{5.12}$$

where T_1 and T_2 are the temperature at the start and the end of the time step. In this case, the integral in Equation (5.11) can be evaluated numerically with the antiderivative function or the Gaussian quadrature rule. A higher order temperature interpolation may be employed here to improve accuracy. However, as the CAFE time step is very small, linear interpolation is enough for solidification simulation.

With increasing time, the growth octahedron of the considered interface cell becomes larger and captures neighboring liquid cells in the Moore neighborhood. For each neighboring liquid cell, a critical growth length l_{crit} for capture is calculated. If the growth length of the consider interface cell reaches the critical growth length l_{crit}, the corresponding liquid cell is then captured and transform into a new interface cell. The capture time t_{cap} is calculated by solving

$$l_1 + \int_{t_1}^{t_{cap}} a\left[T_l - T(t)\right]^{2.5} \mathrm{d}t = l_{crit}. \tag{5.13}$$

After a liquid cell is transformed, a new growth octahedron is formed in the newly transformed interface cell inheriting the orientation of the parent growth octahedron. The center and the initial growth length of the new growth octahedron are determined by truncating the parent growth octahedron with the algorithm described in [16]. Note the calculation of the new growth octahedron is based on the parent octahedron at the time t_{cap}, instead of the parent octahedron at the end of the time increment t_2. After the liquid cell transforms into a new interface cell, the change in the growth length between the capture time t_{cap} and the end of the time step t_2 is calculated with

$$\Delta l = \int_{t_{cap}}^{t_2} v_g(\Delta T)\mathrm{d}t. \tag{5.14}$$

If all the neighboring cells in the Moore neighborhood are interface cells or solid cells, the considered interface cells then transform into solid cells.

5.2.4 Nucleation

In the current CAFE model, homogeneous nucleation inside the undercooled melt is considered. The distribution function of the nucleation density n_n with respect to undercooling ΔT is given by a Gaussian distribution [21, 29]

$$\frac{\mathrm{d}n_n}{\mathrm{d}\Delta T} = \frac{N_0}{\Delta T_\sigma \sqrt{2\pi}} \exp\left[-\frac{\Delta T - \Delta T_m}{2\Delta T_\sigma^2}\right], \tag{5.15}$$

where N_0 is the maximum nucleation density, ΔT_m the mean nucleation undercooling and ΔT_σ the standard deviation for the nucleation undercooling. In the beginning of the CAFE simulations, CAFE cells are randomly selected as potential nucleation sites [23]. The number of potential nucleation sites n_{sites} is calculated by

$$n_{sites} = \frac{N_0 V}{\Delta x^3}, \tag{5.16}$$

where V is the volume of the simulation domain. Each potential nucleation site is assigned with a critical nucleation undercooling ΔT_{crit}, following the Gaussian distribution described by Equation (5.15). In each CAFE time step, nucleation checks are performed for undercooled liquid cells. If the considered liquid cell is a potential nucleation site and has an undercooling larger than ΔT_{crit}, nucleation will be triggered. With linear interpolation of the temperature, the exact nucleation time t_n is given by

$$t_n = t_1 + \frac{(T_l - \Delta T_{crit}) - T_1}{t_2 - t_1}. \tag{5.17}$$

After nucleation, the liquid cell transforms into a new interface cell with a randomly generated orientation. If this occurs in a liquid subdomain, the phase status of the subdomain will change from liquid to mushy.

5.2.5 Time step

The time step Δt is calculated based on the ratio between the cell size Δx and the scanning velocity v_s

$$\Delta t = \xi \frac{\Delta x}{v_s}. \tag{5.18}$$

In traditional CAFE models, small ξ values including 0.024 [30], 0.04 [31], 0.1 [32], 0.2 [33] are employed to minimize the truncation error introduced by Equation (5.10) and avoid a multi-capture problem. In the current CAFE model, the growth length of each interface cell is calculated through direct integration, which reduces the discretization error. Moreover, the capture of liquid cells and the nucleation events occur at specific time points. In this case, the earliest event which transforms a cell from liquid to interface wins the competition, which then avoids the issues with the multi-capture events. In theory, a large time step can be used in the current CAFE model, which reduces the total computational cost.

However, another problem needs to be solved in order to employ a large time step ($\xi > 0.2$). In a CAFE time step, after the newly captured liquid cells transform into interface cells, they can further capture their liquid neighbors in the same time step, even with $\xi < 1.0$. Therefore, a multi-level capture algorithm is proposed to solve this issue, which is described in next section.

5.2.6 The multi-level capture algorithm

In a CA time step, existing interface cells may capture their liquid neighbors in the Moore neighborhood at different time points. After capture, newly transformed interface cells can continue to grow and capture their liquid neighbors. For clarity, the interface cells which exist at the start of the time step are defined as level 0, while the interface cells captured by interface cells in level i are defined as level $i + 1$. Capture trees can be constructed by denoting the interface cells and the neighboring cells they captured with nodes and connecting the parent nodes with their child nodes, as shown in Figure 5.1.

In a large CA time step, a liquid cell near the solid-liquid interface could possibly be captured by multiple interface cells at different levels. Consequently, the considered liquid cell may be related to multiple capture nodes at different levels in the capture tree. The status of the considered liquid cell should be determined by the node with the shortest capture time, which does not necessarily have the smallest level number. To find the node with the shortest capture time for the considered liquid cell, it is necessary to calculate all possible capture nodes related to the considered cell. The same is true for other liquid cells near the solid-liquid interface.

To find the earliest capture node for each liquid cell near the solid-liquid interface, a direct algorithm is computing all the possible nodes within the capture trees. This can be done by performing capture checks for each newly transformed interface cell in its Moore neighborhood until no new interface cells are captured. However, this is computationally expensive. Assuming each interface cell captures 10 liquid neighbors, the time complexity

of this algorithm is $\Theta(n_0 10^{n_l-1})$, where n_0 is the number of interface cells in generation 0 and n_l the number of levels. As the time step increases, the number of levels increases linearly and the computational cost increases exponentially.
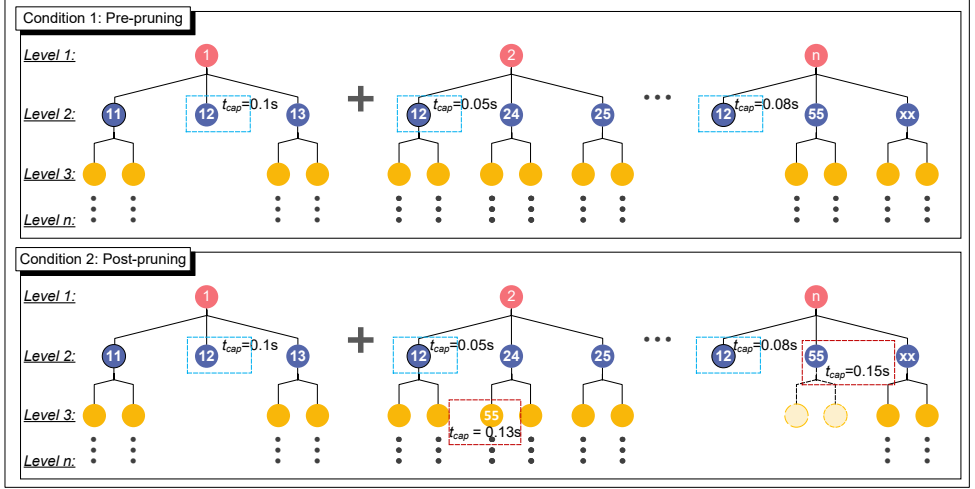

Figure 5.1: A schematic illustration of the pruning conditions in the multi-level capture algorithm. Capture trees are constructed by denoting the interface cells and the neighboring cells they captured with nodes and connecting the parent nodes with their child nodes. To reduce the computational tasks, two kinds of pruning conditions are given here. Pre-pruning: if multiple nodes in the same level are related the same cell (cell index), only the node with the smallest capture time is allowed to have child nodes; Post-pruning: if a node has a capture time smaller than a node in a older level and they have the same cell index, then the node in the older level is invalid and its child nodes are removed.

To reduce the computational cost, a multi-level capture algorithm is employed, which computes the capture trees level by level and pruning is performed to reduce the computational tasks. Consider nodes at a level i. Pre-pruning is performed based on capture time and cell index of nodes in level i. A schematic illustration of the pruning conditions is shown in Figure 5.1. If two or more nodes in level i correspond to the same liquid cell, only the node with shortest capture time is allowed to have child nodes. The capture time comparison is also performed between the nodes at level i and the nodes in previous levels. If the considered node at level i is later than any node in previous layers and they are related to the same cell, then the considered node at level i is not allowed to have child nodes, which is considered as pre-pruning. If the considered node at level i is earlier than a node at a level j ($j < i$) and they are related to the same liquid cell, then the node at level j is invalid. If the invalid node at level j has descendants, then its descendant nodes are also invalid and will be removed from the capture trees. This operation is called post-pruning as pruning is performed after the calculation of the descendant of the invalid nodes. The level-by-level iterations continue until no new liquid cells are captured. The complexity level for this algorithm is approximately $\Theta(26n_0 n_l)$ if we assume the number of nodes in each layer is similar. The pseudocode of the multi-level capture algorithm is given in Algorithm 1.

Algorithm 1: The multi-level capture algorithm.

```
 1  N₀ ;                              // set of interface cells at the beginning of the time step
 2  Nc ← N₀ ;                                         // set of valid capture nodes in current level
 3  Nv ← {} ;                            // set of valid capture nodes in current and previous levels
 4  /* Iterate until there are no nodes in current level                            */
 5  while Nc ≠ ∅ do
 6      Nn ← {} ;                                     // set of valid capture nodes in next level
 7      Ni ← {} ;                                      // set of invalid capture nodes in Nv
 8      /* Add nodes in current level into Nv                                        */
 9      Nv ← Nv ∪ Nc;
10      /* Pre-pruning                                                               */
11      Nc ← {the capture node with the shortest capture time for each captured cell in Nc};
12      /* Loop over all valid nodes in current level to get nodes in next level     */
13      foreach nc ∈ Nc do
14          /* The corresponding interface cell cc                                   */
15          cc ← the interface cell related to nc
16          /* Update growth length l of cell cc                                     */
17          Update growth length l of cell cc;
18          /* Check all neighboring cells in the neighborhood of cell cc            */
19          Cnb ← {cnb|cnb is a cell in the Moore neighborhood of the cell cc};
20          foreach cnb ∈ Cnb do
21              /* Check if cnb is captured by cc                                    */
22              lcrit ← the critical growth length to capture cnb;
23              if cnb is not Liquid or l ≤ lcrit then
24                  continue;
25              /* Calculate the capture time tcap for cnb                           */
26              tcap ← the capture time for cnb;
27              /* Check if cnb is captured in current or previous level             */
28              Nnb,v ← {nv|nv is related to cnb and nv ∈ Nv};
29              if Nnb,v ≠ ∅ then
30                  nnb,v ← the node with the shortest capture time in Nnb,v;
31                  if tcap > capture time of nnb,v then
32                      /* Collect invalid node in Nv and save it into Ni            */
33                      Ni ∪ {nnb,v} ;
34                  else
35                      /* Pre-pruning by ignore this capture event safely           */
36                      continue;
37              /* Collect the new capture node for the next level                   */
38              Nn ∪ {the new capture node related to cnb} ;
39      /* Post-pruning by remove invalid nodes in Nv and Nc                         */
40      Nc ← Nc − Nc ∩ Ni;
41      Nv ← Nv − Nv ∩ Ni;
42      /* Update nodes in current level                                             */
43      Nc ← Nn;
44  Update interface cells based on Nv for next time step;
```

5.2.7 Parallelism and memory management

In this work, the simulation is parallelized with Open MP (multiprocessing) in a shared memory environment. The simulation data is saved in a shared memory space which is accessible for all the processors, which is useful to balance the loads between all the processors. However, the memory size is usually limited by the available memory in a single machine. In this case, saving the data of all the cells in the simulation domain is not possible, as a simulation domain may include hundreds of millions of cells. In this case, efforts have been made to reduce the memory requirement of the solidification simulation.

To reduce the memory requirement and to accelerate the simulation, the subdomains are activated or deactivated based on the temperature at their vertices and their phase status. The criteria for activation and deactivation of the subdomains are given below.

- Rule A: a subdomain is always inactive if is not deposited yet.

- Rule B: an inactive subdomain is activated if the temperature of any of its vertices is between $T_l - \Delta T_l$ and $T_l + \Delta T_l$.

- Rule C: an active subdomain is deactivated if the temperature of all of its vertices are above $T_l + \Delta T_l$.

- Rule D: an active solid subdomain is deactivated if the temperature of all of its vertices are below $T_l - \Delta T_l$ and all the neighboring subdomains are solid.

With Rule A-D, the subdomains near the melt pool are active, while the liquid subdomains in the melt pool center and the solid subdomains far from the melt pool are inactive. When a subdomain is deactivated, the grain IDs of the cells in the deactivated subdomain are saved on the hard disk in a HDF5[34] file. The data of cells in the deactivated subdomains will then be cleared from the memory and the cells in the deactivated subdomains will not be considered for solidification simulation until the subdomain is re-activated. When a subdomain is activated, the grain IDs of its cells will be loaded from the hard disk.

The data storage is optimized to increase computational efficiency. In each active subdomain, the cells data is saved in vectors, which ensures a contiguous memory allocation and thus a good caching performance when looping over all the cells. The data of the interface cells is saved within a free list which allows dynamic memory allocation.

Load balancing is easier to achieve in a shared memory environment than in a distributed memory environment. As mentioned earlier, all the processors in a shared memory environment can directly access all the data in the memory. In this case, the computational tasks can be equally assigned to all the processors without a large overhead.

5.2.8 The overall algorithm

The overall algorithm for the current CAFE solidification model is Algorithm 2. The simulation domain is first initialized with a random Voronoi tessellation. Then, the simulation proceeds with a constant time step Δt. In each time step, the temperature at the vertices of all subdomains are firstly updated. Then, the program iterates over each subdomain and performs activation or deactivation based on Rule A-D. After that, the temperature of the cells in the active subdomains is updated. Interface cells which melt are then removed from the free list. Then, the program loops over each undercooled liquid cell to check if

nucleation is triggered. Subsequently, the program updates the growth length and captures new interface cells with the decentered growth algorithm and the multi-level capture algorithm. New interface cells will be added into the free list for interface cells. The interface cells which do not have liquid neighbors are removed from the free list.

Algorithm 2: The overall algorithm for the CAFE solidification model.

---
1   Initialize the simulation domain with Voronoi tessellation;
2   $t \leftarrow 0$;
3   $\Delta t \leftarrow \xi \frac{\Delta x}{v_s}$;
4   **while** $t < t_{end}$ **do**
5   Update temperature at the vertices of all subdomains;
6   Activate or deactivate the subdomains;
7   Update temperature for cells in the active subdomains;
8   Remove interface cells which melt;
9   Check nucleation for each undercooled liquid cell;
10   Update growth length for each interface cell and perform capture check;
11   Add new interface cells;
12   Remove interface cells which transform into solid;
13     $t = t + \Delta t$;
14   Check if deposit a new layer in the simulation domain;

5.2.9 Material properties

In this work, additive manufacturing simulations are performed for two different materials, namely a 316L steel and a Ni-Ti alloy. The parameters for velocity calculation of the 316L steel are taken from the work of Teferra and Rowenhorst [22], while the parameters for velocity calculation of the Ni-Ti alloy are obtained from Thermo-Calc. To match the dilute solution approximation for Equation (5.7), the Ni-Ti alloy (49.4 wt%) is considered as a binary system (NiTi-Ni) with Ni (1.2 wt%) dissolved in NiTi. The parameters for the 316L steel and the transformed parameters for the NiTi-Ni system are given in Table 5.1.

Table 5.1: Material properties of a 316L steel [22] and a NiTi alloy.

Symbol	Description	Value for 316L	Value for NiTi
c_0	The nominal concentration	4.85 wt%	1.2 at% (NiTi-Ni)
k	The partitioning coefficient	0.48	0.50 (NiTi-Ni)
m_l	The slope of the liquidus line	$-10.9 \, \mathrm{K/wt\%}$	$-7.70 \, \mathrm{K/at\%}$ (NiTi-Ni)
D_l	The diffusion coefficient in the liquid	$3 \times 10^{-9} \, \mathrm{m^2/s}$	$3 \times 10^{-9} \, \mathrm{m^2/s}$
Γ	The Gibbs Thomson coefficient	$1 \times 10^{-7} \, \mathrm{K \cdot m}$	$2 \times 10^{-7} \, \mathrm{K \cdot m}$
ρ	The density	$8000 \, \mathrm{kg/m^3}$	$6450 \, \mathrm{kg/m^3}$
κ	The thermal conductivity	$18 \, \mathrm{W/(m \cdot K)}$	$30 \, \mathrm{W/(m \cdot K)}$
c_p	The specific heat	$500 \, \mathrm{J/(kg \cdot K)}$	$489 \, \mathrm{J/(kg \cdot K)}$
T_l	The liquidus temperature	$1609 \, \mathrm{K}$	$1583 \, \mathrm{K}$

5.3 Results

5.3.1 Influence of the time step size

To verify the independency of the proposed model on the time step size, different time steps ($\xi = 0.05$, 0.5, 1.0, 1.5, 2.0) have been employed to simulate a directional solidification case. The simulation is performed in a $400 \times 400 \times 400\,\mu m^3$ domain with a cell size of $1.0\,\mu m$. The bottom is initialized with a Voronoi microstructure. A temperature gradient of 1.0×10^6 K/m is applied in the z direction. As the simulation domain cools at a rate of 5.0×10^5 K/s, directional solidification occurs. The fully solidified microstructure in the two simulations with $\xi = 0.05$ and $\xi = 2.0$ are given in Figure 5.2. The microstructure in the simulations with $\xi = 0.05$ and $\xi = 2.0$ are similar to each other in the XY-plane and YZ-plane. This indicates the time step size has little influence on the simulation result. With increasing ξ, the time step size increases and the number of time steps to finish the simulation decreases, leading to a decrease in the computational time. However, with increasing time step size, the number of captured interface cells increases, which increases the computational cost for each time step. In this case, the total computation time first decrease and then increase with increasing ξ. The minimum computation time is obtained with $\xi = 1.0$ for the directional solidification case.
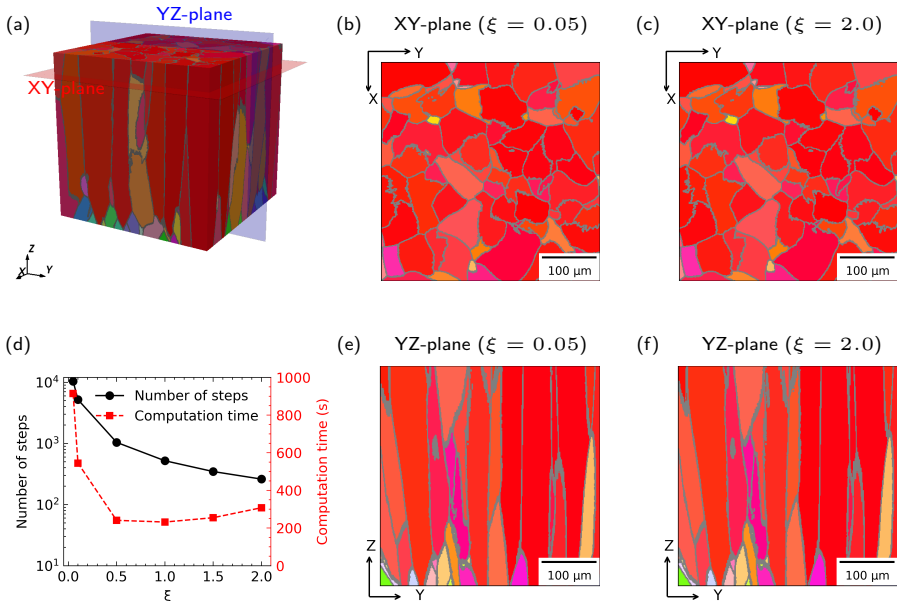
Figure 5.2: The results of directional solidification simulations: 3D view (a), grain morphology in XY-plane in simulations with $\xi = 0.05$ (b) and $\xi = 2.0$ (c), grain morphology in YZ-plane in simulations with $\xi = 0.05$ (e) and $\xi = 2.0$ (f). The number of steps and the simulation time are given with respect to ξ (d).

5.3.2 Model validation with a 316L steel sample

The current model is validated by simulating the microstructure of a 316L component with a $\{110\}\langle001\rangle$ Goss texture, which was reported in the work of Andreau et al. [35]. The simulation is performed in a $720 \times 720 \times 570\,\mu m^3$ domain with a cell size of $1.5\,\mu m$. The simulation parameters are given in Table 5.2. The initial microstructure is generated with a Voronoi tessellation. In the simulation, the scanning direction (SD) is parallel or anti-parallel with the X+ direction, while the building direction (BD) is in the Z+ axis. The simulation results are given in Figure 5.3. The color is determined as the inverse pole figure (IPF) color in the Z+ direction. For a better illustration, two slices are made in the XY-plane and YZ-plane which are perpendicular to the Z axis and the X axis, respectively. The simulated microstructure in the YZ-plane (BD-TD) (Figure 5.3 (c)) agrees with the microstructure (Figure 5.3 (f)) from the experiments. The green grains dominate in the boundary of the melt pool as a result of the orientation selection effect of the neighboring laser passes. In the center of the melt pool, the temperature gradient is parallel with the Z axis, leading to the formation of the red grains. In addition, some yellow grains and purple grains are observed in the simulation, which are also found in the experiment. The orientation distribution (Figure 5.3 (d)) from the simulation matches with the experimental orientation distribution (Figure 5.3 (e)), which is close to the $\{110\}\langle001\rangle$ Goss texture.

Table 5.2: Parameters for the CAFE simulation of the 316L sample.

Parameter	316L sample
Laser power P (W)	175
Absorption efficiency η	0.509
Scanning velocity v_s (m/s)	0.5
Laser shape parameter σ (μm)	50.0
Laser shape parameter σ_z (μm)	33.5
Hatch distance h_d (μm)	140.0
Layer thickness l_t (μm)	30.0
Maximum nucleation density N_0 ($\times10^{14}\,m^{-3}$)	5.0
Mean nucleation undercooling ΔT_m (K)	60
Deviation of nucleation undercooling ΔT_σ (K)	30
Melt pool width (μm)	190
Melt pool height (μm)	80

With the current CAFE model, the simulation for the 316L sample with a $\{110\}\langle001\rangle$ Goss texture takes 31 minutes with 64 AMD EPYC 7452 cores at 2.35 GHz. Teferra and Rowenhorst [22] simulated the same sample with a $400 \times 400 \times 300$ grid taking 65 hours with 144 Intel Xeon Platinum 8168 cores at 2.7 GHz. In this case, the current CAFE model is around 280 times faster, even though a finer grid ($480 \times 480 \times 380$ grid) is employed in the simulations. This acceleration comes from three sources. First, a larger time step is used in the current CAFE model, which is safely achieved due to the implementation of the integration calculation of the growth length and the multi-level capture algorithm. Secondly, the implementation of the subdomain activation and deactivation method, which limits the calculation to the active region near the melt pool boundary. The use of the
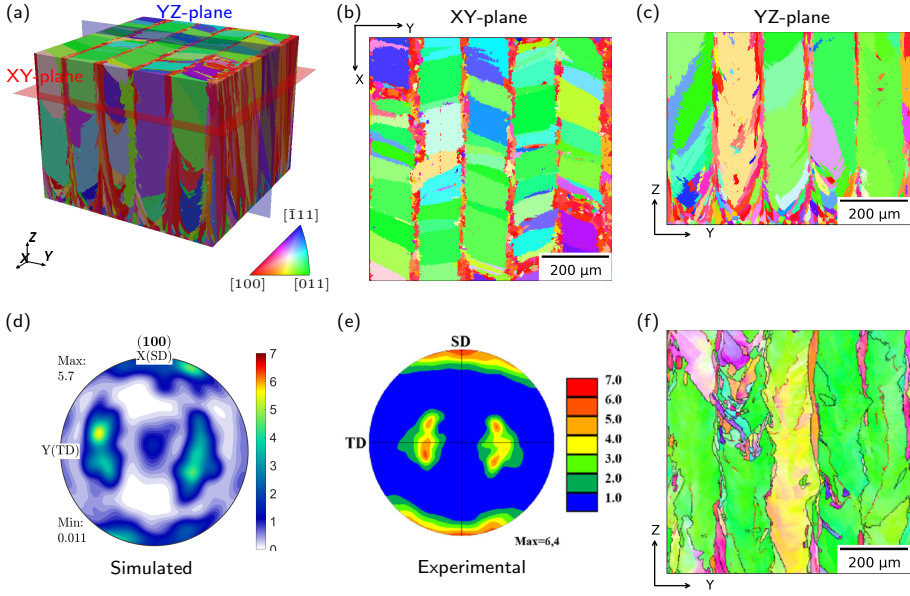
Figure 5.3: The simulated microstructure of the 316L sample with a $\{110\}\langle001\rangle$ Goss texture in 3D view (a), XY-plane (b) and YZ-plane (c) and the simulated pole figure (d). The experimental pole figure (e) and the microstructure in the BD-TD plane (f) are from the work of Andreau et al. [35].

subdomains also reduces the computational cost of locating the cells in the active region. Thirdly, the parallelism is achieved with a shared memory method. In this case, time-consuming communication between different processors is avoided and the computation loads can be evenly redistributed over all the processors.

5.3.3 Model validation with NiTi samples

The current model is further validated by simulating the microstructure of additively manufactured NiTi samples (sample-A, sample-B and sample-C, corresponding to low, medium and high laser powers, respectively). The process parameters can be found in Table 5.3. To avoid cracking, the scanning direction is rotated by 67 degrees when depositing a new layer. Different process conditions lead to different melt pool shapes and thus different microstructures. The melt pool shapes are measured in the experiments and then fitted with the analytical thermal model by tuning the absorption efficiency and the shape parameters of the heat source. Other parameters including density, thermal conductivity, the specific heat and the nucleation parameters are constant for all the simulations. In both the simulations and the experiments, a coordinate system is defined based on the building direction and the sample geometry. The Z axis is parallel with the build direction, while the X and Y axes are perpendicular to the building direction. Note the X axis does not represent the scanning direction, as the scanning direction rotates by 67 degrees for each new layer.

EBSD measurements are performed in the XY-plane and the YZ-plane of the additively manufactured samples. Due to experimental error introduced during sample preparation, the measured XY-plane might not be exactly perpendicular to the building direction. The EBSD measurement for the XY-plane might include microstructure in more than one layer, since the layer thickness is very small (30 μm or 40 μm). For comparison, slices are made from the simulated three-dimensional microstructure in the XY-plane and YZ-plane. At the beginning of the simulations, three or four layers are deposited to make sure the bottom of the melt pool does not go beyond the simulation domain. This leads to the appearance of a random microstructure in the bottom of the YZ-plane of the simulations. However, it disappears quickly after a few layers and has little influence on the dominant texture.

Table 5.3: Parameters for CAFE simulations of NiTi samples.

Parameter	sample-A	sample-B	sample-C
Laser power P (W)	250	400	950
Absorption efficiency η	0.829	0.847	0.631
Scanning velocity v_s (m/s)	1.25	1.2	0.65
Laser shape parameter σ (μm)	40.0	60.0	30.0
Laser shape parameter σ_z (μm)	76.4	80.0	44.5
Hatch distance h_d (μm)	120.0	120.0	180.0
Layer thickness l_t (μm)	30.0	30.0	40.0
Maximum nucleation density N_0 ($\times 10^{14}\,\mathrm{m}^{-3}$)	5.0	5.0	5.0
Mean nucleation undercooling ΔT_m (K)	60	60	60
Deviation of nucleation undercooling ΔT_σ (K)	30	30	30
Melt pool width (μm)	160	234	600
Melt pool height (μm)	120	139	120

The microstructure of sample-A (low laser power) is simulated with a domain of $800 \times 800 \times 810\,\mu\mathrm{m}^3$ and a cell size of 1.0 μm. The simulated and the experimental microstructure and pole figures are given in Figure 5.4. In sample-A, the grains are randomly oriented in both the simulation and the experiment. This is because the preferential orientation changes as the scanning direction rotates by 67 degrees when a new layer is deposited. A grain which grows preferentially in one layer may lose the growth competition after a few layers. Before it disappears, the considered grain may last a few layers. This explains why some large grains are observed in the YZ-plane in both simulation (Figure 5.4 (c)) and the experiment (Figure 5.4 (f)). In the XY-plane of the simulation (Figure 5.4 (b)), the microstructure is characterized by large polygonal grains, which are surrounded by several small columnar grains. The small columnar grains form a ring around the polygon. Some polygons may include two or more grains. The edges of the polygon are parallel or perpendicular to the scanning direction. With the scanning direction rotating by 67 degrees for each new layer, a polygon shape is thus formed. The feature of large polygonal grains surrounded by smaller grains can also be found in the XY-plane of the experiment, as shown in Figure 5.4 (e). Note the measured XY-plane (Figure 5.4 (e)) may include several deposition layers due to experimental limitations, which might be the reason why some densely stacked columnar grains are observed in Figure 5.4 (e). In the simulated pole figure

Figure 5.4 (g), a global maxima is observed along the Z axis and multiple local maximum points are observed in other directions, while the maximum points in the experimental pole figure (Figure 5.4 (h)) are more randomly distributed. This mismatch might be caused by the error in melt pool shape estimation. However, the maximum intensity in the simulation is around 1.8, which indicates that sample-A has a very weak texture. This value is also close to the maximum intensity in the experiment pole figure. In this case, the simulation is in acceptable agreement with the experimental results.
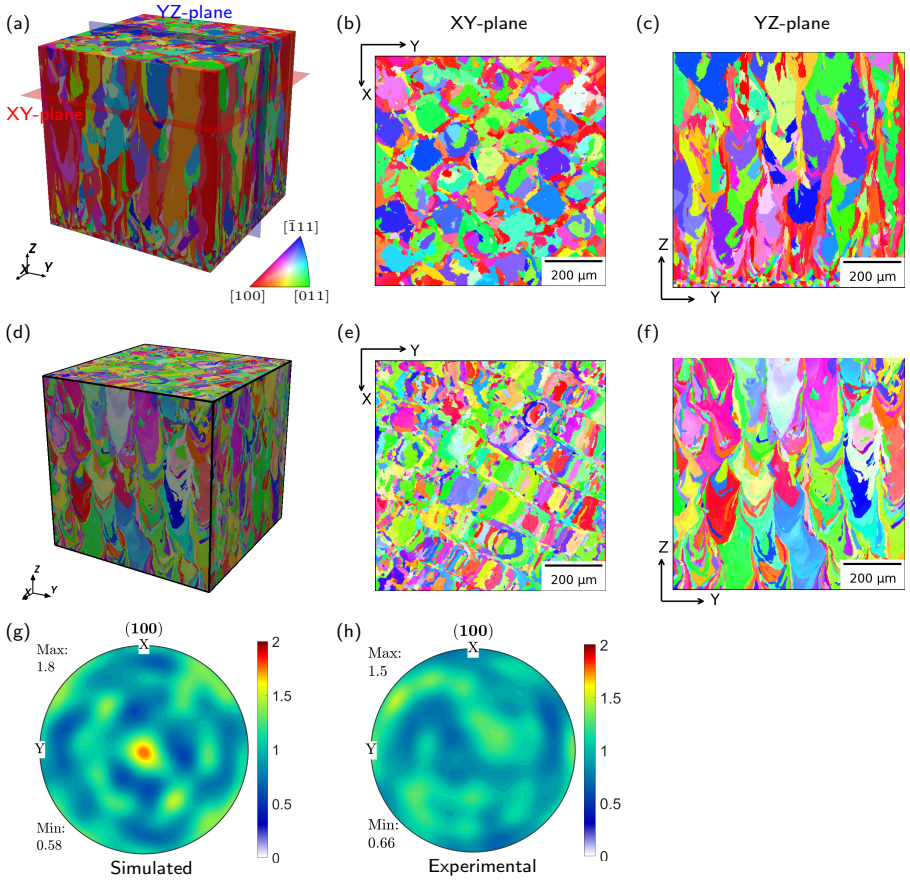
Figure 5.4: The simulated microstructure of the NiTi sample-A in 3D view (a), XY-plane (b) and YZ-plane (c) and the simulated pole figure (g). The experimental microstructure in pseudo-3D view (d), the XY-plane (e) and the YZ-plane (f) and the experimental pole figure (h).

Similar to the simulation of sample-A, the microstructure of sample-B (intermediate laser power) is simulated with a domain of $800 \times 800 \times 810\,\mu m^3$ and a cell size of $1.0\,\mu m$. The simulated microstructure, as well as the experimental microstructure, is presented in Figure 5.5 for comparison. Unlike sample-A, the microstructure of sample-B is dominated

by red grains, with one of their ⟨100⟩ crystallographic directions parallel with the Z axis. In the XY-plane in the simulation (Figure 5.5 (b)), grains with distinct colors including blue, purple and green scatter in the red grain matrix. This agrees with the experimental observation in Figure 5.5 (e). In the YZ-plane (Figure 5.5 (c)), those scattered grains with different colors propagate along the build direction (Z axis) as stripes, extending over a few layers. Similar stripe-shaped grains with different colors can be identified in the YZ-plane of the experiment, as shown in Figure 5.5 (f). For red grains in sample-B, one of their ⟨100⟩ crystallographic directions is parallel with the Z axis, while the other two ⟨100⟩ crystallographic directions are oriented randomly. This leads to a ⟨100⟩ fiber texture, as shown in Figure 5.5 (g). A similar ⟨100⟩ fiber texture is also observed in the experimental pole figure.
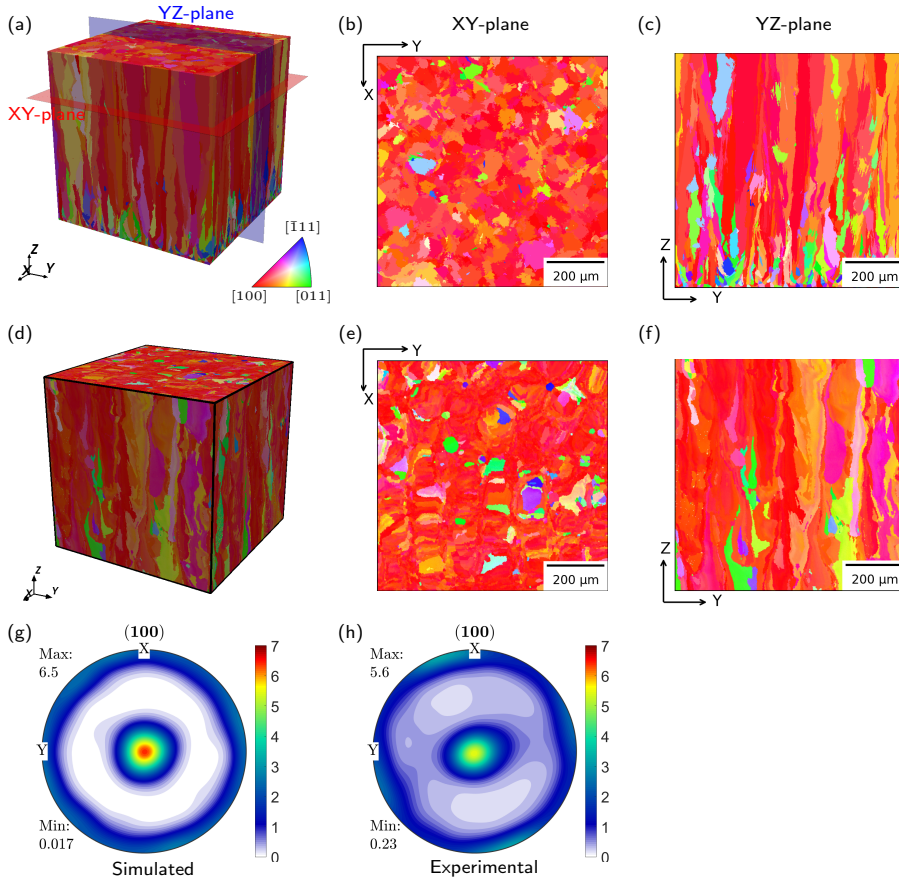
Figure 5.5: The simulated microstructure of the NiTi sample-B in 3D view (a), XY-plane (b) and YZ-plane (c) and the simulated pole figure (g). The experimental microstructure in pseudo-3D view (d), the XY-plane (e) and the YZ-plane (f) and the experimental pole figure (h).
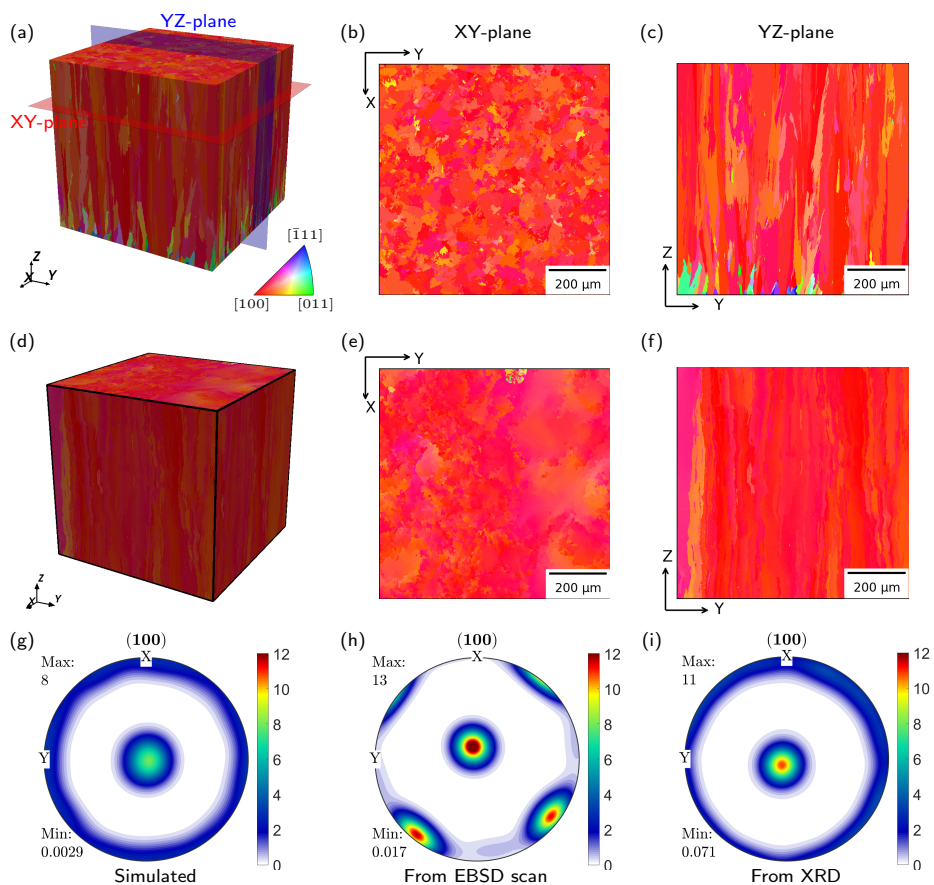
Figure 5.6: The simulated microstructure of the NiTi sample-B in 3D view (a), XY-plane (b) and YZ-plane (c) and the simulated pole figure (g). The experimental microstructure in pseudo-3D view (d), the XY-plane (e) and the YZ-plane (f) and the experimental pole figure from EBSD scan (h) and XRD (i).

In the simulation for sample-C (high laser power), a domain size of $800 \times 800 \times 800\,\mu m^3$ and a cell size of $1.0\,\mu m$ are employed. The results from the simulation and the experiment are given in Figure 5.6. Similar to the microstructure of sample-B, red grains dominate in the microstructure of the simulation and the experiment. In the XY-plane of the simulation (Figure 5.6 (b)), the microstructure is composed of red, purple and fuchsia grains. Compared to the sample-B, the fraction of the red grains in sample-C is larger and the orientation of the non-red grains (orange and fuchsia) are more close to the red grain. This agrees with the experimental result in Figure 5.6 (e). In the YZ-plane of the simulation, randomly oriented grains are observed in the bottom region. After first few layers, red grains win the growth competition and thus dominate in the microstructure. In the simulation (Figure 5.6 (c)), the red grains propagate in the Z direction, which agrees with the experimental result as shown in Figure 5.6 (f). Similar to the simulation of the sample-B, a fiber texture is observed in the pole figure of the sample-C. However, a ring shape is absent in the experimental pole figure. This discrepancy arises because grain size in the sample-C is much larger than the grain size in the simulation for sample-C. As a result, the EBSD region only encompasses 5 or 6 grains, which is not quantitative for texture evaluation. To address this limitation, XRD (X-ray diffraction) measurement was then performed to accurately evaluate the texture of the sample-C. Based on the orientation distribution function determined with XRD, a pole figure is plotted in Figure 5.6 (i), which agrees well with the simulation result.

5.4 Discussion

For a crystal with a cubic symmetry, the preferential growth direction is always the $\langle 100 \rangle$ direction. In a solidification problem, the preferential orientation which dominates the growth has one of its $\langle 100 \rangle$ crystallographic direction parallel with the temperature gradient. In other words, the temperature gradient selects the preferential orientation. How the selection effect of the temperature gradient forms the $\{110\}\langle 001 \rangle$ texture and the $\langle 100 \rangle$ fiber texture is considered here.

The 316L steel sample is employed as an example to explain the formation of the $\{110\}\langle 001 \rangle$ texture. The unit vectors of the temperature gradient in the enlarged region of YZ-plane and XY-plane in Figure 5.3 are plotted in Figure 5.7 (b) and (e), respectively. During additive manufacturing, a CAFE cell may melt and solidify many times. The direction of the temperature gradient for each CAFE cell is determined as the direction of the temperature gradient when the considered CAFE cell is at the liquidus temperature for the last time. In this case, the unit vector of the temperature gradient shown in Figure 5.7 (b) and (e) are generated with multiple melt pools in different laser passes. In the YZ-plane (Figure 5.7 (b)), the temperature gradient is parallel with the build direction (Z axis) in the center of the melt pool, while the temperature gradient in the junction of two laser passes has an angle of around 45 degrees with the building direction (Z axis).

Consider a junction region between two laser passes in the same deposition layer. The fist laser pass selects a few preferential orientations with one of their $\{110\}\langle 001 \rangle$ crystallographic directions parallel with the temperature gradient of the first pass. The second pass performs the same selection but with a different temperature gradient. As a result, the preferential orientation for this junction region should have two of its $\{110\}\langle 001 \rangle$ directions parallel with the temperature gradient in the first laser pass and the second laser pass, respectively. If the out-of-plane component of the temperature gradient is neglected,

then the preferential orientation can be determined, which is presented in the pole figure in Figure 5.7 (c). In fact, the orientation shown in Figure 5.7 (c) is the main component of the {110}⟨001⟩ Goss texture. However, the out-of-plane component of the temperature gradient is not negligible, although it is small in the example case as shown in Figure 5.7 (e). When the out-of-plane component is small, its influence on the preferential orientation can be approximated by a rotation around the build direction (Z axis) for a certain angle. The rotation is either clockwise or anticlockwise depending on which side (left or right) of the laser pass the considered cell is located. As the scanning direction is anti-parallel for the neighboring laser passes in the same layer, the cells in the junction region are on the same side of the two passes. The preferential orientations of the two marked points in Figure 5.7 (e) are shown in Figure 5.7 (f), which matches the simulated and the experimental pole figures for the 316L steel. It should be noted that this rotation approximation is only valid when the out-of-plane component is small. With increasing out-of-plane component, the temperature gradient direction in the neighboring passes shifts towards the X+ and X− directions, respectively. In this case, the preferential orientation will change in a more complex way.
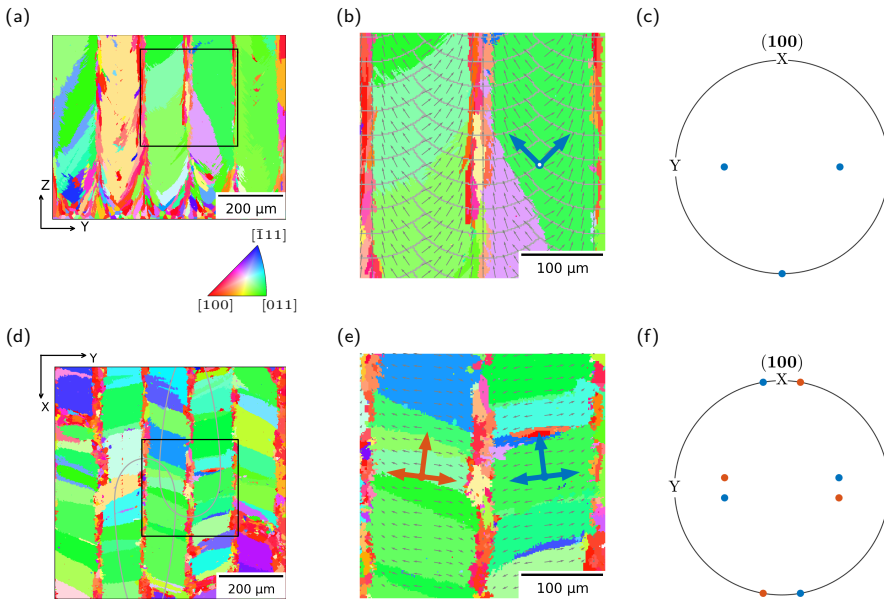
Figure 5.7: Illustration of the formation of the {110}⟨001⟩ Goss texture in AM samples: the microstructure in the YZ plane (a) and the XY plane (d), the temperature gradient in the enlarged region of the YZ plane (b) and the XY plane (e). Neglecting the temperature gradient component in the X direction, the preferential orientation can be determined and its ⟨100⟩ directions are plotted as arrows in (b) and dots in (c). If the temperature gradient component in the X direction is considered, the ⟨100⟩ directions of the preferential orientation are modified, as shown in (e) and (f).

The formation of the ⟨100⟩ fiber texture can be illustrated by comparing the texture

and the temperature gradient in NiTi sample-A, sample-B and sample-C. Similarly, the temperature gradient here refers to the temperature gradient of each cell when it is at the liquidus temperature for the last time. The temperature gradient of sample-A, sample-B and sample-C in the YZ-plane are given in Figure 5.8 (a), (b) and (c), where the black arrows are the unit vector of the temperature gradient and the color represents different layers. For a better view, the center regions of Figure 5.8 (a), (b) and (c) are enlarged in Figure 5.8 (d), (e) and (f), respectively.
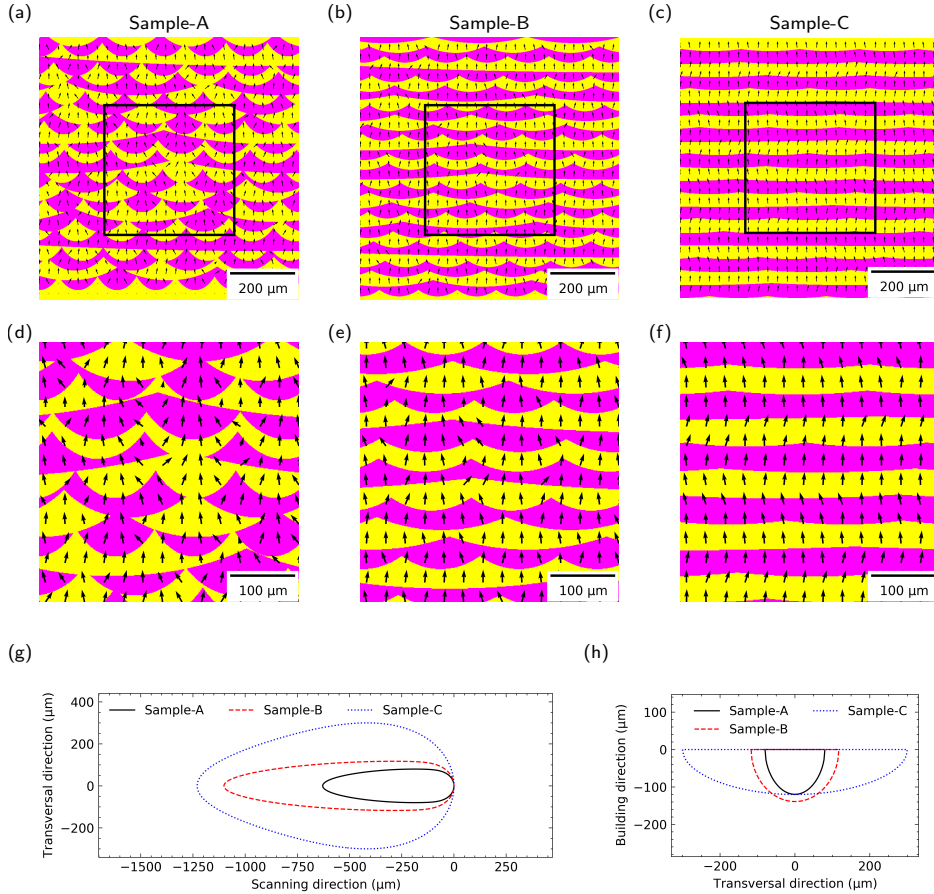
Figure 5.8: The direction of the temperature gradient in the YZ plane of sample-A (a), sample-B (b) and sample-C (c), where neighboring deposition layers are differentiated with different colors. The center region of (a), (b) and (c) are enlarged in (d), (e) and (f), respectively. The melt pool shape in the horizontal plane (g) and in the plane (h) perpendicular to the scanning direction are also given here.

For NiTi samples, the scanning direction is rotated by 67 degrees for each new layer. In this case, the scanning direction of each layer is not necessarily perpendicular to the

YZ plane, leading to different layer shapes in the YZ plane, as shown in Figure 5.8 (a), (b) and (c). The influence of the rotating scanning direction on the layer shape is dependent on the melt pool shapes. The width and the length of the melt pool in sample-A is the smallest among the three samples, as shown in Figure 5.8 (g) and (h). As a result, the layer shape changes drastically with the rotating scanning direction. Compared to sample-A, sample-B is manufactured with a wider and longer melt pool, leading to flatter layer shapes. In sample-C, the width and the length of the melt pool is the largest. Thus, the layer shapes in sample-C are nearly flat.

Due to the frequently changed layer shape and the small melt pool in sample-A, the direction of the temperature gradient in sample-A is highly inhomogeneous. In this case, a global preferential orientation cannot be found and the texture in sample-A is very weak. The melt pool in sample-B is wider and longer than the weld pool in sample-A. The temperature gradient in most CAFE cells is parallel with the Z axis. As a result, the preferential orientations have one of their $\langle 100 \rangle$ crystallographic directions parallel with the Z axis, while the other two $\langle 100 \rangle$ crystallographic directions are oriented randomly. This leads to the formation of a $\langle 100 \rangle$ fiber texture. In sample-C, the melt pool is even wider than the melt pool in sample-B. In this case, almost all cells have a temperature gradient parallel with the Z axis, as shown in Figure 5.8 (f). As a result, the $\langle 100 \rangle$ fiber texture of sample-C is stronger than the texture of the sample-B.

In summary, two different mechanisms exist to form a strong texture during additive manufacturing. The first mechanism leads to the $\{110\}\langle 001 \rangle$ texture, where the preferential orientation is selected by two temperature gradients which are nearly perpendicular to each other. In this case, the preferential orientation is unique. The temperature gradient component in the scanning direction may change the preferential orientation, leading to a deviation from the Goss texture. This means one can design the melt pool shapes to tune this deviation and obtain a desired texture. Note this deviation is mirror-like in the different sides of the melt pool. As a result, the final texture is composed of two strong components. The second mechanism forms a fiber texture, where only one temperature gradient is performing the selection. The preferential orientations are not unique. To the author's knowledge, it is difficult to employ this mechanism to form any texture other than the $\langle 100 \rangle$ fiber texture.

Note that the two mechanisms may be present at the same time during additive manufacturing, for example in the 316L steel sample. It is possible to tune the weld pool shape, so that one mechanism is suppressed and the other mechanism is enhanced and then dominates the texture evolution. Moreover, suppressing both the mechanisms during additive manufacturing results in a component without a strong texture, which is favored in cases where anisotropy is not required.

5.5 Conclusion

In this chapter, a novel cellular automata finite element (CAFE) model has been described, which significantly accelerates the simulation of crystallographic texture and grain morphologies in additively manufactured metallic materials, enabling the development of a digital twin for additive manufacturing. This acceleration is achieved by the synergistic effects of three key aspects in the model: the employment of large time steps without compromising simulation accuracy, the implementation of the subdomain activation and

deactivation method, and the utilization of parallelism through a shared memory approach. With experimental validations, the optimized CAFE model demonstrates its robustness as a tool for microstructure prediction. Through the analysis of both simulated and experimental results, this research uncovers the governing mechanisms behind texture evolution and selection. This work represents a significant advancement towards efficient microstructure prediction in additive manufacturing, contributing to the realization of a digital twin approach.

REFERENCES

[1] RG Li, HR Li, HC Pan, DS Xie, JH Zhang, DQ Fang, YQ Dai, DY Zhao, and H Zhang. Achieving exceptionally high strength in binary mg-13gd alloy by strong texture and substantial precipitates. *Scripta Materialia*, 193:142–146, 2021.

[2] Chokkakula LP Pavithra, Bulusu V Sarada, Koteswararao V Rajulapati, M Ramakrishna, Ravi C Gundakaram, Tata N Rao, and G Sundararajan. Controllable crystallographic texture in copper foils exhibiting enhanced mechanical and electrical properties by pulse reverse electrodeposition. *Crystal Growth & Design*, 15(9):4448–4458, 2015.

[3] HJ Bunge. Texture and magnetic properties. *Textures and microstructures*, 11, 1970.

[4] Dongsheng Zhang, Wei Liu, Yuxiao Li, Darui Sun, Yu Wu, Shengnian Luo, Sen Chen, Ye Tao, and Bingbing Zhang. In situ observation of crystal rotation in ni-based superalloy during additive manufacturing process. *Nature Communications*, 14(1):2961, 2023.

[5] Jinglei Li, Wanbo Qu, John Daniels, Haijun Wu, Linjing Liu, Jie Wu, Mingwen Wang, Stefano Checchia, Shuai Yang, Haobin Lei, et al. Lead zirconate titanate ceramics with aligned crystallite grains. *Science*, 380(6640):87–93, 2023.

[6] Jia-Ning Zhu, Kai Liu, Ton Riemslag, Frans D Tichelaar, Evgenii Borisov, Xiyu Yao, Anatoly Popovich, Richard Huizenga, Marcel Hermans, and Vera Popovich. Achieving superelasticity in additively manufactured ni-lean niti by crystallographic design. *Materials & Design*, 230:111949, 2023.

[7] I Bitharas, N Parab, C Zhao, T Sun, AD Rollett, and AJ Moore. The interplay between vapour, liquid, and solid phases in laser powder bed fusion. *Nature Communications*, 13(1):2959, 2022.

[8] Tarasankar Debroy, Wei Zhang, J Turner, and Sudarsanam Suresh Babu. Building digital twins of 3d printing machines. *Scripta Materialia*, 135:119–124, 2017.

[9] Minh-Son Pham, Bogdan Dovgyy, Paul A Hooper, Christopher M Gourlay, and Alessandro Piglione. The role of side-branching in microstructure development in laser powder-bed fusion. *Nature communications*, 11(1):749, 2020.

[10] Tridibesh Mukherjee and Tarasankar DebRoy. A digital twin for rapid qualification of 3d printed metallic components. *Applied Materials Today*, 14:59–65, 2019.

[11] A Phua, CHJ Davies, and GW Delaney. A digital twin hierarchy for metal additive manufacturing. *Computers in Industry*, 140:103667, 2022.

[12] Arden Phua, Peter S Cook, Chris HJ Davies, and Gary W Delaney. Smart recoating: A digital twin framework for optimisation and control of powder spreading in metal additive manufacturing. *Journal of Manufacturing Processes*, 99:382–391, 2023.

[13] T DebRoy, T Mukherjee, HL Wei, JW Elmer, and JO Milewski. Metallurgy, mechanistic models and machine learning in metal printing. *Nature Reviews Materials*, 6(1):48–68, 2021.

[14] Yuze Huang, Tristan G Fleming, Samuel J Clark, Sebastian Marussi, Kamel Fezzaa, Jeyan Thiyagalingam, Chu Lun Alex Leung, and Peter D Lee. Keyhole fluctuation and pore formation mechanisms during laser powder bed fusion additive manufacturing. *Nature Communications*, 13(1):1170, 2022.

[15] Tommy Carozzani, Ch-A Gandin, and Hugues Digonnet. Optimized parallel computing for cellular automaton–finite element modeling of solidification grain structures. *Modelling and Simulation in Materials Science and Engineering*, 22(1):015012, 2013.

[16] Ch-A Gandin and Michel Rappaz. A 3d cellular automaton algorithm for the prediction of dendritic grain growth. *Acta Materialia*, 45(5):2187–2195, 1997.

[17] Shijia Chen, Gildas Guillemot, and Charles-André Gandin. Three-dimensional cellular automaton-finite element modeling of solidification grain structures for arc-welding processes. *Acta materialia*, 115:448–467, 2016.

[18] Johannes A Koepf, Martin R Gotterbarm, Matthias Markl, and Carolin Körner. 3d multi-layer grain structure simulation of powder bed fusion additive manufacturing. *Acta Materialia*, 152:119–126, 2018.

[19] Yanping Lian, Zhengtao Gan, Cheng Yu, Dmitriy Kats, Wing Kam Liu, and Gregory J Wagner. A cellular automaton finite volume method for microstructure evolution during additive manufacturing. *Materials & Design*, 169:107672, 2019.

[20] Dong-Rong Liu, Shuhao Wang, and Wentao Yan. Grain structure evolution in transition-mode melting in direct energy deposition. *Materials & Design*, 194:108919, 2020.

[21] Rongpei Shi, Saad A Khairallah, Tien T Roehling, Tae Wook Heo, Joseph T McKeown, and Manyalibo J Matthews. Microstructural control in metal laser powder bed fusion additive manufacturing using laser beam shaping strategy. *Acta Materialia*, 184:284–305, 2020.

[22] Kirubel Teferra and David J Rowenhorst. Optimizing the cellular automata finite element model for additive manufacturing to simulate large microstructures. *Acta Materialia*, 213:116930, 2021.

[23] Yanping Lian, Stephen Lin, Wentao Yan, Wing Kam Liu, and Gregory J Wagner. A parallelized three-dimensional cellular automaton model for grain growth during additive manufacturing. *Computational Mechanics*, 61:543–558, 2018.

[24] Matt Rolchigo, Samuel Temple Reeve, Benjamin Stump, Gerald L Knapp, John Coleman, Alex Plotkowski, and James Belak. Exaca: A performance portable exascale cellular automata application for alloy solidification modeling. *Computational Materials Science*, 214:111692, 2022.

[25] Edwin J Schwalbach, Sean P Donegan, Michael G Chapman, Kevin J Chaput, and Michael A Groeber. A discrete source model of powder bed fusion additive manufacturing thermal history. *Additive Manufacturing*, 25:485–498, 2019.

[26] W 1 Kurz, B Giovanola, and R Trivedi. Theory of microstructural development during rapid solidification. *Acta metallurgica*, 34(5):823–830, 1986.

[27] A Zinoviev, O Zinovieva, V Ploshikhin, V Romanova, and R Balokhonov. Evolution of grain structure during laser additive manufacturing. simulation by a cellular automata method. *Materials & Design*, 106:321–329, 2016.

[28] De-Chang Tsai and Weng-Sing Hwang. A three dimensional cellular automaton model for the prediction of solidification morphologies of brass alloy by horizontal continuous casting and its experimental verification. *Materials transactions*, 52(4):787–794, 2011.

[29] Xuxiao Li and Wenda Tan. Numerical investigation of effects of nucleation mechanisms on grain structure in metal additive manufacturing. *Computational Materials Science*, 153:159–169, 2018.

[30] Yi Zhang and Jing Zhang. Modeling of solidification microstructure evolution in laser powder bed fusion fabricated 316l stainless steel using combined computational fluid dynamics and cellular automata. *Additive Manufacturing*, 28:750–765, 2019.

[31] MR Rolchigo and R LeSar. Application of alloy solidification theory to cellular automata modeling of near-rapid constrained solidification. *Computational Materials Science*, 163:148–161, 2019.

[32] A Pineau, G Guillemot, D Tourret, A Karma, and Ch-A Gandin. Growth competition between columnar dendritic grains–cellular automaton versus phase field modeling. *Acta Materialia*, 155:286–301, 2018.

[33] Xiaohui Ao, Huanxiong Xia, Jianhua Liu, and Qiyang He. Simulations of microstructure coupling with moving molten pool by selective laser melting using a cellular automaton. *Materials & Design*, 185:108230, 2020.

[34] The HDF Group. Hierarchical Data Format, version 5, 1997-NNNN. https://www.hdfgroup.org/HDF5/.

5

[35] Olivier Andreau, Imade Koutiri, Patrice Peyre, Jean-Daniel Penot, Nicolas Saintier, Etienne Pessard, Thibaut De Terris, Corinne Dupuy, and Thierry Baudin. Texture control of 316l parts by modulation of the melt pool morphology in selective laser melting. *Journal of Materials Processing Technology*, 264:21–31, 2019.

5

6

Multi-scale modelling of solidification cracking during welding

In this chapter, a multi-scale multi-physics modelling framework to predict solidification cracking susceptibility during welding is presented. The modelling framework includes a thermo-mechanical model to simulate temperature and strain rate profiles during welding, a cellular automata model to simulate the solidified microstructure in the weld pool and a granular model to calculate the pressure profile in the liquid channel network. The developed modelling framework is verified by comparing with welding experiments of a TRIP steel. The modelling framework is capable of capturing the influence of the process parameters, grain refinement and alloy composition on solidification cracking susceptibility, which agree with experimental findings in the literature.

6

6.1 Introduction

Nowadays, advanced high strength steels, which possess high strength and ductility, have been widely employed in the automotive industry to reduce car body weight and thus CO_2 emissions [1]. The high strength and ductility of the advanced high strength steels are achieved by adding high alloying contents. However, some alloying elements may lead to a poor weldability. During welding, the detrimental elements may accumulates in the liquid, resulting in the existence of liquid channels at a low temperature. As a result of thermal contraction and solidification shrinkage, the interfaces of the liquid channels may separate from each other. If liquid feeding throughout the liquid channel is not enough to compensate for such a separation, cracks form, known as solidification cracking.

Solidification cracking is a complex problem which is associated with multi-physics phenomena. The occurrence of solidification cracking during welding is associated with three factors: the driving force to separate liquid channel interfaces, the existence of liquid channels at a low temperature and insufficient liquid feeding. The three factors correspond to different physics and have to be studied at different length scales. The driving force to separate the liquid channel interfaces comes from thermo-mechanical interactions between the solidified weld pool and the base material. As the weld pool is usually at the scale of millimeters, the driving force to separate liquid channel interfaces needs to be evaluated at a macroscale. The second and the third factors are related to the micro-segregation and fluid flow within the liquid channel, which needs to be studied at a microscale.

Experimental works [2, 3] have been performed to study the influence of the processing parameters including power and welding velocity on solidification cracking. Slyvinsky et al. [4] reported that increasing the welding velocity v_s with a constant power Q leads to a decrease in solidification cracking susceptibility (SCS) for a nickel-base alloy. The decrease in SCS with increasing welding velocity while keeping the power constant was confirmed by Goodwin [5] and Agarwal et al. [6]. This was explained by the smaller thermal strain generated during welding at a faster welding velocity v_s [6]. Conversely, when the welding velocity v_s is increased with a constant Q/v_s ratio, an increase in SCS was reported by Ohshita et al. [7], Shibahara et al. [8], Suyitno et al. [9], Cicală et al. [10] and Goodwin [5]. Nevertheless, it was also found [11] that increasing the welding velocity promotes the transition from a columnar to an equiaxed structure in the weld pool and thus inhibits solidification cracking in aluminum alloy 6082.

To further understand and avoid solidification cracking, efforts [12–14] have been made to determine the critical strain or strain rate conditions for solidification cracking. Gao et al. [12] investigated solidification cracking in laser welded TRIP steel with digital image correlation and finite element modelling and determined the critical strain for hot cracking in the range of 3.2% to 3.6%. Soysal and Kou [13] developed a test to assess the critical deformation rate for solidification cracking. In their test, a stationary sheet is welded to a sheet moving at a varying speed. The critical deformation rate can thus be determined by plotting the crack length against the moving velocity.

Physics-based microscopic models have been developed to predict solidification cracking for liquid channels in the mushy zone. The RDG (Rappaz-Drezet-Gremaud) model [15] and the SCS model developed by Kou [16, 17] are widely used to predict SCS of different alloys. The RDG model calculates the pressure drop from the dendrite tip to the coalescence of the liquid channel, assuming that liquid feeding is enough to compensate

for the solid deformation. Solidification cracking occurs when the maximum pressure drop is larger than a critical value. With the critical pressure drop value, a critical strain rate can be determined. In Kou's model [16], solidification cracking occurs when the separation velocity of the liquid channel interfaces is larger than the sum of velocity terms from transversal grain growth and liquid feeding. A SCS index [16] has been proposed as a criterion to qualitatively compare the SCS of alloys with different compositions. Based on Scheil-Gulliver solidification calculations, both the RDG model [15] and Kou's model [16, 17] have successfully predicted the SCS peak in Al-Cu alloy between 1 wt.% and 2 wt.%. Later, the RDG model [18] and Kou's model [18–20] have been coupled with phase field models, which can simulate the dendrite structure in the mushy zone explicitly and provide a more realistic solidification path compared to Scheil-Gulliver calculations. Geng et al. [20] simulated the dendritic microstructure with a phase field model and evaluated the cracking susceptibility of an Al-Mg (4.0 wt.%) alloy using Kou's SCS index. It was found that back diffusion reduced the segregation within the liquid channel, leading to a small SCS despite the freezing temperature range of the considered alloy. With a multi-phase phase field model, Han et al. [18] studied the influence of the grain boundary energy σ_{ss} on the coalescence behavior of the liquid channel and SCS. It was reported that a high σ_{ss} value suppresses the coalescence of the liquid channel and increases SCS. Yang et al. [21] calculated the maximum pressure drop with the RDG model under different alloy compositions and different grain boundary conditions. His results showed that coupled with a quantitative phase field model, the RDG model is capable of accurately predicting the liquid rupture state associated with solidification cracking. Liang et al. [22] studied the influence of the pulling velocity and the temperature gradient on SCS under directional solidification conditions and found that increasing the pulling velocity or decreasing the temperature gradient results in an increase in the maximum pressure drop and thus an increase in SCS. Despite the successful applications of the RDG model and Kou's model in SCS prediction, due to the high computational cost of phase field models, the aforementioned works are limited to a small domain, which is at the scale of several hundred micrometers or even smaller. Full-dimensional simulations, which include a whole weld pool or mushy zone, are still challenging.

Efforts have been made to achieve SCS prediction in a full-dimensional simulation. Sistaninia et al. [23] developed a three-dimensional granular model to simulate the fluid flow within the liquid channel network during casting. By assuming Poiseuille flow and mass balance in each liquid channel, a partial differential equation was derived, which describes the evolution of the liquid pressure in the liquid channel network. It was shown that deep in the mushy zone where the permeability is low, the local pressure can be significantly lower than the pressure predicted by averaging techniques [23]. Later, the proposed granular model was combined with a deformation model and a failure model [24]. The failure model assumed that cracks form when the pressure reaches a critical level, which is related to the liquid channel width. The developed model [24] was then verified with a semi-solid tensile test. The simulated stress and shear deformation agreed well with the experimental data. Following the work of Sistaninia et al. [23, 24], Rajani and Phillion [25–27] developed a multi-scale model to predict solidification cracking during fusion welding of AL-Mg-Si alloys. According to their simulations, SCS decreased when increasing the welding velocity while keeping the power constant, which agreed with experimental results

[4–6, 28]. However, in their simulations, SCS decreased when increasing the power at a constant velocity, which contradicted experimental results [5, 6, 28]. Moreover, the simulations were performed on a microstructure which was artificially generated with a Voronoi tessellation. The simulation domain was also limited to a small part of the weld pool. Due to the limitations of existing works, a full-dimensional modelling framework to evaluate SCS with real microstructures is still not available.

In this work, a multi-scale multi-physics modelling framework is developed to evaluate solidification cracking susceptibility under different welding conditions. This framework includes three models, which are coupled sequentially. Firstly, a thermomechanical model, which calculates the profiles of temperature, stress and strain during welding; then, a cellular automata model is employed to simulate the solidification microstructure based on the thermal profiles. The simulated grain boundary structure in the mushy zone is extracted and employed as a liquid channel network. A granular model is then employed to calculate the pressure profiles within the liquid channel network. The developed modelling framework is employed to study the influence of the welding velocity and grain refinement on SCS and compared with experimental results.

6.2 Method

6.2.1 Thermomechanical modelling

The temperature profile T in a welded component Ω is simulated with a finite element (FE) model by solving

$$\rho c_p \frac{\mathrm{d}T}{\mathrm{d}t} = \nabla \cdot (k \nabla T) + Q \qquad \text{in } \Omega, \tag{6.1}$$

where ρ is the density, c_p the specific heat capacity, t the time, k the thermal conductivity and Q the volumetric source, which is given by a truncated-cone Gaussian heat source model [6, 12, 29],

$$Q = \frac{3 \exp(3) \eta P}{(\exp(3) - 1) V_{tc}} \exp\left(\frac{-3r^2}{r_0^2}\right), \tag{6.2}$$

where P is the power and η the efficiency. V_{tc} is the volume of the truncated cone given by

$$V_{tc} = \frac{\pi}{3}(z_e - z_i)(r_e^2 + r_e r_i + r_i^2). \tag{6.3}$$

Here r_e and r_i are the radius of the heat source on the top and the bottom surface and z_e and z_i the z coordinates of the top and the bottom surface, respectively. The radial distance r of a given point (x, y, z) to the heat source center (x_c, y_c) is given by

$$r = \sqrt{(x - x_c)^2 + (y - y_c)^2}. \tag{6.4}$$

r_0 is the radius of the truncated-cone heat source, which varies linearly with z,

$$r_0 = r_i + (r_e - r_i) \frac{z - z_i}{z_e - z_i}. \tag{6.5}$$

Heat loss through convection and radiation is applied with a Neumann boundary condition,

$$\vec{n} \cdot \vec{q} = h_c(T - T_{amb}) + \varepsilon_r \sigma \left(T^4 - T_{amb}^4\right) \qquad \text{on } \partial\Omega, \tag{6.6}$$

where $\vec{n}$ is the interface normal on the boundary, h_c the heat transfer coefficient for convective heat loss, T_{amb} the ambient temperature, ε_r the surface emissivity and σ the Stefan-Boltzmann constant. The initial temperature is set to room temperature.

For the mechanical model, the governing equation for the quasi-static analysis is

$$\nabla \cdot \sigma = 0. \tag{6.7}$$

where σ is the stress tensor. Considering geometric nonlinearity, the strain tensor ε is related to the displacement vector $\vec{u}$ by

$$\varepsilon = \frac{1}{2}\left[(\nabla\vec{u})^T + \nabla\vec{u} + (\nabla\vec{u})^T\nabla\vec{u}\right]. \tag{6.8}$$

The strain tensor can be decomposed into three components,

$$\varepsilon = \varepsilon_T + \varepsilon_e + \varepsilon_p, \tag{6.9}$$

where ε_T, ε_e and ε_p are the thermal strain, elastic strain and the plastic strain, respectively. The material is modelled with linear elasticity and perfect plasticity without hardening,

$$\sigma = C : \varepsilon_e, \tag{6.10}$$

where C is the elasticity tensor. The thermal strain ε_T, as a function of the temperature, is only considered below the liquidus temperature. During welding, the welded component is fixed at certain boundaries Γ, where a Dirichlet boundary condition is applied,

$$\vec{u} = \vec{0} \qquad \text{on } \Gamma. \tag{6.11}$$

The thermomechanical analysis is performed with the commercial FE modelling software COMSOL. Lagrange quadratic elements are employed in the FE simulation.

6.2.2 Microstructure modelling

The solidification microstructure is simulated with a cellular automata (CA) model, in which the solidification growth velocity v_g is calculated as a function of local undercooling ΔT based on the LGK (Lipton-Glicksman-Kurz) model; details of this CA model are given in Chapter 5. In the previous chapter, the CA simulation is performed based on the temperature profile from an analytical model. Here, the temperature profile from the thermomechanical FE model is employed as input for the solidification CA simulation. With the Lagrange quadratic interpolation, the temperature T at the center (x_{cell}, y_{cell}) of a CA cell is calculated by summing up the product of the shape function N_i and the FE node temperature T_i in the corresponding FE element

$$T = \sum_i T_i N_i(x_{cell}, y_{cell}). \tag{6.12}$$

As the interfacial energy is not considered in the decentered growth algorithm in the CA model, a jagged interface may be observed at the grain boundaries, which is unfavorable for the subsequent liquid drop calculation. To remove this effect, the solidification microstructure is post-processed with a smoothing procedure. The smoothing procedure

follows the physics of grain growth and checks the curvature at each CA cell at the grain boundary. According to Nastac [30], the curvature κ of a CA cell can be estimated with

$$\kappa = \frac{1}{\Delta x}\left(1 - 2f_g\right), \tag{6.13}$$

where Δx is the CA cell size, f_g the volume fraction of the grain in the Moore neighborhood, to which the considered cell belongs. Different from Nastac's solidification model, the CA cell in this work does not have a grain fraction and only belongs to one grain. In this case, an extended Moore neighborhood is employed for the curvature calculation to achieve a better accuracy. If the curvature κ is larger than a critical value κ_{crit} or if the volume fraction f_g of the grain in the extended Moore neighborhood is smaller than a critical value $f_{g,crit}$, the considered CA cell then transforms into the grain which has the largest volume fraction in the extended Moore neighborhood. The smoothing algorithm is performed for several iterations.

After grain boundary smoothing, the microstructure in the mushy zone during welding is extracted. The mushy zone is determined as the zone between two isotherms: the liquidus temperature T_l and the solidus temperature T_s. The solidus temperature T_s is determined as the temperature at which the solid fraction f_s is equal to 0.98 in the Scheil-Gulliver calculation. Then, the grain boundary structure is extracted with Dream3D [31] using quick surface meshing and Laplacian smoothing. The resultant hypersurface is employed as the liquid channel network for the subsequent pressure drop calculation.

6.2.3 Modeling of pressure drop
Following the work of Sistaninia [23, 24], assuming Poiseuille flow in the liquid channel, the pressure p evolution in the liquid channel network Ω_l is governed by

$$\frac{2h^3}{3\mu_v}\nabla^2 p = v_s + v_m \qquad \text{in } \Omega_l, \tag{6.14}$$

where h is the half width of the liquid channel, μ_v the viscosity, v_s the separation velocity due to solidification shrinkage and v_m the separation velocity due to mechanical constraints. A Dirichlet boundary condition is applied at the liquid interface $\Gamma_{l,D}$ defined by $T = T_l$,

$$p = 0 \qquad \text{on } \Gamma_{l,D}. \tag{6.15}$$

A Neumann boundary condition is applied on the remaining boundaries $\Gamma_{l,N}$,

$$\vec{n} \cdot \nabla p = 0 \qquad \text{on } \Gamma_{l,N}. \tag{6.16}$$

Consider a liquid film between two columnar grains, as shown in Figure 6.1. Following Kou's work [16], the radius of a columnar grain is proportional to the square root of the solid fraction $\sqrt{f_s(T)}$. The half width of the liquid channel h can be calculated with

$$h = \frac{\lambda}{2}\left(1 - \sqrt{f_s(T)}\right), \tag{6.17}$$

where λ is the grain distance, which is calculated by summing up the radius of the two neighboring grains,

$$\lambda = R_t + R_b, \tag{6.18}$$
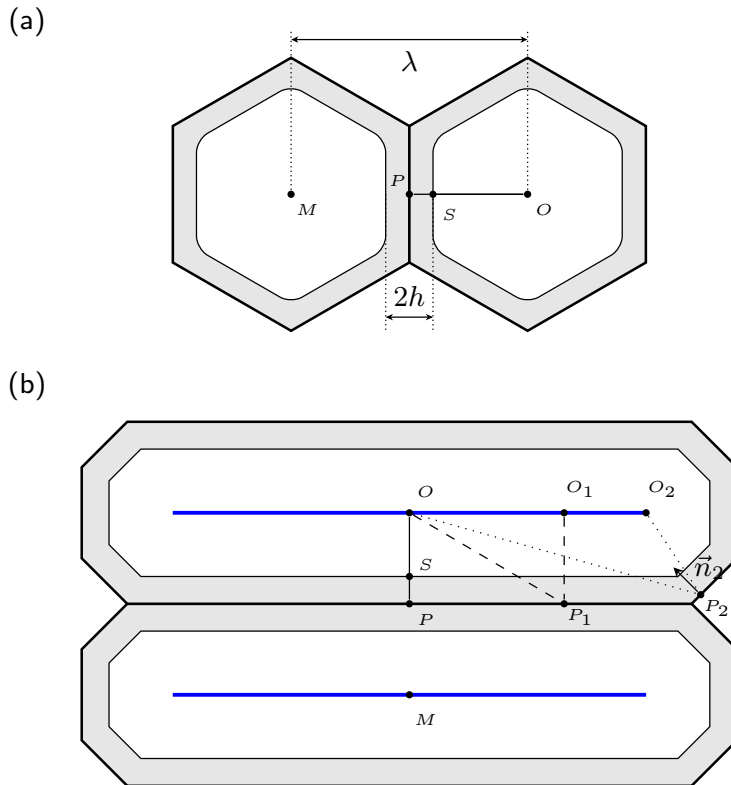
Figure 6.1: Illustration of the liquid channel between two columnar grains in the cross sections perpendicular to the columnar axis (a) and parallel to the columnar axis (b).

where R_t and R_b are the radius of the top grain and bottom grain in Figure 6.1 (b). In the simulated microstructure, the grains are not perfect cylindrical shapes. In this case, the grain radius is determined for each interface element locally and the grain radius varies at different locations. For example, for an interface element with its center at point P_1, the radius of the top grain is calculated with

$$R_t = \overrightarrow{O_1 P_1} \cdot \vec{n}_s, \tag{6.19}$$

where O_1 is the nearest point on the axis of the top grain to the considered point P_1 and $\vec{n}_s$ the unit vector of the considered interface element. Here, the nearest point O_1 on the grain axis instead of the grain center O is employed, to avoid overestimating the liquid channel width at the ends of the columnar grains. The grain axis passes the grain center and is in the direction in which the columnar grain propagates. The distance of the grain axis endpoints to the nearby end of the columnar grains is equal to the mean radial distance of all the interface elements to the grain axis. The radius of the bottom grain at point P_1 can be calculated similarly.

The separation velocity due to solidification shrinkage is calculated with

$$v_s = \beta \lambda \frac{d\sqrt{f_s(T)}}{dT} \dot{T}, \tag{6.20}$$

where β is the shrinkage factor ($\beta = \rho_s/\rho_l - 1$) and $\dot{T}$ the temperature changing rate.

The separation velocity v_m due to mechanical constraints is calculated assuming the deformation is localized in the liquid. Consider an interface element in the liquid channel with its center at P, as shown in Figure 6.1 (a) and (b). The center of the top columnar grain is O. The line OP intersects the solid-liquid interface at point S. The velocity of the point P with respect to the point O can be obtained by integrating the strain rate $\dot{\varepsilon}$,

$$\vec{v}_{m,1} = \int_O^P \dot{\varepsilon} \, d\vec{x}. \tag{6.21}$$

Meanwhile, due to thermal contraction, the length of PS and SO decrease, leading to a contribution $\vec{v}_{m,2}$ to the separation velocity v_m,

$$\vec{v}_{m,2} = -\int_S^P \alpha_l \dot{T} \, d\vec{x} - \int_O^S \alpha_s \dot{T} \, d\vec{x}, \tag{6.22}$$

where α_l and α_s are the linear thermal expansion coefficients of the liquid and the solid respectively. Here, it is assumed that $\alpha_l \approx \alpha_s \approx \alpha$, where α is the temperature dependent thermal expansion coefficient used in the thermal-mechanical analysis. The $\vec{v}_{m,2}$ velocity component can be written as

$$\vec{v}_{m,2} = -\int_O^P \alpha \dot{T} \, d\vec{x}. \tag{6.23}$$

The separation velocity v_m^r due to mechanical constraints from the top columnar dendrite is then given by

$$v_m^r = \vec{n}_s \cdot (\vec{v}_{m,1} + \vec{v}_{m,2}) = \vec{n}_s \cdot \int_O^P \left(\dot{\varepsilon} - \alpha \dot{T} I \right) d\vec{x}, \tag{6.24}$$

where $\vec{n}_s$ is the interface normal unit vector of the considered interface element and I the identity matrix. Similarly, the separation velocity v_m^l due to mechanical constraints from the left columnar dendrite can be obtained and the total mechanical contribution v_m is given by

$$v_m = v_m^r + v_m^l$$
$$= \vec{n}_s \cdot \int_O^P \left(\dot{\varepsilon} - \alpha\dot{T}I\right) d\vec{x} - \vec{n}_s \cdot \int_M^P \left(\dot{\varepsilon} - \alpha\dot{T}I\right) d\vec{x}. \tag{6.25}$$

$\dot{\varepsilon} - \alpha\dot{T}I$ is the strain rate part which needs to be compensated by liquid feeding. In this work, it is called the effective strain rate.

In the current work, the liquid channel network, which is basically a hyper-surface in a three-dimensional space, is discretized into multiple triangular elements. An in-house finite element solver is then employed to solve Equation (6.14) on the liquid channel network.

6.2.4 The experimental conditions and material properties

The current modelling framework has been employed to simulate the welding experiments performed by Agarwal et al. [29]. Bead-on-plate laser welding experiments were performed on TRIP steel plates at a distance of 5 mm to the free edge, as shown in Figure 6.2. Four welding experiments were performed at different welding velocities (10 mm/s, 9 mm/s, 8 mm/s and 7 mm/s) and different powers (1100 W, 990 W, 880 W and 770 W), respectively. In the four experiments, the ratio between the power and the welding velocity was constant. In the samples with welding velocities of 10 mm/s, 9 mm/s and 8 mm/s, longitudinal cracks were observed in the center of the weld, while there was no crack in the sample with welding velocity 7 mm/s.
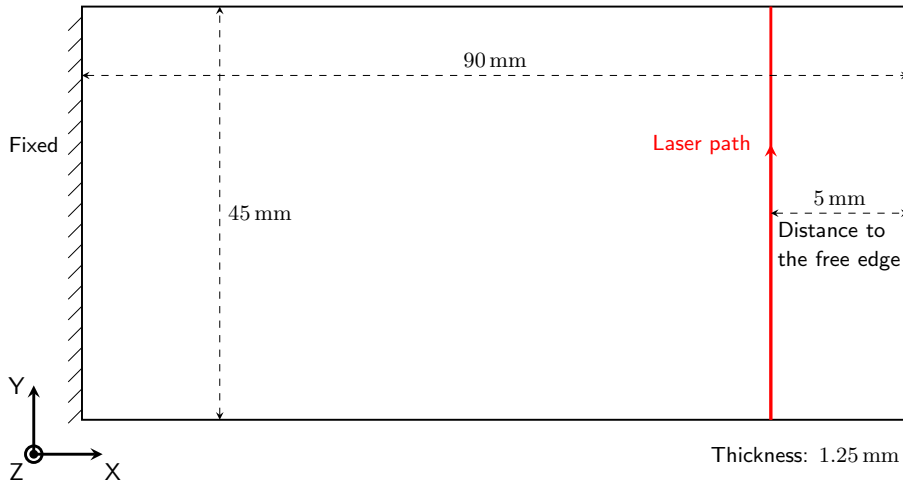
Figure 6.2: The experimental configuration in the work of Agarwal et al. [29].

The composition of the TRIP steel is given in Table 6.1 [29].The properties of the TRIP steel are given in Figure 6.3. Thermal properties including the specific heat c_p, thermal conductivity k and density ρ are obtained from the work of Agarwal et al. [29]. Properties for the FE mechanical analysis including thermal expansion, yield stress and Young's modulus are obtained from the work of Ahmed [32]. The temperature dependent solid fraction f_s and the solidification shrinkage factor β are obtained from the Scheil-Gulliver calculations in Thermo-Calc. Note the sharp transition in the curve of shrinkage factor β comes from the peri-eutectic reaction.

Table 6.1: Composition of the TRIP steel [29].

Elements (wt%)	C	Mn	Al	Si	Cr	P	S
TRIP	0.19	1.63	1.1	0.35	0.019	0.089	0.005
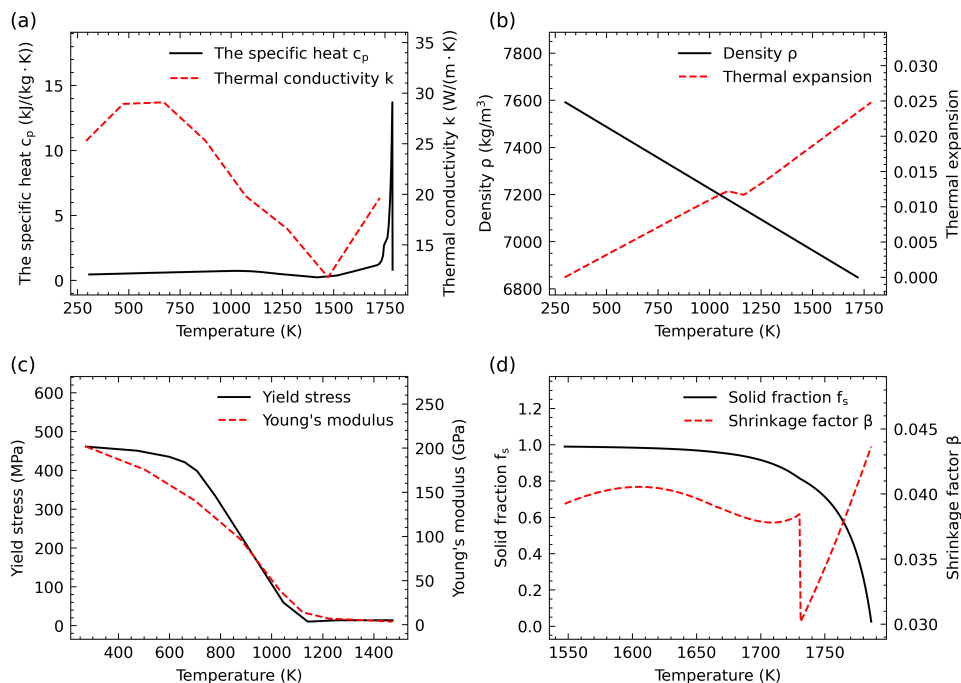
Figure 6.3: The temperature dependent properties of the TRIP steel employed in the welding experiments of Agarwal et al. [29].

6.3 Results

6.3.1 The profiles of the temperature and the strain rate

With the thermal-mechanical analysis, the profiles of the temperature and the strain rate during welding are obtained. The profile of strain rate components $\dot{\varepsilon}_{xx}$, $\dot{\varepsilon}_{yy}$ and $\dot{\varepsilon}_{zz}$ in the

simulation with $v = 10\,\mathrm{mm/s}$ at the time when the laser center is at $y = 20\,\mathrm{mm}$ are shown in Figure 6.4 (a), (c) and (e), respectively. As shown in Section 6.2.3, the separation velocity is related to the effective strain rate $\dot{\varepsilon} - \alpha \dot{T} I$. In this case, the components of the effective strain rate $\dot{\varepsilon} - \alpha \dot{T} I$ are given in Figure 6.4 (b), (d) and (f). Additionally, isotherms of the liquidus temperature T_l and the solidus temperature T_s are plotted as red lines; the region between the two red lines is determined as the mushy zone where the liquid is partially solidified. The strain rate in the mushy zone determines the loading conditions of the liquid channels in the mushy zone. As shown in Figure 6.4 (a), a small zone with positive strain rate $\dot{\varepsilon}_{xx}$ is observed near the tail of the weld pool, which is surrounded by a large region with a negative strain rate. After considering the strain rate contribution from thermal contraction, the positive strain rate region near the tail of the weld pool is elongated to the end of the mushy zone, favoring solidification cracking in the welding direction. Similar to the profile of $\dot{\varepsilon}_{xx}$, in the profile of $\dot{\varepsilon}_{yy}$ (Figure 6.4 (c)), a positive strain rate region, which spans over the weld pool tail and part of the mushy zone, is surrounded by a negative strain rate region. After considering the strain rate contribution from thermal contraction, the effective strain rate $(\dot{\varepsilon} - \alpha \dot{T} I)_{yy}$ is positive in the whole mushy zone, favoring the solidification cracking perpendicular to the welding direction. In the profile of $\dot{\varepsilon}_{zz}$ (Figure 6.4 (c)), negative strain rate dominates in the mushy zone. After considering the strain rate contribution from thermal contraction, the effective strain rate $(\dot{\varepsilon} - \alpha \dot{T} I)_{zz}$ in the mushy zone is still negative but with a smaller value.

To study the influence of the welding velocity, the results of simulations with different welding velocity are compared, as shown in Figure 6.5. The length of the weld pool and the length of the mushy zone along the center line are determined based on the temperature profile in each simulation. As shown in Figure 6.5 (b), with increasing welding velocity, both the weld pool length and the mushy zone length increase. With increasing mushy zone length, the liquid feeding in the tail of the mushy zone is more difficult, leading to an increase in solidification cracking susceptibility.

In the experiments, solidification cracks form along the weld path, which is attributed to the strain rate in the x direction; therefore, the strain rate component $\dot{\varepsilon}_{xx}$ along the center line in the different simulations is studied. The strain rate profile $\dot{\varepsilon}_{xx}$ along the center line in the simulation with $v = 10\,\mathrm{mm/s}$ is given in Figure 6.5 (c). A strain rate peak is observed at the boundary near the liquidus temperature. As temperature drops in the mushy zone, the solidified material contracts and the strain rate changes from positive to negative. A strain rate valley exists near the solidus temperature. Following the strain rate valley, due to the interaction between the solidified material and material in the heat affected zone which undergoes thermal expansion and contraction sequentially, the strain rate along the center line fluctuates and eventually goes back to 0. For comparison, the strain rate profiles $\dot{\varepsilon}_{xx}$ in the center of the mushy zone in each simulation are given in Figure 6.5 (d). As the weld pool length in each simulation is different, the strain rate curves are at different locations. With increasing welding velocity, the strain rate (positive) at the liquidus temperature becomes larger, while the strain rate (negative) at the solidus temperature becomes smaller. In other words, the strain rate curve shifts in the positive direction with increasing welding velocity. As shown in Figure 6.5 (e), as temperature drops from the liquidus temperature to the solidus temperature, the cooling rate increases. Moreover, the cooling rate at the tail of the mushy zone is larger in the simulation with
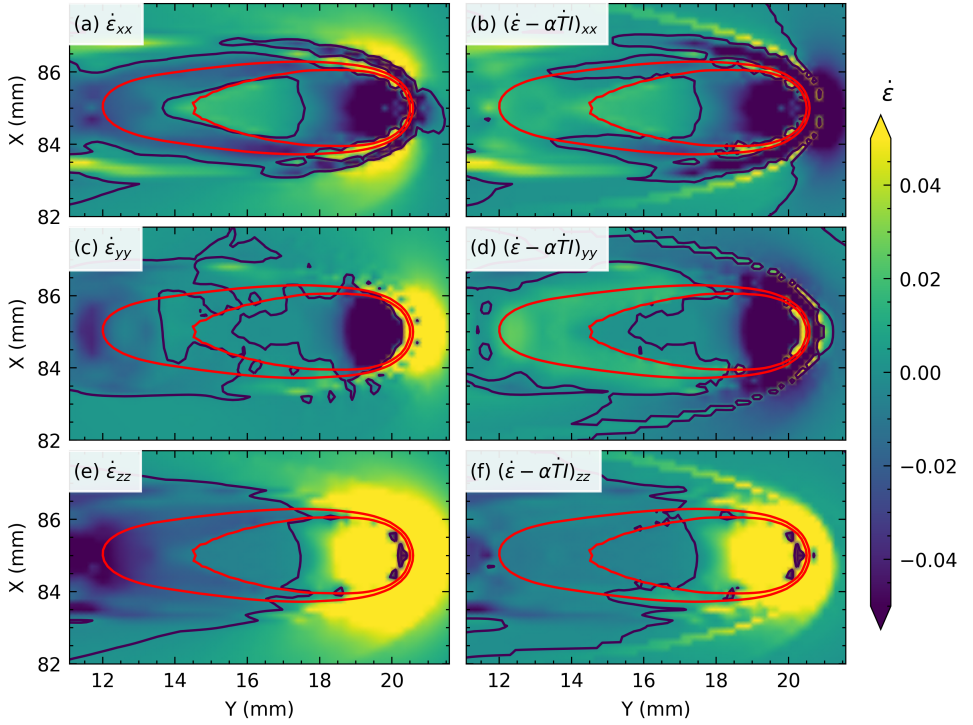
Figure 6.4: The profiles of $\dot{\varepsilon}_{xx}$ (a), $\dot{\varepsilon}_{yy}$ (c), $\dot{\varepsilon}_{zz}$ (e), $(\dot{\varepsilon} - \alpha\dot{T}I)_{xx}$ (b), $(\dot{\varepsilon} - \alpha\dot{T}I)_{yy}$ (d) and $(\dot{\varepsilon} - \alpha\dot{T}I)_{zz}$ (f) in the simulation with $v = 10\,\text{mm/s}$ at the time when laser center is at $y = 20\,\text{mm}$. The blue lines are the contour lines for zero strain rate. The red lines are the isotherms of the liquidus temperature T_l and the solidus temperature T_s.
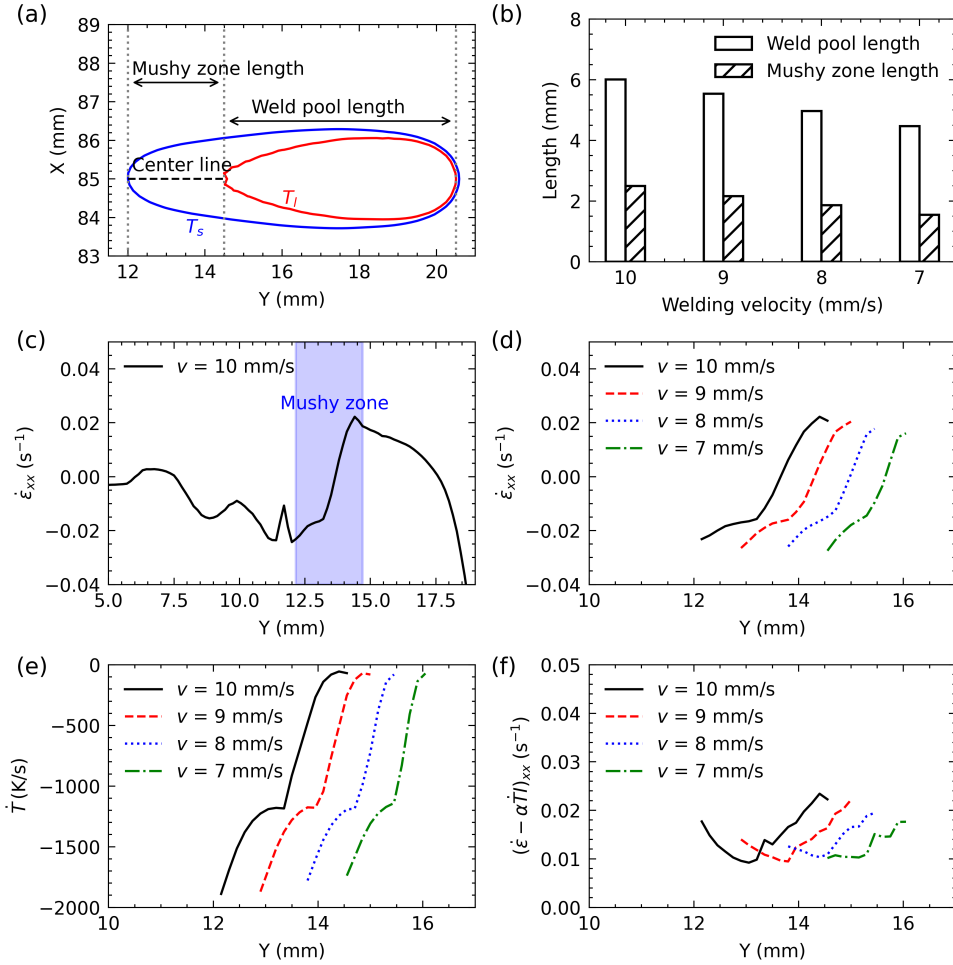
Figure 6.5: The weld pool length and the mushy zone length in the simulations with different welding velocities are determined based on the configuration shown in (a), and the results are given in (b). The strain rate component $\dot{\varepsilon}_{xx}$, the temperature changing rate $\dot{T}$ and the effective strain rate component $(\dot{\varepsilon} - \alpha \dot{T} I)_{xx}$ along the center line in the mushy zone of different simulations are given in (d), (e) and (f), respectively.

a larger welding velocity. When the strain rate contribution from thermal contraction is considered, the effective strain rate $(\dot{\varepsilon} - \alpha \dot{T} I)_{xx}$ is positive in the mushy zone of each simulation, as shown in Figure 6.5 (f). With decreasing temperature, the strain rate $\dot{\varepsilon}_{xx}$ decreases while the cooling rate increases, resulting in a valley shape in the effective strain curve. Moreover, the effective strain rate in the simulation with a larger welding velocity tends to be larger, representing a higher solidification cracking susceptibility.

6.3.2 The microstructure

Based on the temperature profile from the thermal-mechanical analysis, the microstructure in the weld pool is simulated with a 3D CAFE model with a cell size of $5.0\,\mu m$. The simulated microstructures on the top plane with different welding velocities are shown in Figure 6.6. The microstructure is initialized randomly with a Voronoi tessellation. As the laser moves along the welding path, solid grains melt and the weld pool forms. Upon cooling, the grains at the boundary of the weld pool grow epitaxially into the weld pool and compete with each other. The grains with their preferential growth directions parallel with the temperature gradient win the competition and form large columnar grains. As solidification proceeds from the weld pool boundary to the center, the solid-liquid interface changes from parallel to the welding direction to perpendicular to the welding direction, leading to an increase in the solidification velocity. The increase in the solidification velocity promotes the columnar-to-equiaxed transition (CET). As shown in Figure 6.6 (a), some small equiaxed grains are observed in the center of the solidified microstructure. For a better illustration, the grain morphology in the cross section (YZ-plane) in the different simulations are shown in Figure 6.7. With increasing welding velocity, the number of equiaxed grains in the weld center increases. This agrees with the experimental finding that increasing welding velocity promotes CET [11]. In the simulation with the lowest welding velocity ($v = 7.0\,mm/s$), as shown in Figure 6.6 (d) and Figure 6.7 (d), some columnar grains propagating in the welding direction are observed in the weld center. Those grains are formed due to the elliptical weld pool shape and the low fraction of equiaxed grains. This agrees with the experimental observation from Agarwal et al. [29], in which grains bend towards the weld center line.

It has been reported [33] that grain refinement helps to prevent solidification cracking. In the work of Schempp et al. [11], the grain refinement effect introduced by CET successfully inhibits solidification cracking. In general, a finer microstructure reduces the separation velocity exerted on each liquid channel, leading to a decrease in solidification cracking susceptibility. In the current case, the fraction of the equiaxed grains increases with increasing welding velocity. However, the fraction of equiaxed grains is still very small, which is not enough to prevent solidification cracking.

6.3.3 The pressure profile in the mushy zone

The pressure profile in the liquid channel can be obtained by solving Equation (6.14) based on the temperature profile, strain rate profile and the microstructure. In each simulation, the pressure calculation is performed at the time when the laser center is at $y = 20\,mm$. The profiles of variables including pressure p, grain distance λ and separation velocities due to solidification shrinkage v_s and mechanical constraints v_m on the top plane in the pressure calculation with $v = 10\,mm/s$ are given in Figure 6.8. In the pressure drop calculation, the
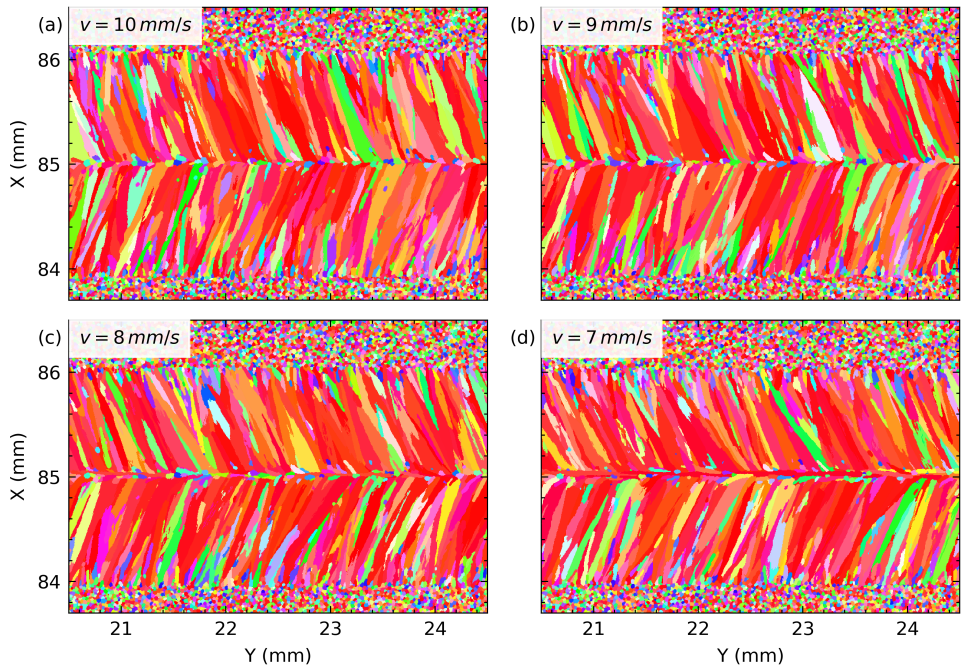
Figure 6.6: The microstructure in the top plane (XY-plane) in the simulations with different welding velocities: $v = 10\,mm/s$ (a), $v = 9\,mm/s$ (b), $v = 8\,mm/s$ (c) and $v = 7\,mm/s$ (d).
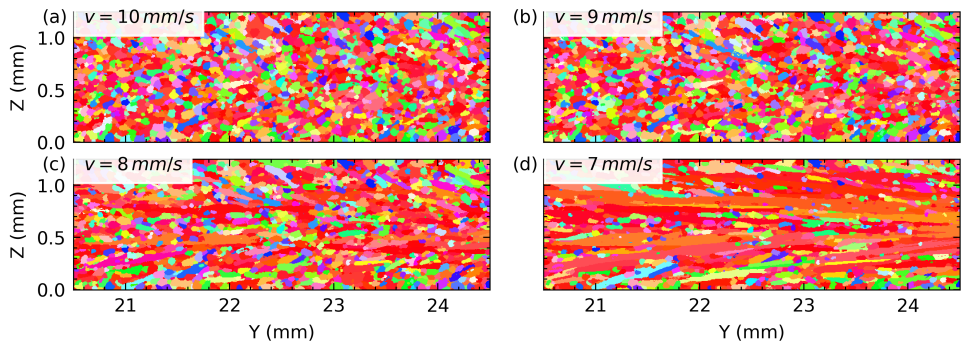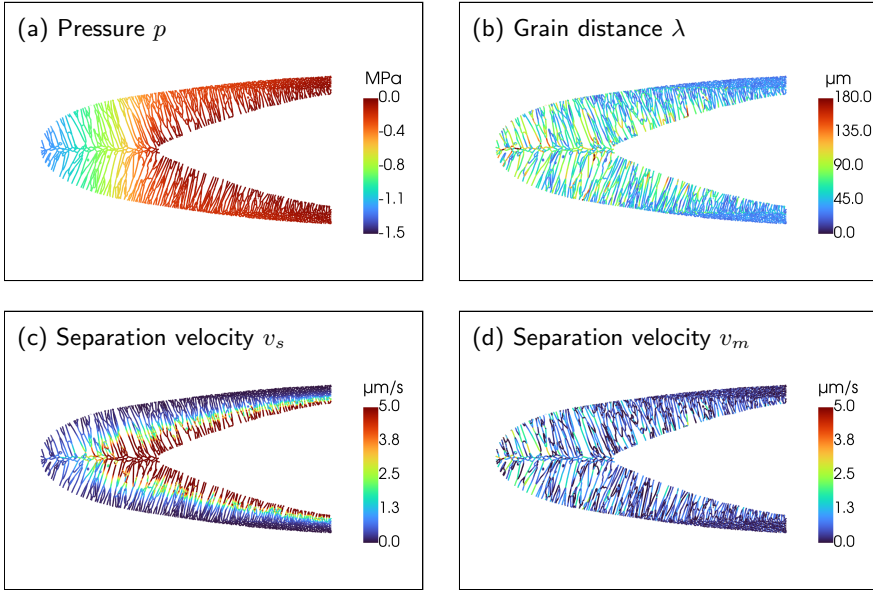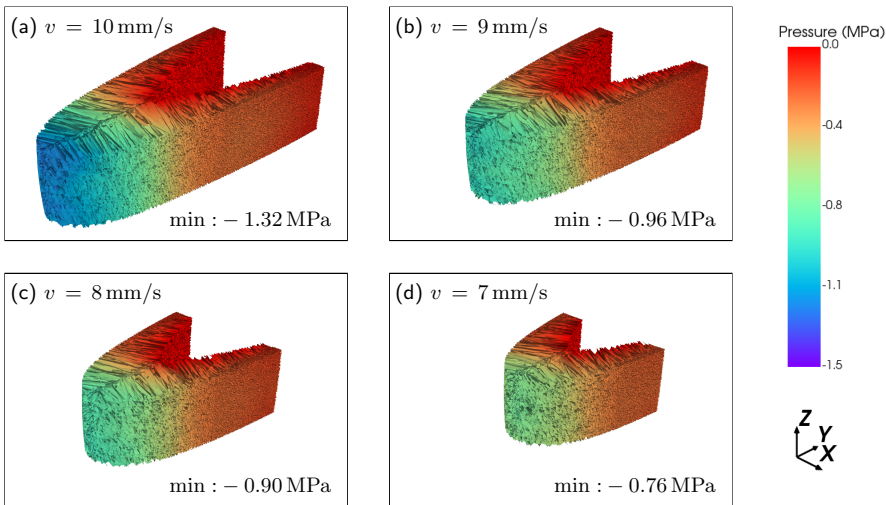

Figure 6.7: The microstructure in the cross section (YZ-plane) in the simulations with different welding velocities: $v = 10\,mm/s$ (a), $v = 9\,mm/s$ (b), $v = 8\,mm/s$ (c) and $v = 7\,mm/s$ (d).

grain distance is estimated based on the simulated microstructure, as shown in Figure 6.8 (b). The grain distance near the weld pool boundary is small due to the growth competition between the grains with different orientations. As solidification proceeds to the weld pool center, the grains with favorable orientations win the competition and grow into large columnar grains, leading to large grain distance values. In the weld pool center, some small grain distance values are observed between equiaxed grains. Based on the estimated grain distance for each liquid channel element, the half width of the liquid channel h and the separation velocities due to solidification shrinkage v_s and mechanical constraints v_m can be calculated. As shown in the Figure 6.8 (c), the separation velocity due to solidification shrinkage v_s is large in the high temperature region, where the solid fraction increases rapidly. Conversely, the separation velocity due to mechanical constraints v_m is large in the liquid channel segments related with large grain distances. Thus, the separation velocity due to mechanical constraints v_m dominates the liquid channel separation at the tail of the mushy zone, contributing to an increased pressure drop and hence increased sensitivity to solidification cracking. With the profiles of the half width of the liquid channel h and the separation velocities (v_s and v_m), the profile of liquid pressure in the liquid channel network can be obtained by solving Equation (6.14), as shown in Figure 6.8 (a). At the solid-liquid interface, a Dirichlet boundary condition is applied, where the pressure is set to zero. Due to liquid channel separation introduced by solidification shrinkage and mechanical constraints, the liquid pressure drops along the liquid channel network. The pressure drop is more rapid in the direction parallel to the welding direction compared to the pressure drop in the direction perpendicular to the welding direction. In this case, the lowest pressure is observed at the tail of the mushy zone. This agrees with the fact that solidification cracking occurs in the center of the weld.

A 3D view of the pressure profiles in the simulations with different welding velocities is presented in Figure 6.9. With increasing welding velocity, the minimum pressure decreases, indicating an increase in the hot cracking susceptibility. According to Agarwal et al. [6], solidification cracking occurs in the experiments with $v = 10\,\mathrm{mm/s}$, $v = 9\,\mathrm{mm/s}$ and $v = 8\,\mathrm{mm/s}$, while no solidification crack is observed in the experiment with $v = 7\,\mathrm{mm/s}$. Thus, the simulation results agree well with the experimental observations.

Figure 6.8: The profiles of pressure p (a), grain distance λ (b) and separation velocities due to solidification shrinkage v_s (c) and mechanical constraints v_m (d) on the top plane in the pressure calculation with $v = 10\,\text{mm/s}$.

Figure 6.9: The pressure profiles in the liquid channel network in the mushy zone in the different simulations with different welding velocities: $v = 10\,\text{mm/s}$ (a), $v = 9\,\text{mm/s}$ (b), $v = 8\,\text{mm/s}$ (c) and $v = 7\,\text{mm/s}$ (d).

6.4 Discussion

6.4.1 Influence of the welding velocity on solidification cracking

In the current work, the effects of increasing welding velocity while keeping the ratio between the power and the welding velocity constant have been studied within a multi-scale multi-physics framework. With increasing welding velocity, the mushy zone length increases, which is unfavorable for liquid feeding. Moreover, with increasing welding velocity, the strain rate component ε_{xx} in the mushy zone shifts towards the tensile region and the cooling rate in the tail of the mushy zone becomes larger. In this case, the effective strain rate becomes larger. Increasing welding velocity promotes CET and increases the fraction of equi-axed grains in the center of the weld pool. However, the fraction of the equi-axed grains is too small to prevent solidification cracking. In the pressure drop calculation, with increasing welding velocity, as a result of the increased mushy zone length, increased cooling rate and increased effective strain rate, the minimum pressure becomes lower, indicating a higher chance of solidification cracking. The findings from the simulations match the observation from the work of Agarwal et al. [29], in which decreasing welding velocity to 7 mm/s inhibits solidification cracking. That increasing welding velocity increases solidification cracking susceptibility was also confirmed in other experimental works [7, 34, 35].

6.4.2 Influence of grain refinement on solidification cracking

Grain refinement has proven to be an effective method to prevent solidification cracking. In the work of Schempp et al. [11], the grain refinement introduced by the columnar-to-equiaxed transition when increasing the welding velocity inhibits solidification cracking. Opprecht et al. [33] employed yttrium stabilized zirconia as a grain refiner and successfully eliminated solidification cracking in aluminum alloys manufactured by laser beam melting.

The current modelling framework is employed to investigate the influence of the grain refinement on SCS. To mimic the grain refinement effect, the nucleation density N_0 has been artificially increased from $5 \times 10^{12}\,\mathrm{m}^{-3}$ to $2 \times 10^{13}\,\mathrm{m}^{-3}$, $4 \times 10^{13}\,\mathrm{m}^{-3}$ and $8 \times 10^{13}\,\mathrm{m}^{-3}$ for the microstructure simulation with welding velocity 10 mm/s. With increasing nucleation density, the fraction of equiaxed grains in the center of the weld pool increases and the grain size decreases, as shown in Figure 6.10. The simulated microstructure is then employed for pressure drop calculation. The simulated pressure drop values are given in Figure 6.11 (b). With decreasing grain size, the minimum pressure drops, indicating an increase in SCS. This contradicts the experimental observations [11, 33]. However, this can be explained with the governing equation for the pressure drop calculation Equation (6.14). The separation velocities v_s and v_m and the half width of the liquid channel h are approximately linear with the grain radius r. With decreasing grain radius r, the separation velocities and the half width of the liquid channel h becomes smaller. The decrease in the separation velocities favors a decrease in SCS, while the decrease in the half width of the liquid channel h indicates a decrease in the permeability, leading to an increase in SCS. After transformation of Equation (6.14), it is clear that $\nabla^2 p$ is proportional to $(v_s + v_m)/h^3$ or $1/r^2$. In this case, with decreasing grain radius, the effect of permeability dominates and
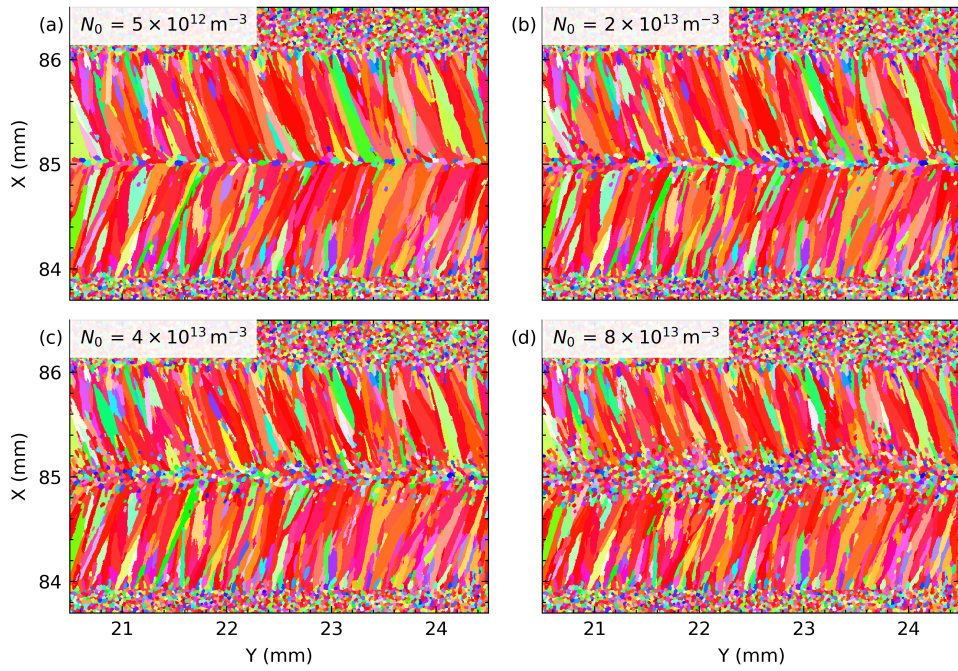
Figure 6.10: The simulated microstructure on the top surface with different nucleation density, N_0: $5 \times 10^{12} \, \text{m}^{-3}$ (a), $2 \times 10^{13} \, \text{m}^{-3}$ (b), $4 \times 10^{13} \, \text{m}^{-3}$ (c) and $8 \times 10^{13} \, \text{m}^{-3}$ (d).
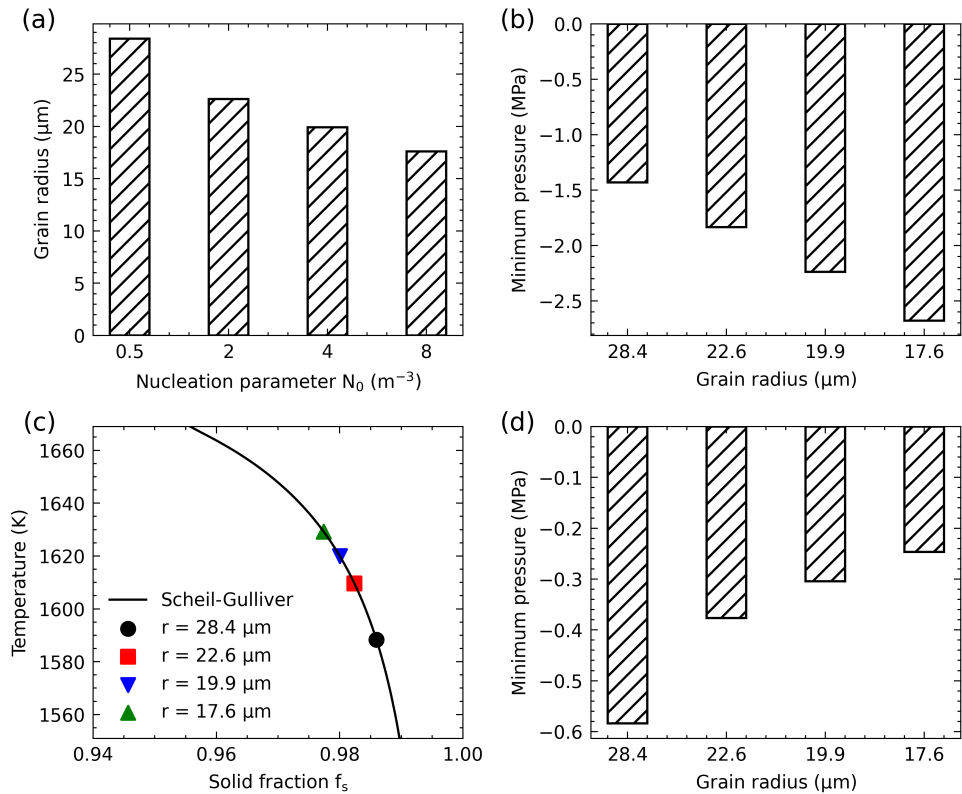
Figure 6.11: The grain size in the equiaxed zone of simulations with different nucleation density N_0 is shown in (a). The calculated minimum liquid pressure for each simulation is given in (b). Different grain size corresponds to different critical solid fraction and temperature for liquid channel coalescence (c). The minimum pressure for each simulation is recalculated considering the influence of the grain size on the coalescence temperature (d).

SCS increases. Although this is mathematically correct, the result is still not physically reasonable. The reason is that the influence of the grain size on the coalescence temperature of the liquid channel is not considered. As shown in the previous section, decreasing the primary dendrite arm spacing leads to an earlier coalescence of the liquid channel. Here, by assuming the liquid channel closes at a critical width (0.2 μm), the critical solid fraction and temperature for liquid channel coalescence can be determined, as shown in Figure 6.11 (c). Then, the pressure profiles in the mushy zone are recalculated for each simulation and the minimum pressures in the liquid channel network of each simulation are given in Figure 6.11 (d). With decreasing grain radius, the minimum pressure decreases, indicating a decrease in SCS, which agrees well with the experimental results.

6.4.3 INFLUENCE OF ALLOY COMPOSITION ON SOLIDIFICATION CRACKING

Alloy composition has a large impact on the solidification path and thus SCS. Here, the SCS of the considered TRIP steel is compared with the SCS of a DP steel, which is not susceptible to solidification cracking [29]. The solidification curves of the TRIP steel and the DP steel are obtained with Scheil-Gulliver calculations in Thermo-Calc, as shown in Figure 6.12. The liquidus temperature of the TRIP steel and the DP steel is similar. For the two steel grades, ferrite forms at the beginning of the solidification. After the peri-eutectic temperature is reached, austenite forms. Due to the compositional difference, TRIP steel has a more significant segregation in the liquid and has a larger freezing temperature range. The corresponding solidification temperature for $f_s = 0.98$ for the TRIP steel is around 200 K lower than that of the DP steel. Thus, it can be expected that the TRIP steel has a larger SCS compared to the DP steel. To quantify the difference in SCS, the solidification curve of the DP steel is employed in the pressure drop calculation with $v = 10$ mm/s. Here, only the solidification path is changed, while the temperature profile, the strain rate profile and the microstructure are still from the simulations for TRIP steel experiments. With the solidification path of the DP steel, the freezing temperature range is smaller, leading to a smaller mushy zone. The minimum pressure calculated with the DP solidification curve is −0.095 MPa, which is higher compared to the value −1.32 MPa calculated with the TRIP solidification curve. This agrees with the experimental result that the DP steel is not susceptible to solidification cracking [29].

Note that alloy composition also has an impact on the thermal material properties including the specific heat c_p, the thermal conductivity k and the latent heat, which influences the weld pool shape and the mushy zone length. In general, with a smaller specific heat or a larger thermal conductivity, the length of the mushy zone becomes shorter, leading to a smaller SCS. In addition, the columnar-to-equiaxed transition can be promoted by tuning the alloy composition to achieve favorable solidification kinetics and nucleation behavior, which reduces SCS.
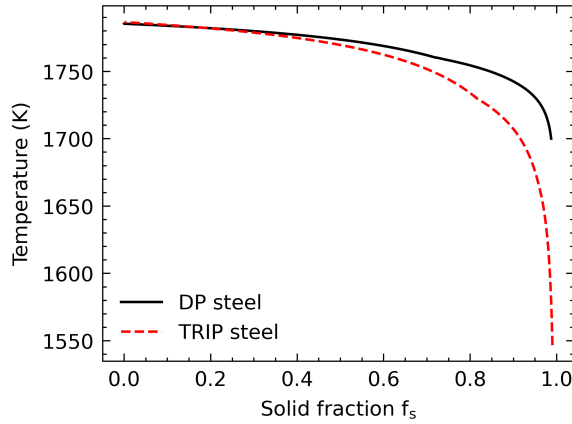
Figure 6.12: The $T \sim f_s$ solidification curves from Scheil-Gulliver calculations for the considered TRIP steel and DP steel.

6.5 CONCLUSIONS

In this work, a multi-scale multi-physics modelling framework has been developed to predict solidification cracking susceptibility (SCS) during welding. The modelling framework includes a thermo-mechanical model to simulate temperature and strain rate profiles during welding, a cellular automata model to simulate solidified microstructure in the weld pool and a granular model to calculate pressure profiles in the liquid channel network. The developed modelling framework is verified by comparing with welding experiments of TRIP steel. The modelling framework is able to capture the influence of the process parameters, grain refinement and alloy composition on SCS.

For welding with a constant ratio between the power and the welding velocity, increasing welding velocity increase the length of the mushy zone, resulting in a drop in the minimum pressure in the liquid channel network and thus an increase in SCS. Meanwhile, increasing welding velocity promotes columnar to equiaxed transition, which can inhibit solidification cracking for some alloys.

Grain refinement leads to a decrease in the separation velocities of the liquid channel interfaces and the permeability of the liquid channel network, favoring an increasing in SCS. Meanwhile, it also increases the coalescence temperature of liquid channels, favoring a decrease in SCS. As a combined effect, SCS decreases by refining the microstructure.

For alloys with a smaller freezing temperature range, the size of the mushy zone and the pressure drop in the mushy zone are smaller, resulting in a decrease in solidification cracking susceptibility.

REFERENCES

[1] Stuart Keeler and Menachem Kimchi. *Advanced high-strength steels application guidelines V5.* WorldAutoSteel, 2015.

[2] Nicolas Coniglio and CE Cross. Effect of weld travel speed on solidification cracking

behavior. part 1: weld metal characteristics. *The International Journal of Advanced Manufacturing Technology*, 107:5011–5023, 2020.

[3] Nicolas Coniglio and CE Cross. Effect of weld travel speed on solidification cracking behavior. part 2: testing conditions and metrics. *The International Journal of Advanced Manufacturing Technology*, 107:5025–5038, 2020.

[4] A Slyvinsky, H Herold, and M Streitenberger. Influence of welding speed on the hot cracking resistance of the nickel-base alloy nicr25fealy during tig-welding. *Hot Cracking Phenomena in Welds*, pages 42–58, 2005.

[5] GM Goodwin. The effects of heat input and weld process on hot cracking in stainless steel. *Weld J*, 67(4):88s–94s, 1988.

[6] Gautam Agarwal, He Gao, Murugaiyan Amirthalingam, and Marcel Hermans. Study of solidification cracking susceptibility during laser welding in an advanced high strength automotive steel. *Metals*, 8(9):673, 2018.

[7] S Ohshita, N Yurioka, N Mori, and T Kimura. Prevention of solidification cracking in very low carbon steel welds. *WELDING J.*, 62(5):129, 1983.

[8] Masakazu Shibahara, Hisashi Serizawa, and Hidekazu Murakawa. Finite element method for hot cracking using temperature dependent interface element (report ii): Mechanical study of houldcroft test (mechanics, strength & structure design). *Transactions of JWRI*, 29(1):59–64, 2000.

[9] Suyitno, VI Savran, L Katgerman, and DG Eskin. Effects of alloy composition and casting speed on structure formation and hot tearing during direct-chill casting of al-cu alloys. *Metallurgical and Materials Transactions A*, 35:3551–3561, 2004.

[10] E Cicală, G Duffet, H Andrzejewski, D Grevey, and S Ignat. Hot cracking in al–mg–si alloy laser welding–operating parameters and their effects. *Materials Science and Engineering: A*, 395(1-2):1–9, 2005.

[11] Philipp Schempp, CE Cross, Andreas Pittner, Gabriele Oder, R Saliwan Neumann, Heidemarie Rooch, Ilona Dörfel, Werner Österle, and Michael Rethmeier. Solidification of gta aluminum weld metal: Part 1—grain morphology dependent upon alloy composition and grain refiner content. *Weld. J*, 93(2):53s–59s, 2014.

[12] He Gao, Gautam Agarwal, Muru Amirthalingam, MJM Hermans, and IM Richardson. Investigation on hot cracking during laser welding by means of experimental and numerical methods. *Welding in the World*, 62:71–78, 2018.

[13] Tayfun Soysal and Sindo Kou. A simple test for assessing solidification cracking susceptibility and checking validity of susceptibility prediction. *Acta Materialia*, 143:181–197, 2018.

[14] Nasim Bakir, V Pavlov, S Zavjalov, S Volvenko, Andrey Gumenyuk, and Michael Rethmeier. Development of a novel optical measurement technique to investigate the hot cracking susceptibility during laser beam welding. *Welding in the World*, 63:435–441, 2019.

[15] M Rappaz, J M Drezet, and Met Gremaud. A new hot-tearing criterion. *Metallurgical and materials transactions A*, 30:449–455, 1999.

[16] Sindo Kou. A criterion for cracking during solidification. *Acta Materialia*, 88:366–374, 2015.

[17] Jiangwei Liu and Sindo Kou. Crack susceptibility of binary aluminum alloys during solidification. *Acta Materialia*, 110:84–94, 2016.

[18] Chu Han, Ping Jiang, Shaoning Geng, Song Gao, Gaoyang Mi, and Chunming Wang. Multiphase-field simulation of grain coalescence behavior and its effects on solidification cracking susceptibility during welding of al-cu alloys. *Materials & Design*, 211:110146, 2021.

[19] Lei Wang, Nan Wang, and Nikolas Provatas. Liquid channel segregation and morphology and their relation with hot cracking susceptibility during columnar growth in binary alloys. *Acta Materialia*, 126:302–312, 2017.

[20] Shaoning Geng, Ping Jiang, Xinyu Shao, Gaoyang Mi, Han Wu, Yuewei Ai, Chunming Wang, Chu Han, Rong Chen, Wei Liu, et al. Effects of back-diffusion on solidification cracking susceptibility of al-mg alloys during welding: A phase-field study. *Acta Materialia*, 160:85–96, 2018.

[21] Laishan Yang, Jing Yang, Fang Han, Zhihang Zhang, Qinghua Li, Zhibo Dong, Lei Wang, Nana Ofori-Opoku, and Nikolas Provatas. Hot cracking susceptibility prediction from quantitative multi-phase field simulations with grain boundary effects. *Acta Materialia*, 250:118821, 2023.

[22] Xiaohui Liang, Cornelis Bos, Marcel Hermans, and Ian Richardson. Influence of the temperature gradient and the pulling velocity on solidification cracking susceptibility during welding: A phase field study. *Materials & Design*, 235:112424, 2023.

[23] M Sistaninia, AB Phillion, J-M Drezet, and M Rappaz. Three-dimensional granular model of semi-solid metallic alloys undergoing solidification: Fluid flow and localization of feeding. *Acta materialia*, 60(9):3902–3911, 2012.

[24] M Sistaninia, S Terzi, AB Phillion, J-M Drezet, and M Rappaz. 3-d granular modeling and in situ x-ray tomographic imaging: A comparative study of hot tearing formation and semi-solid deformation in al–cu alloys. *Acta materialia*, 61(10):3831–3841, 2013.

[25] HR Zareie Rajani and AB Phillion. A mesoscale solidification simulation of fusion welding in aluminum–magnesium–silicon alloys. *Acta materialia*, 77:162–172, 2014.

[26] HR Zareie Rajani and AB Phillion. 3-d multi-scale modeling of deformation within the weld mushy zone. *Materials & Design*, 94:536–545, 2016.

[27] HR Zareie Rajani and AB Phillion. 3d multi-scale multi-physics modelling of hot cracking in welding. *Materials & Design*, 144:45–54, 2018.

[28] Aurélie Niel, Frédéric Deschaux-Beaume, Cyril Bordreuil, Gilles Fras, and J-M Drezet. Hot tearing test for tig welding of aluminum alloys: application of a stress parallel to the fusion line. In *Hot cracking phenomena in welds III*, pages 43–58. Springer, 2011.

[29] Gautam Agarwal, A Kumar, IM Richardson, and MJM Hermans. Evaluation of solidification cracking susceptibility during laser welding in advanced high strength automotive steels. *Materials & Design*, 183:108104, 2019.

[30] L Nastac. Numerical modeling of solidification morphologies and segregation patterns in cast dendritic alloys. *Acta Materialia*, 47(17):4253–4262, 1999.

[31] Michael A Groeber and Michael A Jackson. Dream. 3d: a digital representation environment for the analysis of microstructure in 3d. *Integrating materials and manufacturing innovation*, 3:56–72, 2014.

[32] Essam Ahmed Ali Ahmed. *Laser welding of advanced high strength steels*. PhD thesis, Aachen, Techn. Hochsch., Diss., 2011, 2011.

[33] Mathieu Opprecht, Jean-Paul Garandet, Guilhem Roux, Camille Flament, and Mathieu Soulier. A solution to the hot cracking problem for aluminium alloys manufactured by laser beam melting. *Acta Materialia*, 197:40–53, 2020.

[34] TW Nelson, JC Lippold, W Lin, and WA Baeslack III. Evaluation of the circular patch test for assessing weld solidification cracking, part i–development of a test method. *Welding Journal-Including Welding Research Supplement*, 76(3):110–119, 1997.

[35] Z Feng, T Zacharia, and S David. On the thermomechanical conditions for weld metal solidification cracking. In *77 th Annual AWS Convention Abstracts*, page 1996, 1996.

7

General discussions, conclusions and outlook

7

7.1 General discussions and conclusions

In this research, solidification cracking has been studied with two different approaches: a microscopic modelling approach (Chapter 3 and Chapter 4) and a multi-scale modelling approach (Chapter 5 and Chapter 6).

In Chapter 3, solidification microstructure is studied with a cellular automata (CA) model. Two improvements have been made to enhance the accuracy of the CA model, which calculates the growth velocity based on the kinetic undercooling at the interface.

Firstly, a new diffusion term has been proposed to handle the diffusion between the interface cells and the liquid cells, in which the diffusion out of an interface cell is calculated by summing up the projections of diffusion fluxes onto the interface normal direction. The new diffusion term minimizes the overestimation of tip velocity when the tip cell is surrounded by three liquid cells in its von Neumann neighborhood and improves the behavior in mesh size convergence. Secondly, a solute redistribution method has been applied for each interface cell to resolve the mass balance error introduced by the virtual liquid cell assumption, which is common in existing CA models. The improved CA model is validated by simulating single dendritic solidification and comparing the tip velocity with the Kurz-Giovanola-Trivedi (KGT) model. With the improvements in the aspects of mesh-size independency and mass balance, the developed CA model is suitable for solidification simulation with a high undercooling, as is common in welding. It also provides an easier way to achieve multi-component solidification simulation compared to conventional CA solidification models, which need to solve a system of mass balance equations in interface cells. Despite the improvements made, due to the poor discretization of the solid-liquid interface, the CA method is less accurate compared to the phase field method. Another limitation of the CA approach is that no CA models can reproduce the dendrite tip velocity predicted by a Green function method in single-dendritic solidification simulations; this remains a challenge for future research.

For better accuracy, a phase field (PF) model has been employed to simulate the segregation in the liquid channels in the mushy zone during welding (Chapter 4). The solidification cracking susceptibility (SCS) is quantified by calculating the pressure drop from the dendrite tip to the coalescence point of the liquid channels with the Rappaz-Drezet-Gremaud (RDG) model. In this microscopic approach, the complex solidification condition in the weld pool is approximated with a directional solidification condition defined with constant temperature gradient and pulling velocity, while the tensile load on the liquid channel is estimated with a fixed strain rate. With the modelling setup, the influence of the temperature gradient and the pulling velocity on SCS has been studied with and without considering the dependence of the primary dendrite arm spacing on the temperature gradient and the pulling velocity. In this work, large-scale simulations are achieved by reducing the computational cost with adaptive mesh refinement. By explicitly simulating the formation of dendrites and liquid channels, the PF simulations at the microscopic scale include the influence of the pulling velocity on the dendrite tip temperature and the effects introduced by finite diffusivities, thus providing a more accurate prediction of the segregation in the liquid channels and the coalescence of the liquid channels compared to Scheil-Gulliver calculations, which assume infinite diffusivities in the liquid. Coupled with the RDG model, the microscopic approach successfully captures the influence of parameters governing behaviors at the microscopic scale like the temperature gradient, the pulling velocity and the primary dendrite arm

spacing, etc. However, due to the fine discretization and the high computational cost, the simulation domain size is limited. Moreover, the influence of processing parameters cannot be directly captured, due to the lack of macroscopic modelling. Additionally, the solidification condition and strain rate employed in the RDG model come from estimations at a specific site of the weld pool and do not represent the whole weld pool.

Different from the microscopic approach, which has a limited domain size, the multi-scale approach aims to derive a full-field simulation of the full weld pool. To this purpose, a cellular automata finite element (CAFE) model has been developed to simulate microstructure evolution within the whole weld pool, which is described in Chapter 5. Compared to conventional CAFE models, the CAFE model presented in this work is faster by up to two orders of magnitude due to the adoption of a large time step without compromising the accuracy, and by implementing shared-memory parallelism and a subdomain activation-and-deactivation method. The developed CAFE model is validated by simulating the grain morphology and the texture in additively manufacturing samples, which match the experimental results. With the improvements in the simulation speed, the developed CAFE model is applicable in the development of digital twins of additive manufacturing. However, it is necessary to indicate that segregation in the liquid channels and sub-grain structures like columnar dendrites cannot be obtained from the CAFE simulations, as CAFE models do not solve the concentration profile numerically.

With microstructure modelling of the whole weld pool achievable, a multi-scale multi-physics modelling framework was further developed to predict solidification cracking under various welding conditions, as described in Chapter 6. This modelling framework includes three models: a finite element thermal-mechanical model to simulate the profiles of temperature and strain rate of the welded component, a CAFE model to simulate solidified microstructure in the weld pool and a granular model to calculate pressure drop in the mushy zone. The multi-scale multi-physics modelling framework has been validated with the laser welding experiments of a TRIP steel. By capturing major physical mechanisms for solidification cracking, the multi-scale multi-physics modelling framework successfully predicts the influence of alloy composition, microstructure and processing parameters on SCS, which agrees with the experimental results. However, it does have some limitations. The liquid channel network is estimated based on Scheil-Gulliver calculations and the simulated grain morphology, which is less accurate than phase field simulations. Additionally, the strain rate profile is directly mapped from the thermal-mechanical analysis to the granular model for pressure drop calculation, which is a coarse approximation and limits the accuracy of the modelling framework. It is also assumed that deformation only occurs in the liquid, which is not valid near the coalescence point of the liquid channels. In this case, the pressure drop in the liquid channel network might be overestimated.

The following conclusions can be drawn based on the studies with different approaches.

- In the microscopic modelling approach, the microstructure model explicitly simulates the structure and the coalescence behavior of the liquid channel and the segregation in the liquid. The segregation calculation is more accurate compared to Scheil-Gulliver calculations. The microscopic approach is favorable when the influence of microscopic features on SCS is of interest.

- The multi-scale multi-physics modelling framework incorporates major physical

mechanisms associated with solidification cracking. It is capable of predicting solidification cracking under various welding conditions and captures the influence of alloy composition, microstructure and processing parameters like power and welding velocity, etc. Therefore, it provides a theoretical basis to avoid solidification cracking in real applications.

- At a microscale, decreasing the pulling velocity decreases the tensile load due to solidification shrinkage, leading to a decrease in the pressure drop and SCS. Increasing the temperature gradient decreases the liquid channel length, leading to a decrease in the pressure drop and SCS. Decreasing the PDAS promotes the liquid channel coalescence, resulting in a decrease in SCS. Therefore, solidification cracking can be reduced by decreasing the pulling velocity or increasing the temperature gradient or refining the grains.

- For welding with a constant ratio between the power and the welding velocity, decreasing the welding velocity leads to a smaller mushy zone length and thus a smaller pressure drop in the mushy zone, which is favorable to reduce the risk of solidification cracking. Conversely, for welding with a constant power, increasing the welding velocity leads to a smaller weld pool and smaller tensile loading in the mushy zone, which reduces solidification cracking risk.

- For alloys with a high nucleation rate, increasing the welding velocity can promote the columnar-to-equiaxed transition in the center of the weld pool, which inhibits solidification cracking. Reducing the grain size by adding grain refiners has a similar effect.

- The alloy composition can be tuned to reduce the freezing temperature range and the heat transfer coefficients, leading to a smaller mushy zone and a decrease in SCS. It is the most efficient way to reduce the risk of solidification cracking.

7.2 OUTLOOK

In this thesis, solidification cracking has been studied with a microscopic approach and a multi-scale approach. Both approaches have their limitations and require further improvement. Future work could be done in the following aspects.

- The microscopic approach has never been employed to study solidification cracking with peri-eutectic reaction, which, nevertheless, is common for solidification of steels. In steels, solidification starts with the formation of ferrite and then austenite forms after the peri-eutectic temperature is reached. Simulations of the peri-eutectic reaction are achievable with phase field models but require lots of efforts. The peri-eutectic reaction has an impact on the segregation, the structure and the coalescence behavior of the liquid channels, which influence SCS.

- In the multi-scale multi-physics modeling framework, the liquid channel network is approximated based on the grain boundary structure and the Scheil-Gulliver calculation, which is less accurate compared to the microscopic phase field simulations. In this case, the influence of the sub-grain structure like the columnar dendrites

which belong to the same grain can not be captured. This limits the application of the macroscopic approach in additive manufacturing. It is an interesting topic to quantify and minimize the error introduced by this approximation.

- In the multi-scale multi-physics modeling framework, the strain rate profile is directly mapped from the thermal-mechanical analysis to the granular model when calculating the separation velocity for the liquid channels, which is a coarse approximation. In the future, a hydromechanical simulation should be performed to determine the separation velocity of the liquid channels in the mushy zone under the boundary conditions determined from the thermal-mechanical analysis, in which the pressure in the liquid should be balanced by the stress in the solid. However, it is a challenging task to perform such a calculation for the whole mushy zone.

- In the multi-scale multi-physics modeling framework, it is assumed that deformation occurs only in the liquid upon a tensile load. This assumption is correct when the solid fraction is small and the liquid channel width is large. For the liquid channel part near the coalescence point, the solid fraction is close to 1.0 and the deformation in the solid cannot be neglected. Neglecting the deformation in the solid may lead to an overestimation of the separation velocity for the liquid channel and thus an overestimated SCS. Further studies are necessary to reduce this error.

- The multi-scale multi-physics modelling framework has been validated with the laser welding experiments of a TRIP steel. To make this modelling framework more robust and to improve this modelling framework, more welding experiments can be performed under different welding conditions and with different alloys.

- In the current CAFE models for microstructure simulations, the nucleation parameters have been determined by fitting experimental results. Further work could implement a physics-based nucleation model considering both homogeneous and heterogeneous nucleation in the weld pool. The homogeneous nucleation can be modelled by considering the undercooling in front of the solid-liquid interface while the heterogeneous nucleation needs to consider the effects of dendrite fracture due to fluid flow, which is challenging.

Acknowledgments

Xiaohui
Delft, November 2023

Curriculum Vitæ

Xiaohui Liang

Born on November 16 1993 in Henan, China

Education

10.2018-11.2023	PhD in Material Science and Engineering Delft University of Technology, the Netherlands
09.2015-06.2018	Master of Science in Metallurgical Engineering RWTH Aachen University, Germany
09.2011-06.2015	Bachelor of Science in Metallurgical Engineering University of Science and Technology Beijing, China

List of Publications

Journal articles

1. **Xiaohui Liang**, Cornelis Bos, Marcel Hermans, and Ian Richardson. "An Improved Cellular Automata Solidification Model Considering Kinetic Undercooling." Metallurgical and Materials Transactions B 54, no. 3 (2023): 1088-1098.

2. **Xiaohui Liang**, Cornelis Bos, Marcel Hermans, and Ian Richardson. "Influence of the temperature gradient and the pulling velocity on solidification cracking susceptibility during welding: A phase field study." Materials & Design 235 (2023): 112424.

3. **Xiaohui Liang**, Jianing Zhu, Vera Popovich, Marcel Hermans, Ian Richardson and Cornelis Bos. "Efficient texture prediction for additive manufacturing." Submitted to Nature Communications. Major revision.

4. **Xiaohui Liang**, Marcel Hermans, Cornelis Bos, and Ian Richardson. "Multi-scale modelling of solidification cracking during welding." To be submitted.

Co-authored articles

1. Jianing Zhu, Evgenii Borisov, **Xiaohui Liang**, Richard Huizenga, Anatoly Popovich, Vitaliy Bliznuk, Roumen Petrov, Marcel Hermans, and Vera Popovich. "Controlling microstructure evolution and phase transformation behavior in additive manufacturing of nitinol shape memory alloys by tuning hatch distance." Journal of Materials Science 57, no. 10 (2022): 6066-6084.

2. Jianing Zhu, Evgenii Borisov, **Xiaohui Liang**, Eduard Farber, M. J. M. Hermans, and V. A. Popovich. "Predictive analytical modelling and experimental validation of processing maps in additive manufacturing of nitinol alloys." Additive Manufacturing 38 (2021): 101802.

Included in this thesis.